

ABSTRACT

PETROCHENKO, PETER EVGENIYEVICH. Fabrication and Biological Evaluation of Micro- and Nanostructured Surfaces, Coatings, and 3D-printed Scaffolds to Improve Function and Biocompatibility of Medical Devices. (Under the direction of Dr. Roger J. Narayan and Dr. Peter L. Goering).

There is a considerable gap in nanotoxicological research on nanofeatured surfaces. The current understanding of nanomaterials and their toxicity is largely based from studies using discrete nanoparticle systems, which do not translate to surface mediated toxicity but are nevertheless useful for understanding the means of nanomaterials toxicity. Cytotoxicity in a discrete rare earth engineered nanoparticle model was investigated; internalization of nanoparticles by cells, supernatant toxicity, as well as the role of endotoxin in nanoparticle formulations was reported and discussed. Aside from nanoparticles, however, numerous current and proposed immobilized nanomaterials are of benefit to the medical device industry. Nanomaterials can be coated, etched or formed directly into the surface of a medical device, improving its antimicrobial activity, biocompatibility, material properties and much more. Several methods for reliable coating of immobilized nanomaterials were investigated in detail and a 3D printing method using two photon polymerization for creating free standing constructs was reported. Pulsed laser deposition was shown to have the capability of fabricating uniform controllable antimicrobial zinc oxide coatings as well as creating composite polymer/metal material coatings such as PMMA and silver. The leaching parameters from such surfaces were evaluated and toxicological *in vitro* exposure endpoints were drawn based on a given concentration of a toxic leachate, such as ionic zinc or silver. The amount of nanosilver coating into the PMMA composite was optimized to create a coating that was antibacterial but non-cytotoxic to human cells. Initial characterization of fabricated nanomaterials was given high importance due to the fundamental need of

understanding the physical and chemical basis of both adverse and desired toxicological outcomes. A variety of nanoscale features were characterized for their unique physicochemical characteristics (controllable roughness, enhanced UV absorption, adjustable stiffness) and were examined for their contribution to a number of observed unique biological responses (increased protein adsorption, enhanced cell proliferation, antimicrobial activity, and many others). Advancements in chemical coating methods of delicate nanomaterials structures were reported in both a ceramic nanoporous alumina model as well as a polymeric polyethersulfone (PES) model. Atomic layer deposition of titanium dioxide was shown to successfully coat intricate nanoporous alumina membranes without affecting their intrinsic permeability, while drastically improving the UV-protection of PES and preventing the resulting toxicity. In the field of 3D printing, the first instance of medium throughput fabrication of custom scaffold materials with submicron texture was demonstrated. The scaffold constructs were 3D printed from a custom designed elastomer that matched both the stiffness and the nanotexture experienced by cells in the bodily environment. The improvements in nanoscale fabrication of device surface coatings, chemical surface modification, and submicron 3D printing described in this thesis have advanced the current understanding of parameters that affect toxicity, biocompatibility, and long term success of medical devices incorporating nanotechnology.

© Copyright 2015 Peter Evgeniyevich Petrochenko

All Rights Reserved

Fabrication and Biological Evaluation of Micro- and Nanostructured Surfaces, Coatings, and
3D-printed Scaffolds to Improve Function and Biocompatibility of Medical Devices

by
Peter Evgeniyevich Petrochenko

A dissertation submitted to the Graduate Faculty of
North Carolina State University
in partial fulfillment of the
requirements for the degree of
Doctor of Philosophy

Biomedical Engineering

Raleigh, North Carolina
2015

APPROVED BY:

Dr. Roger J. Narayan
Committee Chair

Dr. Peter L. Goering

Dr. Albert Banes

Dr. Girish Kumar

Dr. H. Troy Nagle

Dr. Harold Pillsbury

DEDICATION

To my parents for inspiring me to pursue a career in science through their hard work and supporting me throughout this challenging and rewarding journey.

BIOGRAPHY

Peter Petrochenko received a B.S. in Biomedical Engineering with Distinction from the University of North Carolina at Chapel Hill, where he was also employed as a Research Assistant in Applied Mathematics. He continued with graduate studies in Biomedical Engineering at the joint Department of Biomedical Engineering at UNC-Chapel Hill and NC State Universities in August 2010 under the guidance of Dr. Roger J. Narayan. In November of 2010, he became a National Science Foundation Scholar-in-Residence at the U.S. Food and Drug Administration Center for Devices and Radiological Health under the supervision of Dr. Peter L. Goering. There he contributed to the scientific knowledge base for regulating devices incorporating nanotechnology. His work received a best poster award at the Nanotechnology Regulatory Science Research Workshop and he was a selected speaker at the Symposium on Toxicity Associated with Nanomaterials. He received the International Research Experience for Students in Micro Medical Manufacturing Award and the CV Starr Scholarship to travel to Vienna, Austria for the summers of 2012-2014, where he developed 3D printed cell scaffolds under the direction of Dr. Aleksandr Ovsianikov. He has been awarded several travel awards to present his work, including the Bern Schwetz travel award from the Society of Toxicology and a 1st place poster travel award from the International Society of Pharmaceutical Engineering.

ACKNOWLEDGMENTS

Throughout my graduate studies I have had the unique opportunity to conduct research in a variety of environments and none of this would have been possible without the help of Dr. Roger J. Narayan. Thank you for all your help and guidance throughout the years. You are truly an inspiration through your work ethic and you are always looking out for what is best for your students.

During my time at FDA I have had the pleasure to be mentored by Dr. Peter Goering, who has been the best mentor a student could ask for. Thank you for always being there through all the problems and obstacles and for all the hours spent polishing posters, presentation slides, and manuscripts to perfection.

Thank you to Dr. Girish Kumar, for all the encouragement and troubleshooting during lab experiments. So much of the techniques and skills I have gained were passed down from you.

The rest of the FDA Nano Group members: Qin Zhang, Shelby Skoog, Brendan Casey, Jiwen Zheng, Martha Betz, Bridget Wildt, Rene Vinas, and Anurag Mishra have always been there to discuss and troubleshoot any problems.

Many thanks to Dr. Aleksandr Ovsianikov and the team members at TU Wien, Peter Gruber, Marica Markovic and Jan Torgersen for introducing me to nanoscale 3D printing and for making my time in Vienna a rich and rewarding experience.

TABLE OF CONTENTS

LIST OF TABLES.....	ix
LIST OF FIGURES	x
INTRODUCTION.....	1
The case for understanding the nanotoxicology of immobilized nanomaterials in medical devices.	1
Literature Review: Nanostructured surfaces for preventing bacterial contamination of medical device surfaces.....	4
References:.....	20
Literature Review: Novel Approaches to Bone Grafting: Porosity, BMPs, Stem Cells, and the Periosteum	37
Conclusions:.....	58
References:.....	59
CHAPTER 1: In-vitro cytotoxicity of rare earth oxide nanoparticles for imaging applications	79
Abstract:.....	80
Introduction:.....	81
Materials and Methods:.....	84
Results:.....	88
Discussion:	101
Conclusions:.....	108
References:.....	110

CHAPTER 2: Cytotoxic evaluation of nanostructured zinc oxide (ZnO) thin films and leachates.....	119
Abstract:.....	120
Introduction:.....	121
Methods:.....	124
Results:.....	131
Discussion:.....	148
Conclusions:.....	153
References:.....	155
CHAPTER 3: Antibacterial nanosilver and PMMA composite coatings for supporting human bone stem cells.....	163
Abstract:.....	163
Introduction:.....	165
Methods:.....	168
Results:.....	173
Discussion:.....	186
Conclusions:.....	189
References:.....	190
CHAPTER 4: Cytotoxicity of cultured macrophages exposed to antimicrobial zinc oxide (ZnO) coatings on nanoporous aluminum oxide membranes.....	195
Abstract:.....	196
Introduction:.....	197

Materials and Methods:.....	200
Results:.....	205
Discussion:.....	213
Conclusion:.....	217
References:.....	218
CHAPTER 5: Nanoporous aluminum oxide membranes coated with atomic layer deposition- grown titanium dioxide for biomedical applications: An in vitro evaluation.....	
Abstract:.....	225
Introduction:.....	226
Methods:.....	227
Results and Discussion:.....	230
Conclusions:.....	237
References:.....	259
CHAPTER 6: Surface damage and cytotoxicity induced by ultraviolet irradiation of nanoporous polysulfone is prevented by atomic layer deposition of titanium dioxide.....	
Abstract:.....	267
Introduction:.....	268
Materials and Methods:.....	270
Results:.....	273
Discussion:.....	277
References:.....	282

CHAPTER 7: Laser 3D printing with sub-microscale resolution of porous elastomeric scaffolds for supporting human bone stem cells 295

 Abstract: 296

 Keywords: 296

 Introduction: 297

 Methods: 302

 Results: 310

 Discussion: 324

 Conclusions: 328

 Acknowledgments: 328

 References: 329

CONCLUSIONS 337

LIST OF TABLES

Table 1. Physical properties of tested nanoparticles.	89
Table 1. Roughness measurements using atomic force microscopy. Root mean square (RMS) roughness presents a measure where high deviations are weighed more heavily than in the mean roughness calculation (Ra), where all deviations are equated into a single average. Max height (Rmax) represents the single highest peak to valley distance measured. All measurements shown in nm with mean \pm standard deviation values.	133
Table 1. EDX analysis of weight and atom percentages for the composite PMMA/silver pulsed laser deposited thin films.	179

LIST OF FIGURES

Figure 1. TEM characterization of nanoparticles. A. Erbium-doped yttrium vanadate colloid (YVER 1004). B. Samarium-doped yttrium vanadate colloid (YVS 1101). C. Europium-doped yttrium vanadate colloid (YVE 1005).89

Figure 2. Cytotoxicity of six rare earth oxide nanoparticle types in RAW 264.7 macrophages. Cells were exposed to different concentrations of each type of rare earth oxide nanoparticle for 24 and 48 hours. Cell viability was measured by MTT assay. Cell viability was expressed as percentage of control for six rare earth oxide nanoparticles: A. YVS 1101, B. YVS 1101 - COOH, C. YVER 1004, D. YVD 1001, E. YVE 1005, F. YVE 1005 - COOH. Results are expressed as mean \pm SD from three independent experiments. The positive control, 5% DMSO, exhibited cell viability of 7% after 24 hour exposure and 4% after 48 hour exposure. Statistical significance is shown as the difference between nanoparticle-treated and control cells for raw data values. The symbol * indicates $p < 0.05$. 91

Figure 3. Cytotoxicity of dispersant/solvent supernatants of three rare earth nanoparticle types in RAW 264.7 macrophages. Cells were exposed to the same concentration of each supernatant for 24 hours. Cell viability was measured by MTT assay. Cell viability was expressed as percentage of cell and media control. Results are expressed as mean \pm SD from three independent experiments. Significance is shown as the difference between supernatant-treated and control cells for raw data values. The symbol * indicates $p < 0.05$95

Figure 4. Representative images of cell-nanoparticle interactions obtained using high resolution CytoViva® dark field microscope in RAW 264.7 macrophages. Cells were incubated with different nanoparticle samples for 6 hours before observation with the

microscope. The cells were rinsed several times so that unattached and excess nanoparticles were removed prior to imaging. Exposure times and acquisition parameters were kept constant for all samples and the experiment was repeated independently three times to ensure that the results were consistent. A. Control cells, B. YVS 1101, C. YVS 1101 - COOH, D. YVER 1004, E. YVD 1001, F. YVE 1005, G. YVE 1005 - COOH. All of the images were acquired using the same light exposure level of 303 ms. The bar represents 10 μ m.....97

Figure 5. High resolution CytoViva® dark field images of nanoparticles without cells. A. No particles, B. YVS 1101, C. YVS 1101 COOH. All of the images were acquired using the same light exposure level of 303 ms. The bar represents 10 μ m. 100

Figure 1. Energy-dispersive X-ray spectroscopy analysis of uncoated smooth silicon (A) and ZnO-coated silicon (B). The results shown in (A) show a strong single peak representing “Si”, and (B) confirm the presence of the ZnO thin-film layer by the peaks labeled “O” and “Zn.” 131

Figure 2. AFM analysis of the ZnO thin film. Rough AFM images of (A) smooth Si and (B) ZnO-coated Si. 3D stack of (C) AFM images of ZnO coating and (D) 3D reconstruction rendered using SurfaceJ plugin for ImageJ software to emphasize grains. 134

Figure 3. Macrophages growing on (A) smooth and (B) ZnO-coated Si wafers surfaces. Stained with DAPI (blue nucleus) and green-fluorescent Alexa Fluor® 488 dye (green actin filaments). Cells on the ZnO-coated surface were fewer in number, showed more rounded morphology and were loosely adherent, causing them to be easily detached. 136

Figure 4. ZnO-coated wafer (5x5 cm) shown inside a single well of a 48-well plate. Void area is shown in a well of a 48-well plate after seeding cells on wafer surfaces. Wafers were transferred to another 48-well plate in order to avoid interferences, e.g., diluting assay outputs, from cells growing in the void areas. 138

Figure 5. Exposure to ZnO-coated Si significantly decreases cell viability by inducing apoptosis and necrosis in macrophages. (A) Cell viability (MTT reduction) of macrophages exposed to ZnO-coated Si and smooth Si wafers for 24 h. Viability of cells grown on ZnO-coated Si was lower compared to Si controls. Data was normalized to cells grown on smooth Si (100%). (B) Live, apoptotic, and necrotic cell populations as a percentage of total cells (% Live +% Apoptotic + % Necrotic = 100%) measured with flow cytometry. ZnO-coated Si showed significantly decreased viability with predominantly necrotic as well as apoptotic cells. Data in (A) and (B) are expressed as mean \pm SD (N = 3 independent experiments). (C) and (D) show representative cell distributions between live, necrotic, and apoptotic cells for (C) smooth Si, which shows predominantly live cells and (D) ZnO-coated Si, which shows significant necrotic and apoptotic subpopulations. When normalized to live cells on the smooth Si control, cells on ZnO-coated Si have 32% viability measured with flow cytometry as compared to 57% when measured with MTT. Significance level notation: $** (p < 0.01)$. . 140

Figure 6. Effect of 24 hrs exposure to extracts collected after 24 hrs from Zn-coated Si and smooth Si wafers on cell viability and cytotoxicity. Undiluted extracts = 100%; 50 and 25% extracts represent serial dilutions for the 100% extract. (A) Cell viability (MTT reduction) in macrophages 24 hrs after exposure to extracts of ZnO-coated wafers. Viability significantly decreased with undiluted (100% = 12.1 μ g/mL) extract treatment only. (B) Cell death (%)

cytotoxicity) measured with LDH release in macrophages 24 hrs after exposure to extracts of ZnO-coated wafers. Cell death measured by LDH release increased only in response to undiluted (100%) ZnO extracts. 5% DMSO was used for positive controls. Cytotoxicity (%) was calculated as a percentage of total LDH release with the Triton X-100 positive control. Data are expressed as mean \pm SD (N = 3 independent experiments). Significance level notation: ******($P < 0.01$)..... 143

Figure 7. Intracellular ROS generation in (A) 24-hr and (B) 48-hr extracts from Zn-coated Si and smooth Si wafers over a 30 min – 24 hr exposure. All values for undiluted (100%) ZnO 24 and 48-hr extracts had significantly higher ROS generation ******($p < 0.01$) than the cell media control. Values for 50% diluted ZnO 24-h extract and 100% Si extract were significantly higher *****($p < 0.05$) than cell media at 1 hr only. The 48-hr, 100% extract from smooth Si was significantly higher at 18 h compared to cell media controls. Data are expressed as mean \pm SD (N = 3 independent experiments). 145

Figure 8. Levels of Zn ions present in extracts. ICP-MS analysis revealed elevated levels of Zn ions present in media of extracts from ZnO-coated wafers following both 24- and 48-hr wafer incubations. Both smooth silicon wafers and DMEM cell media alone were used as controls and each only had trace amounts of zinc present in cell media. 48-hr extracts served as the maximal possible release of ZnO from the relatively thin 96 nm film. Data are expressed as mean \pm SD (N = 3 independent experiments). 147

Figure 1. Scanning electron micrograph (SEM) of four thin films deposited with pulsed laser deposition. (A): PMMA only thin film deposited with 10,000 pulses, showing the porous

uniform morphology of PMMA, (B): 10,000 pulses of PMMA with silver, showing that more PMMA is deposited per pulse in terms of volume; a darker hue is visible from the silver particulates. (C) Increasing the number of pulses to 14,000 creates a uniform thin film of PMMA and silver, while (D) shows a thicker film made with 20,000 pulses. 174

Figure 2. SEM side-view of the 20,000 pulse PMMA/silver composite thin film. Thickness varied between approximately 5-11 μm 176

Figure 3. EDX Spectrum of PMMA/silver composite thin film deposited with 14,000 pulses. Highest count rate peaks were C and O, largely present in PMMA, while Ag had a minor, but distinguishable peak. 177

Figure 4. ICP-MS of PMMA/Ag composite thin films showing that 0.76, 1.05, and 1.67 $\mu\text{g/mL}$ Ag was released into cell media after 24 hrs from thin films deposited with 10,000, 14,000 and 20,000 pulses, respectively. 180

Figure 5. Antimicrobial efficacy of PMMA/Ag composite thin films using dynamic contact conditions. All silver containing samples has significant bacterial activity compared to controls. Uncoated Si wafers and PMMA thin films showed no inherent antimicrobial activity. 182

Figure 6. Cell viability of hBMSCs grown on PMMA/Ag composite thin films, measured with the MTT assay after 24 hrs of incubation. 183

Figure 7. Flow cytometry assay with hBMSCs stained with 7AAD dye for necrosis and Annexin V dye for apoptosis detection. Thin films with PMMA alone or PMMA and 0.8 $\mu\text{g/mL}$ eluted silver did not cause significant toxicity, while higher amounts of silver caused considerable apoptosis and necrosis in the cell population. 185

Figure 1. SEM images of both sides of a 100 nm anodized aluminum oxide membrane. **A:** Side A of an uncoated anodized aluminum oxide membrane, showing 200 nm circular pores. **B:** Side A of an 8 nm ZnO-coated anodized aluminum oxide membrane, showing 200 nm circular pores. **C:** Side B of an uncoated anodized aluminum oxide membrane, showing 100 nm branching pores. **D:** Side B of an 8 nm ZnO-coated anodized aluminum oxide membrane, showing 100 nm branching pores. 206

Figure 2. Cross-sectional SEM and elemental analysis of a 20 nm nanoporous anodized aluminum oxide with an 8 nm ZnO coating. **A:** Cross-sectional view of the membrane, showing the crystals present on the surface. **B:** EDX spectrum obtained from the 200 nm circular pore side, showing Al and Zn peaks (Side B)..... 208

Figure 3. Cell viability (MTT assay) in macrophages cultured on nanoporous uncoated anodized aluminum oxide membranes and nanoporous Zn-coated anodized aluminum oxide membranes. No statistical differences are present at 24 hours. After 48 hours, cells cultured on both 20 and 100 nm ZnO-coated anodized aluminum oxide membranes showed a reduction in cell viability compared with cells cultured on corresponding uncoated anodized aluminum oxide membranes and cells grown on standard tissue culture wells. Statistical significance *** $p < 0.001$, ** $p < 0.01$ from cell and media only control. 210

Figure 4. ROS production in macrophages treated with 24-hour extracts from ZnO-coated membranes over 1 hour, 3 hours, 12 hours, and 24 hours. Cells were treated with H_2O_2 as a positive control. All experimental groups, including ZnO-coated and uncoated anodized aluminum oxide, had similar responses to cells grown with fresh media, indicating no significant ROS generation for any surface extract..... 212

Figure 1. Scanning electron microscope images of a double-sided 200 nm/100 nm AAO membrane before and after atomic layer deposition of TiO₂. (A): Top side, 200 nm circular pores of uncoated and (B): TiO₂-coated nanoporous AAO. (C): Uncoated bottom side, showing smaller 100 nm branching pores before and (D): after coating with TiO₂. All membranes had one side with circular 200 nm pores; in the 20 nm and 100 nm AAO membranes, smaller branched pores appeared on the opposite side. Scale bar is 200 nm.... 238

Figure 2. EDX analysis of a TiO₂-coated AAO membrane. A: Split channels show the presence of Al, O, and Ti on the surface. B: Uncoated samples show no Ti signal, confirming that the Ti signal appears only after the coating, annealing, and sterilization process. 240

Figure 3. AFM topographical analysis of three porous surfaces: A) 20 nm branchlike pores, B) 100 nm branch-like pores, and C) 200 nm circular pores. Roughness parameters, including skewness, kurtosis and surface area, are reported. Root mean square (RMS) roughness provides the overall mean magnitude of surface variations. Maximum (Max) and minimum (Min) measurements provide the highest peak numbers and lowest valley numbers, respectively. Skewness measures whether the surface has more deep valleys (negative) or protruding narrow peaks (positive). Kurtosis is a relative measure of whether the collected force data is more flat (negative) or peaked (positive) compared with a normal curve shape. 242

Figure 4. Total protein content measured by the micro-BCA assay after 30 seconds incubation for uncoated AAO membranes and TiO₂-coated AAO membranes with 10% FBS culture medium. 20 nm TiO₂-coated AAO membranes had the highest total amount of adsorbed protein compared to all of the other membranes..... 244

Figure 5. Viability of L929 mouse fibroblast cells and RAW 264.7 mouse macrophage cells grown on uncoated AAO membranes and TiO₂-coated AAO membranes; measurements were obtained using the MTT assay. Results are expressed as percent of uncoated AAO controls for 24 hour and 48 hour exposures. Fibroblasts grown on TiO₂-coated AAO showed higher cell viability after 48 hours, which was statistically significant (p < 0.05). 245

Figure 6. Cell viability measured using the Neutral Red assay for L929 fibroblasts grown on uncoated AAO membranes and TiO₂-coated AAO membranes for 4 and 24 hours. Results were expressed as a percentage of uncoated AAO membrane controls for TiO₂-coated AAO membranes with pore diameters of A) 20 nm, B) 100 nm, and C) 200 nm. Although TiO₂-coated AAO membranes had the highest viabilities at 4 and 24 hours, the differences were only statistically significant (p < 0.05) for 20 nm porous membranes after 24 hours. 248

Figure 7. Cell proliferation measured by the DNA PicoGreen® Assay involving L929 fibroblasts grown for 4, 24, and 72 hours on uncoated and TiO₂-coated AAO membranes with pore sizes of 20, 100, and 200 nm. No statistically significant differences between the amounts of DNA were observed at any of the time points..... 251

Figure 8. TNF-alpha production measured after 24 hour exposure for mouse macrophages with or without addition of 10 ng/ml LPS. While macrophages activated by LPS produced higher levels of TNF-alpha than macrophages not activated by LPS, differences in TNF-alpha release were observed for macrophages grown on uncoated AAO membranes and TiO₂-coated AAO membranes compared to macrophages grown on TCPS controls. 253

Figure 1. SEM images of PES: (A) 21 nm layer of TiO₂ on PES with smaller pores at 5 kV; (B) Uncoated, non-UV treated PES at 5 kV with visible fine pore structure; (C) Uncoated non-UV treated PES at 20 kV to emphasize large pores; (D) Uncoated UV-treated PES with visible crack formations (red arrows)..... 277

Figure 2. EDX Spectra confirming presence of (A) TiO₂ layer on PES, and nearly identical spectra of (B) UV-treated PES and (C) untreated PES..... 279

Figure 3. Color difference in uncoated PES cutouts before and after 30 min UV exposure on each side..... 280

Figure 4. Macrophage cell viability of different PES surfaces and controls expressed as a percentage of the cell and media control. Percentages were calculated by comparing raw absorbance values from reduced MTT dye. Results are expressed as mean ± SD from independent experiments. Significance is shown as the difference between a given group and control cells for raw data values * $p < 0.05$ 281

Figure 1. Scanning electron micrographs (A, B), optical micrograph (C), and color photograph (D) of scaffold structure. Enlarged views of 2PP scaffolds with overlapping offset cylinder layers (A), which are composed of a hexagonal porous features (B), a visible nanoscale texture, and structural reinforcements; visual monitoring of scaffold fabrication was performed using optical microscopy (C). Fabricated scaffolds were easily handled without damage and placed into 96-well plates (shown in (D)) for biological evaluation. .. 311

Figure 2. Sample 5 x 4 array of double layer cylinder test structures after developing in ethyl alcohol/acetone. Insufficient laser power causes structures to collapse during development.

Similar arrays were used to determine multiple processing parameters..... 313

Figure 3. Scaffold cell culture method schematic, which describes cleaning of scaffolds in ethanol and PBS followed by vacuum drying. Cells were aliquoted in a small drop to the 3D scaffold, allowed to attach for 2 hours, covered in media, and examined with the appropriate assays..... 315

Figure 4. Human bone marrow stromal cell viability measured by the MTT assay after 48 hours of incubation. Cells growing on the 3D structure had higher viability, reflecting a higher number of adherent and metabolically active cells (asterisk indicates statistical significance, $p < 0.05$). Values shown are expressed as percent of tissue culture polystyrene controls. 317

Figure 5. Total DNA content measured by the PicoGreen dsDNA fluorescent nucleic acid stain after 72 hours. 3D scaffolds show the largest amount of DNA present, possibly due to a greater surface area available for cell spreading and proliferation. The asterisk indicates that the 3D mean was statistically significant ($p < 0.05$) from tissue culture polystyrene. 319

Figure 6. Total adsorbed protein content per unit projected area of a tissue culture polystyrene well plate, smooth elastomer material, and 3D scaffold elastomer material. 3D scaffold elastomer materials were shown to adsorb twice as much protein after 30 seconds as smooth elastomer materials or tissue culture polystyrene materials. Projected area was estimated as a circle for tissue culture polystyrene, as a circle for smooth elastomer, and as a

hexagon for the 3D elastomer. The asterisk indicates that the 3D mean value was statistically significant ($p < 0.001$) for tissue culture polystyrene. 321

Figure 7. Representative SEM images of human bone marrow stem cell morphology on smooth and 3D samples. (A) The smooth elastomer shows normal cell spreading in two dimensions. The cylindrical structure allows for 3D cellular spreading (B-D) and formation of intricate filament networks as seen in (C). After approximately 14 days, the scaffolds are covered with a thick “tissue-like” cover as seen in (D). This cover penetrates into the pores and completely covers them when viewed from above. 323

INTRODUCTION

The case for understanding the nanotoxicology of immobilized nanomaterials in medical devices.

The concept of nanotechnology evolved from the ideas of physicist Richard Feynman, who suggested the possibility of “molecular” machines and the manipulation of materials on much smaller scales than was previously done. Since then numerous scientific fields and disciplines have formed to study this idea, later termed nanotechnology by Norio Taniguchi. Taniguchi promoted the idea of nanotechnology as a subset of materials with unique properties compared to bulk materials in the 70s.¹ Since then many types of materials have been examined for altered properties in nanoscale creating promise for improved drugs for cancer treatment², faster bone healing³, more stable imaging probes⁴, and much more. As a result of this rapid advancement and potential benefits, engineered nanomaterials have raised serious health, environmental, and ethical concerns.⁵⁻⁷ From a toxicological standpoint, the vast array of toxicity concerns from a range of exposure routes, target organs, and selective material toxicities spurred the development of an entire discipline of nanotoxicology.⁸ Since scaling down materials to nanoscale formulations provides numerous desirable properties, it is only reasonable to assume that undesirable toxicological properties may form as a result as well. The field of nanotoxicology is built upon the idea of finding information about the undesirable properties of nanomaterials and forming unique means of avoiding such properties.

Nanoscale modification of medical materials:

The field of nanotoxicology has largely relied on toxicological endpoints from discrete nanoparticle studies.⁸ The unique interactions between nanomaterials and cells, including the major signaling pathways, intracellular trafficking, endocytosis and other cellular events have been largely studied through discrete particle interactions⁹ but the information gained is only partially translatable to examining surfaces coated with nanoparticles or other immobilized particulates. There is a considerable gap in understanding whether there are events specific to nanofeatured surfaces, since nanoscale surfaces have been shown to modulate a variety of cell functions including cell motility¹⁰, proliferation¹¹, and differentiation¹². A literature characterization study by Ostrowski et al, showed that nano-enabled products, including immobilized nanomaterials constitute a large subset of all nanomaterials; the bulk of nanotoxicological research, however, focuses on discrete particle systems and does not paint a complete picture of nanomaterial use.¹³ In the medical device industry, it is increasingly important to understand the toxicology of products with immobilized nanomaterials, especially those on the device surface, to ensure safety and efficacy of said devices. An implant's surface is a barrier that interacts with the bodily environment and is a major factor in determining the overall success of an implant. Surface modification techniques have been in use for decades and gained more attention with the rapid development of nano-scale topographical and chemical patterning methods such as pulsed laser deposition¹⁴, atomic layer deposition¹⁵, two photon polymerization¹⁶, photolithography, nanoimprinting, surface roughening, anodic oxidation, dip-pen lithography, and many others.¹⁷ Present techniques allow for manipulation of surface shape

on the order of nanometers. Surfaces can be optimized on to create microporous and nanoporous scaffolds and tissue replacement implants. Electrospun fibrous meshes can be manufactured with nanoporosity to increase surface area and improve cell adhesion and viability,¹⁸ nanoporous ceramic surfaces have the potential to promote bone cell differentiation¹⁹, and Ti modified with nanotubes may improve aspects ranging from cell adhesion, proliferation, migration, and differentiation of several cell types.²⁰ One of the main uses of nanometer-scale patterning has been to improve on two aspects of surfaces: (1) to fabricate surface features with small enough length scales with which cells can easily interact for motility, adhesion, and growth (with some claims establishing a specific length scale, ex. 15 nm)²⁰ and to (2) increase the overall surface area for cells to adhere to.²¹

Literature Review: Nanostructured surfaces for preventing bacterial contamination of medical device surfaces.

Nanoparticles and antimicrobial resistance:

Creating notexture surfaces, such as polystyrene, for example, can alter their physical properties including friction and hydrophobicity.²² For medical devices, however, an area of increasing interest has been to fabricate biocompatible device materials that additionally have antimicrobial properties. The intuitive approach involves simply embedding antimicrobial agents directly into the material surface. However, nanotechnology has allowed for several advancements in combating bacterial contamination of surfaces. Nanoparticle formulations of antimicrobial agents such as silver or copper have been shown to be highly effective against multiple species of bacteria.^{23,24} Such nanoparticles can be coated onto complex polymeric²⁵ and other surfaces²⁶ to impart their antimicrobial efficacy into a surface that is otherwise susceptible to bacterial colonization.

Nanoscale topography and bacterial biofilm resistance:

Aside from immobilizing nanoparticulate antimicrobial agents, direct surface modification has been postulated to prevent and reduce bacterial contamination. Using nanoscale topography for bacterial fouling control may bring superior surface properties that can selectively promote a specific cell type and simultaneously resist bacterial adhesion.²⁷ Bacterial adhesion to surfaces is of major importance to any implantable device due to its connection with the formation of antibiotic-resistant biofilms. Certain implantable devices such as catheters, pacemakers, stents, valves, and others²⁸ are more susceptible to formation of a biofilm on the implant surface. The formation of a biofilm on medical devices may constitute a failed device or result in prolonged infections, increased treatment time, and treatment revisions.²⁹ Initial bacterial surface attachment is both a critical and vulnerable step in biofilm development that may be modulated to a degree with surface topography in the nanoscale size range. Bacterial adhesion initiates many organizational signaling pathways between neighboring cells that eventually lead to the formation of an interconnected protective biofilm.³⁰ Possible tactics for interrupting or slowing the critical initial adhesion step could prove to be an additional anti-microbial measure to supplement and improve existing antimicrobial treatments. Some possible advantages of topographical modification is that it does not directly contribute to chemically resistant strains resulting from high dose antibiotic treatments, and may reduce the requirement for damaging sterilization procedures that can alter surface properties in sensitive materials.³¹

Background on bacterial infection of biomaterial surfaces:

Biofouling in medicine is defined as any undesirable accumulation of cells, proteins, and other biological materials on a device surface. It is a common phenomenon, since it occurs to some extent on any implant surface and begins immediately upon implantation. Adhesive and adsorptive interactions form between cells and proteins in a biological environment and the material surface, alter surface properties, cause infections and heighten immune responses.³² Biofilms are exceptionally difficult to treat due to their increased antibiotic resistance and account for over 60% of human infections.¹ In this text, a biofilm is defined as any matrix-encased community of bacteria that are tightly attached and networked between each other and a material surface. Once individual bacteria form such a close proximity colony, they experience a phenotype shift that usually makes them more virulent and strongly embedded in a self-produced dense polysaccharide matrix, which, in turn, can respond to even minute environmental stresses such as shear forces.³³ Bacteria also communicate between individual cells and colonies and form distinct spatial patterns on hard surfaces based on environmental conditions.³⁴ The microorganisms then disperse along the material surface using “rolling migration”³⁵ and secrete protective compounds that build up the matrix and create a physical barrier to antimicrobial agents. Tight packing of neighboring microbes additionally promotes lateral gene transfer that accelerates the development of immunity to antibiotics. Bacteria are thought to rely on direct contact-dependent communication to modulate growth and behavior within a biofilm.^{36,37} After a detectable biofilm has formed, some bacteria strains have been shown to activate genes that result in efflux of antibiotics and other chemicals out of the colony, trap antibiotic-degrading enzymes

and inactivate the antibiotic.^{38,39} However, that is only one of the many defenses formed within a biofilm including but not limited to quorum sensing of neighboring bacteria for gene transcription, activation of the RpoS stress factor that limits growth and controls biofilm growth rate⁴⁰, changes in outer membrane proteins, and efflux of chemically unrelated antimicrobial agents using multidrug pumps.³⁹

To prevent the spread and development of biofilms it is first necessary to prevent successful attachment and disrupt contact communication of bacteria to the material surface. Unattached bacteria are more susceptible to antibiotics and are more easily controlled by bodily host defense mechanisms.⁴¹ Surface features such as pores are known to contribute to biofouling by physically trapping cells and proteins in the material surface. The reverse, however, is also possible. Microorganisms are known to selectively prefer specific surfaces for attachment.⁴² Due to their relatively small size and interaction with sub-micron environments, it is important to focus on the nano-scale surface properties when examining bacterial adhesion and biofilm formation. Human cells, for example, are also known to interact with nanometer-size features. The extracellular matrix is composed of nanometer sized features, such as pores, fibers, and ridges that have an effect on cell migration and orientation.^{43,44} Comparatively less is known about the nanoscale behavior and material properties of bacterial biofilms than human cells.

Unique examples of functional nanostructured surfaces found in nature.

Many biological organic surfaces are intrinsically nanoscale⁴⁵ and serve functional purposes as a result of their size. A famous example is the lotus leaf which exhibits superhydrophobicity in a phenomenon called the Lotus effect. It has micron-sized papillae with nano-sized branchlike structures covered with a dense layer of epicuticular waxes. The nano branchlike structures along with the wax layer are thought to be responsible for the superhydrophobic lotus leaf surface. Some nano surface structures present in nature are attributed to having biofouling resistance.⁴⁶ For example, species of cetaceans have a surface free of all fouling organisms⁴⁷. The pilot whale (*Globicephala melas*) has nano-ridge pores (0.1–1.2 μm^2) on the surface of the skin⁴⁸ which are smaller than most fouling organisms and provide fewer contact points for adhesion. Microtopographies mimicking the skin of the shark have been produced (Sharklet Technologies LLC) and shown viable in reducing the adhesion of algae spores.⁴⁹ The application of nanotechnology in medicine has several rapidly developing fields such as biomolecular and cell analysis, microfluidics, drug delivery and so on, but the possibility of successfully mimicking or generating a biological resistance to microbial biofouling is truly novel. Bacteria are much smaller than other organisms responsible for biofouling. Biofouling resistance is a common concept in water treatment and marine applications. These fields deal with microorganisms on length scales far larger than bacteria. However, the same concepts of employing topography to modulate adhesion of unwanted organisms can be scaled down for bacterial resistance. The methods for fabricating controlled nanoscale topographies for bacterial resistance are rapidly developing, but several limitations still exist. The major milestones required for large-scale use of nanomaterials

surfaces are the availability of high resolution microscopy such as electron and atomic force microscopy and cost-effective large scale fabrication of consistent nanotopographies. Many of the current approaches discussed in this review are very costly and time consuming, leaving the opportunity for advancements in high throughput nanosurface fabrication techniques.

Bacterial adhesion on the nanoscale.

Bacteria come in a variety of sizes and cell shapes. The average size of a bacterium is about 0.5-1.0 microns in diameter and 2.0-5.0 microns in length but can get as large as 50-100 microns and 0.5 mm in diameter and length, respectively.⁵⁰ Cells may be shaped like rods, cones, spirals, spheres, helices and may additionally be branched or tapered.⁵¹ Cell shape in a bacterial cell regulates nutrient flow, motility, reproduction, attachment, differentiation and more.⁵² Cell shape is primarily determined and maintained by the continuous reorganization of the peptidoglycan network of the cell wall.⁵³ This stress and load-bearing element consists of a meshwork of glycan strands cross-linked by peptide bridges⁵⁴ for enhanced rigidity. Analysis of bacterial adhesion and attachment is also complicated by the variety of surface structures present. Many bacteria have a capsule structure covered by a slime layer, which some bacteria can excrete for attachment functions.⁵⁵ Additionally, a mass of tangled polysaccharides, called the glycocalyx is usually present. The glycocalyx must be present for biofilm formation and is the “glue” that holds it together. Finally, some bacteria have hair-like appendages called pili, which also aid in attachment and adhesion by physically “grabbing” the substrate.⁵⁰ Altogether bacterial attachment is a complex multi-dimensional and not an entirely clearly understood process.

Bacterial cell adhesion depends on a number of surface properties. Aside from topography, hydrophobic and hydrophilic interactions, surface charge of both the substrate and the bacteria play a role. Ionic strength and pH also play a role since they determine the surface charges.⁵⁶ Chemical properties can sometimes be altered in bodily environments, leaving topography as the more influential factor for bacterial adhesion. A recent study

cultured bacteria on microstructured and nanostructured metal surfaces and found that topography affected bacterial adhesion more than the physicochemical properties of the metals.⁵⁷ The patterns were kept constant between metals with different physicochemical properties (defined as charge and contact angle). The metals used were gold (an inert substrate), copper (a biocidal material) and polyisobutylcyanoacrylate (PBCA) (a highly biocompatible material). The results showed that the structure of bacterial aggregates during biofilm formation was strongly affected by surface topography, roughness, and toxicity, but did not depend on physicochemical surface properties. Bacterial cells responded similarly to the same topographical features on chemically different substrates. This study and similar studies⁵⁸ underline the importance of topographical surface features in addition to chemical features when engineering an implant surface with anti-bacterial properties. The authors hypothesize that the chemical surface features may be masked by the excreted bacterial extracellular polymeric substance (EPS) during early biofilm formation or adsorbed organic species from the culture media.

Masking of chemical properties of a material is a known problem for antimicrobial materials. For example, if bacteria cannot directly attach to a material, protein fouling or attachment of wetting agents may provide an intermediate substrate for bacterial adhesion.⁵⁹ Bacteria do seem to have a similar response to topography on different surfaces, although they may use different strategies for adhesion. One study looked at the effects of topographical features with dimensions similar to that of *Pseudomonas aeruginosa* cells on cell ordering and biofilm development.⁶⁰ Nanostructured substrates were fabricated with high-aspect ratio nanometer-scale polymer posts and selectively sputter-coated with thin

layers of bimetallic Pt-Pd or Au-Pd. The post spacing had a direct effect on bacterial arrangement and was consistent on both coated and uncoated substrates. Bacteria preferentially maximized their contact area by using the posts as extensions of the surface. The underlying topography of the substrate directly influenced spatial arrangements, which could be fine tuned by altering the distance between neighboring posts. If the distance between adjacent posts was larger than the length of a bacterial cell, the bacteria adhered in a random packing arrangement as they would during biofilm formation on a flat surface. The study also showed that this phenomenon may be independent of species type, adhesion mechanism, and shear flow. Mutants without either pili or flagella and two other species, *Bacillus subtilis* and *Escherichia coli* that exhibited similar spatial ordering as the *Pseudomonas aeruginosa* cells.⁶⁰ In order to disturb the local interactions necessary for bacterial aggregation and biofilm formation it will become increasingly useful to understand and control bacterial spatial arrangement on their native nanoscale dimensions.

Preferential adhesion of mammalian cells over bacterial cells:

Aside from preventing bacterial contamination, nanoscale surface modifications may create a preferential adhesion property for desired cells. The selective adhesion of osteoblasts over fibroblasts has been previously demonstrated with the use of carbon nanotube modified surfaces.⁶¹ Going from the microscale to the nanoscale has the potential to create preferential attachment of human cells over bacterial cells.^{62,63} Materials such as ZnO, TiO, and AlO are known for their use as scaffold materials for bone tissue regeneration. A primary example with effective preferential properties and antimicrobial activity is nanophase ZnO. ZnO is a well-known and widely used antimicrobial agent.^{64,65} Topographic shapes and effects of ZnO have been extensively studied for tissue engineering and scaffold applications. ZnO is used as an antimicrobial both in the food⁶⁶ and medical⁶⁷ industries. ZnO can be fabricated in a variety of nanostructures, such as wires, rods, flowers, free particles, and many more. For example, ZnO nanorods⁶⁸ have an effect on cell adhesion and macrophage responses³³, whereas ZnO nanoflowers⁶⁹ demonstrate an effective structure for improved bone tissue ingrowth. There are significant differences between bulk and nanostructured ZnO, yet both types have antimicrobial properties. Nanophase zinc has several benefits over its microscale and bulk forms. For example, antibacterial activity of ZnO increases as particle size decreases from the micro to the nano scale. Nano-scaled zinc, as well as aluminum and silicon all show higher toxicity towards *Bacillus subtilis*, *Escherichia coli* and *Pseudomonas fluorescens* in comparison with the original bulk oxide material.⁷⁰ Nanostructured ZnO has been shown to modulate macrophage activity as well. ZnO nanorods, for example, tend to have lower macrophage adhesion numbers than similar flat ZnO substrates.⁷¹

Specializing and combining properties such as mammalian cell modulation and increased bacterial toxicity is a useful tactic in modulating osteoblast response for bone tissue engineering. Both nanophase TiO₂ and ZnO have been shown to have decreased bacterial adhesion along with increased osteoblast adhesion, alkaline phosphatase activity, and calcium mineral deposition in comparison to their microscale counterparts.⁷² Another study found that antibacterial activity of ZnO was dependent on concentration and also increased with decreasing particle size.⁷³ Substantial loss of membrane integrity and changes in cell morphology were seen in *E. coli* as a result of ZnO exposure. The proposed mechanism occurs through interactions between the oxygen deficient (positive) zinc surface and the negatively charged cell wall. The smallest particle size was the most effective antimicrobial agent above a specific concentration. As particle size decreases, both surface area to mass ratio and surface charge increase. The proposed action of ZnO is attributed to a stronger electrostatic interaction between ZnO and the cell wall for smaller particles. The antimicrobial effect of ZnO was noticeably less on Gram positive bacteria (*S. aureus*), which may be due to Gram positive bacteria having a considerably thicker cell wall than the Gram negative *E. coli*. Nanophase ZnO was also less toxic towards normal osteoblasts and more toxic towards cancerous osteoblasts than micron sized ZnO. Selective anticancer activity of ZnO nanoparticles suggests a highly complex mechanism for the material's mechanism of interaction with human cancer cells.⁷³

Understanding bacterial and eukaryotic adhesion in a single controlled model is critical to understanding the modes of bacterial and human cellular adhesion. While the two cell types exhibit differences in membrane plasticity they do have similarities in their modes

of attachment such as the pili-like structures in their membranes. One study compared bacterial and eukaryotic cells on plasma polymer deposited thin films patterned with nano grooves and varying surface charge.⁷⁴ The most negatively charged UV-treated polymer as well as the UV-patterned surface resisted bacterial adhesion at 2 and 14h of incubation. The rate of osteoblast adhesion, however, was not straightforward or similar to the dynamics of bacterial adhesion. Cell number increased at different rates between substrates, with the UV-treated surfaces having the highest adhesion at 6h and UV-patterned at 3 days. Osteoblast progenitor cells also showed alignment with the nano grooves even with variations in surface chemistry. Bacterial cells, however, remained randomly oriented possibly due to contradictory effects of surface chemistry and topography.⁷⁴

Besides utilizing topographical arrays for cell adhesion and orientation with controlled spacing of features, many prior studies have focused primarily on a roughness value of amorphous material surfaces. A recent study differentiated between four types of surface roughening and textures (conventional, nanorough, nanotextured, and nanotubular) on TiO₂ samples based on fabrication method.⁷⁵ Unmodified titanium had micron-rough (nano-smooth) surface features, that became nano-rough after electron beam evaporation. Anodization for 1 min resulted in nanotextured surface features, while increasing the anodization time and HF concentration to 10 min and 1.5% resulted in nanotubular-like structures with an inner diameter from 60 to 70 nm.⁷⁵

All bacteria lines (*S. aureus*, *S. epidermidis*, and *P. aeruginosa*) attached the least to the nanorough Ti substrates. Nanotubular Ti, followed by nanotextured, showed the highest bacterial adhesion for all cell lines when compared to both conventional and nanorough Ti.⁷⁵

This could support the idea that moving down from micro to the nano regime does not necessarily bring better bacterial resistance simply due to a larger surface area to volume ratio, but this study is somewhat inconclusive in terms of topography. The authors mention that the high numbers of bacterial attachment to nanotextured and nanotubular surfaces may have come from a higher surface concentration of fluorine. Fluorine is known to increase bacterial adhesion⁷⁶⁻⁷⁹ and was likely left over on the surface after the anodization process. If that is the case, it is unclear whether topography tends to have a prevailing effect on bacterial adhesion. In the study discussed above,⁷⁵ the nanorough Ti surfaces had both the lowest adhesion and the lowest number of living cells after a period of 1hr. The surface energy of each sample correlated proportionally with the amount of protein adsorption. Samples with the highest surface energy had the highest amount of adsorbed fibronectin: nanotubular (highest) > nanotextured > nanorough > conventional (lowest).⁷⁵

Increased surface area of nanomaterials inherently allows more sites for chemical and physical interactions with its environment. One of the main events in a biological or bodily environment is the adhesion of proteins to the device surface. Nanorough features have been shown to increase protein attachment⁸⁰⁻⁸² and selective protein attachment or coating has been shown to consequently control whether bacterial or mammalian cells adhere in greater numbers.^{83,84} Bacterial adhesion is influenced by many chemical factors and cues. Maintaining similar physiochemical surface characteristics between experimental groups is essential to successfully determining whether topography plays a significant role. There is a large number of available nano-fabrication techniques.⁸⁵ Since bacterial adhesion is responsive to many chemical and physical cues, it is useful to characterize the chemical

properties of similar geometrical patterned surfaces made by different fabrication methods. Ultimately such comparisons would establish an approach for optimizing a widely used medical material, such as titanium for cellular invasion that will additionally act as a barrier for bacterial adhesion.⁸⁶

Modulating ion release on the nanoscale.

There are certain concerns with the introduction of nanoroughened, nanotextured or other nanoscale surface modifications.^{87,88} Certain metallic materials are then well known antimicrobial agents due to their chemical properties. Silver and zinc, for example, are used in antimicrobial nanostructured surface coatings, also known as thin films.⁸⁹ The antimicrobial property of silver thin films is related to Ag^+ ion release from the nanoparticles into the surrounding aqueous medium and can be confirmed by using inductively coupled plasma mass spectrometry (ICP-MS).⁹⁰ This release is mediated by preliminary oxidation of inert silver when exposed to an aqueous environment. Little attention is paid to topography since ion release is mainly determined by the surface area to volume ratio. Nanosilver coatings can be fabricated by methods such as flame assisted chemical vapor deposition⁹¹ and plasma spraying onto substrates such as titanium.⁹² When nanosurfaces are fabricated by using a powdered starting material, the resulting surface morphology is not necessarily on the same size scale as the starting powder, but it is greatly dependent on the size distribution of the starting powder. Nanostructured surface coatings used in the plasma sprayed silver study had distinct morphologies with isolated structures as a result of a starting powder material of a controlled size. Control over the amount of silver powder mixed with titanium powder additionally allowed to create a surface which released a concentration of ions that would be less than the maximum cytotoxic concentration.⁹² Aside from metallic powders like titanium, silver and zinc nanoparticles can be combined with other materials to successfully impart antimicrobial efficacy. Nanostructured polymer surfaces have used elemental silver nanoparticles as an additive or a coating with good antimicrobial results. Organosilicon,⁹⁰

polyamide,⁹³ polyurethane,^{94,95} polyethylene,^{94,96,97} polyethylene oxide,⁹⁸ chitin^{99,100} and many others have all shown improved resistance to various bacteria when incorporated with metallic nanoparticles such as silver or zinc.

References:

- 1 Taniguchi, N. in *Proc. Intl. Conf. Prod. Eng. Tokyo. Part II, Japan Society of Precision Engineering*. 18-23.
- 2 Ferrari, M. Cancer nanotechnology: opportunities and challenges. *Nat. Rev. Cancer* **5**, 161-171 (2005).
- 3 Stylios, G., Wan, T. & Giannoudis, P. Present status and future potential of enhancing bone healing using nanotechnology. *Injury* **38**, S63-S74 (2007).
- 4 Baker, M. Nanotechnology imaging probes: smaller and more stable. *Nat. Methods* **7**, 957-962 (2010).
- 5 Maynard, A. D. *et al.* Safe handling of nanotechnology. *Nature* **444**, 267-269 (2006).
- 6 Bennett-Woods, D. *Nanotechnology: Ethics and society*. (CRC Press, 2008).
- 7 Kagan, V. E., Bayir, H. & Shvedova, A. A. Nanomedicine and nanotoxicology: two sides of the same coin. *Nanomedicine: nanotechnology, biology and medicine* **1**, 313-316 (2005).

- 8 Oberdörster, G., Oberdörster, E. & Oberdörster, J. Nanotoxicology: an emerging discipline evolving from studies of ultrafine particles. *Environ. Health Perspect.*, 823-839 (2005).
- 9 Zhao, F. *et al.* Cellular uptake, intracellular trafficking, and cytotoxicity of nanomaterials. *Small* **7**, 1322-1337 (2011).
- 10 Yim, E. K. *et al.* Nanopattern-induced changes in morphology and motility of smooth muscle cells. *Biomaterials* **26**, 5405-5413 (2005).
- 11 Zanello, L. P., Zhao, B., Hu, H. & Haddon, R. C. Bone cell proliferation on carbon nanotubes. *Nano Lett.* **6**, 562-567 (2006).
- 12 Dalby, M. J., Gadegaard, N. & Wilkinson, C. D. The response of fibroblasts to hexagonal nanotopography fabricated by electron beam lithography. *J. Biomed. Mater. Res. Part A* **84**, 973-979 (2008).
- 13 Ostrowski, A. D., Martin, T., Conti, J., Hurt, I. & Harthorn, B. H. Nanotoxicology: characterizing the scientific literature, 2000-2007. *Journal of Nanoparticle Research* **11**, 251-257, doi:10.1007/s11051-008-9579-5 (2009).

- 14 Christen, H. M. & Eres, G. Recent advances in pulsed-laser deposition of complex oxides. *Journal of Physics-Condensed Matter* **20**, doi:264005
10.1088/0953-8984/20/26/264005 (2008).
- 15 Hyde, G. *et al.* Atomic layer deposition and biocompatibility of titanium nitride nano-coatings on cellulose fiber substrates. *Biomed. Mater.* **4**, 025001 (2009).
- 16 Claeysens, F. *et al.* Three-dimensional biodegradable structures fabricated by two-photon polymerization. *Langmuir* **25**, 3219-3223 (2009).
- 17 Liu, X., Chu, P. K. & Ding, C. Surface nano-functionalization of biomaterials. *Materials Science and Engineering: R: Reports* **70**, 275-302 (2010).
- 18 Leong, K. F., Cheah, C. M. & Chua, C. K. Solid freeform fabrication of three-dimensional scaffolds for engineering replacement tissues and organs. *Biomaterials* **24**, 2363-2378, doi:10.1016/s0142-9612(03)00030-9 (2003).
- 19 Popat, K. C. *et al.* Osteogenic differentiation of marrow stromal cells cultured on nanoporous alumina surfaces. *J. Biomed. Mater. Res. Part A* **80**, 955-964 (2007).
- 20 Park, J. *et al.* TiO₂ nanotube surfaces: 15 nm—an optimal length scale of surface topography for cell adhesion and differentiation. *Small* **5**, 666-671 (2009).

- 21 Webster, T. J. & Ejiófor, J. U. Increased osteoblast adhesion on nanophase metals: Ti, Ti6Al4V, and CoCrMo. *Biomaterials* **25**, 4731-4739 (2004).
- 22 Di Mundo, R., Palumbo, F. & d'Agostino, R. Nanotexturing of polystyrene surface in fluorocarbon plasmas: From sticky to slippery superhydrophobicity. *Langmuir* **24**, 5044-5051 (2008).
- 23 Yoon, K.-Y., Byeon, J. H., Park, J.-H. & Hwang, J. Susceptibility constants of *Escherichia coli* and *Bacillus subtilis* to silver and copper nanoparticles. *Sci Total Environ* **373**, 572-575 (2007).
- 24 Dastjerdi, R. & Montazer, M. A review on the application of inorganic nano-structured materials in the modification of textiles: focus on anti-microbial properties. *Colloids and Surfaces B: Biointerfaces* **79**, 5-18 (2010).
- 25 Gittard, S. *et al.* Pulsed laser deposition of antimicrobial silver coating on Ormocer® microneedles. *Biofabrication* **1**, 041001 (2009).
- 26 Samuel, U. & Guggenbichler, J. Prevention of catheter-related infections: the potential of a new nano-silver impregnated catheter. *Int. J. Antimicrob. Agents* **23**, 75-78 (2004).

- 27 Anselme, K. *et al.* The interaction of cells and bacteria with surfaces structured at the nanometre scale. *Acta Biomater.* **6**, 3824-3846 (2010).
- 28 Donlan, R. M. Biofilms and device-associated infections. *Emerg. Infect. Dis.* **7**, 277 (2001).
- 29 Ramage, G., Tunney, M. M., Patrick, S., Gorman, S. P. & Nixon, J. R. Formation of *Propionibacterium acnes* biofilms on orthopaedic biomaterials and their susceptibility to antimicrobials. *Biomaterials* **24**, 3221-3227 (2003).
- 30 Davey, M. E. & O'toole, G. A. Microbial biofilms: from ecology to molecular genetics. *Microbiol. Mol. Biol. Rev.* **64**, 847-867 (2000).
- 31 Fleith, S., Ponche, A., Bareille, R., Amedee, J. & Nardin, M. Effect of several sterilisation techniques on homogeneous self assembled monolayers. *Colloids and Surfaces B: Biointerfaces* **44**, 15-24 (2005).
- 32 Campoccia, D., Montanaro, L. & Arciola, C. R. The significance of infection related to orthopedic devices and issues of antibiotic resistance. *Biomaterials* **27**, 2331-2339 (2006).

- 33 Oh, Y., Jo, W., Yang, Y. & Park, S. Influence of culture conditions on *Escherichia coli* O157: H7 biofilm formation by atomic force microscopy. *Ultramicroscopy* **107**, 869-874 (2007).
- 34 Ben-Jacob, E., Cohen, I. & Gutnick, D. L. Cooperative organization of bacterial colonies: from genotype to morphotype. *Annual Reviews in Microbiology* **52**, 779-806 (1998).
- 35 Rupp, C. J., Fux, C. A. & Stoodley, P. Viscoelasticity of *Staphylococcus aureus* biofilms in response to fluid shear allows resistance to detachment and facilitates rolling migration. *Appl. Environ. Microbiol.* **71**, 2175-2178 (2005).
- 36 Keller, L. & Surette, M. G. Communication in bacteria: an ecological and evolutionary perspective. *Nat. Rev. Microbiol.* **4**, 249-258 (2006).
- 37 Blango, M. G. & Mulvey, M. A. Persistence of uropathogenic *Escherichia coli* in the face of multiple antibiotics. *Antimicrob. Agents Chemother.* **54**, 1855-1863 (2010).
- 38 Davies, J. & Davies, D. Origins and evolution of antibiotic resistance. *Microbiol. Mol. Biol. Rev.* **74**, 417-433 (2010).

- 39 Mah, T.-F. C. & O'Toole, G. A. Mechanisms of biofilm resistance to antimicrobial agents. *Trends Microbiol* **9**, 34-39 (2001).
- 40 Corona-Izquierdo, F. P. & Membrillo-Hernández, J. A mutation in rpoS enhances biofilm formation in *Escherichia coli* during exponential phase of growth. *FEMS Microbiol. Lett.* **211**, 105-110 (2002).
- 41 Costerton, J., Stewart, P. S. & Greenberg, E. Bacterial biofilms: a common cause of persistent infections. *Science* **284**, 1318-1322 (1999).
- 42 Geesey, G. *et al.* The influence of surface features on bacterial colonization and subsequent substratum chemical changes of 316L stainless steel. *Corros. Sci.* **38**, 73-95 (1996).
- 43 Flemming, R., Murphy, C., Abrams, G., Goodman, S. & Nealey, P. Effects of synthetic micro-and nano-structured surfaces on cell behavior. *Biomaterials* **20**, 573-588 (1999).
- 44 Wan, Y. *et al.* Adhesion and proliferation of OCT-1 osteoblast-like cells on micro- and nano-scale topography structured poly (L-lactide). *Biomaterials* **26**, 4453-4459 (2005).

- 45 Aizenberg, J. *et al.* Skeleton of *Euplectella* sp.: structural hierarchy from the nanoscale to the macroscale. *Science* **309**, 275-278 (2005).
- 46 Scardino, A. J. & de Nys, R. Mini review: Biomimetic models and bioinspired surfaces for fouling control. *Biofouling* **27**, 73-86 (2011).
- 47 Baum, C., Meyer, W., Roessner, D., Siebers, D. & Fleischer, L.-G. A zymogel enhances the self-cleaning abilities of the skin of the pilot whale (*Globicephala melas*). *Comparative Biochemistry and Physiology Part A: Molecular & Integrative Physiology* **130**, 835-847 (2001).
- 48 Baum, C., Meyer, W., Stelzer, R., Fleischer, L.-G. & Siebers, D. Average nanorough skin surface of the pilot whale (*Globicephala melas*, Delphinidae): considerations on the self-cleaning abilities based on nanoroughness. *Marine Biology* **140**, 653-657 (2002).
- 49 Schumacher, J. F. *et al.* Engineered antifouling microtopographies—effect of feature size, geometry, and roughness on settlement of zoospores of the green alga *Ulva*. *Biofouling* **23**, 55-62 (2007).
- 50 Srivastava, S. *Understanding bacteria*. (Springer Science & Business Media, 2003).

- 51 Young, K. D. Bacterial shape. *Mol. Microbiol.* **49**, 571-580 (2003).
- 52 Young, K. D. The selective value of bacterial shape. *Microbiol. Mol. Biol. Rev.* **70**, 660-703 (2006).
- 53 Mukhopadhyay, R. & Wingreen, N. S. Curvature and shape determination of growing bacteria. *Physical Review E* **80**, 062901 (2009).
- 54 Höltje, J.-V. Growth of the stress-bearing and shape-maintaining murein sacculus of *Escherichia coli*. *Microbiol. Mol. Biol. Rev.* **62**, 181-203 (1998).
- 55 Shapiro, L., McAdams, H. H. & Losick, R. Generating and exploiting polarity in bacteria. *Science* **298**, 1942-1946 (2002).
- 56 An, Y. H., Dickinson, R. B. & Doyle, R. J. in *Handbook of Bacterial Adhesion* 1-27 (Springer, 2000).
- 57 Diaz, C., Salvarezza, R. C., de Mele, M. & Schilardi, P. L. Organization of *Pseudomonas fluorescens* on Chemically Different Nano/Microstructured Surfaces. *Acs Applied Materials & Interfaces* **2**, 2530-2539, doi:10.1021/am100313z (2010).

- 58 Díaz, C., Schilardi, P., Salvarezza, R. & Fernández Lorenzo de Mele, M. Nano/microscale order affects the early stages of biofilm formation on metal surfaces. *Langmuir* **23**, 11206-11210 (2007).
- 59 Bos, R., Van der Mei, H. C. & Busscher, H. J. Physico-chemistry of initial microbial adhesive interactions—its mechanisms and methods for study. *FEMS Microbiol. Rev.* **23**, 179-230 (1999).
- 60 Hochbaum, A. I. & Aizenberg, J. Bacteria pattern spontaneously on periodic nanostructure arrays. *Nano Lett.* **10**, 3717-3721 (2010).
- 61 Price, R. L., Waid, M. C., Haberstroh, K. M. & Webster, T. J. Selective bone cell adhesion on formulations containing carbon nanofibers. *Biomaterials* **24**, 1877-1887 (2003).
- 62 Groll, J., Fiedler, J., Bruellhoff, K., Moeller, M. & Brenner, R. E. Novel surface coatings modulating eukaryotic cell adhesion and preventing implant infection. *The International journal of artificial organs* **32**, 655-662 (2009).
- 63 Gutwein, L. G. & Webster, T. J. Increased viable osteoblast density in the presence of nanophase compared to conventional alumina and titania particles. *Biomaterials* **25**, 4175-4183 (2004).

- 64 Padmavathy, N. & Vijayaraghavan, R. Enhanced bioactivity of ZnO nanoparticles—
an antimicrobial study. *Science and Technology of Advanced Materials* **9**, 035004
(2008).
- 65 Ruffolo, S. *et al.* ZnO and ZnTiO₃ nanopowders for antimicrobial stone coating.
Applied Physics A **100**, 829-834 (2010).
- 66 Emamifar, A., Kadivar, M., Shahedi, M. & Soleimani-Zad, S. Evaluation of
nanocomposite packaging containing Ag and ZnO on shelf life of fresh orange juice.
Innovative Food Science & Emerging Technologies **11**, 742-748,
doi:10.1016/j.ifset.2010.06.003 (2010).
- 67 Saha, N., Keskinbora, K., Suvaci, E. & Basu, B. Sintering, microstructure,
mechanical, and antimicrobial properties of HAp-ZnO biocomposites. *Journal of
Biomedical Materials Research Part B-Applied Biomaterials* **95B**, 430-440,
doi:10.1002/jbm.b.31734 (2010).
- 68 Lee, J. Y. *et al.* The control of cell adhesion and viability by zinc oxide nanorods.
Biomaterials **29**, 3743-3749, doi:10.1016/j.biomaterials.2008.05.029 (2008).

- 69 Park, J. K. *et al.* The topographic effect of zinc oxide nanoflowers on osteoblast growth and osseointegration. *Advanced Materials* **22**, 4857, doi:10.1002/adma.201002255 (2010).
- 70 Jiang, W., Mashayekhi, H. & Xing, B. S. Bacterial toxicity comparison between nano- and micro-scaled oxide particles. *Environ. Pollut.* **157**, 1619-1625, doi:10.1016/j.envpol.2008.12.025 (2009).
- 71 Zaveri, T. D. *et al.* Contributions of surface topography and cytotoxicity to the macrophage response to zinc oxide nanorods. *Biomaterials* **31**, 2999-3007, doi:10.1016/j.biomaterials.2009.12.055 (2010).
- 72 Colon, G., Ward, B. C. & Webster, T. J. Increased osteoblast and decreased *Staphylococcus epidermidis* functions on nanophase ZnO and TiO₂. *J. Biomed. Mater. Res. Part A* **78A**, 595-604, doi:10.1002/jbm.a.30789 (2006).
- 73 Rani, V. V. D., Manzoor, K., Menon, D., Selvamurugan, N. & Nair, S. V. The design of novel nanostructures on titanium by solution chemistry for an improved osteoblast response. *Nanotechnology* **20**, doi:195101 10.1088/0957-4484/20/19/195101 (2009).

- 74 Ploux, L. *et al.* Opposite Responses of Cells and Bacteria to Micro/Nanopatterned Surfaces Prepared by Pulsed Plasma Polymerization and UV-Irradiation. *Langmuir* **25**, 8161-8169, doi:10.1021/la900457f (2009).
- 75 Puckett, S. D., Taylor, E., Raimondo, T. & Webster, T. J. The relationship between the nanostructure of titanium surfaces and bacterial attachment. *Biomaterials* **31**, 706-713, doi:10.1016/j.biomaterials.2009.09.081 (2010).
- 76 Eick, S., Glockmann, E., Brandl, B. & Pfister, W. Adherence of Streptococcus mutans to various restorative materials in a continuous flow system. *J. Oral Rehabil.* **31**, 278-285 (2004).
- 77 Correa, C. B., Pires, J. R., Fernandes-Filho, R. B., Sartori, R. & Vaz, L. G. Fatigue and Fluoride Corrosion on Streptococcus mutans Adherence to Titanium-Based Implant/Component Surfaces. *J. Prosthodont.* **18**, 382-387 (2009).
- 78 Li, B. & Logan, B. E. Bacterial adhesion to glass and metal-oxide surfaces. *Colloids and Surfaces B: Biointerfaces* **36**, 81-90 (2004).
- 79 Katsikogianni, M., Spiliopoulou, I., Dowling, D. & Missirlis, Y. Adhesion of slime producing Staphylococcus epidermidis strains to PVC and diamond-like carbon/silver/fluorinated coatings. *J. Mater. Sci.: Mater. Med.* **17**, 679-689 (2006).

- 80 Woo, K. M., Chen, V. J. & Ma, P. X. Nano-fibrous scaffolding architecture selectively enhances protein adsorption contributing to cell attachment. *J. Biomed. Mater. Res. Part A* **67**, 531-537 (2003).
- 81 Khang, D. *et al.* Enhanced fibronectin adsorption on carbon nanotube/poly (carbonate) urethane: independent role of surface nano-roughness and associated surface energy. *Biomaterials* **28**, 4756-4768 (2007).
- 82 Webster, T. J., Ergun, C., Doremus, R. H., Siegel, R. W. & Bizios, R. Specific proteins mediate enhanced osteoblast adhesion on nanophase ceramics. *J. Biomed. Mater. Res.* **51**, 475-483 (2000).
- 83 Kinnari, T. J. *et al.* Bacterial adherence to titanium surface coated with human serum albumin. *Otol Neurotol* **26**, 380-384 (2005).
- 84 Anagnostou, F. *et al.* Osteoblast functions on functionalized PMMA-based polymers exhibiting Staphylococcus aureus adhesion inhibition. *Biomaterials* **27**, 3912-3919 (2006).
- 85 Gates, B. D. *et al.* New approaches to nanofabrication: molding, printing, and other techniques. *Chem. Rev.* **105**, 1171-1196 (2005).

- 86 Zile, M. A., Puckett, S. & Webster, T. J. Nanostructured titanium promotes keratinocyte density. *J. Biomed. Mater. Res. Part A* **97A**, 59-65, doi:10.1002/jbm.a.33028 (2011).
- 87 Petrochenko, P. E. *et al.* Cytotoxic evaluation of nanostructured zinc oxide (ZnO) thin films and leachates. *Toxicol In Vitro*, doi:<http://dx.doi.org/10.1016/j.tiv.2014.05.004>.
- 88 Petrochenko PE, S. S., Zhang Q, Comstock DJ, Narayan RJ. Cytotoxicity of cultured macrophages exposed to antimicrobial zinc oxide (ZnO) coatings on nanoporous aluminum oxide membranes. *Biomatter* (2013).
- 89 Petrella, A., Deng, H., Roberts, N. & Lamb, R. Single-source chemical vapor deposition growth of ZnO thin films using Zn4O (CO₂NEt₂)₆. *Chem. Mater.* **14**, 4339-4342 (2002).
- 90 Saulou, C. *et al.* Plasma deposition of organosilicon polymer thin films with embedded nanosilver for prevention of microbial adhesion. *Appl. Surf. Sci.* **256**, S35-S39 (2009).
- 91 Sheel, D. W., Brook, L. A. & Yates, H. M. Controlled nanostructured silver coated surfaces by atmospheric pressure chemical vapour deposition. *Chem. Vap. Deposition* **14**, 14-24 (2008).

- 92 Li, B., Liu, X., Meng, F., Chang, J. & Ding, C. Preparation and antibacterial properties of plasma sprayed nano-titania/silver coatings. *Mater. Chem. Phys.* **118**, 99-104 (2009).
- 93 Damm, C. & Münstedt, H. Kinetic aspects of the silver ion release from antimicrobial polyamide/silver nanocomposites. *Applied Physics A* **91**, 479-486 (2008).
- 94 Davenas, J., Thevenard, P., Philippe, F. & Arnaud, M. Surface implantation treatments to prevent infection complications in short term devices. *Biomol. Eng.* **19**, 263-268 (2002).
- 95 Guggenbichler, J. Central venous catheter associated infections pathophysiology, incidence, clinical diagnosis, and prevention—A review. *Materialwissenschaft und Werkstofftechnik* **34**, 1145-1154 (2003).
- 96 Holder, I. A., Durkee, P., Supp, A. P. & Boyce, S. T. Assessment of a silver-coated barrier dressing for potential use with skin grafts on excised burns. *Burns* **29**, 445-448 (2003).
- 97 Dunn, K. & Edwards-Jones, V. The role of Acticoat™ with nanocrystalline silver in the management of burns. *Burns* **30**, S1-S9 (2004).

- 98 Zapata, P. A. *et al.* Nanocomposites based on polyethylene and nanosilver particles produced by metallocenic “in situ” polymerization: synthesis, characterization, and antimicrobial behavior. *Eur. Polym. J.* **47**, 1541-1549 (2011).
- 99 Kumar, P. S. *et al.* Preparation and characterization of novel β -chitin/nanosilver composite scaffolds for wound dressing applications. *Carbohydr. Polym.* **80**, 761-767 (2010).
- 100 Kumar, P. T. S., Lakshmanan, V. K., Biswas, R., Nair, S. V. & Jayakumar, R. Synthesis and Biological Evaluation of Chitin Hydrogel/Nano ZnO Composite Bandage as Antibacterial Wound Dressing. *J. Biomed. Nanotechnol.* **8**, 891-900, doi:10.1166/jbn.2012.1461 (2012).

Literature Review: Novel Approaches to Bone Grafting: Porosity, BMPs, Stem Cells, and the Periosteum

Abstract:

The disadvantages involving the use of a patient's own bone as graft material have led surgeons to search for alternative materials. In this review, several characteristics of a successful bone graft material are discussed. In addition, novel synthetic materials and natural bone graft materials are being considered. Various factors can determine the success of a bone graft substitute; for example, design considerations such as porosity, pore shape and interconnection play significant roles in determining graft performance. Effective delivery of bone morphogenetic proteins and the ability to restore vascularization play significant roles in determining the success of a bone graft material. Among current approaches, shorter bone morphogenetic protein sequences, more efficient delivery methods, and periosteal graft supplements have shown significant promise for use in autograft substitutes or autograft extenders.

Current bone grafting techniques:

Critical size bone defects result from one or more pathological events (e.g., tumor, trauma, inflammation, or radiotherapy)¹ and can lead to a delayed union or a nonunion of fracture. The lost bone mass can be replaced using a number of techniques and materials. In some cases, a patient's own bone may not be available or may not be obtainable in sufficient volume to repair a given defect. In these cases, natural, synthetic, and artificial materials can be used to replace autograft materials; a variety of clinical outcomes have been achieved with these bone graft materials.

Autogenous iliac crest bone graft (AICBG) is considered the gold standard for bone grafting procedures due to its natural osteoinductivity; however, the disadvantages of autografting procedures such as donor site pain, increased operative time, and the limited amount of obtainable material have led surgeons to search for alternative materials.

Acceptable bone substitutes should offer one or more of three characteristics that are provided by autograft materials: osteoinductivity, osteoconductivity, and osteogenicity. For example, allograft materials eliminate the need for donor site tissue removal and provide good osteoconductivity; however, these materials are associated with poor osteoinductivity.²

Unlike patients receiving autograft materials, patients receiving allograft materials undergo shorter operative times as well as receive satisfactory outcomes; however, allograft recipients have been shown to experience longer post-operative fevers.³ In addition, allograft transplantation is relatively safe from infection transmission; current sterilization practices used in hospital bone banks virtually eliminate infection transmission from frozen cadaver bone.⁴

Synthetic materials exhibit several beneficial properties, including unlimited supply, straightforward sterilization, and simple storage⁵. Novel composite materials such as nano-hydroxyapatite/poly-lactic acid are fabricated to mimic both the natural porosity of bone as well as having similar mineral properties.⁶ Such novel composite nanomaterials can be engineered to exhibit osteoinductive properties through the incorporation of bone morphogenic proteins (BMPs).⁷ BMPs are important supplements to synthetic materials since they can induce bone and cartilage formation as well as other biological activities, such as cell proliferation, migration, and apoptosis.⁸ Their increased application in clinical fracture healing, however, raises efficacy and dose concerns⁹; in addition, there is room for possible improvement through use of shorter bone morphogenetic protein 2 related peptide sequences.¹⁰ Ensuring good vascularity is also a problem that faces any bone graft material. Use of periosteal grafts, growth factors, and porous surfaces in combination may provide an approach for increasing the success of graft vascularization. Advances in cell harvesting, three-dimensional matrices, and recombinant signaling molecules may also provide graft material improvements. This review will consider advances in synthetic materials, tissue engineering approaches, and allograft enhancements that are used in bone grafting procedures. It will also outline the necessary general evaluation criteria that must be considered for any given bone graft material including nanomaterials. The optimal bone graft material should possess mechanical and structural properties similar to bone, provide controllable BMP delivery, and exhibit sufficient porosity as well as microscale and nanoscale features for bone regeneration. In addition, the material should be simple to sterilize, nontoxic, and dissolve at a controlled rate.

Pore Size and Shape:

Porosity is an important factor in determining tissue-implant material integration. Porosity can be incorporated within natural and synthetic scaffold materials in order to impart desirable properties to these materials. For example, polymers such as poly(lactic-co-glycolic acid) (PLGA) and polycaprolactone (PCL) can be prepared with porous structures in order to obtain improved protein loading and controllable degradation rates.¹¹ Porous ceramics and composites such as beta tricalcium phosphate and hydroxyapatite can be prepared with strength equaling or exceeding that of human cancellous bone.^{12,13} In addition, these materials can be prepared with interconnected porosity, including both macroporous and microporous features similar to that of bone.¹⁴ Nanoporosity may additionally be introduced into hydroxyapatite through the use of composite HA and polymer materials such as polyvinyl alcohol. The polymer can act as a pore former to create open interconnected pore structures as well as improve the bending strength of the ceramic HA component.¹⁵ Features such as pores are known to facilitate BMP loading and delivery.¹⁴ The properties of natural materials as well may be improved through incorporation of porous structures and BMP loading. For example, a recent study involving collagen scaffolds found that cell spreading and migration in collagen were more dependent on porosity and pore size than on matrix stiffness.¹⁶ It should be noted that an increase in porosity is associated with several drawbacks. Collagen and scaffold materials exhibit increases in absorption rates and decreases in mechanical properties with decreases in density (i.e., increases in porosity).¹⁷ Scaffold materials are commonly engineered to have interconnected porosity and controlled pore dimensions, which may be used to modulate cell growth, seeding, and differentiation.¹⁸

Novel advancements in scaffold fabrication, such as computer-assisted solid freeform fabrication (SFF), facilitate preparation of structures with precise shapes and uniform pore characteristics.¹⁹ In addition to scaffolds with large pores, porous scaffolds with multiscale porosity more closely resembling that of natural bone have been created. Sponge-like iliac crest bone, which is commonly used as an autograft material, exhibits a natural supporting structure that is made up of a network of smaller trabeculae (micropores); these trabeculae enclose larger voids (macropores), providing 55–70% interconnected porosity.²⁰ Macroporosity alone, however, does not completely replicate the native bone structure. Calcium phosphate ceramics have been fabricated with both micro- and nano-porosity as well as inherent nanotexture which was shown to decrease soft tissue ingrowth while improving new bone formation in a rabbit model.²¹ Pore size and pore shape in scaffolds must be similar to those of natural bone for the given type of bone defect; in addition, the pore characteristics, such as interconnection, must facilitate diffusion of oxygen and other nutrients. Although there has been significant discussion regarding optimal micropore size, most studies focus on scaffolds with pore sizes above 100 μm .²² One concern regarding pore size involves optimizing the surface area that is available for cell attachment. If the pores are too small, they may inhibit cellular migration and produce necrosis²³; if the pores are too large, they may not provide sufficient surface area for cell attachment^{24,25} and they may compromise structural integrity.^{12,17} A recent study of interconnected porous polycaprolactone (PCL) scaffolds found that 350 μm and 800 μm pores play a limited role in bone regeneration, indicating that pore features other than size may play important roles.²⁶ Another study showed that while initial cell adhesion (48 hour post seeding) reaches a

maximum value for a mean pore size of 120 μm , overall cell migration is greatest for pore sizes larger than 300 μm .²⁷ This study suggests that it is important to consider parameters other than size (e.g., pore shape, interconnection and overall permeability). In addition, cone-shaped (diameter gradient) pores were associated with significantly higher oxygen concentrations and cell proliferation than uniform-diameter pores.²⁸ An increase in porosity, particularly with interconnected pores, may be associated with a decrease in mechanical stability; this relationship is dependent on the material. For example, scaffolds based on pure hydroxyapatite (HA) have much better mechanical properties than biphasic composites based on HA/beta-tricalcium phosphate (HA/ β -TCP).²⁹

Oxygen Diffusion and Permeability

The role of oxygen diffusion through pores has been studied extensively by means of in vitro studies, which indicate that oxygen diffusion plays an important role in angiogenesis. A problem for bone graft materials has been the inability to induce angiogenesis at the center of the scaffold as well as at the periphery of the scaffold³⁰; in addition, there are difficulties associated with maintaining a nutrient supply to newly formed tissue.^{31,32} The lack of oxygen can reduce cellular respiration as well as pore invasion; alternatively, lack of oxygen (when reduced to a degree) promotes angiogenesis through the hypoxia-inducible factor-1 pathway.³³ When cells adhere to a given surface, they need additional space in the form of interconnected pores for acquisition of nutrients, removal of wastes, and transport of proteins.^{34,35} An alternative approach to looking at pore size and structure alone is to determine the overall permeability of a scaffold material. One study used Forchheimer's equation and Darcy's Law to find values for overall permeability that are consistent with literature data for porous hydroxyapatite scaffolds.³⁴ Forchheimer's equation is an empirical relationship that describes a parabolic dependence of the pressure drop (DP) through a scaffold with the resulting superficial velocity.³⁵⁻³⁸ Darcy's Law is a linear relationship between fluid velocity and pressure drop.³⁵ This relation accurately determines flow permeability and takes porosity, pore size, and tortuosity (amount of curvature in the network) into account. Permeability should be obtained in a simulated environment that resembles in vivo fluid, pressure, temperature, and velocity conditions as closely as possible.

Roughness and Microporosity on the Nanoscale:

Scaffold surface properties have a significant influence on cell-material interactions; these properties should be examined at the nanometer and micrometer scale. The extracellular matrix of a cell is composed of nanometer sized features, such as pores, fibers, and ridges; these features have influence on cell migration and orientation.^{39,40} It is a goal of scaffold processing to fabricate a scaffold that exhibits the appropriate surface topography for a desired cell response. The relationship between titanium implant surface roughness and osteoblast behavior or Staphylococcus behavior has been examined; osteoblasts and Staphylococci had dissimilar preferences for surface roughness types.⁴¹ The study suggests that lateral lengths of topographical features and vertical roughness parameters on a titanium surface can be optimized to simultaneously promote osteoblast adhesion and minimize bacterial interaction. These effects of surface topography are independent of scaffold chemistry; surface topography-dependent properties provide specific contribution to toxicity,⁴² immune response,⁴³ cell motility,⁴⁴ and other factors. Recent advances have provided more precise control over the surface features of nanoscale materials. Cell proliferation studies have been used to examine various surface features, including the incorporation of microporous features within bone scaffold materials. In a study comparing TiO₂ nanotubes to moderately rough blasted surfaces that are used in bone implants, nanotube surfaces were shown to provide significantly increased osseointegration and new bone formation; in addition, more cell contact at the bone-implant interface was noted. The diameters and heights of the nanotubes were modulated by altering reaction times; nanotubes with diameters of around 90 and 108 nm were obtained. These dimensions are orders of

magnitude smaller than those of macroporous features; macroporous features are typically one hundred micrometers or more in diameter.²² Studies have also shown the positive effects of incorporating microporosity within macroporous scaffolds in animals.⁴⁵⁻⁴⁷ For example, significant increases in capillary penetration, bone volume, and mineral apposition rates have been observed with ceramic constructs, including hydroxyapatite (HA).⁴⁵ In addition, the amount of the increase varied with different levels of microporosity.²⁸ Ceramic composites made from calcium phosphate and hydroxyapatite are attractive scaffolds since one can obtain structures with microporous features, such as pores and rods.^{22,48-51} Macroporous biphasic calcium phosphate (MBCP) is a ceramic material that is similar in composition to the mineral phase of bone; it forms a very strong attachment to host tissue.⁵²⁻⁵⁵ In addition, it can be custom prepared for bone grafting procedures⁵⁶ and it can be modified with microporous features.⁵⁷ For example, one study used micro-robotic deposition to create microporosity within MBCP rods; it was found that recombinant human bone morphogenetic protein 2 was associated with a microscale positive effect; however, no positive macroscale effect was observed. BMP was not necessary for bone formation within the micropores.²² Microporosity also theoretically eliminated “dead space” in the scaffold, which theoretically improves load transfer between the tissue and the material and overall toughness. In addition, it facilitates use of the material for establishment of a continuous mechanosensory network.^{11,12,16,19} In addition to ceramics, polymers may also be fabricated with microporous features.^{58,59} For example, resorbable polyurethane materials have been fabricated into three-dimensional microporous scaffolds, which may be used for cartilage tissue reconstruction⁵⁸ with an autogenous periosteal flap^{60,61} (discussed later in this review). Biodegradable

polyurethane scaffolds have been used to support attachment and proliferation of chondrocytes and osteogenic cells⁶²⁻⁶⁴; these materials, which contain open interconnections, can be used as microporous templates.⁶⁵ Phase-inversion techniques have been used to prepare such microporous polymeric membranes with well-controlled and well-defined pore sizes and geometries.⁵⁸ Satisfactory mechanical properties make these materials an attractive choice for microporous tissue engineering scaffolds, providing the ability to supplement or replace periosteal flaps.⁵⁸

Bone Morphogenic Proteins:

At the present time, two BMPs are clinically available, bone morphogenetic protein 7 (BMP-7) and recombinant human bone morphogenetic protein 2. BMP-7 (osteogenic protein-1), which is distributed by Olympus Biotech (Hopkinton, MA), uses a bovine collagen carrier in granular form. Recombinant human bone morphogenetic protein 2, which is distributed by Medtronic (Minneapolis, MN), uses a collagen sponge carrier. The carrier materials slow the release of BMP during administration.^{5,8,9} Collagen sponges and similar carrier materials exhibit excellent biocompatibility and have good cell and macromolecule interactions.⁶⁶ Collagen is also an attractive material for use as a delivery vehicle and as a material coating due to the fact that it has a favorable influence on cellular infiltration and wound healing. Collagen can also be processed in an aqueous base, which minimizes potential contact with toxic chemicals. It is a well-studied material; aqueous injectable collagen dispersions, powders, sutures, wound dressings, shields, sealants and spongy implants have been utilized in a clinical setting.⁶⁷ It is also a well-known hemostatic agent; furthermore, it is suitable for carrying pharmacologic agents, including protein-based agents and antibiotics. It should be noted that collagen carriers do have several drawbacks. Bone grafting substitutes require a large amount of BMP to be delivered to the fracture site. Recombinant human bone morphogenetic proteins are known to become soluble and can escape the delivery site, particularly when administered in large doses.⁶⁸ Due to these factors, recombinant human bone morphogenetic protein collagen carriers are not ideal materials for sustained rate-controlled delivery of BMPs. The high market price and the need for large doses of BMPs have driven the development of highly-controlled delivery vehicles. When used in large

doses, BMPs have been shown to cause side effects, including local inflammation during spinal fusion as well as unwanted ectopic bone formation.⁶⁹

Gelatin as a BMP Carrier

Gelatin is an attractive alternative to collagen as a BMP carrier. It is a natural biodegradable polymer that is used in various medical applications, including skin regeneration,⁷⁰ bone grafting,⁷¹ and controlled drug release.⁷² Gelatin contains denatured collagen; it also exhibits lower antigenicity than collagen. The isoelectric point of gelatin can be selected to be acidic or basic.⁷³ This property allows growth factors with several isoelectric point values to be loaded into gelatin, while maintaining the biological activity of these factors. The degradation rate and growth factor release can be varied by controlling the amount of cross-linking in the gelatin, which influences the in vivo rate of enzymatic decay. Thermal stability, resistance to water dissolution, and collagenase digestion are all dependent on the amount of cross-linking that is present.⁷⁴ One study addressed the problem of early diffusion and absorption of BMP through use of a slow-release gelatin hydrogel layered on top of a biodegradable poly-L-lactide/ε-caprolactone copolymer. The results showed that BMP was released over a period of several days; formation of new healthy bone was noted in a canine model.⁷⁵ Gelatin is also suitable for cell delivery; this material may be used for tissue engineering of bone and other tissues.⁷⁶ The delivery and slow release properties of gelatin can be combined with other materials to create protein-loaded gelatin microspheres. A recent study examined the effect of incorporating gelatin microspheres within calcium phosphate bone cement (CPC); in this study, the CPC/gelatin composite healed defects more quickly and had a higher bone mineralization rate than CPC loaded with recombinant human bone morphogenetic protein 2 without gelatin.⁷⁷ More recently it has been shown that even

smaller, nanoscale gelatin colloidal gels can successfully deliver biological molecules such as BMP-2 to create a stimulatory effect on bone regeneration.⁷⁸

Gelatin-based Absorbable Polymer Matrices.

Gelatin can be cross-linked with chitosan in order to create porous scaffolds for bone tissue engineering. These scaffolds are able to support adhesion and osteogenic differentiation of bone marrow mesenchymal stem cells in a rat model.⁷⁹ Gelatin/beta-chitosan porous scaffolds can be used to immobilize the amine groups of recombinant human bone morphogenetic protein 2 on the carboxylic groups of the scaffold surface; this material may be used for dental applications.⁸⁰ Gelatin scaffolds can also be used to carry lyophilized adenovirus encoding BMP-2 (AdBMP-2). This study points to the possibility of using lyophilized viral BMP and gelatin to prepare pre-made constructs for treatment of bone defects.⁸¹

Another notable gelatin scaffold is an injectable product called E-Matrix (Pioneer Surgical, Marquette, MI), which is derived from porcine collagen. E-matrix contains gelatin that is copolymerized with a high-molecular weight branched glucose polysaccharide (dextran).⁸² The large carbohydrate molecules stabilize unwound collagen strands, which typically exhibit helical structures. The scaffold attempts to mimic the open extracellular matrix structure of embryonic mesenchymal tissue in order to encourage increased interactions between cells and the scaffold surface. Ionic and molecular interactions hold the copolymer matrix together; polar amino acids (e.g., cysteine, glutamic acid, arginine, and lysine) also provide structural stability. The exposed polar amino acid binding sites are thought to interact with host cells, which participate in growth and repair of bone as well as other tissues. Polar amino acid sequences are typically obscured from host cells in the extracellular matrix by the tightly wound triple-stranded helix of collagen.⁸² The modified open gelatin scaffold has the

potential to promote tissue-specific responses depending on growth factor loading and enhanced cellular responses (e.g., the osteoinductive response to BMPs). A recent study of E-matrix showed that it enhanced spinal fusion; in this study, it was used as a recombinant human bone morphogenetic protein 2 carrier in a rat spinal fusion model.⁸³ Overall, gelatin scaffolds and sponges have promising futures for use as BMP carriers. They have been shown to be effective in several animal models, including rabbits⁸⁴ and mice⁸⁵; in addition, they are an attractive alternative to collagen BMP carriers for clinical applications.

P24 Oligopeptide:

Even if delivery can be provided in a controlled manner, natural BMPs have several shortcomings that limit their clinical use. BMPs are susceptible to rapid degradation; furthermore, they exhibit complex structures, limited availability, and the potential to contribute to unwanted reactions.⁸⁶ Bone morphogenetic protein 2 is known to have the strongest ability to induce formation of new bone.⁸⁷ It has two subunits, which are antigenic determinant epitopes that bind to either receptor type I or type II.⁸⁸ These epitopes are known as the “wrist epitope” and the “knuckle epitope.” The knuckle epitope of bone morphogenetic protein 2 binds to BMP receptor type II.⁸⁹ The bone morphogenetic protein 2 receptor is thought to merge at the 73–92 peptide of the knuckle epitope of bone morphogenetic protein 2.⁸⁷ An alternative to using costly natural BMPs involves creating a synthetic version of this functional region. The most well-known approach uses solid state synthesis and chromatography to achieve high yields of oligopeptide P24, which designated the number 24 due to the fact that it contains a 24 amino acid sequence from the bone morphogenetic protein 2 functional region. Several studies investigated the feasibility of coupling the P24 oligopeptide to alginate; these materials have been evaluated in in vivo studies involving small animals. Synthetic P24 has been shown to significantly increase osteoinduction on mineralized recombinant collagen, nano-hydroxyapatite/recombinant human-like collagen/poly(lactic acid) (nHA/RHLC/PLA) porous scaffold⁹⁰ and PLGA materials⁹¹ when implanted into rat and rabbit models.⁹² Another study suggested that P24 exhibits the same biological activity as natural bone morphogenetic protein 2; in this study, P24 and natural bone morphogenetic protein 2 showed equal potential to induce ectopic bone formation.⁹³

Vascularity and the Periosteum

Allograft material (i.e., cadaveric bone) is commonly used for bone replacement. Allograft material is utilized in a wide variety of structures, including whole bone segments, demineralized matrix, and bone chips. One benefit of allograft material over autograft material is that a donor site is not required. In a follow-up study that involved the use of autogenous iliac crest bone graft and banked allograft bone in scoliosis surgery, patients receiving allograft bone demonstrated significantly better post-operative results. Three months after surgery, half of the patients receiving autograft material had physically limiting donor site pain at the wound site. On the other hand, patients receiving allograft material had successful results and returned to their preoperative level of function soon after surgery.⁹⁴ There are theoretical concerns regarding donor harvesting, donor screening,⁹⁵ and allograft material storage; there are also theoretical concerns regarding infection transmission if allograft material is not properly processed. Allograft material is an effective alternative to autograft material for anterior cruciate ligament reconstruction.⁹⁶ One study looked at postoperative surgical site infection one year following spinal fusion surgery; no significant difference in the rate of infection was noted among irradiated allograft, nonirradiated allograft, and autograft materials.⁹⁷ This result may in part be attributed to the compatibility of cadaver bone with sterilization methods. Another study evaluated the effect of sterilization processes on the mechanical strength of cortical bone allograft material prior to implantation. Cylindrical cortical bone cadaveric materials were sterilized by chemical sterilization; chemical and gamma irradiation; as well as chemical treatment, lyophilization, and terminal sterilization with rehydration. Untreated materials were examined for

comparison purposes. The cadaveric materials were subsequently tested to failure by means of axial compression, diametral compression, shear, and bending studies; no significant differences in ultimate stress, strain, or fracture energy data among the groups were noted.⁹⁸ Allograft materials are associated with some shortcomings; for example, these materials exhibit limited resorption and new bone replacement, which tends to occur at the periphery of the allograft material. The challenge for allograft materials is to achieve well-vascularized new bone by means of a process known as allograft revitalization. Retrieval studies involving human subjects have shown only 15-20 % replacement with new bone after five years.^{99,94} Implanted allografts demonstrate good soft tissue attachment; >80% coverage of graft surface area after two years has been noted. In addition, they become enveloped by well-vascularized muscle. On the other hand, allograft failure is often associated with insufficient vascularity. A study involving use of allograft materials in rabbits found no vascularization in these materials despite the fact that the allograft materials were combined with autograft adipose-derived stem cells.¹⁰⁰ Additional studies have examined a combined approach and have obtained different outcomes. A more successful study involving a combination of adipose-derived stem cells, recombinant human bone morphogenetic protein 2, periosteum, and structural bony porcine mandibular allograft constructs suggested that periosteum plays a significant role in determining allograft vascularization. The allograft constructs were implanted within a periosteal envelope after rib extraction (thoracic) or wrapped within rectus abdominis muscle. The rectus abdominis implants showed little vasculature and were encased within scar tissue. On the other hand, the periosteal envelope implants resembled normal healthy bone and were superior in many ways. All of the periosteal envelope

implants had bony processes in development between them and the native ribs; in addition, these materials were more firmly affixed and had predominately smoother surfaces.¹⁰⁰ Although the individual effects of recombinant human bone morphogenetic protein 2, stem cells and periosteum could not be determined, the study underscored the importance of periosteum. In addition, the rectus abdominis implants showed limited new bone growth, which occurred in locations with sufficient vascularity. In contrast, the periosteal envelope implants were highly vascular throughout, suggesting that the periosteum was a critical factor in establishing a good vascular supply.¹⁰⁰ It is important to note that the origin of the periosteal graft material plays an important contribution. The use of periosteum has been studied extensively for use in chondrogenesis. The chondrogenic potential of periosteum is known to significantly vary based on the donor site; iliac grafts show the highest potential. On the other hand, skull grafts show almost no chondrogenesis.¹⁰¹ This variation is likely caused by differences in mesenchymal stem cell amounts for various locations and by differences in the structure of periosteum found in various locations. In vivo studies involving animal models have indicated the possibility of optimizing periosteal graft performance by pretreatment with transforming growth factor beta 1 (TGF-beta 1)¹⁰² or insulin-like growth factor-I (IGF-1)¹⁰³ via subperiosteal injection. Although the studies focused exclusively on osteochondral defects, they suggest possible use in fracture treatment; TGF-beta injection resulted in increased extracellular matrix production in the region surrounding a bone graft.¹⁰⁴

Periosteal cells have been shown to be biocompatible with synthetic and natural scaffolds in vivo¹⁰⁵; furthermore, these cells have been shown to induce new vascularized

bone formation on scaffolds in animal studies. The periosteum is composed of an osteogenic layer that is known to contain mesenchymal stem cells (MSCs), a fibrovascular intermediate that contains fibroblasts and endothelial cells, and a collagenous outer layer. These layers contain cellular components that promote osteogenesis and vascularization; in addition, these layers contain collagenous matrix, which is vital to the success of a bone graft. One study proposed a technique that gently inverts the periosteum in a manner that allows the collagenous layer to contact the bone and allows the osteogenic layer to contact the graft material and the surrounding tissue.¹⁰⁶ Although inverted periosteum has less stem cell potential than bone marrow aspirate, it is considered to be a viable supplement to bone graft material.¹⁰⁶ A human case study using a combination of adipose-derived stem cells, bone morphogenetic protein 2, allograft material, and periosteum resulted in healthy lamellar craniofacial bone, obviating the need for osteocutaneous free flaps or additional allograft material.¹⁰⁷ Another study stressed the importance of harvesting the periosteum with the cortical components, which contain the cambium layer that is thought to be responsible for osteogenesis. This study further confirmed the efficacy of periosteal flaps; a 75% success rate in treating recalcitrant nonunions that were resistant to conventional therapies, including cancellous autografts and cadaveric allografts, was demonstrated.¹⁰⁸ Such findings suggest the possibility of preparing periosteal grafts for both allograft enhancement and synthetic graft enhancement in situ. Periosteum supplements are a promising solution to poor vasculature for both synthetic materials and allograft materials; these materials may be used in combination with BMPs and stem cells. If available, periosteum should be utilized as a graft or preserved at the site of implantation for improved graft vascularity and osteogenesis.

Conclusions:

The ideal alternative to autogenous bone grafts is a combination of existing materials, which impart the desirable characteristics of the component materials. The surface should exhibit optimal permeability, cellular ingrowth, and cellular differentiation characteristics. Porosity should also be optimized in terms of size, shape, distribution, and interconnection on the macro, micro, and nano scales. Delivery of BMPs should be through the use of slow-release carriers as well as shorter, more precise peptide sequences, which facilitate controlled delivery and decrease the unwanted effects of natural BMP, respectively. In addition, allografts and synthetic materials stand to benefit from periosteal supplements for improved vascularity.

References:

- 1 Ma, D. Y. *et al.* Reconstruction of Rabbit Critical-size Calvarial Defects Using Autologous Bone Marrow Stromal Cell Sheets. *Ann. Plast. Surg.* **65**, 259-265, doi:10.1097/SAP.0b013e3181c9c3f5 (2010).
- 2 Samartzis, D., Khanna, N., Shen, F. H. & An, H. S. Update on bone morphogenetic proteins and their application in spine surgery. *J. Am. Coll. Surg.* **200**, 236-248 (2005).
- 3 Sun, K. *et al.* Anterior Cruciate Ligament Reconstruction With Bone-Patellar Tendon-Bone Autograft Versus Allograft. *Arthroscopy-the Journal of Arthroscopic and Related Surgery* **25**, 750-759, doi:10.1016/j.arthro.2008.12.023 (2009).
- 4 Kappe, T., Cakir, B., Mattes, T., Reichel, H. & Floren, M. Infections after bone allograft surgery: a prospective study by a hospital bone bank using frozen femoral heads from living donors. *Cell Tissue Bank* **11**, 253-259, doi:10.1007/s10561-009-9140-5 (2010).
- 5 Bucholz, R. W. Nonallograft osteoconductive bone graft substitutes. *Clin. Orthop.*, 44-52 (2002).

- 6 Wei, G. & Ma, P. X. Structure and properties of nano-hydroxyapatite/polymer composite scaffolds for bone tissue engineering. *Biomaterials* **25**,4749-4757 (2004).
- 7 Li, J. *et al.* Enhancement of bone formation by BMP-7 transduced MSCs on biomimetic nano-hydroxyapatite/polyamide composite scaffolds in repair of mandibular defects. *J. Biomed. Mater. Res. Part A* **95**, 973-981 (2010).
- 8 Sakou, T. Bone morphogenetic proteins: From basic studies to clinical approaches. *Bone* **22**, 591-603 (1998).
- 9 Garrison, K. R. *et al.* Bone morphogenetic protein (BMP) for fracture healing in adults. *Cochrane Database Syst. Rev.*, 154, doi:Cd006950
10.1002/14651858.CD006950.pub2 (2010).
- 10 Lin, Z. Y. *et al.* Bone induction by biomimetic PLGA-(PEG-ASP)_n copolymer loaded with a novel synthetic BMP-2-related peptide in vitro and in vivo. *J. Controlled Release* **144**, 190-195, doi:10.1016/j.jconrel.2010.02.016 (2010).
- 11 Oh, S. H. *et al.* Degradation Behavior of 3D Porous Polydioxanone-b-Polycaprolactone Scaffolds Fabricated Using the Melt-Molding Particulate-Leaching Method. *J. Biomater. Sci.-Polym. Ed.* **22**, 225-237,
doi:10.1163/092050609x12597621891620 (2011).

- 12 Schumacher, M., Deisinger, U., Detsch, R. & Ziegler, G. Indirect rapid prototyping of biphasic calcium phosphate scaffolds as bone substitutes: influence of phase composition, macroporosity and pore geometry on mechanical properties. *J. Mater. Sci.-Mater. Med.* **21**, 3119-3127, doi:10.1007/s10856-010-4166-6 (2010).
- 13 Ramay, H. R. R. & Zhang, M. Biphasic calcium phosphate nanocomposite porous scaffolds for load-bearing bone tissue engineering. *Biomaterials* **25**, 5171-5180, doi:10.1016/j.biomaterials.2003.12.023 (2004).
- 14 Sohier, J., Daculsi, G., Sourice, S., de Groot, K. & Layrolle, P. Porous beta tricalcium phosphate scaffolds used as a BMP-2 delivery system for bone tissue engineering. *J. Biomed. Mater. Res. Part A* **92A**, 1105-1114, doi:10.1002/jbm.a.32467 (2010).
- 15 Raksujarit, A., Pengpat, K., Rujjanagul, G. & Tunkasiri, T. Processing and properties of nanoporous hydroxyapatite ceramics. *Materials & Design* **31**, 1658-1660 (2010).
- 16 Miron-Mendoza, M., Seemann, J. & Grinnell, F. The differential regulation of cell motile activity through matrix stiffness and porosity in three dimensional collagen matrices. *Biomaterials* **31**, 6425-6435, doi:10.1016/j.biomaterials.2010.04.064 (2010).

- 17 Yunoki, S. *et al.* Effects of increased collagen-matrix density on the mechanical properties and in vivo absorbability of hydroxyapatite-collagen composites as artificial bone materials. *Biomed. Mater.* **6**, 10, doi:015012
10.1088/1748-6041/6/1/015012 (2011).
- 18 Liu, X. & Ma, P. X. Polymeric scaffolds for bone tissue engineering. *Ann. Biomed. Eng.* **32**, 477-486 (2004).
- 19 Lee, J. W., Ahn, G., Kim, J. Y. & Cho, D. W. Evaluating cell proliferation based on internal pore size and 3D scaffold architecture fabricated using solid freeform fabrication technology. *J. Mater. Sci.-Mater. Med.* **21**, 3195-3205,
doi:10.1007/s10856-010-4173-7 (2010).
- 20 Innocentini, M. D. M. *et al.* Permeability of porous gelcast scaffolds for bone tissue engineering. *Journal of Porous Materials* **17**, 615-627, doi:10.1007/s10934-009-9331-2 (2010).
- 21 Tovar, N. *et al.* The physicochemical characterization and in vivo response of micro/nanoporous bioactive ceramic particulate bone graft materials. *Materials Science and Engineering: C* **43**, 472-480 (2014).

- 22 Lan Levensgood, S. K. *et al.* The effect of BMP-2 on micro- and macroscale osteointegration of biphasic calcium phosphate scaffolds with multiscale porosity. *Acta Biomater.* **6**, 3283-3291 (2010).
- 23 Rose, F. R. *et al.* In vitro assessment of cell penetration into porous hydroxyapatite scaffolds with a central aligned channel. *Biomaterials* **25**, 5507-5514, doi:10.1016/j.biomaterials.2004.01.012 (2004).
- 24 O'Brien, F. J., Harley, B. A., Yannas, I. V. & Gibson, L. J. The effect of pore size on cell adhesion in collagen-GAG scaffolds. *Biomaterials* **26**, 433-441, doi:10.1016/j.biomaterials.2004.02.052 (2005).
- 25 Yannas, I. Tissue regeneration by use of collagen-glycosaminoglycan copolymers. *Clin. Mater.* **9**, 179-187 (1992).
- 26 Roosa, S. M. M., Kemppainen, J. M., Moffitt, E. N., Krebsbach, P. H. & Hollister, S. J. The pore size of polycaprolactone scaffolds has limited influence on bone regeneration in an in vivo model. *J. Biomed. Mater. Res. Part A* **92A**, 359-368, doi:10.1002/jbm.a.32381 (2010).
- 27 Murphy, C. M., Haugh, M. G. & O'Brien, F. J. The effect of mean pore size on cell attachment, proliferation and migration in collagen-glycosaminoglycan scaffolds for

- bone tissue engineering. *Biomaterials* **31**, 461-466,
doi:10.1016/j.biomaterials.2009.09.063 (2010).
- 28 Ahn, G. *et al.* Effect of Pore Architecture on Oxygen Diffusion in 3D Scaffolds for Tissue Engineering. *J. Biomech. Eng.-Trans. ASME* **132**, 5, doi:10.1115/1.4002429 (2010).
- 29 Impens, S. *et al.* Production and characterisation of porous calcium phosphate structures with controllable hydroxyapatite/beta-tricalcium phosphate ratios. *Adv. Appl. Ceram.* **108**, 494-500, doi:10.1179/174367609x422243 (2009).
- 30 Wang, L. *et al.* Osteogenesis and angiogenesis of tissue-engineered bone constructed by prevascularized beta-tricalcium phosphate scaffold and mesenchymal stem cells. *Biomaterials* **31**, 9452-9461, doi:10.1016/j.biomaterials.2010.08.036 (2010).
- 31 Cartmell, S. H., Porter, B. D., Garcia, A. J. & Guldberg, R. E. Effects of medium perfusion rate on cell-seeded three-dimensional bone constructs in vitro. *Tissue Eng* **9**, 1197-1203 (2003).
- 32 Karande, T. S., Ong, J. L. & Agrawal, C. M. Diffusion in musculoskeletal tissue engineering scaffolds: Design issues related to porosity, permeability, architecture, and nutrient mixing. *Ann. Biomed. Eng.* **32**, 1728-1743 (2004).

- 33 Malda, J., Klein, T. J. & Upton, Z. The roles of hypoxia in the In vitro engineering of tissues. *Tissue Eng* **13**, 2153-2162, doi:10.1089/ten.2006.0417 (2007).
- 34 Agrawal, C. M., McKinney, J. S., Lanctot, D. & Athanasiou, K. A. Effects of fluid flow on the in vitro degradation kinetics of biodegradable scaffolds for tissue engineering. *Biomaterials* **21**, 2443-2452 (2000).
- 35 Innocentini, M., Sepulveda, P., Ortega, F., Scheffler, M. & Colombo, P. Permeability. Cellular Ceramics: Structure, Manufacturing, Properties and Applications. *Permeability. Cellular Ceramics: Structure, Manufacturing, Properties and Applications* (2005).
- 36 Innocentini, M. D. M., Salvini, V. R., Pandolfelli, V. C. & Coury, J. R. The permeability of ceramic foams. *Am. Ceram. Soc. Bull.* **78**, 78-84 (1999).
- 37 Moreira, E. A., Innocentini, M. D. M. & Coury, J. R. Permeability of ceramic foams to compressible and incompressible flow. *J. Eur. Ceram. Soc.* **24**, 3209-3218, doi:10.1016/j.jeurceramsoc.2003.11.014 (2004).
- 38 Biasetto, L., Colombo, P., Innocentini, M. D. M. & Mullens, S. Gas permeability of microcellular ceramic foams. *Ind. Eng. Chem. Res.* **46**, 3366-3372, doi:10.1021/ie061335d (2007).

- 39 Flemming, R. G., Murphy, C. J., Abrams, G. A., Goodman, S. L. & Nealey, P. F. Effects of synthetic micro- and nano-structured surfaces on cell behavior. *Biomaterials* **20**, 573-588 (1999).
- 40 Wan, Y. Q. *et al.* Adhesion and proliferation of OCT-1 osteoblast-like cells on micro- and nano-scale topography structured pply(L-lactide). *Biomaterials* **26**, 4453-4459, doi:10.1016/j.biomaterials.2004.11.016 (2005).
- 41 Wu, Y., Zitelli, J. P., TenHuisen, K. S., Yu, X. J. & Libera, M. R. Differential response of Staphylococci and osteoblasts to varying titanium surface roughness. *Biomaterials* **32**, 951-960, doi:10.1016/j.biomaterials.2010.10.001 (2011).
- 42 Dalby, M. J., Gadegaard, N. & Wilkinson, C. D. The response of fibroblasts to hexagonal nanotopography fabricated by electron beam lithography. *J. Biomed. Mater. Res. Part A* **84**, 973-979 (2008).
- 43 Zaveri, T. D. *et al.* Contributions of surface topography and cytotoxicity to the macrophage response to zinc oxide nanorods. *Biomaterials* **31**, 2999-3007, doi:10.1016/j.biomaterials.2009.12.055 (2010).

- 44 Lamers, E. *et al.* THE INFLUENCE OF NANOSCALE TOPOGRAPHICAL CUES ON INITIAL OSTEOBLAST MORPHOLOGY AND MIGRATION. *Eur Cells Mater* **20**, 329-343 (2010).
- 45 Hing, K. A., Annaz, B., Saeed, S., Revell, P. A. & Buckland, T. Microporosity enhances bioactivity of synthetic bone graft substitutes. *J. Mater. Sci.-Mater. Med.* **16**, 467-475, doi:10.1007/s10856-005-6988-1 (2005).
- 46 Yuan, H. P. *et al.* A comparison of the osteoinductive potential of two calcium phosphate ceramics implanted intramuscularly in goats. *J. Mater. Sci.-Mater. Med.* **13**, 1271-1275 (2002).
- 47 Habibovic, P. *et al.* 3D microenvironment as essential element for osteoinduction by biomaterials. *Biomaterials* **26**, 3565-3575, doi:10.1016/j.biomaterials.2004.09.056 (2005).
- 48 Habibovic, P. *et al.* Comparative in vivo study of six hydroxyapatite-based bone graft substitutes. *J. Orthop. Res.* **26**, 1363-1370, doi:10.1002/jor.20648 (2008).
- 49 Habibovic, P., Sees, T. M., van den Doel, M. A., van Blitterswijk, C. A. & de Groot, K. Osteoinduction by biomaterials - Physicochemical and structural influences. *J. Biomed. Mater. Res. Part A* **77A**, 747-762, doi:10.1002/jbm.a.30712 (2006).

- 50 Hing, K. A., Best, S. M., Tanner, K. E., Bonfield, W. & Revell, P. A. Quantification of bone ingrowth within bone-derived porous hydroxyapatite implants of varying density. *J. Mater. Sci.-Mater. Med.* **10**, 663-670 (1999).
- 51 Liu, Y. L., Schoenaers, J., De Groot, K., De Wijn, J. R. & Schepers, E. Bone healing in porous implants: a histological and histometrical comparative study on sheep. *J. Mater. Sci.-Mater. Med.* **11**, 711-717 (2000).
- 52 Daculsi, G. Biphasic calcium phosphate concept applied to artificial bone, implant coating and injectable bone substitute. *Biomaterials* **19**, 1473-1478 (1998).
- 53 Daculsi, G., LeGeros, R., Heughebaert, M. & Barbieux, I. Formation of carbonate-apatite crystals after implantation of calcium phosphate ceramics. *Calcif. Tissue Int.* **46**, 20-27 (1990).
- 54 Daculsi, G., LeGeros, R., Nery, E., Lynch, K. & Kerebel, B. Transformation of biphasic calcium phosphate ceramics in vivo: ultrastructural and physicochemical characterization. *J. Biomed. Mater. Res.* **23**, 883-894 (1989).
- 55 Daculsi, G. & Passuti, N. Effect of the macroporosity for osseous substitution of calcium phosphate ceramics. *Biomaterials* **11**, 86-87 (1990).

- 56 Jegoux, F. *et al.* Mandibular Segmental Defect Regenerated With Macroporous Biphasic Calcium Phosphate, Collagen Membrane, and Bone Marrow Graft in Dogs. *Archives of Otolaryngology-Head & Neck Surgery* **136**, 971-978 (2010).
- 57 Yuan, H. P. *et al.* Osteoinductive ceramics as a synthetic alternative to autologous bone grafting. *Proc Natl Acad Sci U S A* **107**, 13614-13619, doi:10.1073/pnas.1003600107 (2010).
- 58 Tsui, Y. K. & Gogolewski, S. Microporous biodegradable polyurethane membranes for tissue engineering. *J. Mater. Sci.-Mater. Med.* **20**, 1729-1741, doi:10.1007/s10856-009-3722-4 (2009).
- 59 Jiang, X., Gu, J. A., Shen, Y., Wang, S. G. & Tian, X. Z. Formation of Honeycomb-Patterned Microporous Films Based on a Fluorinated Poly(siloxane imide) Segmented Copolymer. *J. Appl. Polym. Sci.* **119**, 3329-3337, doi:10.1002/app.33085 (2011).
- 60 Brittberg, M. *et al.* Treatment of deep cartilage defects in the knee with autologous chondrocyte transplantation. *N Engl J Med* **331**, 889-895 (1994).

- 61 Peterson, L., Minas, T., Brittberg, M. & Lindahl, A. Treatment of osteochondritis dissecans of the knee with autologous chondrocyte transplantation. *The Journal of Bone & Joint Surgery* **85**, 17-24 (2003).
- 62 Hill, C. M. *et al.* in *Macromol. Symp.* 94-97 (Wiley Online Library).
- 63 Lee, C. R. *et al.* Fibrin-polyurethane composites for articular cartilage tissue engineering: A preliminary analysis. *Tissue Eng* **11**, 1562-1573 (2005).
- 64 Chia, S., Gorna, K., Gogolewski, S. & Alini, M. Potential of elastomeric membranes from biodegradable polyurethanes as periosteal flap substitute: A preliminary in vitro evaluation. *Tissue Eng* **12**, 1945-1953 (2006).
- 65 Saki, M., Narbat, M. K., Samadikuchaksaraei, A., Ghafouri, H. B. & Gorjipour, F. Biocompatibility Study of a Hydroxyapatite-Alumina and Silicon Carbide Composite Scaffold for Bone Tissue Engineering. *Yakhteh* **11**, 55-60 (2009).
- 66 Geiger, M., Li, R. H. & Friess, W. Collagen sponges for bone regeneration with rhBMP-2. *Adv. Drug Delivery Rev.* **55**, 1613-1629, doi:10.1016/j.addr.2003.08.010 (2003).

- 67 Friess, W. Collagen - biomaterial for drug delivery. *Eur. J. Pharm. Biopharm.* **45**, 113-136 (1998).
- 68 Louis-Ugbo, J. *et al.* Retention of I-125-labeled recombinant human bone morphogenetic protein-2 by biphasic calcium phosphate or a composite sponge in a rabbit posterolateral spine arthrodesis model. *J. Orthop. Res.* **20**, 1050-1059 (2002).
- 69 Shields, L. B. E. *et al.* Adverse effects associated with high-dose recombinant human bone morphogenetic protein-2 use in anterior cervical spine fusion. *Spine* **31**, 542-547 (2006).
- 70 Tanaka, A., Nagate, T. & Matsuda, H. Acceleration of wound healing by gelatin film dressings with epidermal growth factor. *J. Vet. Med. Sci.* **67**, 909-913 (2005).
- 71 Mozafari, M., Rabiee, M., Azami, M. & Maleknia, S. Biomimetic formation of apatite on the surface of porous gelatin/bioactive glass nanocomposite scaffolds. *Appl. Surf. Sci.* **257**, 1740-1749, doi:10.1016/j.apsusc.2010.09.008 (2010).
- 72 Leeuwenburgh, S. C. G. *et al.* Mineralization, Biodegradation, and Drug Release Behavior of Gelatin/Apatite Composite Microspheres for Bone Regeneration. *Biomacromolecules* **11**, 2653-2659, doi:10.1021/bm1006344 (2010).

- 73 Tabata, Y. & Ikada, Y. Vascularization effect of basic fibroblast growth factor released from gelatin hydrogels with different biodegradabilities. *Biomaterials* **20**, 2169-2175 (1999).
- 74 Lai, J. Y. & Li, Y. T. Influence of Cross-Linker Concentration on the Functionality of Carbodiimide Cross-Linked Gelatin Membranes for Retinal Sheet Carriers. *J. Biomater. Sci.-Polym. Ed.* **22**, 277-295, doi:10.1163/092050609x12603600753204 (2011).
- 75 Asamura, S., Mochizuki, Y., Yamamoto, M., Tabata, Y. & Isogai, N. Bone Regeneration Using a Bone Morphogenetic Protein-2 Saturated Slow-Release Gelatin Hydrogel Sheet Evaluation in a Canine Orbital Floor Fracture Model. *Ann. Plast. Surg.* **64**, 496-502, doi:10.1097/SAP.0b013e31819b6c52 (2010).
- 76 Huang, S. & Fu, X. B. Naturally derived materials-based cell and drug delivery systems in skin regeneration. *J. Controlled Release* **142**, 149-159, doi:10.1016/j.jconrel.2009.10.018 (2010).
- 77 Li, M., Liu, X. Y., Liu, X. D. & Ge, B. F. Calcium Phosphate Cement with BMP-2-loaded Gelatin Microspheres Enhances Bone Healing in Osteoporosis: A Pilot Study. *Clin. Orthop.* **468**, 1978-1985, doi:10.1007/s11999-010-1321-9 (2010).

- 78 Wang, H. *et al.* Combined delivery of BMP-2 and bFGF from nanostructured colloidal gelatin gels and its effect on bone regeneration in vivo. *J. Controlled Release* **166**, 172-181 (2013).
- 79 Miranda, S. *et al.* Three-dimensional culture of rat BMMSCs in a porous chitosan-gelatin scaffold: A promising association for bone tissue engineering in oral reconstruction. *Arch. Oral Biol.* **56**, 1-15, doi:10.1016/j.archoralbio.2010.08.018 (2011).
- 80 Bae, M. S., Kim, D. W., Kim, S. E., Choi, K. K. & Kwon, I. K. BMP-2 Immobilized Gelatin-beta-Chitosan Scaffold for Bone Regeneration. *Tissue Eng. Regen. Med.* **6**, 609-614 (2009).
- 81 Hu, W. W., Ward, B. B., Wang, Z. & Krebsbach, P. H. Bone Regeneration in Defects Compromised by Radiotherapy. *J. Dent. Res.* **89**, 77-81, doi:10.1177/0022034509352151 (2010).
- 82 Marston, W. A., Usala, A., Hill, R. S., Mendes, R. & Minsley, M. A. Initial report of the use of an injectable porcine collagen-derived matrix to stimulate healing of diabetic foot wounds in humans. *Wound Repair Regen* **13**, 243-247 (2005).

- 83 Miyazaki, M. *et al.* A porcine collagen-derived matrix as a carrier for recombinant human bone morphogenetic protein-2 enhances spinal fusion in rats. *Spine J.* **9**, 22-30, doi:10.1016/j.spinee.2008.08.009 (2009).
- 84 Tokuhara, Y. *et al.* Repair of experimentally induced large osteochondral defects in rabbit knee with various concentrations of Escherichia coli-derived recombinant human bone morphogenetic protein-2. *Int. Orthop.* **34**, 761-767, doi:10.1007/s00264-009-0818-x (2010).
- 85 Kimura, Y. *et al.* Controlled Release of Bone Morphogenetic Protein-2 Enhances Recruitment of Osteogenic Progenitor Cells for De Novo Generation of Bone Tissue. *Tissue Eng. Part A* **16**, 1263-1270, doi:10.1089/ten.tea.2009.0322 (2010).
- 86 Groeneveld, E. & Burger, E. Bone morphogenetic proteins in human bone regeneration. *Eur. J. Endocrinol.* **142**, 9-21 (2000).
- 87 Kirsch, T., Sebald, W. & Dreyer, M. K. Crystal structure of the BMP-2-BRIA ectodomain complex. *Nat. Struct. Biol.* **7**, 492-496 (2000).
- 88 Yuan, Q. *et al.* in *Key Eng. Mater.* 1261-1264 (Trans Tech Publ).

- 89 Kirsch, T., Nickel, J. & Sebald, W. BMP-2 antagonists emerge from alterations in the low-affinity binding epitope for receptor BMPR-II. *EMBO J.* **19**, 3314-3324 (2000).
- 90 Wu, B. *et al.* Preparation and ectopic osteogenesis in vivo of scaffold based on mineralized recombinant human-like collagen loaded with synthetic BMP-2-derived peptide. *Biomed. Mater.* **3**, 7, doi:044111
10.1088/1748-6041/3/4/044111 (2008).
- 91 Duan, Z. X., Zheng, Q. X., Guo, X. D., Yuan, Q. & Chen, S. G. Experimental research on ectopic osteogenesis of BMP2-derived peptide P24 combined with PLGA copolymers. *Journal of Huazhong University of Science and Technology-Medical Sciences* **27**, 179-182, doi:10.1007/s11596-007-0219-6 (2007).
- 92 Duan, Z. X. *et al.* Repair of Rabbit Femoral Defects with a Novel BMP2-derived Oligopeptide P24. *Journal of Huazhong University of Science and Technology-Medical Sciences* **28**, 426-430, doi:10.1007/s11596-008-0411-3 (2008).
- 93 Suzuki, Y. *et al.* Alginate hydrogel linked with synthetic oligopeptide derived from BMP-2 allows ectopic osteoinduction in vivo. *J. Biomed. Mater. Res.* **50**, 405-409 (2000).

- 94 Nakazawa, T. *et al.* Autogenous iliac crest bone graft versus banked allograft bone in scoliosis surgery in patients with Duchenne muscular dystrophy. *Int. Orthop.* **34**, 855-861, doi:10.1007/s00264-009-0828-8 (2010).
- 95 Jurgensmeier, D. & Hart, R. Variability in Tissue Bank Practices Regarding Donor and Tissue Screening of Structural Allograft Bone. *Spine* **35**, E702-E707, doi:10.1097/BRS.0b013e3181d2526d (2010).
- 96 Greenberg, D. D., Robertson, M., Vallurupalli, S., White, R. A. & Allen, W. C. Allograft Compared with Autograft Infection Rates in Primary Anterior Cruciate Ligament Reconstruction. *J. Bone Joint Surg.-Am. Vol.* **92A**, 2402-2408, doi:10.2106/jbjs.i.00456 (2010).
- 97 Mikhael, M. M., Huddleston, P. M. & Nassr, A. Postoperative Culture Positive Surgical Site Infections After the Use of Irradiated Allograft, Nonirradiated Allograft, or Autograft for Spinal Fusion. *Spine* **34**, 2466-2468, doi:10.1097/BRS.0b013e3181b1fef5 (2009).
- 98 Milhael, M. M. *et al.* Mechanical strength of bone allografts subjected to chemical sterilization and other terminal processing methods. *J. Biomech.* **41**, 2816-2820, doi:10.1016/j.jbiomech.2008.07.012 (2008).

- 99 Enneking, W. E. & Campanacci, D. A. Retrieved human allografts - A clinicopathological study. *J. Bone Joint Surg.-Am. Vol.* **83A**, 971-986 (2001).
- 100 Runyan, C. M. *et al.* Porcine Allograft Mandible Revitalization Using Autologous Adipose-Derived Stem Cells, Bone Morphogenetic Protein-2, and Periosteum. *Plast. Reconstr. Surg.* **125**, 1372-1382, doi:10.1097/PRS.0b013e3181d7032f (2010).
- 101 Galloway, S. H., Miura, Y., Comisso, C. N., Fitzsimmons, J. S. & O'Driscoll, S. W. Relationship of donor site to chondrogenic potential of periosteum in vitro. *J. Orthop. Res.* **12**, 515-525 (1994).
- 102 Olivos-Meza, A. *et al.* Pretreatment of periosteum with TGF-beta 1 in situ enhances the quality of osteochondral tissue regenerated from transplanted periosteal grafts in adult rabbits. *Osteoarthritis Cartilage* **18**, 1183-1191, doi:10.1016/j.joca.2010.06.003 (2010).
- 103 Reinholz, G. *et al.* Rejuvenation of periosteal chondrogenesis using local growth factor injection. *Osteoarthritis Cartilage* **17**, 723-734 (2009).
- 104 Joyce, M. E., Roberts, A. B., Sporn, M. B. & Bolander, M. E. Transforming growth factor-beta and the initiation of chondrogenesis and osteogenesis in the rat femur. *The Journal of cell biology* **110**, 2195-2207 (1990).

- 105 Becker, S. T. *et al.* Biocompatibility of individually designed scaffolds with human periosteum for use in tissue engineering. *J. Mater. Sci.-Mater. Med.* **21**, 1255-1262, doi:10.1007/s10856-009-3878-y (2010).
- 106 Soltan, M., Smiler, D. & Soltan, C. The Inverted Periosteal Flap: A Source of Stem Cells Enhancing Bone Regeneration. *Implant Dent.* **18**, 373-379, doi:10.1097/ID.0b013e3181b9d7df (2009).
- 107 Taylor, J. A. Bilateral Orbitozygomatic Reconstruction With Tissue-Engineered Bone. *J. Craniofac. Surg.* **21**, 1612-1614, doi:10.1097/SCS.0b013e3181edc829 (2010).
- 108 Choudry, U. H., Bakri, K., Moran, S. L., Karacor, Z. & Shin, A. Y. The vascularized medial femoral condyle periosteal bone flap for the treatment of recalcitrant bony nonunions. *Ann. Plast. Surg.* **60**, 174-180, doi:10.1097/SAP.0b013e318056d6b5 (2008).

CHAPTER 1: In-vitro cytotoxicity of rare earth oxide nanoparticles for imaging applications

Peter E. Petrochenko^{1, 2}, Qin Zhang¹, Haorong Wang³, Ted Sun³, Bridget Wildt¹,
Martha W. Betz¹, Peter L. Goering¹, Roger J. Narayan².

¹Division of Biology, Office of Science and Engineering Laboratories, Center for Devices and Radiological Health, U.S. Food and Drug Administration, Silver Spring, MD 20993

²Joint Department of Biomedical Engineering, UNC – Chapel Hill and North Carolina State University, Raleigh, NC 27965

³Sun Innovations Inc., Fremont, CA 94539

Note:

The mention of commercial products, their sources, or their use in connection with material reported herein is not to be construed as either an actual or implied endorsement of such products by the Department of Health and Human Services.

Abstract:

The *in vitro* cytotoxicity and cellular uptake of commercially available doped YVO_4 was evaluated in RAW 264.7 macrophages using the MTT assay. The results indicated that 20-50 nm diameter samarium-doped YVO_4 showed significant toxicity at concentrations of 25 $\mu\text{g/ml}$ and higher; samples of the same material functionalized with COOH showed less cytotoxicity. At concentrations of 25-100 $\mu\text{g/ml}$, 20-50 nm erbium-doped YVO_4 showed less toxicity compared with 20-50 nm samarium-doped YVO_4 . 10-nm samples showed no toxicity at concentrations of 100-600 $\mu\text{g/ml}$. The cytotoxicity of rare earth metal nanoparticles in macrophages is dependent, at least in part, on size and surface functionalization.

Introduction:

The lanthanide element series along with two chemically similar elements, scandium and yttrium, are known as rare earth elements. Rare earth metal oxides can be synthesized as mixed oxides¹ to obtain a range of desirable physical properties. In our study, we examined commercially available rare earth metal oxide nanoparticles that have a number of possible medical and pharmaceutical applications, namely as imaging agents and diagnostic probes. Rare earth oxides exhibit luminescence and are commonly termed phosphors. Their imaging properties originate from their shielded f-electrons, which give lanthanides their characteristic long luminescence lifetimes. Lanthanide ions by themselves, however, are fairly difficult to excite in order to achieve a sufficiently strong signal. This limitation is overcome by functionalizing the surface with surface modifying organic ligands and transferring incoming energy to the metal core.² The lanthanide surface can be functionalized with a ligand that is appropriate for a given application.³ Alternatively, the rare earth elements can be doped into an inorganic host crystal structure. The host material absorbs photon energy and transfers it through either charge transfer or energy transfer mechanisms to the rare earth atoms for emission. For the nanoparticles used in this study, yttrium vanadate (YVO₄), the host material, absorbs photons and transfers the energy to the rare earth component, which subsequently emits the resulting photons. In the case of nanoparticles, the inorganic compound is generally more stable than the metal complexes at various chemical conditions. Lanthanides themselves possess sufficient chemical stability to make them suitable for use as dopants⁴ and free nanoparticles in solution.⁵ Rare earth metal nanoparticles also tend to exhibit characteristic narrow band emission spectra and slow decay rates. Their

size and dimensions can be optimized⁶ to improve luminescence properties in order to yield a reliable imaging agent with a long lifetime.⁷

Human health safety considerations arise with rare earth metal nanoparticles due to use of these materials in diagnostics,⁸ biolabeling,⁹ drug delivery,¹⁰ and other medical applications. Rare earth metals show varying levels of element-dependent toxicity to certain plant and aquatic life. For example, ecotoxicity studies of rare earth metal oxide nanoparticles such as yttrium, samarium, erbium, and holmium oxides indicate that these materials may pose some risk to aquatic organisms when dissolved in water and present in sediments.¹¹ Other rare earth metal oxide nanoparticles such as lanthanum, gadolinium, and ytterbium severely inhibit root elongation of certain plants and have other phytotoxic effects.¹² In contrast, evidence for human toxicity is somewhat limited and depends on the application. Rare earth doped nanoparticles are cadmium-free alternatives to traditional quantum dots, which commonly contain toxic heavy metals such as cadmium or lead. Although quantum dots can be manufactured with a variety of materials including zinc,¹³ carbon,¹⁴ and various non-cadmium materials,¹⁵ the best characterized and most commonly used quantum dot materials contain cadmium. Cadmium is more toxic than rare earth metals; it should be noted that somewhat considerable cytotoxicity of certain rare earth oxides has been reported in pulmonary alveolar macrophages.¹⁶ In HeLa cells, however, lanthanide complexes enter freely into the cytoplasm and have no apparent toxic effects.¹⁷ When conjugated with heparin, lanthanide hybrid materials may decrease toxicity, improve cell adhesion in a PC-12 pheochromocytoma cell model, and decrease coagulation in rabbit blood.¹⁸

Because of the relative lack of data on the toxicity of rare earth oxides, including in nanoparticle form, this study was designed to address the following two objectives: (1) to evaluate cellular interactions and potential cytotoxicity of rare earth-doped YVO_4 nanoparticles in macrophages, and (2) to select a potential non-toxic imaging agent for future experiments. In order to examine potential effects of size and surface functionalization on cellular response, macrophages were exposed to nanoparticles with two different size distributions; particle samples had either an average diameter of 10 nm or an average diameter range of 20-50 nm. Lanthanide nanoparticles with or without COOH surface functionalization were incubated with macrophages to evaluate the effect of surface functionalization on cytotoxicity. Cellular uptake with nanoparticles was also investigated.

Materials and Methods:

Nanoparticle Characterization:

Phosphor-based lanthanide nanoparticles were obtained from Sun Innovations, Inc. (Fremont, California). The samples consisted of YVO_4 doped with either samarium, erbium, dysprosium, or europium. The YVO_4 doped with samarium and YVO_4 doped with europium samples were acquired with and without COOH surface functionalization. Table 1 shows the various nanoparticle types evaluated in this study with the item number abbreviation. The emission and excitation wavelengths provided by the manufacturer are also noted. YVD 1001 and YVE 1005, both 10 nm, were synthesized in a similar fashion; YVD 1001 was doped with dysprosium and YVE 1005 was doped with europium. The YVD 1001, YVE 1005 and YVER 1004 nanoparticle samples were stabilized by citrate, which also acted as a reducing agent. The YVS 1101 nanoparticle samples did not contain citrate and were instead stabilized by polyvinylpyrrolidone (PVP). PVP and citrate are both common capping agents used to prevent aggregation of individual nanoparticles. PVP is known to chelate lanthanide ions and cover the surface of nanoparticles. It is also used to control size, morphology, and shape of rare earth nanoparticles while giving them good aqueous dispersibility and a relatively narrow size distribution.^{19, 20} After completing nanoparticle synthesis, two samples, YVE 1005 and YVS 1101, were additionally surface functionalized with carboxyl groups ($-\text{COOH}$). Surface functionalization was performed using ligand exchange methods. Nanoparticle size and shape were characterized using transmission electron microscopy (TEM). Samples for microscopy were prepared on holey carbon-coated copper grids and

TEM images were obtained using a Tecnai 12 transmission electron microscope (FEI, Hillsboro, Oregon).

Cell Culture:

Mouse macrophages (RAW 264.7 cells, TIB-71, American Type Culture Collection, Manassas, VA) were cultured in Dulbecco's Modified Eagle Media with 10% fetal bovine serum. Cells were plated at a density of 2×10^4 per well in a 96-well plate. Prior to nanoparticle exposure, the cells were allowed to reach 50-60% confluence approximately 24 hours after seeding. The cells were maintained in a 5% CO₂ incubator at 37°C and 95% humidified air.

Limus Amebocyte Lysate (LAL) Assay:

All samples were tested for endotoxin using a chromomeric end-point LAL assay kit (Lonza, Walkersville, MD). All materials during the assay, including pipette tips, tubes, reagents, were purchased in endotoxin-free form from the manufacturers. The presence of endotoxin in the test nanoparticle samples was assessed and the endotoxin concentrations were calculated from a standard curve. The concentration of endotoxin was expressed as EU/ml. In order to assess whether nanoparticles interfered with the assay readout, identical amounts of test samples used in the cytotoxicity experiments were diluted in endotoxin-free water and run in parallel with the test samples.

Cell Imaging:

To investigate the cell uptake and interactions with test nanoparticles, the macrophages were plated at a density of 2.4×10^4 cells/ml overnight in Lab-Tek II™ chamber slides (NUNC, Rochester, NY). After overnight incubation, YVS 1101, YVS 1101 COOH, and

YVER 1004 nanoparticles at a concentration of 25 µg/ml and YVE 1005, YVE 1005 COOH, and YVD 1001 nanoparticles at a concentration of 300 µg/ml were added to the cells. After 6 hours incubation, cells were washed with PBS to remove unbounded particles. Cells were fixed with 4% paraformaldehyde and were sealed with ProLong® mounting medium (Life Technologies, Grand Island, NY) and a cover slip. Images were acquired using a CytoViva® high resolution dark field microscope (CytoViva, Inc. Auburn, AL) with a 100x oil immersion objective.

MTT cell viability assay:

Cell viability was measured by MTT (3-(4,5-dimethyl-2-thiazol)-2, 5-diphenyl-2H-tetrazolium bromide) assay (Promega, WI, USA). Cells were seeded in 96-well plate as described above and exposed to different concentrations of nanoparticles for 24 and 48 hours.

Pre-mixed dye (15

□l) was then ad

°C. After each incubation period, the solubilization solution/stop buffer was added and the plate was incubated for 1 hour before the measurement. Absorbance was measured at wavelength of 570 nm (the reference wavelength was 650 nm) using a 96-well OPTIMax plate reader (Molecular Devices, Sunnyvale, CA). Cells treated with 5% and 10% dimethyl sulfoxide (DMSO) served as a positive control group. In order to assess whether nanoparticles interfered with the assay readout, cell-free controls with different concentrations of nanoparticles were included in the assay. Final values were calculated by subtracting the background absorbance of the nanoparticles and the medium alone group.

In order to evaluate the potential toxicity of chemicals present in the nanoparticle dispersant/solvent, supernatants were collected from the stock solutions supplied by the

manufacturer. Supernatants were collected after centrifuging nanoparticles for 60 minutes at 13,300 rpm. An aliquot from the top half layer of the resulting supernatant was assessed for cytotoxicity in the MTT assay.

Statistical Analysis:

The results from each data set were analyzed using Prism statistical software (GraphPad Inc., La Jolla, CA). Results were expressed as mean \pm standard deviation. Statistical differences between control and treated groups were assessed using one-way ANOVA with a Bonferroni *post hoc* test. Each experiment was repeated at least 3 times with each assay in duplicate. A *P* value of less than 0.05 was considered to be significantly different from the control group.

Results:

Characterization of nanoparticles:

The size distribution of nanoparticles was assessed using TEM. The average diameters for the six samples of nanoparticles are summarized in Table 1. YVER 1004 nanoparticles had a slightly elongated shape (Fig. 1A). YVS 1101 nanoparticles (Fig. 1B), which were stabilized by polyvinylpyrrolidone (PVP), are shown in Fig. 1B. No differences in nanoparticle morphologies between YVD 1001 and YVE 1005 (Fig. 1C) were seen from TEM images; this result may be attributed to their similar synthesis and (citrate) stabilization methods. COOH functionalization was performed through ligand exchange methods following synthesis; therefore, no variation in morphology between nanoparticles with COOH functionalization and nanoparticles without COOH functionalization was observed. YVER 1004 nanoparticles had a slightly different morphology from YVS 1101 nanoparticles (Fig. 1A). On the other hand, YVS 1101 nanoparticles with or without COOH functionalization exhibited similar shapes.

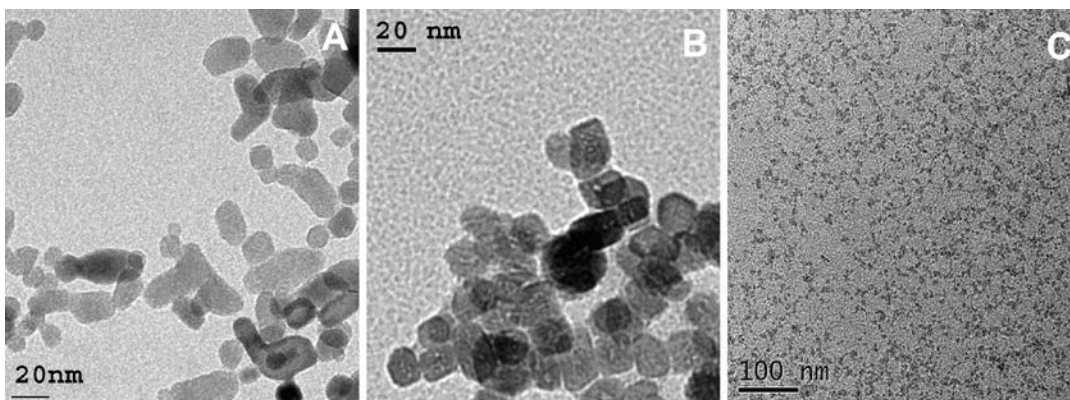


Figure 1. TEM characterization of nanoparticles. A. Erbium-doped yttrium vanadate colloid (YVER 1004). B. Samarium-doped yttrium vanadate colloid (YVS 1101). C. Europium-doped yttrium vanadate colloid (YVE 1005).

Table 1. Physical properties of tested nanoparticles.

Description	Sample code	Excitation (nm)	Emission (nm)	Average size range (nm)
Dysprosium-doped yttrium vanadate colloid	YVD 1001	300	486, 576	10
Europium-doped yttrium vanadate colloid (/with COOH coating)	YVE 1005/YVE 1005-COOH	350	617	10
Erbium-doped yttrium vanadate colloid	YVER 1004	300	527, 556	20–50
Samarium-doped yttrium vanadate colloid (/with COOH coating)	YVS 1101/YVS 1101-COOH	300	568, 607, 650	20–50

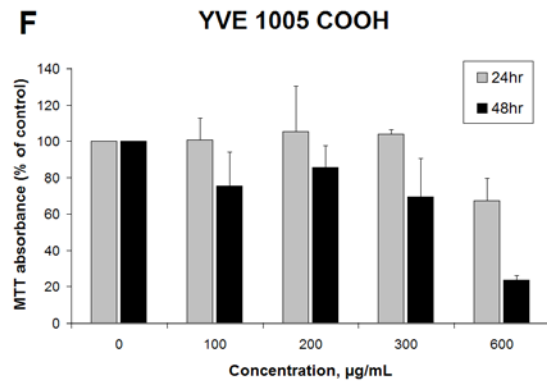
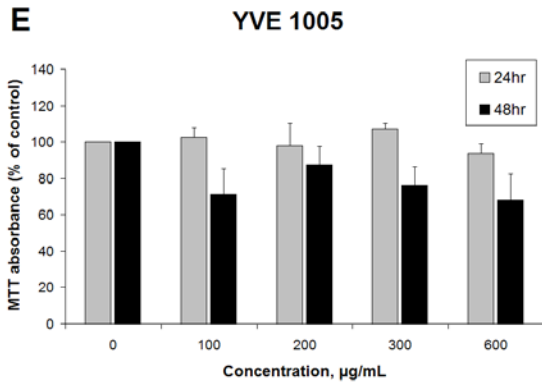
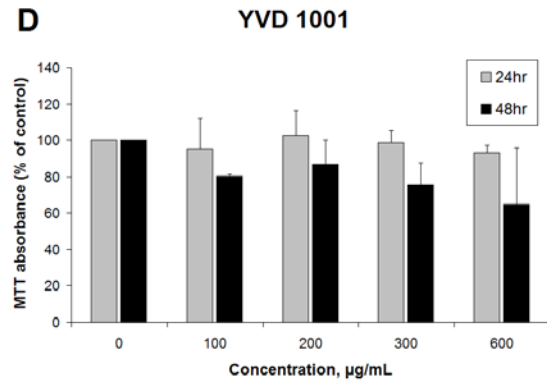
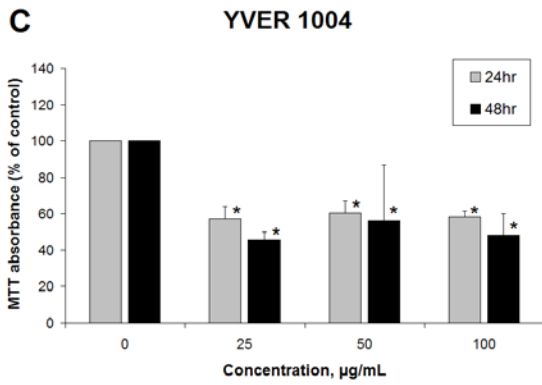
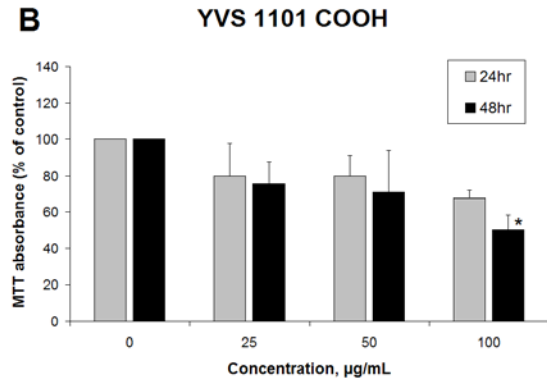
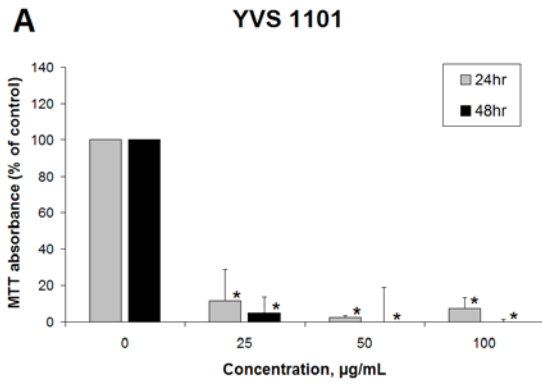
Contamination of medical products with endotoxin due to non-sterile conditions during fabrication is an important consideration for patient health. Endotoxin can cause life-threatening reactions and endotoxin limits exist for medical devices.²¹ Endotoxin contamination in test samples can activate macrophages and induce an inflammatory response, including oxidative stress, in macrophages. High levels of endotoxin could cause or potentiate cell toxicity following exposure to nanomaterials. In this study, we assessed endotoxin levels in each type of nanoparticle preparation using the LAL assay. The results showed that two samples were contaminated with endotoxin. YVS 1101 and YVS 1101 with COOH functionalization had concentrations of approximately 560 and 224 EU/ml of endotoxin, respectively. The rest of the samples had undetectable amounts of endotoxin.

Cytotoxicity of nanoparticles

To determine the potential toxicity of nanoparticles in macrophages, cell viability was studied using the MTT assay (Fig. 2). None of the test nanoparticles in cell-free control experiments were noted to significantly interfere with the identical or similar absorbance readout wavelengths of the MTT assay. The results indicated that there was no toxicity observed in cells treated with dysprosium-doped YVO_4 colloid (YVD 1001) or europium-doped YVO_4 colloid without COOH functionalization (YVE 1005) after 24 hour exposure at all tested (100 – 600 $\mu\text{g/ml}$) concentrations (Fig. 2D and 2E). The cell viability trend for the 48 hour exposed cells was lower than that for the 24 hour exposed cells; however, no significant concentration-dependent response was observed. Dysprosium-doped YVO_4 colloid (YVD 1001) and europium-doped YVO_4 colloid (YVE 1005) were characterized as 10 nm diameter nanoparticles.

Figure 2. Cytotoxicity of six rare earth oxide nanoparticle types in RAW 264.7

macrophages. Cells were exposed to different concentrations of each type of rare earth oxide nanoparticle for 24 and 48 hours. Cell viability was measured by MTT assay. Cell viability was expressed as percentage of control for six rare earth oxide nanoparticles: A. YVS 1101, B. YVS 1101 - COOH, C. YVER 1004, D. YVD 1001, E. YVE 1005, F. YVE 1005 - COOH. Results are expressed as mean \pm SD from three independent experiments. The positive control, 5% DMSO, exhibited cell viability of 7% after 24 hour exposure and 4% after 48 hour exposure. Statistical significance is shown as the difference between nanoparticle-treated and control cells for raw data values. The symbol * indicates $p < 0.05$.



Compared to dysprosium-doped YVO_4 colloid (YVD 1001) and europium-doped YVO_4 colloid (YVE 1005) above, samarium-doped YVO_4 colloid (YVS 1101) (Fig. 2A) and erbium-doped YVO_4 colloid (YVER 1004) (Fig. 2C) represented a population of large diameter nanoparticles (20-50 nm) and were highly cytotoxic. YVS 1101 was highly cytotoxic at all tested concentrations (25, 50 and 100 $\mu\text{g}/\text{ml}$); cell viability was below 11% after 24 hours of exposure and approached 0-5% after 48 hours of exposure. Compared to YVS 1101, YVER 1004 was mildly cytotoxic, with cell viability approximately 50-60% that of control cells for both 24 and 48 hour exposures. An apparent size effect may be present, since the larger size range (20-50 nm) nanoparticles were more cytotoxic than the 10 nm materials; this effect may be caused in part by the dispersant/solvent (see below).

To determine the effects of nanoparticle surface functionalization on cell toxicity, macrophages were treated with nanoparticles in which the nanoparticle surfaces were modified with COOH (YVS 1101 COOH and YVE 1005 COOH). Cell responses for nanoparticles with COOH functionalization and nanoparticles without COOH functionalization were compared. The results demonstrated that COOH functionalization improved cell viability for YVS 1101, with cell viability ranging from 50 to 80% (Fig. 2B). In contrast, COOH-functionalized YVE 1005 (Fig. 2F) showed no significant changes among 100, 200, and 300 $\mu\text{g}/\text{ml}$ compared to non-functionalized YVS 1101 (Fig. 2A) or non-functionalized YVE 1005 (Fig. 2E). Cell viability for the COOH-functionalized YVE 1005 nanoparticles decreased to 68% after 24 hour exposure and to 24% after 48 hour exposure to the highest concentration of 600 $\mu\text{g}/\text{mL}$ (Fig. 2F); in comparison, cell viability for the non-functionalized YVE 1005 nanoparticles decreased to 93% after 24 hour exposure and to 68%

after 48 hour exposure (Fig. 2E). No statistically significant differences were noted between functionalized and non-functionalized YVE 1005 except for the higher concentration of the COOH-coated YVE 1005 after 48 hour exposure.

To determine if the dispersant/solvent of test nanoparticles contributed to cytotoxicity following exposure to nanoparticles of YVS 1101 and YVER 1004, cell viability was evaluated after incubation with an aliquot of dispersant supernatant for each test sample. The results indicated that supernatants of YVS 1101 and YVER 1004 significantly decreased cell viability following 24 hour exposure (Fig. 3). Distilled water used for dilution of nanoparticles was tested to confirm its lack of toxicity. Supernatant collected from YVS 1101 decreased MTT cell viability by 83% while supernatant collected from the COOH-functionalized version showed no significant decrease in cell viability. YVER 1004 supernatant decreased cell viability by 22%. Centrifuging stock solutions of nanoparticles resulted in slightly opaque areas toward the bottom regions of the tubes rather than clearly distinct pellets. These data suggest that the solvent may partially contribute to the cytotoxicity induced by the nanoparticles. Because we were unable to completely separate the solvent from the high concentration stock solutions, we cannot conclude the extent to which the dispersant/solvent contributes to the cytotoxicity of the nanoparticle samples.

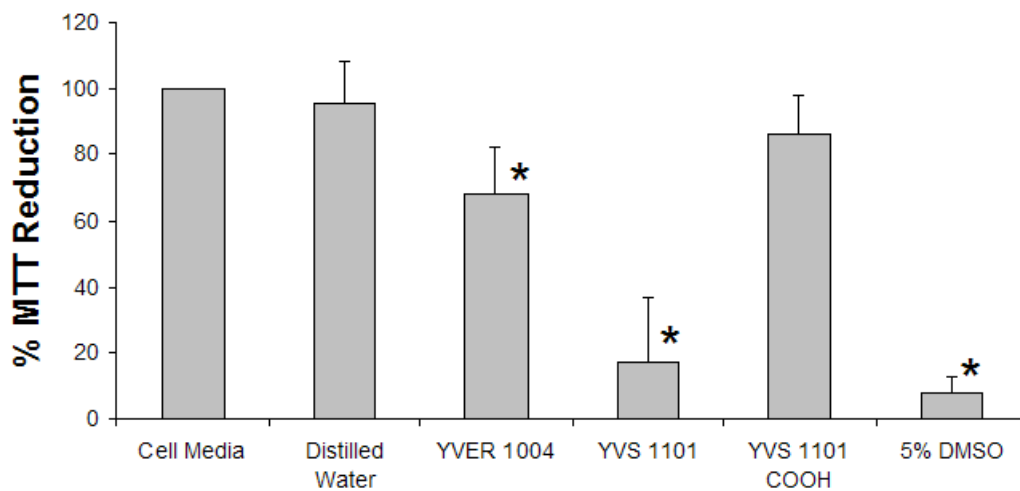
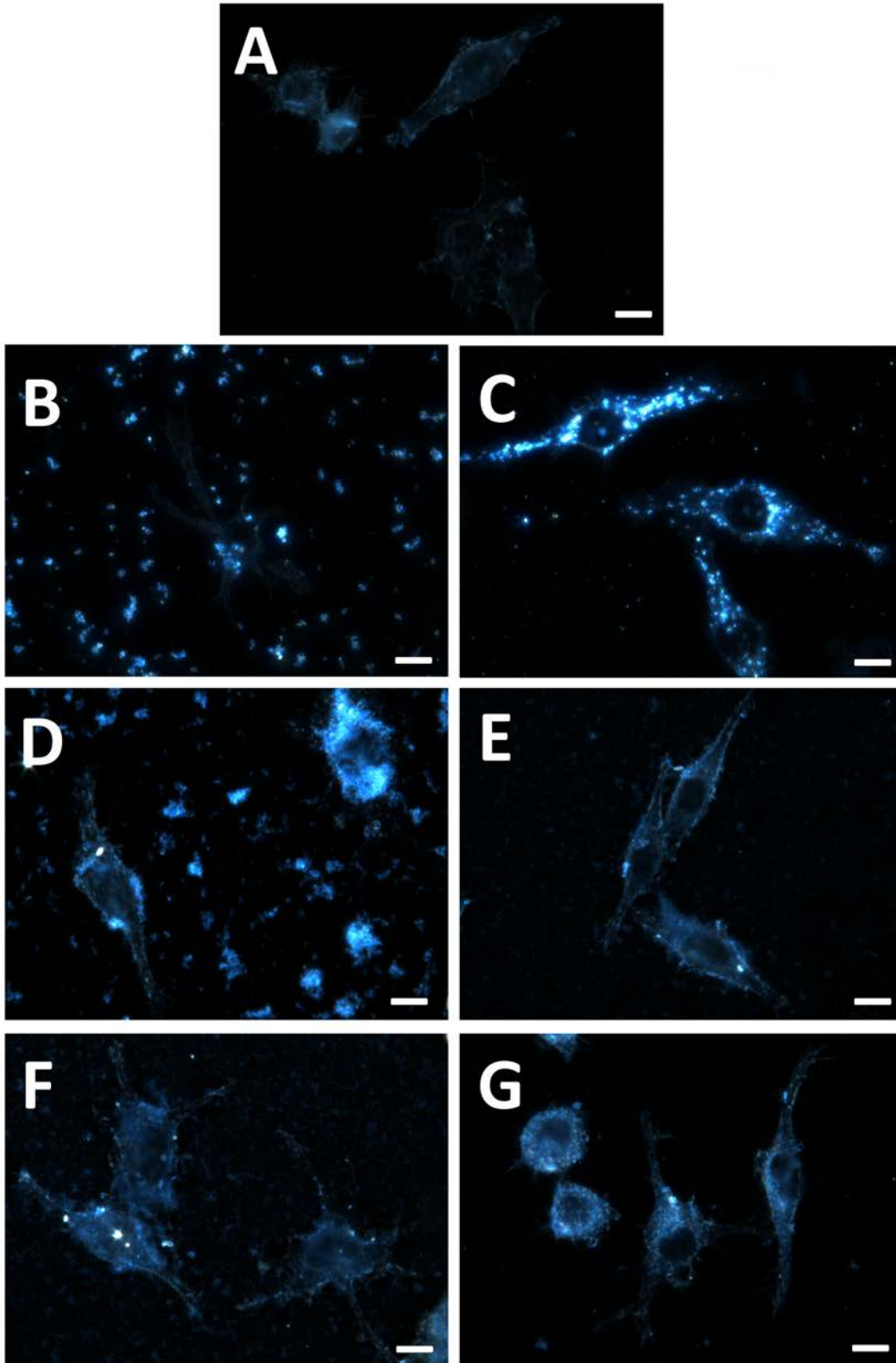


Figure 3. Cytotoxicity of dispersant/solvent supernatants of three rare earth nanoparticle types in RAW 264.7 macrophages. Cells were exposed to the same concentration of each supernatant for 24 hours. Cell viability was measured by MTT assay. Cell viability was expressed as percentage of cell and media control. Results are expressed as mean \pm SD from three independent experiments. Significance is shown as the difference between supernatant-treated and control cells for raw data values. The symbol * indicates $p < 0.05$.

Nanoparticle interaction with cells

High resolution illumination microscopy was performed to investigate cell-rare earth nanoparticle interactions. Fig. 4 shows dark field images of the nanoparticles incubated with macrophages for 6 hours. The darker appearance of control (untreated) cells (Fig. 4A) compared to that of treated cells (Figs. 4B-G) under identical light exposure may be due to nanoparticle uptake in the treated cells. Additionally, there were visible bright spots present in several samples that result from large agglomerates of nanoparticles; these features were not present in the controls. Fig. 4B shows representative images of cells treated by YVS 1101 without COOH. These cells had consistently lower cell numbers due to possible detachment as a result of increased cytotoxicity. In addition, the cells showed possibly altered cell morphology and had darker cytoplasm than other nanoparticle-treated cells.

Figure 4. Representative images of cell-nanoparticle interactions obtained using high resolution CytoViva® dark field microscope in RAW 264.7 macrophages. Cells were incubated with different nanoparticle samples for 6 hours before observation with the microscope. The cells were rinsed several times so that unattached and excess nanoparticles were removed prior to imaging. Exposure times and acquisition parameters were kept constant for all samples and the experiment was repeated independently three times to ensure that the results were consistent. A. Control cells, B. YVS 1101, C. YVS 1101 - COOH, D. YVER 1004, E. YVD 1001, F. YVE 1005, G. YVE 1005 - COOH. All of the images were acquired using the same light exposure level of 303 ms. The bar represents 10 μm .



In contrast, Fig. 4C shows apparent uptake of COOH-functionalized YVS 1101 (brighter illumination of nanoparticles) in the cytoplasm but not in the nucleus. Cell uptake of YVD 1001 (Fig. 4E) and YVE 1005 (Fig. 4F) rare earth nanoparticles was not as evident, possibly due to the smaller average diameter (10 nm) of these nanoparticles. YVER 1004 appeared to be taken up into cells but also was moderately cytotoxic. YVE 1005-COOH appeared to have an even distribution that was restricted to the cytoplasm; cell morphology was normal due to the low cytotoxicity that was observed.

Fig. 5 presents dark field microscopy images of YVS 1101 nanoparticles on glass slides without cells. Fig. 5A shows a representative field in the absence of nanoparticles and cells. Fig. 5B shows images of YVS 1101 nanoparticles without COOH functionalization and Fig. 5C shows images of COOH-functionalized nanoparticles. The YVS 1101 nanoparticles without COOH functionalization (Fig. 5B) showed much greater aggregation and agglomeration than the COOH-functionalized nanoparticles (Fig 5C).

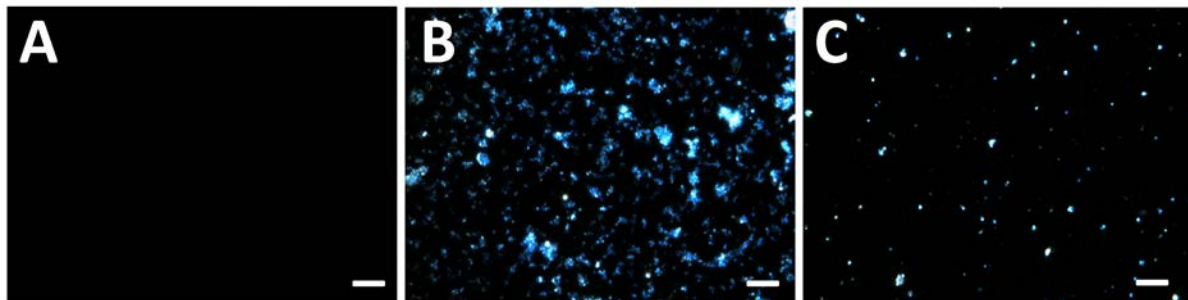


Figure 5. High resolution CytoViva® dark field images of nanoparticles without cells. A. No particles, B. YVS 1101, C. YVS 1101 COOH. All of the images were acquired using the same light exposure level of 303 ms. The bar represents 10 μm .

Discussion:

This study was designed to address the two objectives: to evaluate the cytotoxicity of the rare earth-doped YVO₄ nanoparticles in macrophages and to identify a biocompatible imaging agent for future experiments. The study indicated that a population of samarium-doped YVO₄ (20-50 nm average diameter range) exhibited significant toxicity at concentrations of 25 µg/ml and higher; however, the toxicity was attenuated when the same material was modified with COOH. Erbium-doped YVO₄ (20-50 nm) showed less toxicity at concentrations of 25 to 100 µg/ml than samarium-doped material of the same diameter. All 10 nm diameter samples showed no toxicity at exposure concentrations of up to 600 µg/ml. Thus, the data suggest that factors contributing to cytotoxicity may include particle size (diameter) and surface functionalization.

It is well known that toxicity endpoints for the same cell line differ between assays; therefore, it is important to select the appropriate assay based on the predicted cell death mechanism.²² The MTT assay has been shown to be one of the more sensitive assays for evaluating the cytotoxic potential of nanoparticles.²³ Macrophages are known to phagocytize particles, including nanoparticles, as part of their immunological response to foreign materials.²⁴ Unlike micrometer-sized particles, the smaller size of nanoparticles may allow them to more easily associate with macrophages by both internalizing within cells and attaching to the cell membranes.²⁵ Therefore, macrophages are an appropriate cell model for testing nanoparticle cytotoxicity *in vitro*.

In this study, the toxicity of solvent was evaluated. In order to properly examine the solvent, the majority of nanoparticles should be removed from solution. It is difficult to

completely remove nanoparticles from high concentration stock solutions via centrifugation. A likely possibility exists that a fraction of the nanoparticles is not sufficiently removed from the solvent and/or becomes re-suspended in the solvent immediately following centrifugation. There was no distinctly visible pellet to confirm separation of nanoparticles from the solvent; however, there was a slightly opaque area towards the bottom regions of the centrifuge tubes. Alternatively, a chemical solvent was indeed present in YVS 1101 and YVER 1004 that may account for its toxicity. Possible sources of contamination may come from chemicals used in the manufacturing process and stabilizers present in solution. These possibilities as a source of toxicity warrant further investigation.

The exact mechanism of cytotoxicity of the nanoparticles evaluated in this study is not clear although it is evident from the cell images (Fig. 4) that all of the tested particles, at least to some extent, collect around the cell membrane and may internalize within cells. The non-diffraction limited optical effects and an improved point spread function in the CytoViva microscope allows for a resolution (~ 90 nm) below the typical diffraction limit (~ 240 nm) of ordinary light microscopes.²⁶ While the sizes of some of the rare earth nanoparticles tested in this study are well below the CytoViva limit, 50 nm individual nanoparticles and similarly-sized agglomerates of smaller nanoparticles can be detected. Figs. 4 and 5 present images of the rare earth nanoparticles obtained using the CytoViva microscope. The rare earth nanoparticles used in this study are very bright and highly reflective under dark field microscopy (Figs. 4 and 5), which results in an increase in image illumination. This highly luminescent nature of the rare earth nanoparticles enhances the visibility of the cells by adding a brighter glow to the cell membrane and the cytoplasm. The visible bright spots

present in several treated cells but not in control cells are most likely due to large nanoparticle agglomerates. We cannot conclude with certainty what percentage of nanoparticles are internalized by the cell and what percentage are simply attached to the cell surface. Interestingly, the dim appearance of cells treated with the highly toxic YVS 1101 without COOH (Fig. 4B) suggests that perhaps macrophages did not internalize this specific type of nanoparticle. This observation combined with the fact that this sample contained far fewer cells after treatment as well as the unusual morphology of the surviving cells reinforces the toxicity of these nanoparticles as determined by MTT. It is important to consider nanoparticle agglomeration during *in vitro* cell assays since it may alter cellular uptake of the nanoparticles. The images of the 20-50 nm YVS 1101 and YVER 1004 (Fig. 4B, D) particles show larger agglomerates present in the background; on the other hand, the 20-50 nm COOH-functionalized YVS 1101 nanoparticles (Fig. 4C) and the 10 nm nanoparticles (Fig. 4E-G) are more evenly distributed. It appears that the smaller nanoparticles and the COOH-functionalized nanoparticles distribute more evenly within the cells and on the surface of the cells; in addition, they undergo less agglomeration or aggregation than larger nanoparticles. Comparison of the dark field images of YVS 1101 with (Fig. 5C) and without COOH-functionalization (Fig. 5B) suggests that adding carboxyl moieties to the surface of the rare earth nanoparticles aids nanoparticle dispersion and limits nanoparticle agglomeration. This effect has been exploited in rare earth nanophosphors²⁷ and other nanoparticle systems, including CdSe quantum dots²⁸ and nylon 6/carboxylic silica nanocomposites.²⁹

The possibility that COOH surface functionalization decreases the toxicity of rare earth metal nanomaterials warrants further investigation. Our results show that addition of COOH

groups may make otherwise hydrophobic nanoparticles more hydrophilic and may make them more evenly dispersed in an aqueous solution. However, the idea that hydrophilicity and better dispersion due to COOH alone can make hydrophobic nanoparticles less toxic is not supported by our results. The COOH-functionalized version of YVS 1101 showed remarkable improvement, with a 50 to 77% increase in cell viability values (difference in % of control between the two samples) over the non-functionalized nanoparticles (Fig. 2A and 2B). The COOH-functionalized version of YVE 1005, however, showed no significant changes in cell viability between 100 and 300 µg/ml. At the highest concentration of 600 µg/ml, the cell viability of the COOH-coated YVE 1005 nanoparticles was actually 26% lower after 24 hours and 44% lower after 48 hours than that of the non-functionalized YVE 1005 nanoparticles (difference in % of control between the two samples). This result suggests that while COOH may improve dispersion of nanoparticles, better dispersion may not necessarily decrease the toxicity of rare earth nanoparticles. Due to the already nontoxic nature of certain rare earth metals, additional studies are necessary to look into COOH functionalization and determine if there are instances in which it may have an effect on cell viability. Additionally, the nanoparticle sizes of YVS 1101 and YVD 1001 are somewhat different, approximately ranging from 20-50 nm versus 10 nm, respectively. It is possible that the larger nanoparticles are cytotoxic through absorption of a toxic substrate during the nanoparticle manufacturing process. When large nanoparticles were functionalized by COOH, the stabilization ligands were changed from PVP to a COOH-functionalized ligand, which may have introduced different factors contributing to cytotoxicity. It is not likely that the use of PVP itself over citrate as a stabilizer was responsible for toxicity in YVS 1101

samples. PVP is a relatively non-toxic and common ingredient in medical and pharmaceutical applications. It is used as a solubilizing agent and additive in preparations such as soft-gelatin capsules, oral liquids, gels, lotions, ophthalmic preparations and many more.^{30, 31} A continuously expanding number of nanomaterial fabrication processes have shown PVP as an effective stabilizer and shape controller.^{32, 33} In addition, PVP showed a low toxicity profile *in vitro* and a for variety of exposure routes both *in vivo*.³⁴

Surface charges are also known to affect cellular uptake of nanoparticles. For example, positively charged particles have been shown to end up in high pH microenvironments within the cytosol compartment, while negatively charged particles end up in acidic endosomes.³⁵ Positive surface charges, as opposed to neutral or negative, have been reported to improve cellular uptake of rare earth²⁰ and other nanoparticles.³⁶ Generally, surface charge affects cell uptake depending on what is targeted. For example, if a given target is negatively charged, then the target repels negatively-charged particles. The particles used in this study were negatively charged due to the negative charge of the stabilizer reagents used in the study (citrate and PVP). When nanoparticles absorb protons, they become neutralized, lose their surface charge, and become agglomerated. The particles used in the study agglomerated at low pH values, such as a pH of ~3, which served as additional proof of the particles' negative charge. No direct measurement of the surface potential of the particles was performed in the study.

Many studies point out that particle shape also plays an important role in nanoparticle toxicity. Fibrous TiO₂ has been shown to have much higher toxicity towards macrophages *in vitro* than its spherical alternative³⁷ and needle-like carbon nanotubes have been shown to

have length-dependent toxicity similar to that of asbestos.³⁸ Particle shape has also been connected to the way nanoparticles agglomerate *in vitro*. Brown et al.³⁹ demonstrated that the interaction force between rod-shaped particles will be at least twice that of spherical particles. The proposed mechanism was attributed to the possible lengthwise orientation of rods against one another, which magnified the attractive forces present in biological media. In their study, however, agglomeration was shown to decrease toxicity. In the present study, all of the test nanomaterials had a relatively isotropic shape, with the exception of YVS 1101, which had a slightly cylindrical appearance (Figure 1A). This difference in shape from the other samples was not significant but may have contributed to agglomeration once added to media.

As with any nanomaterial, it is important to consider the dose and routes of exposure for each individual application. In our study, not all samples tested *in vitro* showed a clearly noticeable concentration response. Nevertheless, our cytotoxicity and cell uptake results indicate that of the samples tested, YVS 1101-COOH and YVE 1005 may be the most promising ones to continue to pursue as potentially suitable agents for imaging applications and other medical applications.

Two of the samples tested in this study were contaminated with endotoxin. YVS 1101 and YVS 1101 with COOH functionalization had concentrations of approximately 560 and 224 EU/ml, which translates to 0.056 and 0.0224 $\mu\text{g/ml}$ of lipopolysaccharides (LPS), respectively. A recent study by Kim *et al.* measured cytotoxicity of LPS in RAW 264.7 macrophages and reported an LD₅₀ value of 89.5 $\mu\text{g/ml}$,⁴⁰ which is several orders of magnitude higher than the amount in our tested samples. We spiked RAW 264.7

macrophages with LPS to confirm that endotoxin was not the cause for toxicity (data not shown). Cytotoxicity was evident as measured by the MTT assay starting at an LPS concentration of 50 µg/ml. The LD₅₀ value was approximately 50-100 µg/ml, which was consistent with results reported by Kim *et al.* Therefore, our study showed that endotoxin contamination did not contribute to the toxic effects induced by tested samples. It must be stressed that the concentration of endotoxin contamination producing serious inflammatory responses is much lower than the concentration of endotoxin contamination producing cytotoxicity. Therefore, medical products must meet endotoxin standards prior to marketing.⁴¹

Conclusions:

Our results suggested that some rare earth-containing nanoparticles have the potential to be biocompatible for imaging, diagnosis, and other medical applications. The present study highlighted how particular properties of this class of nanoparticles can influence the cytotoxicity results *in vitro*, such as size, surface ligands, solvents, and stabilizing agents. Samples of larger, 20-50 nm average diameter range nanoparticles were more cytotoxic than samples of different 10 nm diameter particles. Images of nanoparticles with cells revealed that the carboxyl (-COOH) coating improved dispersion *in vitro*. The test nanomaterials tended to localize as agglomerates in the cytoplasm, but did not accumulate in the nucleus. Two of the six nanoparticle preparations had endotoxin contamination, although the amounts present did not affect cytotoxicity. Nevertheless, endotoxin contamination of nanoparticle preparations must be considered for any nanoparticle intended for medical use. Solvents of certain samples may have directly contributed to their overall cytotoxicity. Solvents should be tested prior to suspending nanoparticles, since separation of nanoparticles from solvent afterwards may be challenging. Overall our study underlined that rare earth and other similar nanomaterials should be evaluated and optimized in terms of size, coating, and solvent to ensure patient safety for potential medical applications.

Acknowledgments:

Peter E. Petrochenko is supported in part by an NSF/FDA Scholar-in-Residence Award #1041375. The authors would also like to acknowledge Sun Innovations for providing samples of rare earth metal nanoparticles that were used in the study.

References:

1. S.P.C. Sam, V.S. Prasad, and K.S. Kumar, "Novel Nontoxic Nanopigments Based on Zirconia and Rare Earth Mixed Oxides," *Cryst. Res. Technol.*, 45 [11] 1199-1203 (2010).
2. E.B. van der Tol, H.J. van Ramesdonk, J.W. Verhoeven, F.J. Steemers, E.G. Kerver, W. Verboom, and D.N. Reinhoudt, "Tetraazatriphenylenes as Extremely Efficient Antenna Chromophores for Luminescent Lanthanide Ions," *Chem. Eur. J.*, 4 [11] 2315-2323 (1998).
3. D. Imbert, M. Cantuel, J.C.G. Bunzli, G. Bernardinelli, and C. Piguet, "Extending Lifetimes of Lanthanide-based Near-infrared Emitters (Nd, Yb) in the Millisecond Range through Cr(III) Sensitization in Discrete Bimetallic Edifices," *J. Am. Chem. Soc.*, 125 [51] 15698-15699 (2003).
4. L. S. Zivkovic, V. Lair, O. Lupan, M. Cassir, and A. Ringuede, "Samarium-Doped Ceria Nanostructured Thin Films Grown on FTO Glass by Electrodeposition," *Acta Phys. Pol. A*, 120 [2] 298-302 (2011).
5. C.X. Li and J. Lin, "Rare Earth Fluoride Nano-/microcrystals: Synthesis, Surface Modification and Application," *J. Mater. Chem.*, 20 [33] 6831-6847 (2010).

6. M.A. Zaitoun and S. Al-Tarawneh, "Effect of Varying Lanthanide Local Coordination Sphere on Luminescence Properties Illustrated by Selected Inorganic and Organic Rare Earth Complexes Synthesized in Sol-gel Host Glasses," *J. Lumin.*, 131 [8] 1795-1801 (2011).
7. J.F. Guo, L.S. Fu, H.R. Li, Y.X. Zheng, Q.G. Meng, S.B. Wang, F.Y. Liu, J. Wang, and H.J. Zhang, "Preparation and Luminescence Properties of Ormosil Hybrid Materials Doped with Tb(Tfacac)₃phen Complex via a Sol-gel Process," *Mater. Lett.*, 57 [24-25] 3899-3903 (2003).
8. Q. Liu, M. Chen, Y. Sun, G. Y. Chen, T. S. Yang, Y. Gao, X. Z. Zhang, and F. Y Li, "Multifunctional rare-earth self-assembled nanosystem for tri-modal upconversion luminescence/fluorescence/positron emission tomography imaging," *Biomaterials*, 32 [32] 8243-8253 (2011).
9. M. Wang, C. C. Mi, Y. X. Zhang, J. L. Liu, F. Li, C. B. Mao, and S. K. Xu, "NIR-Responsive Silica-Coated NaYbF₄:Er/Tm/Ho Upconversion Fluorescent Nanoparticles with Tunable Emission Colors and Their Applications in Immunolabeling and Fluorescent Imaging of Cancer Cells," *J. Phys. Chem. C*, 113 [44] 19021-19027 (2009).

10. R. Mukthavaram, W. Wrasidlo, D. Hall, S. Kesari, and M. Makale, "Assembly and Targeting of Liposomal Nanoparticles Encapsulating Quantum Dots," *Bioconjugate Chem*, 22 [8] 1638-1644 (2011).
11. C. Blaise, F. Gagne, J.F. Ferard, and P. Eullaffroy, "Ecotoxicity of Selected Nano-Materials to Aquatic Organisms," *Environ. Toxicol.* 23 [5] 591-598 (2008).
12. Y.H. Ma, L.L. Kuang, X. He, W. Bai, Y.Y. Ding, Z.Y. Zhang, Y.L. Zhao, and Z.F. Chai, "Effects of Rare Earth Oxide Nanoparticles on Root Elongation of Plants," *Chemosphere*, 78 [3] 273-279 (2010).
13. D. Wu, Z. Chen, and X. Liu, "Study of the Interaction between Bovine Serum Albumin and ZnS Quantum Dots with Spectroscopic Techniques," *Spectrochim. Acta, Part A*, 84 [1] 178-83 (2011).
14. G. B. Kim, B. Ramaraj, and K. R. Yoon, "A New Strategy to Assemble CdSe/ZnS Quantum Dots with Multi-Walled Carbon Nanotubes for Potential Application in Imaging and Photosensitization," *Appl. Surf. Sci.*, 258 [3] 1027-1032 (2011).
15. J. Wu, S. Lee, V. R. Reddy, M.O. Manasreh, B. D. Weaver, M. K. Yakes, C. S. Furrow, V. P. Kunets, M. Benamara, G. J. Salamo, "Photoluminescence Plasmonic

- Enhancement in InAs Quantum Dots coupled to Gold Nanoparticles,” *Mater. Lett.*, 65 [23-24] 3605-3608 (2011).
16. R.J. Palmer, J.L. Butenhoff, and J.B. Stevens, “Cytotoxicity of the Rare Earth Metals Cerium, Lanthanum, and Neodymium in vitro: Comparisons with Cadmium in a Pulmonary Macrophage Primary Culture System,” *Environ Res.*, 43 [1] 142-56 (1987).
 17. E. Delgado-Pinar, M. T. Albelda, J. C. Frias, O. Barreiro, E. Tejera, V. Kubicek, L. J. Jimenez-Borreguero, F. Sanchez-Madrid, E. Toth, J. Alarcon, and E. Garcia-Espana, “Lanthanide Complexes as Imaging Agents Anchored on Nano-sized Particles of Boehmite,” *Dalton Trans.*, 40 [24] 6451-6457 (2011).
 18. K.J. Wang, H.X. Li, Y.M. Song, N.N. Luan, and P. Xian, “Study on Syntheses and Anticoagulant Action of Heparin/Rare Earth Nano-Oxides Hybrid Material,” *Biopolymers*, 93 [10] 887-892 (2010).
 19. Z.Q. Li and Y. Zhang, "Monodisperse silica-coated polyvinylpyrrolidone/NaYF₄ nanocrystals with multicolor upconversion fluorescence emission," *Angewandte Chemie-International Edition*, 45[46] 7732-7735 (2006).

20. J. F. Jin, Y. J. Gu, C. W. Y. Man, J. P. Cheng, Z. H. Xu, Y. Zhang, H. S. Wang, V. H. Y. Lee, S. H. Cheng, and W. T. Wong, "Polymer-Coated NaYF₄:Yb(3+), Er(3+) Upconversion Nanoparticles for Charge-Dependent Cellular Imaging," *Acs Nano*, 5[10] 7838-7847 (2011).
21. D. Williams, "Endotoxins and Medical Devices: The Significance of Dead Bacteria," *Medical Device Technology*, 14 [2] 8 (2003).
22. J. Weyermann, D. Lochmann, and A. Zimmer, "A Practical Note on the Use of Cytotoxicity Assays," *Int. J. Pharm.*, 288 [2] 369-376 (2005).
23. S. Lanone, F. Rogerieux, J. Geys, A. Dupont, E. Maillot-Marechal, J. Boczkowski, G. Lacroix, and P. Hoet, "Comparative Toxicity of 24 Manufactured Nanoparticles in Human Alveolar Epithelial and Macrophage Cell Lines," *Part. Fibre Toxicol.*, 6 14 (2009).
24. N. Luciani, F. Gazeau, and C. Wilhelm, "Reactivity of the Monocyte/macrophage System to Superparamagnetic Anionic Nanoparticles," *J. Mater. Chem.*, 19 [35] 6373-80 (2009).
25. J. Choi, Q. Zhang, V. Reipa, N.S. Wang, M.E. Stratmeyer, V.M. Hitchins, and P.L. Goering, "Comparison of Cytotoxic and Inflammatory Responses of

- Photoluminescent Silicon Nanoparticles with Silicon Micron-sized Particles in RAW 264.7 Macrophages,” *J. Appl. Toxicol.*, 29 [1] 52-60 (2009).
26. A. Vainrub, O. Pustovyy, and V. Vodyanoy, “ Resolution of 90 nm ($\lambda/5$) in an Optical Transmission Microscope with an Annular Condenser,” *Opt. Lett.*, 31 [19] 2855-2857 (2006).
27. C. Liu, Z. Wang, X. Wang, and Z. Li, “Surface Modification of Hydrophobic NaYF₄:Yb,Er Upconversion Nanophosphors and their Applications for Immunoassay,” *Science China-Chemistry*, 54 [8] 1292-1297 (2011).
28. H. S. Mansur, and A. A. P. Mansur, “CdSe Quantum Dots Stabilized by Carboxylic-Functionalized PVA: Synthesis and UV-vis Spectroscopy Characterization,” *Mater. Chem. Phys.*, 125 [3] 709-717 (2011).
29. L. L. Zhang, Y. Z. Xiong, E. C. Ou, Z. M. Chen, Y. Q. Xiong, and W. J. Xu, “Preparation and Properties of Nylon 6/Carboxylic Silica Nanocomposites via In Situ Polymerization,” *J. Appl. Polym. Sci.*, 122 [2] 1316-1324 (2011).
30. C. Doherty, P. York, "The in vitro pH-dissolution dependence and in vivo bioavailability of frusemide-PVP solid dispersions,” *Journal of Pharmacy and Pharmacology*, 41[2] 73-78 (1989).

31. D.S. Jones, M.S. Lawlor, and A.D. Woolfson, "Rheological and mucoadhesive characterization of polymeric systems composed of poly(methylvinylether-co-maleic anhydride) and poly(vinylpyrrolidone), designed as platforms for topical drug delivery," *Journal of Pharmaceutical Sciences*, 92[5] 995-1007 (2003).
32. H. Tsunoyama, N. Ichikuni, H. Sakurai, T. Tsukuda, "Effect of Electronic Structures of Au Clusters Stabilized by Poly(N-vinyl-2-pyrrolidone) on Aerobic Oxidation Catalysis," *Journal of the American Chemical Society*, 131[20] 7086-7093 (2009).
33. M. Zhou, B. X. Wang, Z. Rozynek, Z. H. Xie, J. O. Fossum, X. F. Yu, S. Raaen, "Minute synthesis of extremely stable gold nanoparticles," *Nanotechnology*, 20[50] (2009).
34. W. F. Bergfeld, D. V. Belsito, W. W. Carlton, C. D. Klaassen, A. L. Schroeter, R. C. Shank, T. J. Slaga, and C. I. R. E. P. Cosmetic Ingredient Review, "Final report on the safety assessment of polyvinylpyrrolidone (PVP)," *International Journal of Toxicology*, 17 95-130 (1998).
35. Y.P. Chen, H. A. Chen, Y. Hung, F. C. Chien, P. L. Chen, C. Y. Mou, "Surface charge effect in intracellular localization of mesoporous silica nanoparticles as probed by fluorescent ratiometric pH imaging," *Rsc Advances*, 2[3] 968-973 (2012).

36. A. Musyanovych, J. Dausend, M. Dass, P. Walther, V. Mailander, and K. Landfester, "Criteria impacting the cellular uptake of nanoparticles: A study emphasizing polymer type and surfactant effects," *Acta Biomaterialia*, 7[12] 4160-4168 (2011).
37. S. Hirano, C.D. Anuradha, S. Kanno, "Transcription of krox-20/egr-2 is upregulated after exposure to fibrous particles and adhesion in rat alveolar macrophages," *American Journal of Respiratory Cell and Molecular Biology*, 23[3] 313-319 (2000).
38. C. A. Poland, R. Duffin, I. Kinloch, A. Maynard, W. A. H. Wallace, A. Seaton, V. Stone, S. Brown, W. MacNee, K. Donaldson,, "Carbon nanotubes introduced into the abdominal cavity of mice show asbestos-like pathogenicity in a pilot study," *Nature Nanotechnology*, 3[7] 423-428 (2008).
39. S. C. Brown, M. Kamal, N. Nasreen, A. Baumuratov, P. Sharma, V. B. Antony, and B. M. Moudgil, "Influence of shape, adhesion and simulated lung mechanics on amorphous silica nanoparticle toxicity," *Advanced Powder Technology*, vol. 18, pp. 69-79, 2007.
40. I. D. Kim and B. J. Ha, Paeoniflorin Protects RAW 264.7 Macrophages from LPS-Induced Cytotoxicity and Genotoxicity, *Toxicol. in Vitro*, 23 [6] 1014-1019 (2009).

41. Transfusion and Infusion Assemblies and Similar Medical Devices, Recognition
Number 14-305, USP 33:2010, United States Pharmacopeial Convention, Rockville,
MD, USA, 2010.

CHAPTER 2: Cytotoxic evaluation of nanostructured zinc oxide (ZnO) thin films and leachates

Peter E Petrochenko,^{1, 2} Qin Zhang,¹ Mohammad R Bayati,³ Shelby A Skoog,² K Scott Phillips,¹ Girish Kumar,¹ Roger J Narayan,² Peter L Goering¹

¹ *Center for Devices and Radiological Health, US Food and Drug Administration, Silver Spring, MD, 20993, USA.*

² *Joint Dept of Biomedical Engineering, Univ of North Carolina-Chapel Hill and North Carolina State Univ, Raleigh, NC, 27695 USA.*

³ *Intel Corporation, IMO-SC, SC2, Santa Clara, CA, 95054, USA.*

Note:

The mention of commercial products, their sources, or their use in connection with material reported herein is not to be construed as either an actual or implied endorsement of such products by the Department of Health and Human Services.

Keywords: Zinc oxide (ZnO); surface toxicity; metal leaching; nano roughness; pulsed laser deposition; macrophage.

Abstract:

Nanostructured ZnO films have potential use as coatings on medical devices and food packaging due to their antimicrobial and UV-protection properties. However, their influence on mammalian cells during clinical use is not fully understood. This study investigated the potential cytotoxicity of ZnO thin films in RAW 264.7 macrophages. ZnO thin films (~96 nm thick with a 50 nm grain) were deposited on silicon by pulsed laser deposition. The study showed that growing cells directly on a ZnO coating was less toxic than administering the same coating in dissolved form, when measured with the MTT assay, but not using flow cytometry. ZnO surfaces had decreased cell viability by 43% and 68% using the MTT and flow cytometry assays, respectively, after a 24-hr exposure. Only undiluted 100% 24- and 48-hr extract decreased viability by 89%, increased cell death by LDH release to 76% 24 hrs after treatment, and increased ROS after 5 to 24 hrs of exposure. In contrast, no cytotoxicity or ROS were observed for 25% and 50% extracts, indicating a tolerable concentration. Roughly 24 and 34 $\mu\text{g}/\text{m}^2$ Zn leached off the surfaces after 24 and 48 hrs of incubation, respectively. ZnO coatings may produce gradual ion release which becomes toxic after a certain level and should be evaluated using both direct exposure and extraction methods.

Introduction:

Zinc oxide (ZnO) is a versatile material with a number of consumer applications due to its antimicrobial and UV-protection properties ^{1,2}. Such properties can be imparted to device and product surfaces using high-precision nanoscale coating techniques. Nanometer film fabrication allows for a previously unattainable control of surface uniformity and particulate grain size and has potential to optimize antimicrobial efficacy and mitigate cell toxicity for materials such as ZnO. The PLD approach uses a high-powered laser plume that ablates purified ZnO powder and deposits it onto the desired surface. Physical properties of the resulting layer are customizable by tuning several parameters, such as the number of laser pulses, chamber pressure, temperature and others. Nanoscale ZnO thin films have several applications in the semiconductor industry ^{3,4}; yet represent novel coatings for medical applications. For medical device coatings and biological applications, nanoscale ZnO can be fabricated in a variety of nanoparticles and complex nanostructures, such as rods and flowers. For example, ZnO nanorods ⁵ are shown to modulate cell adhesion and macrophage responses, ⁶ whereas ZnO nanoflowers may improve bone tissue ingrowth ⁷. Such physical properties combined with improved antimicrobial activity ⁸ make nanostructured ZnO a desirable and promising implant coating. With the innovative applications of metal oxide coatings used for medical device coatings, namely those with nanometer scale patterning and thus increased surface area, concerns arise related to potential adverse cellular responses resulting from particulates and metal leaching at the implant site.

Bulk ZnO is a widely used food additive and is listed on the FDA's Generally Recognized as Safe (GRAS) database as a dietary supplement (21 CFR 182.5991), nutrient

(21 CFR 182.5991), and a resinous/polymeric coating (21 CFR 175.300). ZnO can be used as an antimicrobial coating for both food and medical materials; for example, it has been shown to increase shelf life of orange juice ⁹ and is known to improve healing when coated on medical tape ¹⁰. Additionally, it may serve as an effective UV blocker ¹¹ and antimicrobial ¹² when incorporated in textiles. ZnO is also an attractive alternative or complement to widely used silver (Ag) products when stronger antifungal properties are additionally desired¹³. Zn is an essential nutrient which can cause toxicity through both deficiency (usually defined as a serum concentration below 0.7µg/mL) ^{14,15} and at higher than homeostatic concentrations ¹⁶. The cytotoxicity of both bulk and particulate Zn has been described in several cell culture models ¹⁷⁻¹⁹ and inhalation studies²⁰. Studies which evaluate the cytotoxicity of nanoscale ZnO coatings and surfaces, as opposed to discrete nanoparticles in mammalian cells, however, are scant.

ZnO has a high likelihood of unwanted metal ion release into its environment ^{21,22}, which in some instances may be desired. By coating a precise thickness and by optimizing coating parameters, the rate of dissolution and the total amount of Zn that can leach out may be controlled. Zinc leaching has immunomodulatory properties that may be suited for special applications that require suppressed immune function. For example, ionic zinc has been shown to modulate the immune response from monocytes by suppressing TNF-alpha transcription and release from monocytes ²³. This gives it potential for limiting aseptic loosening in orthopedic implants and possibly increasing their overall lifespan.

Polymorphonuclear cells (PMNs) are known to be activated by hydroxyapatite (HA) wear debris present in inflamed regions; this event may, accordingly, be modulated to an extent by

adding zinc to the scaffold material ²⁴. More specifically, levels of the pro-inflammatory mediator interleukin-8 (IL-8) and the matrix metallo-proteinase-9 in PMNs have been shown to decrease with a 5% Zn-substitution of calcium ions in HA powder ²⁵.

Nanoscale zinc topography may also be beneficial in other orthopedic applications. A comparison study of nanophase and microphase ZnO surfaces revealed that the nm grain surfaces had better bone tissue response and decreased *S. epidermidis* colony forming units than microphase surfaces ²⁶. We previously evaluated the antimicrobial activity² of a uniform atomic layer deposited ZnO coating on a porous substrate and showed that it may also be cytotoxic to macrophages ²⁷. The present study aimed to examine the cytotoxicity and dissolution of nanotextured ZnO. A granular textured layer was deposited using a pulsed laser method onto an inert substrate to isolate the effect of ZnO. Mouse RAW 264.7 macrophages were selected to evaluate the biological responses because: 1) they are an important cell type involved in immune and inflammatory responses and wound healing, and 2) to make inter-laboratory comparisons across different studies using this cell type. Therefore, the goals of the study: (1) develop a “test chip” consisting of a silicon wafer substrate coated with a highly uniform ZnO coating with nanometer scale thickness and grain size, (2) assess the cytotoxicity of ZnO thin film coatings which have previously exhibited considerable antimicrobial activity ²⁸ and (3) determine whether leaching of Zn ions from the surface coating plays a role in cytotoxicity.

Methods:*ZnO Pulsed Laser Deposition on Si:*

A high-purity ZnO powder (Alfa Aesar, Ward Hill, MA) was pressed into round 2-in. diameter pellets. The pellets were subsequently sintered in an oxygen atmosphere at 1000 °C for 12 hrs. Wafers are highly pure, defect free single crystalline Si polished slices. A krypton fluoride excimer laser ($\lambda = 248$ nm, Repetition rate = 10 Hz) was used to ablate the high-purity ZnO target. The thin films were grown under O₂ partial pressure of 5×10^{-5} Torr at room temperature for 5 min. The ZnO thin film deposition rate using a KrF excimer laser was on the order of 0.01 nm/pulse²⁹. The materials were then cut into approximately 0.5 x 0.5 cm (7 cm diagonal) squares to fit a 48-well plate with a diameter of 11 mm.

Surface Characterization:

Atomic force microscopy (AFM) was performed on the ZnO-coated Si substrates and the smooth Si substrates (control) using a Digital Instruments (now Bruker AXS) Dimension 3000 AFM and an Olympus AC160TS tip (resonant frequency of 330 kHz, force constant of 40 N/m). Topographical analysis was done using a scan size of 5 μ m and 1 μ m with a scan rate of 1Hz. A roughness analysis was also conducted using a scan size of 5 μ m for mean roughness (Ra) and 1 μ m for root mean square (RMS) roughness and maximum height (Rmax) to exclude outliers due to dust particles on the surface. 3D reconstruction was performed using the SurfaceJ plugin for ImageJ software (NIH, USA).

Scanning electron microscopy (SEM) was performed using a JEOL 6400 Cold Field Emission Scanning Electron microscope (JEOL, Tokyo, Japan). Energy Dispersive X-Ray Spectroscopy (EDX) was performed in order to confirm the presence of Zn on the surface.

The SEM was equipped with an energy dispersive X-ray spectrometer attachment with a Link Pentafet detector (Link Analytical, Redwood City, CA) and a 4Pi Universal Spectral Engine pulse processor (4Pi Analytical, Hillsborough, NC). An accelerated voltage of 20 keV and 5 keV was used.

Cell Culture:

RAW 264.7 macrophage cells (**TIB-71**, ATCC, Manassas, VA) were cultured until confluent and plated directly onto 48-well plates containing uncoated, smooth Si wafers or the ZnO-coated Si wafers. Cells were plated at a density of 2×10^5 cells/mL and maintained in DMEM with L-glutamine (GIBCO[®] DMEM, Invitrogen, Carlsbad, CA), 10% Fetal Bovine Serum (HyClone FBS, Thermo Scientific, Rockford, IL) and 1% Penicillin-Streptomycin (P/S) solution (Sigma, St. Louis, MO). Coated and uncoated wafers were transferred to new wells prior to performing assays to ensure only cells growing on the wafers were evaluated (see individual assay description for details).

Cell imaging:

To investigate and confirm cell attachment with the test surfaces, macrophages were plated at a density of 2×10^5 cells/mL directly on the ZnO-coated and smooth wafers and incubated for 24 hrs. Media was removed, cells were washed with warm PBS, fixed with 3.7% formaldehyde, washed with PBS again, and permeabilized using 0.2% Triton X-100. Cells were then washed again and incubated with Molecular Probes[®] DAPI and Alexa Fluor[®] 488 (Life Technologies, Grand Island, NY) for 1 hr, then washed with PBS 3 times and allowed to dry in the dark. Samples were sealed with ProLong[®] mounting medium (Life

Technologies, Grand Island, NY) and a cover slip. Images were acquired using a confocal microscope (Leica, Buffalo Grove, IL).

Extracts:

Extracts were collected in order to determine the concentration of Zn leaching into solutions (ICP-MS) and the effects of leached Zn ions on cytotoxicity (MTT and LDH assays) and production of ROS. Wafers were sterilized with ultraviolet light (UVP CL-1000, Upland, CA) for 30 min on each side (rotated 90° every 30 minutes). Upon completion of ultraviolet sterilization, the wafers were placed in 48-well plates and incubated in 0.5 mL DMEM medium at 37 °C and 5% CO₂. Wells with medium but without wafers served as control extracts. The medium extracts were then removed after 24 or 48 hrs and used for further studies. Extracts were then prepared for exposures to cells. Undiluted extracts were considered 100% concentration. The 100% extract was carefully mixed and diluted 1:1 (v:v) with medium to make 50% exposure concentration and 1:3 to make a 25% exposure concentration. Media that was used for dilutions was subjected to the same conditions (24-hr incubation) as the extracts. ICP-MS was used to determine Zn concentration of extracts.

MTT Viability Assay:

Cell viability of macrophages grown on ZnO-coated silicon wafers and smooth Si wafers was determined using the MTT assay (CellTiter 96[®] Non-Radioactive Cell Proliferation Assay, Promega, Madison, WI). Wafers were sterilized with ultraviolet light for 30 min on each side and transferred to 48-well plates. RAW 264.7 macrophages were added to the 48-well plates at a cell density of 2×10^5 cells/mL (1×10^5 cells/well). All well plates were then incubated for either 24 hrs or 48 hrs at 37 °C. The wafers were 0.5 x 0.5 cm

squares (0.7 cm diagonal) and the wells were circular (1.1 cm diameter) leaving a small portion of the well open for cell growth on the polystyrene well surface outside of the ZnO-coated wafer. In order to exclude cells grown on tissue culture polystyrene (TCPS) in these small areas of each well and avoid their influence on assay outputs, wafers were moved to a new 48-well plate after each 24- or 48-hr incubation period. The new wells contained 0.5 mL fresh MTT-DMEM medium. Further procedures were followed as specified by the manufacturer's instructions. Cells spiked with 5% dimethyl sulfoxide (DMSO, Sigma, St. Louis, MO) served as a positive controls. For extract studies, the appropriate dilution was made with cell medium (25%, 50%, or 100% extract) and added directly to cells during plating. The cells were then incubated for 24 hr and assayed.

Flow cytometry analysis of necrosis and apoptosis:

Necrosis and apoptosis of macrophages grown on ZnO-coated silicon and smooth Si wafers were determined using dye-based flow cytometry analysis. After exposure treatments of 24 hrs, supernatants were collected and combined with cells detached with TrypLe (Life Technologies, Grand Island, NY) in a microcentrifuge tube and centrifuged at 1000 rpm for 5 min. The resulting cell pellet was transferred to a flow cytometry tube containing 100 μ L of binding buffer, 20 μ L of 7AAD and 5 μ L of Annexin V dyes as specified by the Annexin V:PE Apoptosis Detection Kit I (BD Pharmingen, San Diego, CA). Each sample was vortexed for 10 sec prior to loading into the flow cytometer (BD FACS Canto II). Live cells and cells killed with AgNO₃ served as the controls used for gating. Data was expressed as % of total cell population, 100% of which was comprised of either live, necrotic or apoptotic cells.

LDH Cytotoxicity Assay:

Cytotoxicity was evaluated by measuring activity of lactate dehydrogenase (LDH). The LDH-cytotoxicity assay kit (BioVision, San Francisco, CA) was used to quantify LDH in cell cultures after 24 hrs of exposure to ZnO extracts collected after 24 hrs. Background and negative controls were smooth Si wafers in media without cells. Total cellular LDH release was measured from cells after treatment with 1% Triton X-100. % Cytotoxicity for cells exposed to ZnO-coated wafers was calculated as specified by the kit as a ratio of LDH released in: $(\text{ZnO} - \text{Si control})/(\text{Triton X} - \text{Si control}) \times 100$.

Reactive Oxygen Species (ROS) Production Assay:

To investigate if oxidant stress is produced by solubilized ZnO in media extracts, the generation of intracellular ROS was measured by the increasing fluorescence of 2',7'-dichlorofluorescein (DCF)³⁰. For this study, different concentrations of ZnO extracts in 100 μL culture medium were added to each well. Cells were treated with 200 mM hydrogen peroxide (H_2O_2) as a positive control. DCF fluorescence was monitored after various treatments from 30 min to 24 hrs.

Inductively coupled plasma mass spectrometry (ICP-MS):

A Varian 820 ICP-MS was used for all elemental analyses to determine the presence of Zn ions in the extracts which have dissolved from the ZnO coated surfaces. The ICP source had a MicroMist nebulizer, max flow rate of 0.4 mL/min, for sample introduction into the plasma. Standard plasma conditions (Power 1.4 kW, plasma flow 18.00 L/min, auxiliary flow 1.80 L/min, sheath gas flow 0.18 L/min, sampling depth 7.5 mm) were used. All solutions were prepared using 18 mega-ohm de-ionized water and trace metal grade nitric acid (Thermo Fisher Scientific Inc., Waltham MA). Initial sample volume of 100 μ L was mixed with 500 μ L of concentrated HNO₃, 500 μ L was removed (out of the total of 600) and diluted to a final volume of 5.0 mL with 2% HNO₃. Samples were introduced with the peristaltic pump at 3 rpm. The spray chamber was cooled to 3 °C. Standards were prepared using ICP standards purchased from Inorganic Ventures (Christiansburg, VA). In all measurements, a 5 ppb solution of indium was used as internal standard and mixed online with each sample through a tee. Indium ion In¹¹⁵ (internal standard), Si²⁹, Zn⁶⁶ (ion abbreviations and isotopes monitored) were monitored in peak hopping mode using a 50,000 micro-sec dwell time, and 5 replicates of an average of 20 data points were measured. The standard curve included at least 8 concentration levels in the quantification range. The standard data set was fitted to a linear curve. The coefficient of correlation was 0.99. Percent errors in calculated concentrations were 15% or lower.

Statistical analysis:

The results from each data set were analyzed using Prism (v. 4) statistical software (GraphPad Inc., La Jolla, CA). Results were expressed as mean \pm standard deviation. Each assay was conducted in duplicate and at least 3 independent experiments were conducted for each assay. Statistical differences between control and treated group were assessed using one-way ANOVA followed by a Bonferroni *post hoc* test. Data were normalized to the smooth silicon wafers and were expressed as percent viability. Significance level notation was expressed as * for $p < 0.05$ and ** for $p < 0.01$.

Results:

Surface characterization:

Custom nanotextured ZnO surfaces were fabricated successfully by optimizing PLD deposition parameters. The krypton fluoride excimer laser operated at 0.08 nm/pulse at 10 pulses/sec for 120 sec, which resulted in an approximated 96 nm thick layer. The presence of the ZnO layer on the Si wafers was confirmed using energy-dispersive X-ray spectroscopy (EDX) shown in Fig. 1. The spectra for uncoated smooth samples had a very strong Si peak present (Fig. 1A), whereas ZnO-coated samples had minor peaks for oxygen and silicon present with a strong Zn peak (Fig. 1B).

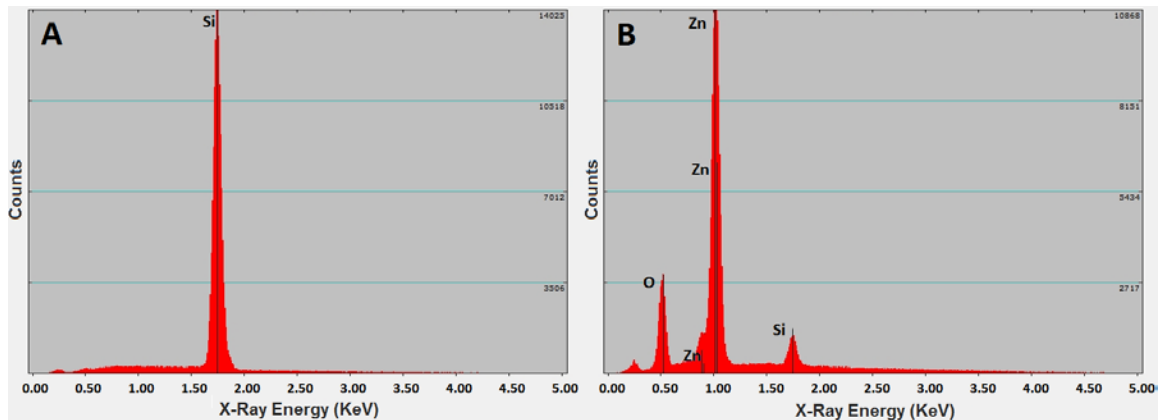


Figure 1. Energy-dispersive X-ray spectroscopy analysis of uncoated smooth silicon (A) and ZnO-coated silicon (B). The results shown in (A) show a strong single peak representing “Si”, and (B) confirm the presence of the ZnO thin-film layer by the peaks labeled “O” and “Zn.”

AFM analysis of the coated surfaces revealed a surface nanotopography consisting of a fine grain size of approximately 50 nm (Fig.2). Root mean-squared roughness (Rq), mean roughness (Ra), and maximum height (Rmax) values were greater for the ZnO-coated surfaces compared to the non-coated Si surfaces (Table 1). The ZnO surface exhibited nanoscale features with a root mean square (RMS) roughness of 1.48 nm compared to RMS = 0.23 for non-coated control wafers. The most protrusive grains on the ZnO-coated samples extended from the surface to a maximum height of 11.00 nm. Fig. 2C shows the surface topography measured with AFM and reveals a relatively uniform grain size consistent across the ZnO-coated surfaces. The difference in roughness between the smooth Si (Fig. 2A) and the ZnO-coated surface (Fig. 2B) can be seen from the AFM scans. The Si surface is visibly smooth with no distinct grains or patterns at the scale of 1 μ m. The degree of grain size uniformity on the coated surfaces is more readily visible with a 3-D reconstruction of a topographical AFM analysis using 3D rendering with the SurfaceJ plugin for ImageJ software from NIH (Fig.2D). The majority of the grains are approximately 50 nm in diameter. A small fraction of grains, however, fall in the 10-20 nm as well as in the 100+ nm range.

Table 1. Roughness measurements using atomic force microscopy. Root mean square (RMS) roughness presents a measure where high deviations are weighed more heavily than in the mean roughness calculation (Ra), where all deviations are equated into a single average. Max height (Rmax) represents the single highest peak to valley distance measured. All measurements shown in nm with mean \pm standard deviation values.

	ZnO-coated	Smooth Si
RMS (Rq), nm	1.48 \pm 0.01	0.232 \pm 0.87
Mean Roughness (Ra), nm	1.25 \pm 0.09	0.39 \pm 0.26
Max Height (Rmax), nm	11.0 \pm 0.79	1.69 \pm 0.45

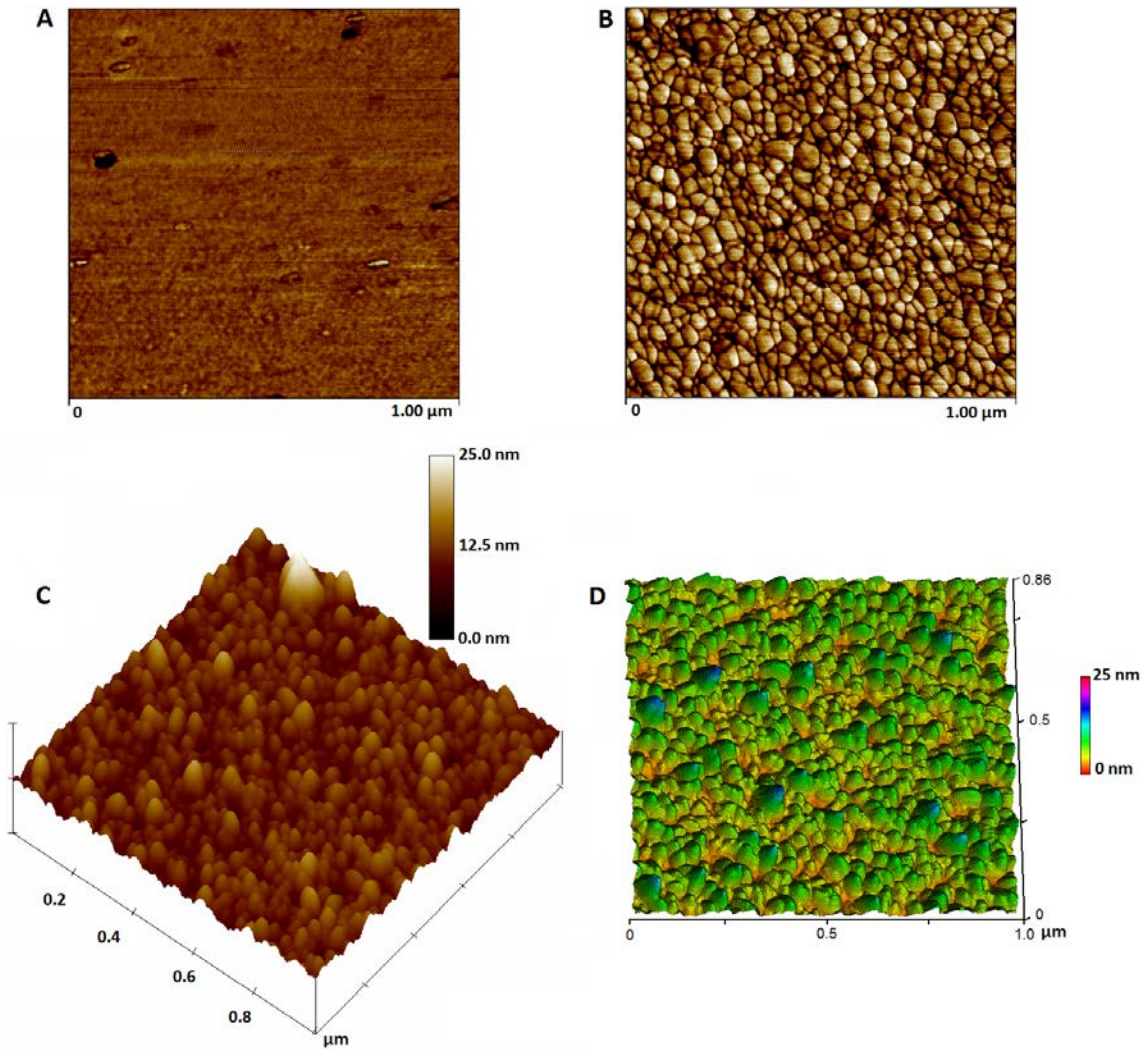


Figure 2. AFM analysis of the ZnO thin film. Rough AFM images of (A) smooth Si and (B) ZnO-coated Si. 3D stack of (C) AFM images of ZnO coating and (D) 3D reconstruction rendered using SurfaceJ plugin for ImageJ software to emphasize grains.

Cell Imaging:

In order to properly analyze cytotoxicity results, smooth Si wafers were confirmed as a suitable control that represented a relatively chemically inert surface, free of nanometer roughness and topography. Confocal microscopy (Fig. 3A) revealed good cell attachment to the Si surface consistent with the amount of cells/area that were plated. Trypan blue staining additionally confirmed the cell membranes were intact and the Si surface did not inherently cause membrane damage. Confocal images also showed a uniform cell distribution on the ZnO-coated samples; however, the cell number was much lower. The morphology of cells on the smooth Si surface was also different from that on ZnO surfaces. Cells spread out more on Si, with visible actin filaments, while cells on the ZnO surface had a slightly more rounded shape. The ZnO surface was fluorescent, however, it was evident in Figure 3B that macrophages growing on ZnO did not have actin projections along the substrate and appeared smaller due to more rounded morphology.

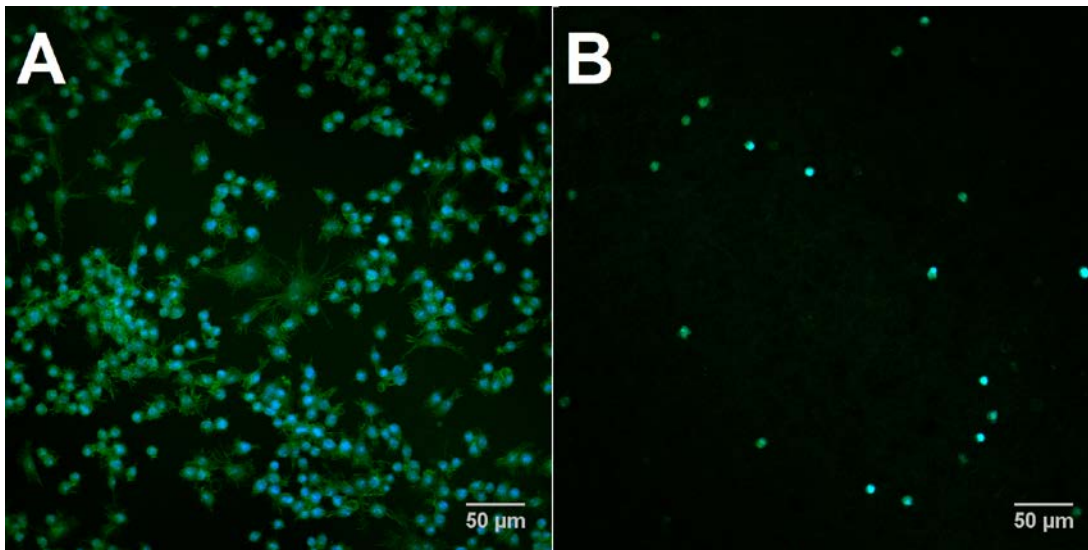


Figure 3. Macrophages growing on (A) smooth and (B) ZnO-coated Si wafers surfaces. Stained with DAPI (blue nucleus) and green-fluorescent Alexa Fluor® 488 dye (green actin filaments). Cells on the ZnO-coated surface were fewer in number, showed more rounded morphology and were loosely adherent, causing them to be easily detached.

Cell Responses to ZnO-coated Surfaces:

For direct cell contact studies with MTT and flow cytometry, wafers were transferred to a new well prior to running the assays to ensure that cells in the void areas shown in Fig. 4 did not produce interference, e.g., dilute out assay outputs. Plating cells directly on the ZnO-coated wafers decreased cell viability as measured by both the MTT and flow cytometry assays (Fig. 5). Following 24 hrs of exposure, the viability of cells grown on the ZnO surface (expressed as percentage of the smooth Si control) was reduced to 56.6% (Figure 5A). After 48 hrs, cell viability decreased to 46.5% (data not shown).

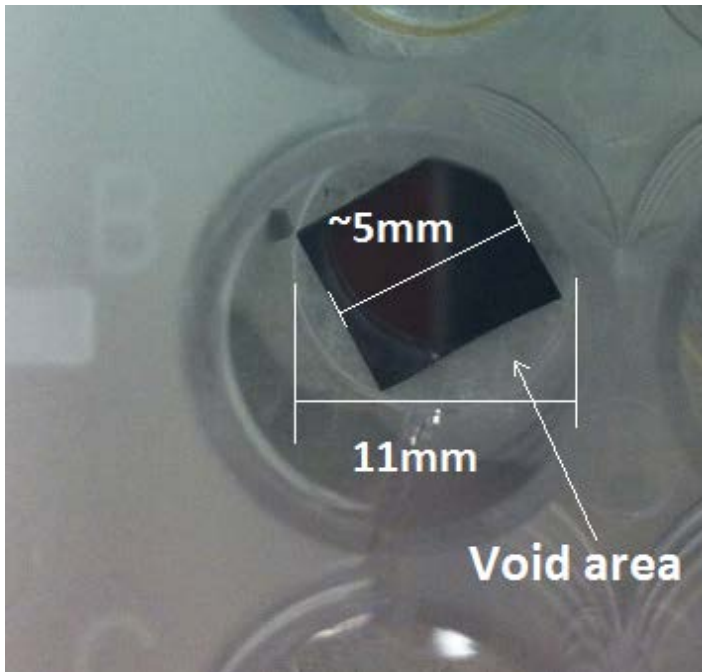
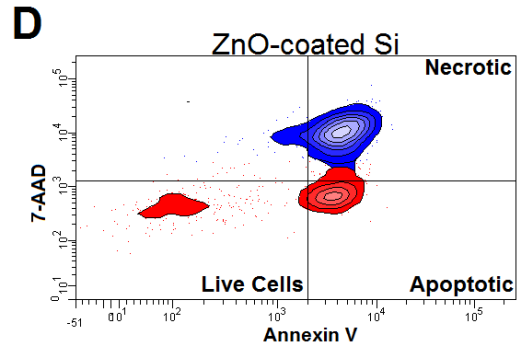
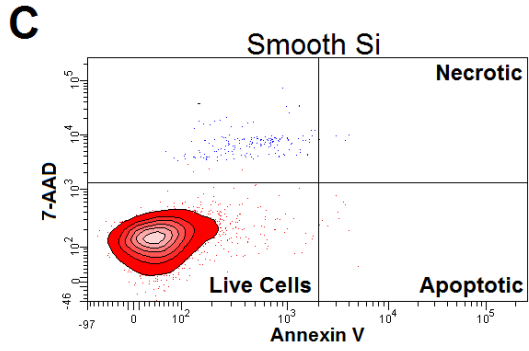
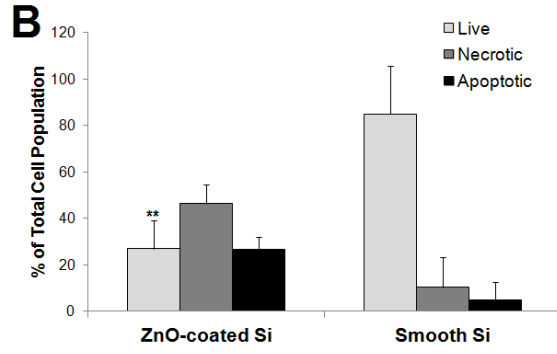
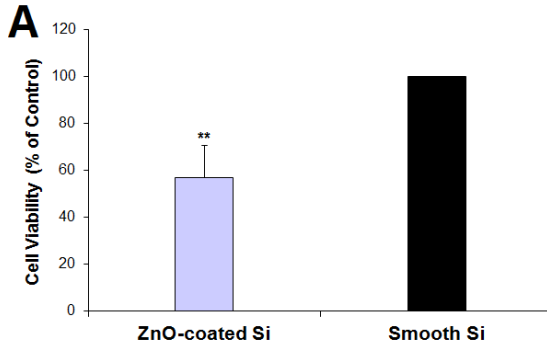


Figure 4. ZnO-coated wafer (5x5 cm) shown inside a single well of a 48-well plate. Void area is shown in a well of a 48-well plate after seeding cells on wafer surfaces. Wafers were transferred to another 48-well plate in order to avoid interferences, e.g., diluting assay outputs, from cells growing in the void areas.

The cause for a decrease in MTT cell viability was further investigated using flow cytometry and fluorescent dyes for necrosis and apoptosis. The results showed that a significant portion of the cells becomes necrotic (46%) and apoptotic (27%), leaving only 27% live cells as seen in Fig. 5B-D. When the percentage of live cells on ZnO-coated surfaces is normalized to smooth Si controls, the cell viability becomes 32% of control, compared to 57% of control when measured with MTT. Fig. 5C-D show a graphical distribution of cell populations with predominantly healthy cells for the Si control (C) and necrotic and apoptotic cells for the ZnO-coated surface (D). A positive control of equimolar soluble $ZnCl_2$ (12 μ g/mL Zn ion) was added and showed a higher amount of apoptosis with 11% live, 18% necrotic and 71% apoptotic cells (data not shown in Fig. 5).

Figure 5. Exposure to ZnO-coated Si significantly decreases cell viability by inducing apoptosis and necrosis in macrophages. (A) Cell viability (MTT reduction) of macrophages exposed to ZnO-coated Si and smooth Si wafers for 24 h. Viability of cells grown on ZnO-coated Si was lower compared to Si controls. Data was normalized to cells grown on smooth Si (100%). (B) Live, apoptotic, and necrotic cell populations as a percentage of total cells (% Live +% Apoptotic +% Necrotic = 100%) measured with flow cytometry. ZnO-coated Si showed significantly decreased viability with predominantly necrotic as well as apoptotic cells. Data in (A) and (B) are expressed as mean \pm SD (N = 3 independent experiments). (C) and (D) show representative cell distributions between live, necrotic, and apoptotic cells for (C) smooth Si, which shows predominantly live cells and (D) ZnO-coated Si, which shows significant necrotic and apoptotic subpopulations. When normalized to live cells on the smooth Si control, cells on ZnO-coated Si have 32% viability measured with flow cytometry as compared to 57% when measured with MTT. Significance level notation: ******($p < 0.01$).



Cell response to ZnO extract:

Extracts collected over 24 hrs of incubation were added to adherent cells at 0, 25, 50, and 100% concentrations (Zn concentrations using ICP-MS estimated to be 3.03, 6.07, and 12.13 $\mu\text{g/mL}$, respectively) for a 24-hr exposure. Cell viability (MTT assay) was affected only by the highest 100% (undiluted) extract concentration (Fig. 6A); after 24 hrs, there was a significant decrease to 11.4% of control. No changes in viability were observed for the 25% and 50% extracts. The highest amount of LDH release (expressed as % cytotoxicity) occurred after 24 hrs with the 100% extract (Fig. 6B); Cell death was estimated at roughly 76% (of the Triton X-100 control) compared to no cell death for the medium-alone control cells (Fig. 6B). No change in cell death was observed for the 25% and 50% extract concentrations. This response was somewhat similar to the MTT results, in that only the undiluted extract elicited both a significant decrease in cell viability (MTT reduction) as well as increase in cell death (LDH release).

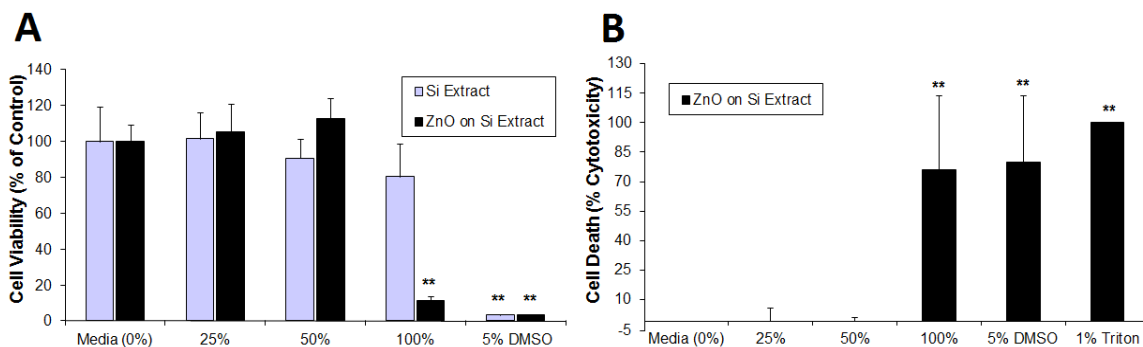


Figure 6. Effect of 24 hrs exposure to extracts collected after 24 hrs from Zn-coated Si and smooth Si wafers on cell viability and cytotoxicity. Undiluted extracts = 100%; 50 and 25% extracts represent serial dilutions for the 100% extract. **(A)** Cell viability (MTT reduction) in macrophages 24 hrs after exposure to extracts of ZnO-coated wafers. Viability significantly decreased with undiluted (100% = 12.1 $\mu\text{g}/\text{mL}$) extract treatment only. **(B)** Cell death (% cytotoxicity) measured with LDH release in macrophages 24 hrs after exposure to extracts of ZnO-coated wafers. Cell death measured by LDH release increased only in response to undiluted (100%) ZnO extracts. 5% DMSO was used for positive controls. Cytotoxicity (%) was calculated as a percentage of total LDH release with the Triton X-100 positive control. Data are expressed as mean \pm SD (N = 3 independent experiments). Significance level notation: ******($P < 0.01$)

Generation of intracellular ROS increased in cells treated with ZnO extracts at various times over 24 hrs exposure (Fig. 7). Cells were treated with extracts from either 24-hr or 48-hr incubations with wafers. ROS production was highest after exposure to the undiluted (100%) 24-hr and 48-hr extracts of the ZnO-coated wafers. All values for both ZnO 24-hr and 48-hr extracts had significantly higher ROS generation ($P < 0.01$) than the cell medium control and showed average values that were roughly 20% higher than the undiluted Si extract at all time points. ROS production after exposure to ZnO 50% concentration extracts (24-h extract) and Si 100% concentration extracts was significantly higher ($p < 0.05$) than cell medium controls after 1 hr exposure only. The last 24-hr time point from the 48-hr extract had the smallest difference where both 100% ZnO and 100% Si extracts had significantly higher ROS generation than cell media controls. All other Si extract values were not significantly different from cell media controls; however, there appeared to be a general trend of increased ROS generation over time.

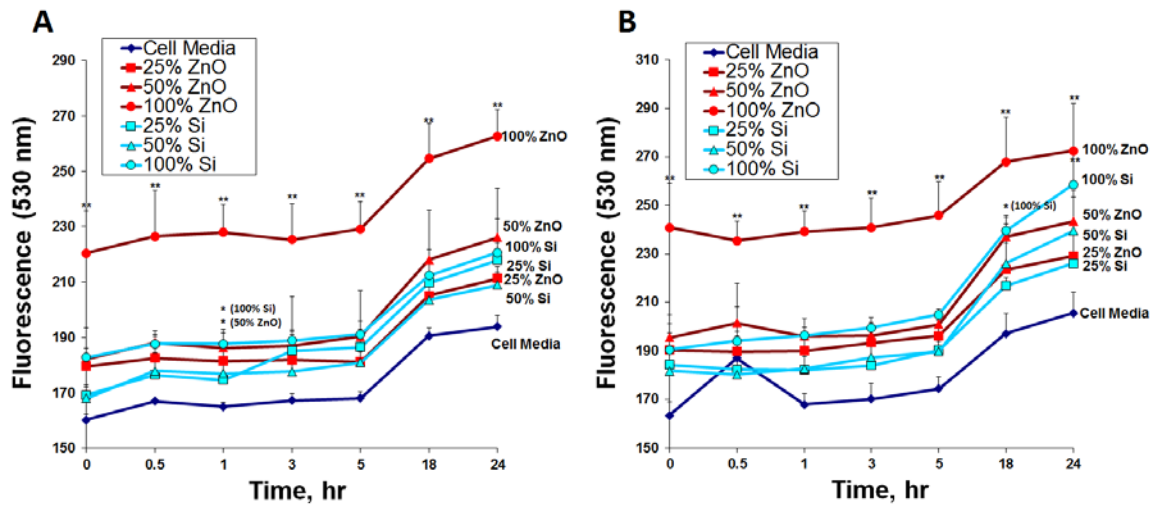


Figure 7. Intracellular ROS generation in (A) 24-hr and (B) 48-hr extracts from Zn-coated Si and smooth Si wafers over a 30 min – 24 hr exposure. All values for undiluted (100%) ZnO 24 and 48-hr extracts had significantly higher ROS generation $** (p < 0.01)$ than the cell media control. Values for 50% diluted ZnO 24-h extract and 100% Si extract were significantly higher $* (p < 0.05)$ than cell media at 1 hr only. The 48-hr, 100% extract from smooth Si was significantly higher at 18 h compared to cell media controls. Data are expressed as mean \pm SD (N = 3 independent experiments).

ICP-MS analysis in ZnO extract:

In extracts from ZnO-coated wafers, Zn concentrations were significantly elevated in the 24 and 48-hr extracts (12.1 and 16.9 $\mu\text{g/mL}$, respectively) compared to very low concentrations present in extracts from smooth wafers and DMEM medium (Fig. 8).

Normalizing for exposed area and 0.5 mL of media per extract, approximately 24.3 and 33.7 $\mu\text{g/m}^2$ were released from the 5 x 5 cm wafers after 24 and 48 hrs, respectively. All 48-hr extracts contained more Zn than 24-hr extracts, but since the results were not doubled, the rate of release of Zn ions into media likely occurred nonlinearly over time.

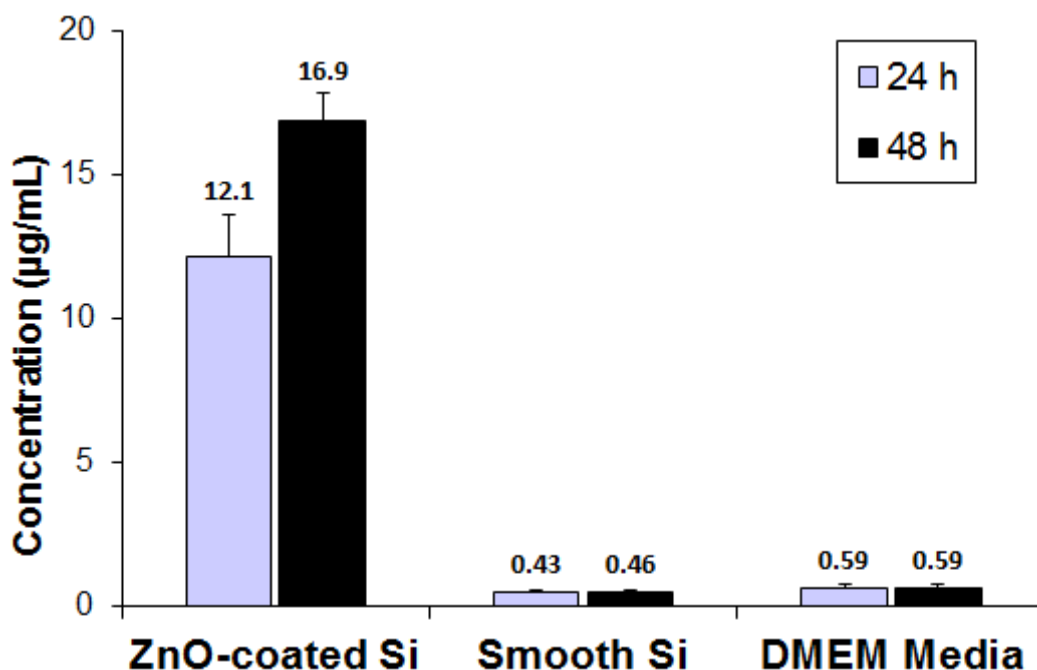


Figure 8. Levels of Zn ions present in extracts. ICP-MS analysis revealed elevated levels of Zn ions present in media of extracts from ZnO-coated wafers following both 24- and 48-hr wafer incubations. Both smooth silicon wafers and DMEM cell media alone were used as controls and each only had trace amounts of zinc present in cell media. 48-hr extracts served as the maximal possible release of ZnO from the relatively thin 96 nm film. Data are expressed as mean \pm SD (N = 3 independent experiments).

Discussion:

The field of nanotoxicology has been focused primarily on the interactions of discrete nanoparticles in biological systems. The number of peer reviewed publications in nanotoxicology grew over 600% between 2000-2007, yet the vast majority of it focused on basic nanomaterials with only a fraction published on integrated nanomaterials and nano-enabled consumer/medical products, such as those with nanotextured coatings³¹. The present study aimed to expand this view beyond discrete particle systems and develop methods for studying the effects of materials with surface nanotopographies. The pulsed laser deposition method used in the present study is a versatile technique for creating surface nanotopographies from metal oxides as well as other materials. The method involves a high-powered pulsed laser aimed at a solid target under vacuum and the solid material is rapidly ablated and vaporized into a high energy plasma plume. The plume then may be directed through an aperture and condensed onto a solid substrate in a highly controlled and consistent manner. In our case, the substrates are smooth silicon wafers and the ablated target is high-purity ZnO. The laser-solid interaction is fairly complex and can be fine-tuned by selecting the appropriate laser wavelength. The emitted photons from the laser undergo several conversions from electronic excitation to thermal, chemical and mechanical energy³² before ablating the target material. Altering the wavelength of the laser can alter the energy characteristics of the plasma plume and vary the characteristics of the deposited layer, namely the presence of particulates boiled off the surface^{33,34}. Although particulates are undesirable in semiconductor applications, it is not known whether they are undesirable in biomedical metal oxide coatings; in fact, the particulates may be useful in medical devices to

modulate properties, such as surface roughness, amount of grain boundaries, and projected surface area, so as to achieve improved performance. The resulting film can be characterized using atomic force microscopy (AFM) to determine morphology, roughness and overall uniformity.

Similar to other physical vapor deposition (PVD) techniques, PLD can be customized for a particular application by selecting the proper ablation material, laser wavelength, pulse duration and other parameters. Techniques such as spin coating^{35,36}, atomic layer deposition³⁷, plasma enhanced chemical vapor deposition (PECVD)³⁸, and spray pyrolysis³⁵ have also been used to deposit ZnO thin films. One of the main advantages of PLD, however, is the ability to control single layer by layer growth of ZnO and other metal oxides. By fine-tuning the amount of laser pulses, the desired thin film height can be achieved^{39,40}. PLD of ZnO can be further modulated by altering the temperature of the reaction chamber. A pulsed laser setup can be modified with a heat source to create various structures and coatings such as ZnO nanoneedles or secondary ZnO nanoscale branches on other substrates⁴¹.

In our study, the selected PLD parameters were useful for depositing nanotextured layers of ZnO on Si. The final thin films were approximately 96 nm thick and nanotexture was produced with a grain size of around 50 nm. EDX elemental analysis confirmed the chemical characteristics of the thin films and AFM confirmed a topographical change on the Si substrate surface. The Si surface was visibly smooth and was a suitable inert control for cell growth. Images of cells growing on Si revealed healthy cell spreading, normal morphology, and a relatively high cell count similar to that of standard polystyrene tissue culture plates (Fig. 3A).

Cell death measured by LDH release and MTT showed relatively higher toxicity when using ZnO in extract form as compared to direct exposure to ZnO surfaces. The soluble ZnCl₂ control for flow cytometry experiments of direct contact to surfaces was equimolar to the amount of Zn ion that gradually dissolves from the ZnO coating. ZnCl₂ showed a lower live cell percentage of 11% as compared to 27% for cells growing directly on the ZnO coating. The results of MTT and LDH using extracts that are added to adherent cells in a tissue culture well additionally showed more cytotoxicity than the endpoints for macrophages grown directly on the ZnO coatings. The possibility for these results could come from a more gradual release of Zn ions into media over 24hrs with which the cells can cope somewhat better than receiving an instant maximum concentration of 12 µg/mL in a single dose.

Nevertheless, the MTT assay for cells grown directly on the ZnO surfaces produced a significant toxic outcome and confocal microscopy revealed a noticeable decrease in adherent cells (Fig. 3B). Images of cells stained with DAPI/phalloidin revealed that fewer cells were attaching to the ZnO-coated surfaces and those that remained had a rounded, rather than spread, morphology. This response could be explained by poor cell adhesion to the ZnO surface or cell death due to the cytotoxic nature of the surface. Macrophages may not have initially properly adhered or they simply detached following cell death in less than 2 hrs. Therefore, only the cells that remained in contact with the ZnO surface were imaged. Another possible explanation for both the morphological change and decreased cell density, aside from effects of chemical toxicity of ZnO, is the immunosuppressive nature of ZnO. ZnO has been shown to decrease monocyte attachment²⁹ which may have contributed to the

low macrophage adhesion to the surface. The sample preparation for imaging may have also washed away some portion of cells if there were loosely adherent cells.

The issue of whether cells initially attached and then detached due to toxic concentrations of Zn ions in the medium was partially addressed by treating cells with medium extracts of ZnO thin films. The extracts were collected and analyzed using ICP-MS to confirm that ZnO was leaching off of the surface. The overall concentration of ZnO was highly consistent between different samples with relatively small standard deviations (12.1 and 16.9 $\mu\text{g/mL}$ after 24 and 48 hrs, respectively). This result supported the assumption of layer consistency between samples, since uniform layers of similar thickness should theoretically have fairly similar leaching characteristics due to a similar amount of projected surface area available for ion dissolution. Therefore, PLD is a suitable technique for applications that require creating uniform and topographically consistent surface coatings with predictable leaching behaviors. In medical applications, leaching modulation is an important parameter for coatings, namely those that require a certain amount of dissolution for antimicrobial, drug delivery, or other properties. The ICP-MS method used, however, does not distinguish between particulates and ions present in solution, but only provides a total elemental concentration. For medical applications, it may be important to consider whether there are particulate or ionic leachates coming off of a surface^{42,43}. Our future studies will make use of recent advances in single particle ICP-MS⁴⁴ to determine both the ion concentration and relative particle content. This is exceptionally important for macrophage cells, which may have a more heightened response to ZnO in nanoparticle as opposed to dissolved form⁴⁵.

The cytotoxicity of ZnO extracts was only evident at the highest (undiluted) concentration. Notably, the 25 and 50% concentrations showed no apparent decrease in cell viability, or increase in LDH release and ROS production, while 100% undiluted extracts resulted a significant cytotoxic and oxidative stress response across all three assays. (Figs 5-7). ROS generation was significantly higher than cell media controls for media incubated with wafers for both 24 hrs and 48 hrs. This suggests that both 24-hr and 48-hr concentrations of Zn measured by ICP-MS have the tendency to generate ROS in macrophages. Although increases in ROS production were statistically significant at 18 hrs and 24 hrs of exposure to ZnO extracts, extracts of non-coated Si wafer surfaces also generated a modest amount of ROS. However, this may have occurred due to an overall basal increase in ROS production, since the cell media only controls increased in production over 24 hrs as well. Since only the undiluted extract had a significant effect on ROS production during all time points, the results suggest that there may be a threshold concentration of zinc in media that causes macrophages to initiate cell death. A distinct gradual dose response along a concentration gradient may not be present or the linear dose response may be a very narrow concentration range. This finding supports the idea that some amounts of ZnO, in our case 50% 24-hr and 48-hr extracts ($\leq 6.07 \mu\text{g/mL}$) are tolerable *in vitro* for both 24 and 48 hrs, while higher undiluted 24 and 48-hr extracts (12.13 and 16.87 $\mu\text{g/mL}$, respectively) may cause considerable cytotoxicity.

Conclusions:

Cells plated directly on the ZnO surface resulted in higher viability compared to controls than those treated with ZnO extracts. The ICP-MS results revealed that Zn was leaching at a gradual rate since the 48-hr extracts had higher concentrations of Zn compared to 24-hr extracts. Therefore, cells cultured directly on the ZnO surface were exposed to a gradually increasing amount of Zn exposure over time, but the experimental conditions were different from the addition of a known, bolus concentration of Zn from extracts. Extracts added to cells reduced cell viability to a greater extent than what occurred in cells grown on the wafers. Cells grown on ZnO wafers may have been able to adapt more readily to a slower release of Zn ions as they gradually leached off of the coated surface into medium. In contrast, when extracts were added to cultured cells, the extracellular Zn ion concentration may have crossed over the threshold for toxicity. This finding notes the importance of defining total allowable exposures with a given exposure time variable. The same amount of ZnO leaching slowly off of a surface may be non-cytotoxic over longer periods of time, but extremely cytotoxic if released within a shorter duration. Future studies will have to look for acceptable concentrations that will provide sustained antimicrobial action over time and will have a negligible effect on cytotoxicity. Additionally, ZnO surfaces with medical applications may need to be modified to slow the dissolution rate of Zn. For such studies requiring a custom surface manufacturing approach, PLD will be a useful technique for fabricating surfaces that have the potential to release Zn in a controllable manner to limit the amount of apoptosis and necrosis that occurs due to contact with the surface as well as dissolved Zn ions.

Acknowledgements:

Peter E. Petrochenko is supported in part by a NSF/FDA Scholar-in-Residence Award #1041375 granted to Roger J. Narayan. The authors would also like to thank Sohrab Habibi for ICP-MS analyses at UNC-Chapel Hill Mass Spectrometry Facility. This research was supported in part by the FDA Medical Countermeasures Initiative (MCMi).

Conflict-of-interest statement: The authors declare no commercial or financial conflict of interest.

References:

- 1 Abd El-Hady, M. M., Farouk, A. & Sharaf, S. Flame retardancy and UV protection of cotton based fabrics using nano ZnO and polycarboxylic acids. *Carbohydr. Polym.* **92**, 400-406, doi:10.1016/j.carbpol.2012.08.085 (2013).
- 2 Skoog, S. A. *et al.* Antibacterial activity of zinc oxide-coated nanoporous alumina. *Materials Science and Engineering B-Advanced Functional Solid-State Materials* **177**, 992-998, doi:10.1016/j.mseb.2012.04.024 (2012).
- 3 Gershon, T., Musselman, K. P., Marin, A., Friend, R. H. & MacManus-Driscoll, J. L. Thin-film ZnO/Cu(2)O solar cells incorporating an organic buffer layer. *Sol. Energy Mater. Sol. Cells* **96**, 148-154, doi:10.1016/j.solmat.2011.09.043 (2012).
- 4 Sonawane, B. K., Shelke, V., Bhole, M. P. & Patil, D. S. Structural, optical and electrical properties of cadmium zinc oxide films for light emitting devices. *J. Phys. Chem. Solids* **72**, 1442-1446, doi:10.1016/j.jpcs.2011.08.022 (2011).
- 5 Lee, J. Y. *et al.* The control of cell adhesion and viability by zinc oxide nanorods. *Biomaterials* **29**, 3743-3749, doi:10.1016/j.biomaterials.2008.05.029 (2008).

- 6 Zaveri, T. D. *et al.* Contributions of surface topography and cytotoxicity to the macrophage response to zinc oxide nanorods. *Biomaterials* **31**, 2999-3007, doi:10.1016/j.biomaterials.2009.12.055 (2010).
- 7 Park, J. K. *et al.* The topographic effect of zinc oxide nanoflowers on osteoblast growth and osseointegration. *Advanced Materials* **22**, 4857, doi:10.1002/adma.201002255 (2010).
- 8 Jansson, T. *et al.* Antibacterial effects of zinc oxide nanorod surfaces. *J. Nanosci. Nanotechnol.* **12**, 7132-7138, doi:10.1166/jnn.2012.6587 (2012).
- 9 Emamifar, A., Kadivar, M., Shahedi, M. & Soleimani-Zad, S. Evaluation of nanocomposite packaging containing Ag and ZnO on shelf life of fresh orange juice. *Innovative Food Science & Emerging Technologies* **11**, 742-748, doi:10.1016/j.ifset.2010.06.003 (2010).
- 10 Hughes, G. & McLean, N. R. Zinc-oxide tape - a useful dressing for the recalcitrant finger-tip and soft-tissue injury. *Archives of Emergency Medicine* **5**, 223-227 (1988).
- 11 Yadav, A. *et al.* Functional finishing in cotton fabrics using zinc oxide nanoparticles. *Bull. Mater. Sci.* **29**, 641-645, doi:10.1007/s12034-006-0017-y (2006).

- 12 Rajendran, R. *et al.* Use of zinc oxide nano particles for production of antimicrobial textiles. *International Journal of Engineering, Science and Technology* **2**, 202-208 (2010).
- 13 Reddy, K. M. *et al.* Selective toxicity of zinc oxide nanoparticles to prokaryotic and eukaryotic systems. *Appl. Phys. Lett.* **90**, 213902-213902-213903 (2007).
- 14 Atasoy, H. B. & Ulusoy, Z. I. A. The relationship between zinc deficiency and children's oral health. *Pediatr. Dent.* **34**, 383-386 (2012).
- 15 Zago, L., Danguise, E., CA, G. I., R o, M. & Callegari, M. Vitamin A and zinc levels in gastroenterological surgical patients: Relation with inflammation and postoperative complications. *Nutricion hospitalaria: organo oficial de la Sociedad Espanola de Nutricion Parenteral y Enteral* **26**, 1462-1468 (2010).
- 16 Tezvergil-Mutluay, A., Carvalho, R. M. & Pashley, D. H. Hyperzincemia from ingestion of denture adhesives. *The Journal of Prosthetic Dentistry* **103**, 380-383 (2010).
- 17 Moos, P. J. *et al.* ZnO particulate matter requires cell contact for toxicity in human colon cancer cells. *Chem. Res. Toxicol.* **23**, 733-739 (2010).

- 18 Daniels, W. M., Hendricks, J., Salie, R. & van Rensburg, S. J. A mechanism for zinc toxicity in neuroblastoma cells. *Metab. Brain Dis.* **19**, 79-88 (2004).
- 19 Sun, J. *et al.* Cytotoxicity, permeability, and inflammation of metal oxide nanoparticles in human cardiac microvascular endothelial cells Cytotoxicity, permeability, and inflammation of metal oxide nanoparticles. *Cell Biol. Toxicol.* **27**, 333-342, doi:10.1007/s10565-011-9191-9 (2011).
- 20 Fuortes, L. & Schenck, D. Marked elevation of urinary zinc levels and pleural-friction rub in metal fume fever. *Vet Hum Toxicol* **42**, 164 (2000).
- 21 Haider, W. & Munroe, N. Assessment of corrosion resistance and metal ion leaching of Nitinol alloys. *J. Mater. Eng. Perform.* **20**, 812-815, doi:10.1007/s11665-011-9892-5 (2011).
- 22 Savarino, L. *et al.* Effects of metal ions on white blood cells of patients with failed total joint arthroplasties. *J. Biomed. Mater. Res.* **47**, 543-550 (1999).
- 23 von Bülow, V. *et al.* Zinc-dependent suppression of TNF- α production is mediated by protein kinase A-induced inhibition of Raf-1, I κ B Kinase β , and NF- κ B. *The Journal of Immunology* **179**, 4180-4186 (2007).

- 24 Grandjean-Laquerrier, A. *et al.* Influence of the zinc concentration of sol-gel derived zinc substituted hydroxyapatite on cytokine production by human monocytes in vitro. *Biomaterials* **27**, 3195-3200, doi:10.1016/j.biomaterial.2006.01.024 (2006).
- 25 Velard, F. *et al.* The effect of zinc on hydroxyapatite-mediated activation of human polymorphonuclear neutrophils and bone implant-associated acute inflammation. *Biomaterials* **31**, 2001-2009 (2010).
- 26 Colon, G., Ward, B. C. & Webster, T. J. Increased osteoblast and decreased Staphylococcus epidermidis functions on nanophase ZnO and TiO₂. *J. Biomed. Mater. Res. Part A* **78A**, 595-604, doi:10.1002/jbm.a.30789 (2006).
- 27 Petrochenko, P. E. *et al.* Cytotoxicity of cultured macrophages exposed to antimicrobial zinc oxide (ZnO) coatings on nanoporous aluminum oxide membranes. *Biomatter* **3** (2013).
- 28 Gittard, S. D. *et al.* Assessing the antimicrobial activity of zinc oxide thin films using disk diffusion and biofilm reactor. *Appl. Surf. Sci.* **255**, 5806-5811, doi:10.1016/j.apsusc.2009.01.009 (2009).
- 29 He, Y. *et al.* Study on pulsed laser ablation and deposition of ZnO thin films by L-MBE. *Science in China Series E: Technological Sciences* **50**, 290-301 (2007).

- 30 Wu, D. & Cederbaum, A. I. Inhibition of autophagy promotes CYP2E1-dependent toxicity in HepG2 cells via elevated oxidative stress, mitochondria dysfunction and activation of p38 and JNK MAPK. *Redox biology* **1**, 552-565 (2013).
- 31 Ostrowski, A. D., Martin, T., Conti, J., Hurt, I. & Harthorn, B. H. Nanotoxicology: characterizing the scientific literature, 2000-2007. *Journal of Nanoparticle Research* **11**, 251-257, doi:10.1007/s11051-008-9579-5 (2009).
- 32 Miotello, A. & Kelly, R. Laser-induced phase explosion: new physical problems when a condensed phase approaches the thermodynamic critical temperature. *Applied Physics a-Materials Science & Processing* **69**, S67-S73, doi:10.1007/s003399900296 (1999).
- 33 Puretzky, A. A., Geohegan, D. B., Jellison, G. E. & McGibbon, M. M. Comparative diagnostics of ArF- and KrF-laser generated carbon plumes used for amorphous diamond-like carbon film deposition. *Appl. Surf. Sci.* **96-8**, 859-865, doi:10.1016/0169-4332(95)00567-6 (1996).
- 34 Christen, H. M. & Eres, G. Recent advances in pulsed-laser deposition of complex oxides. *Journal of Physics-Condensed Matter* **20**, doi:264005 10.1088/0953-8984/20/26/264005 (2008).

- 35 Tarwal, N. L. *et al.* Photoluminescence and photoelectrochemical properties of nanocrystalline ZnO thin films synthesized by spray pyrolysis technique. *Appl. Surf. Sci.* **257**, 10789-10794, doi:10.1016/j.apsusc.2011.07.099 (2011).
- 36 Bubel, S., Mechau, N. & Schmechel, R. Electronic properties of polyvinylpyrrolidone at the zinc oxide nanoparticle surface PVP in ZnO dispersions and nanoparticulate ZnO thin films for thin film transistors. *J. Mater. Sci.* **46**, 7776-7783, doi:10.1007/s10853-011-5757-4 (2011).
- 37 Maeng, W. J., Lee, J. W., Lee, J. H., Chung, K. B. & Park, J. S. Studies on optical, structural and electrical properties of atomic layer deposited Al-doped ZnO thin films with various Al concentrations and deposition temperatures. *Journal of Physics D-Applied Physics* **44**, doi:445305 10.1088/0022-3727/44/44/445305 (2011).
- 38 Panigrahi, J. *et al.* Radio frequency plasma enhanced chemical vapor based ZnO thin film deposition on glass substrate: A novel approach towards antibacterial agent. *Appl. Surf. Sci.* **258**, 304-311, doi:10.1016/j.apsusc.2011.08.056 (2011).
- 39 Hirsch, A. *et al.* Imposed layer-by-layer growth of ZnO on GaN/sapphire substrates using pulsed laser interval deposition. *Thin Solid Films* **519**, 7683-7685, doi:10.1016/j.tsf.2011.05.057 (2011).

- 40 Rijnders, G., Koster, G., Leca, V., Blank, D. H. A. & Rogalla, H. Imposed layer-by-layer growth with pulsed laser interval deposition. *Appl. Surf. Sci.* **168**, 223-226, doi:10.1016/s0169-4332(00)00602-4 (2000).
- 41 Choi, J. *et al.* Brush-shaped ZnO heteronanorods synthesized using thermal-assisted pulsed laser deposition. *ACS applied materials & interfaces* **3**, 4682-4688 (2011).
- 42 Hallab, N. J., Mikecz, K., Vermes, C., Skipor, A. & Jacobs, J. J. in *Molecular Mechanisms of Metal Toxicity and Carcinogenesis* 127-136 (Springer, 2001).
- 43 Doorn, P. F. *et al.* Metal wear particle characterization from metal on metal total hip replacements: transmission electron microscopy study of periprosthetic tissues and isolated particles. *J. Biomed. Mater. Res.* **42**, 103-111 (1998).
- 44 Farkas, J. *et al.* Characterization of the effluent from a nanosilver producing washing machine. *Environ Int* **37**, 1057-1062, doi:10.1016/j.envint.2011.03.006 (2011).
- 45 James, S. A. *et al.* Quantification of ZnO Nanoparticle Uptake, Distribution and Dissolution within Individual Human Macrophages. *ACS Nano* (2013).

CHAPTER 3: Antibacterial nanosilver and PMMA composite coatings for supporting human bone stem cells.

Authors: Peter E Petrochenko,^{1,2} Jiwen Zheng,¹ Brendan Casey,¹ Mohammad R Bayati,³
Roger J Narayan,² Peter L Goering.¹

¹ *Center for Devices and Radiological Health, US Food and Drug Administration, Silver Spring, MD, 20993, USA.*

² *Joint Dept of Biomedical Engineering, Univ of North Carolina-Chapel Hill and North Carolina State Univ, Raleigh, NC, 27695 USA.*

³ *Intel Corporation, IMO-SC, SC2, Santa Clara, CA, 95052, USA.*

Abstract:

PMMA is an attractive biomaterial since it has relatively good biocompatibility, long lasting use in bone cements and does not contain the potentially harmful bisphenol-A component. Like many porous polymers PMMA is prone to bacterial contamination, which may be mediated by incorporating nanoparticulate silver, a known antimicrobial agent. PMMA/silver composites have been shown to decrease biofilm formation in prior studies. The combination of these two materials makes it necessary to determine the thresholds of silver concentration at the site of use, such as that of bone repair with PMMA cements. Outside of bone cement use, it is possible to create a functional PMMA/silver composite thin film coating with pulsed laser deposition (PLD). Our study demonstrates a composite thin film with PMMA and silver by ablating a combined rotating target during PLD. Characterization studies showed that the

layer was uniform and the silver was evenly distributed. Three layer thicknesses were used, and ICP-MS was *used to show* that films deposited using 10,000 pulses released 0.76 µg/mL Ag, while films deposited with 14,000 and 20,000 pulses released 1.05 and 1.67 µg/mL Ag, respectively. All thin films were found to have very strong antimicrobial activity against *E. coli* in dynamic conditions. However, only the thin film that released the lowest amount of silver into cell culture media (0.76 µg/mL) was not cytotoxic to human bone marrow stromal cells (hBMSCs). The remaining two sample types significantly decreased cell viability by causing both necrosis and high amounts of apoptosis in cells.

Introduction:

Poly(methyl methacrylate) (PMMA) is a transparent thermoplastic that is relatively low-cost and straightforward to process. It was initially developed as a thermoplastic shatter-proof alternative to glass, under the trade name “Plexiglas” and has found use in the medical industry in tubing, chromatography, and more recently lab-on-a-chip and microfluidic devices. Unlike similar costlier alternatives (ex. polycarbonate), PMMA does not contain bisphenol-A, which makes it an attractive biomaterial for contact with tissues. One of the first medical uses of PMMA was to form the base of complete dentures,^{1,2} but since then it has gained a variety of uses. The methyl methacrylate (MMA) resin can be molded to produce hardened transparent PMMA, which allowed it to be used in intraocular lenses³ and hard contact lenses for decades. Its use in contact lenses was eventually phased and replaced with soft hydrogel materials due to the poor gas permeability through PMMA to the cornea⁴. In orthopedics, however, PMMA continues to be used for a wide range of applications, including bone cements, screw fixation, bone defect and cavity fillers, and vertebral stabilization.⁵ A long-term follow-up study of cranial reconstructions with bone grafts, hydroxyapatite (HA) cement, and PMMA cement concluded that PMMA had the best overall outcome (97% satisfactory) to bone graft (91.7%) and osteoinductive HA (82.8%). Although patients in the PMMA group also had the lowest number of complications due to infection, the number was fairly high at 13.3% of patients experiencing infection and exposure.⁶ Infection is a common problem in orthopedic surgery; for example, rates of infection for total joint replacement after the initial procedure alone range from 0.5-5%, with infection being the second most common cause of revision, second only to joint instability.⁷

Since PMMA heats up considerably during polymerization at the bone defect site, one option to decrease the chances for periprosthetic infections has been to load PMMA bone cements with heat stable antibiotics such as ancomycin, gentamicin and tobramycin.⁸ A review by Tan et al, argued that antibiotics loaded into PMMA cement have inconsistent effectiveness, lead to emergence of antibiotic-resistant bacterial strains, and have an adverse effect on osteogenic cells.⁹ In place of antibiotics the authors pointed to using chitosan, a less toxic deacetylated derivative of chitin with potential broad antimicrobial properties.⁹ Silver is a known antimicrobial agent that has additionally been incorporated into PMMA and showed a significant decrease in biofilm formation.¹⁰ Systemic accumulation of metals like copper, gold, and silver has prevented their widespread use over antibiotics and has limited them for uses in high risk devices such as catheters or percutaneous implants.^{11,12} The site of bone remodeling is especially sensitive to cytotoxicity, which can lead to significant bone resorption and ultimately implant failure. Therefore, it is exceptionally important to determine the thresholds of silver concentration at the site of bone repair or any other application of silver coatings. It is possible to control the release of silver ions and nanoparticles by immobilizing or binding them in polymers.¹³⁻¹⁵ A recent study of immobilized silver nanoparticles in PMMA fibers compared their antibacterial properties with equal concentrations of silver nitrate and silver sulfadiazine. The PMMA and silver composite released nanoparticles, which had an apparently faster bacterial kill rate than either of the dissolved silver sulfadiazine and silver nitrate solutions.¹⁶ This is not an uncommon finding; however, the exact mechanism of silver nanoparticle bactericidal action remains unclear.

Embedding silver in a known manner within a polymer such as PMMA is key to establishing a controlled release profile. It is possible to deposit PMMA and silver simultaneously using pulsed laser deposition (PLD) to create a composite thin film. PLD has been used to deposit homogeneous, defect-free PMMA films that retain its characteristic amorphous polymer X-ray diffraction pattern but develop a different Raman and XPS Spectra, likely resulting from an increase in C-O bonds from the ablation process.¹⁷ The pulsed laser deposition of pure silver targets can also be conducted at room temperature¹⁸ allowing it to be coated onto delicate heat sensitive polymeric devices, such as microneedles.¹⁹ The high energy state of pulsed laser ablated materials additionally exhibit high adhesion strength, creating a strong bond between the coating and substrate. Aside from ablating silver and PMMA simultaneously it is possible to use a rotating target to create a continuous mixed plume of silver and PMMA, thus effectively trapping silver particulates in the PMMA matrix. The goals of the present study, therefore, were (1) to fabricate a PMMA/Ag composite thin film with varying concentrations of silver, (2) examine its release characteristics in a simulated bodily environment, and finally (3) determine the optimal amount of silver deposition to both ensure cytocompatibility of the composite coating and its antibacterial efficacy.

Methods:*Pulsed Laser Deposition (PLD):*

PMMA and Ag were deposited onto defect free single crystalline Si polished wafers. A krypton fluoride excimer laser ($\lambda = 248$ nm) was used to ablate a smaller high-purity Ag target mounted onto a larger circular PMMA target on a rotational stage. Start and end rotational angles were adjusted so that the Ag and PMMA targets were intermittently ablated creating a continuous deposition as opposed to separate layers. The thin films were grown under N_2 partial pressure of 5×10^{-5} Torr at room temperature. The total number of laser pulses was set to 10000, 14000, or 20000 with a pulse frequency of 20 Hz and pulse energy of 200 mJ. The coated wafers were then cut into approximately 0.35×0.35 cm (0.5 cm diagonal) squares to fit the wells of a 96-well plate.

Scanning Electron Microscopy (SEM) and Energy-Dispersive X-ray Spectroscopy (EDX):

Scanning electron microscopy (SEM) performed using a JSM 6390LV scanning electron microscope (JEOL, Tokyo, Japan). An accelerated voltage of 20 keV was used for imaging.

Inductively Coupled Plasma Mass Spectrometry (ICP-MS):

Coated wafers were placed in 96-well plates and incubated in 0.2 mL Mesenchymal Stem Cell Growth Medium (MSCGM) (Lonza, Walkersville, MD) for 24 hrs at 37 °C and 5% CO_2 . Wells with medium but without wafers served as control extracts. A Thermo X-Series II quadrupole ICP-MS was used to determine the total concentration of the released silver into the medium. The ICP-MS measurement was conducted in Collision Cell Technology (CCT) mode with a gas of He/H₂ (99.999% purity, v/v: 93%/7%). The ICP-MS was tuned using 1 ppb Tune A solution (Thermo Fisher) to meet the required performance. A NIST SRM 3151

Silver Standard solution was used as a calibration standard and a second-source silver standard (Inorganic venture) was used for QC control. An internal standard solution (Perkin Elmer, contains 10mg l⁻¹ Bi Ge In Li Sc TbY) was introduced along with samples through a T-connector to correct signal drift and matrix effects. The dilution of calibration standards and silver extract samples were performed with HNO₃ and HCl (2% HNO₃ and 0.5% HCl, W/V) to avoid precipitation (coating) of silver.

E. Coli Colony Count:

The experimental protocol closely followed ASTM standard E2149-10 (Standard Test Method for Determining the Antimicrobial Activity of Immobilized Antimicrobial Agents Under Dynamic Conditions). A 1 mL frozen aliquot of Escherichia coli (ATCC[®] 25922[™] FDA strain Seattle 1946, Serotype O6) was allowed to defrost and then added to 10 mL of nutrient broth (8 g of dry Difco[®] nutrient broth powder per 1000 mL of deionized water), diluted further according to the protocol and incubated (37°C, 60 rpm) until the optical density reached 0.28 ± 0.02 , which, according to ASTM standard E2149-10, should be a bacteria concentration of approximately $1.5\text{-}3.0 \times 10^8$ colony forming units (CFUs)/mL. The bacterial solution was then diluted 1000-fold by placing 150 μ L into 149.85 mL of sterilized (121°C, 20 minutes) DI water.

Four separate samples were tested in each experiment, PMMA alone and PMMA with silver in 3 different thicknesses. Uncoated Si served as a positive control, and pure silver deposited without PMMA was used as a negative control. For each experiment 2 mL of bacterial solution were added to each well of a 24 well plate containing the samples. Each test sample, was mixed with the bacterial solution. Samples were then placed in the orbital incubator

(37°C, 60 rpm) for 1 hour. After 1 hour the test solutions were removed from the incubator for culturing on agar plates. One (1) mL of each solution was then removed and added to 9 mL of sterilized (121°C, 20 minutes) DI water in a conical centrifuge tube to yield a dilution of 10-fold. This dilution was diluted again to achieve a 100-fold, 1000-fold, and 10,000-fold dilution.

For culturing on agar plates, 500 µL of solution were added to the top of the agar plate. A metal spreader was used to spread the bacteria evenly across the entire surface of the agar plate. The metal spreader was sterilized using isopropanol, which was immediately burned off, between each sample to prevent cross contamination. Three separate agar plates were used for each solution (n = 3). After inoculation the agar plates were incubated (37°C) in a standard incubator (New Brunswick (Enfield, CT) Galaxy 170R) for 24 hours. The plates were inverted to prevent contamination from water condensation.

After 24 hours the colonies on each plate were counted. The plates that contained less than 200 colonies were manually counted. Plates which contained greater than 200 colonies were analyzed using a Synbiosis (Frederick, MD) ProtoCOL 3 automatic colony counting and zone measuring machine.

Cell Culture:

Samples were sterilized by washing with diluted Penicillin-Streptomycin for 10 min, followed by PBS for 1 hour and dried thoroughly under vacuum. A single 10 µL droplet of concentrated suspension containing approximately 8,000 human bone marrow stromal cells (hBMSCs) (Lonza, Walkersville, MD) was dropped onto the scaffold and allowed to adhere for two hours at 37 °C. A 0.2 mL aliquot of Mesenchymal Stem Cell Growth Medium

(MSCGM) (Lonza, Walkersville, MD) was added to the 96-well and incubated for the appropriate time for biological assays in a humidified atmosphere containing 5% CO₂. Following incubation, the scaffolds were moved to a new well plate so cells grown on the polystyrene surfaces of the wells did not influence assay measurements, supernatants were collected where appropriate.

MTT Dye Cell Viability:

Samples were assayed for potential cytotoxicity using the MTT (3-[4,5-dimethyl-2-thiazol]-2,5-diphenyl-2H-tetrazolium bromide) assay (CellTiter 96[®] Non-Radioactive Cell Proliferation Assay) (Promega, Madison, WI). The MTT assay is based on an assessment of mitochondrial metabolic activity. MTT medium was prepared by adding dye solution at a 15:100 ratio to media as specified by the kit. A 15 µL aliquot of MTT dye was added to each well in order to obtain a total adjusted volume of 100 µL. The plates were then incubated under 37° C, 5% CO₂, 95 % humidity cell culture conditions for three hours. After the incubation period, the Solubilization Solution/Stop Mix was added and the plates were incubated again for one hour at 37°C. The wells were then mixed and the contents were transferred to duplicate wells in a 96-well plate for absorbance measurements. Absorbance was measured at a wavelength of 570 nm (reference wavelength=650 nm) using a 96-well OPTIMax plate reader (Molecular Devices, Sunnyvale, CA). Cells spiked with 5% and 10% dimethyl sulfoxide (DMSO) served as a positive cytotoxicity control. The MTT dye was tested for interactions with all sample materials and controls; no interference was recorded. The data were normalized to uncoated Si wafers and expressed as percent viability.

Necrosis and Apoptosis Detection using Flow Cytometry:

Necrosis and apoptosis of hBMSCs grown on PMMA+Ag coated Si wafers were determined using dye-based flow cytometry analysis. After exposure treatments of 24 hrs, supernatants were collected, remaining adherent cells were detached with TrypLe, (Life Technologies, Grand Island, NY), both solutions combined in a microcentrifuge tube, and centrifuged at 1000 rpm for 5 min. The resulting cell pellet was transferred to a flow cytometry tube containing 100 μ L of binding buffer, 20 μ L of 7AAD and 5 μ L of Annexin V dyes as specified by the Annexin V:PE Apoptosis Detection Kit I (BD Pharmingen, San Diego, CA). Each sample was gently vortexed for 10 sec prior to loading into the flow cytometer (BD FACS Canto II). Live cells and cells killed with AgNO₃ served as the controls used for gating. Data was expressed as % of total cell population, 100% of which was comprised of either live, necrotic and/or apoptotic cells.

Statistical Analysis:

The results from each data set were analyzed using Prism (v. 4) statistical software (GraphPad Inc., La Jolla, CA). Results were expressed as mean \pm standard deviation. Each assay was conducted in duplicate and at least 3 independent experiments were conducted for each assay. Statistical differences between control and treated groups were assessed using one-way ANOVA followed by a Bonferroni *post hoc* test. Data were normalized to the smooth silicon wafers and were expressed as percent viability. Significance level notation was expressed as * for $p < 0.05$ and ** for $p < 0.01$.

Results:*Physicochemical characterization of PMMA/Ag composite thin films:*

Pulsed laser deposition using a constant pulse energy of 200 mJ was used to deposit PMMA and silver simultaneously using a rotating target. Three sets of silver containing samples were created by adjusting the total number of laser pulses. 10,000 pulses were used to deposit a thin film of PMMA to be used as a silver-free control (Figure 1A). The same total number of pulses was used to create a partial PMMA and silver film where the silver coating was not fully embedded into the PMMA seen in Figure 1B. The remaining two thin films were made with a total of 14,000 (Figure 1C) and 20,000 pulses (Figure 1D), respectively. The ratio of silver:PMMA was kept constant and only the thickness of the film was varied. The total amount of silver that could be released, however, increased from the 10,000 pulses film (Figure 1B) being the lowest, to the 20,000 film theoretically having double the PMMA and silver content (Figure 1D).

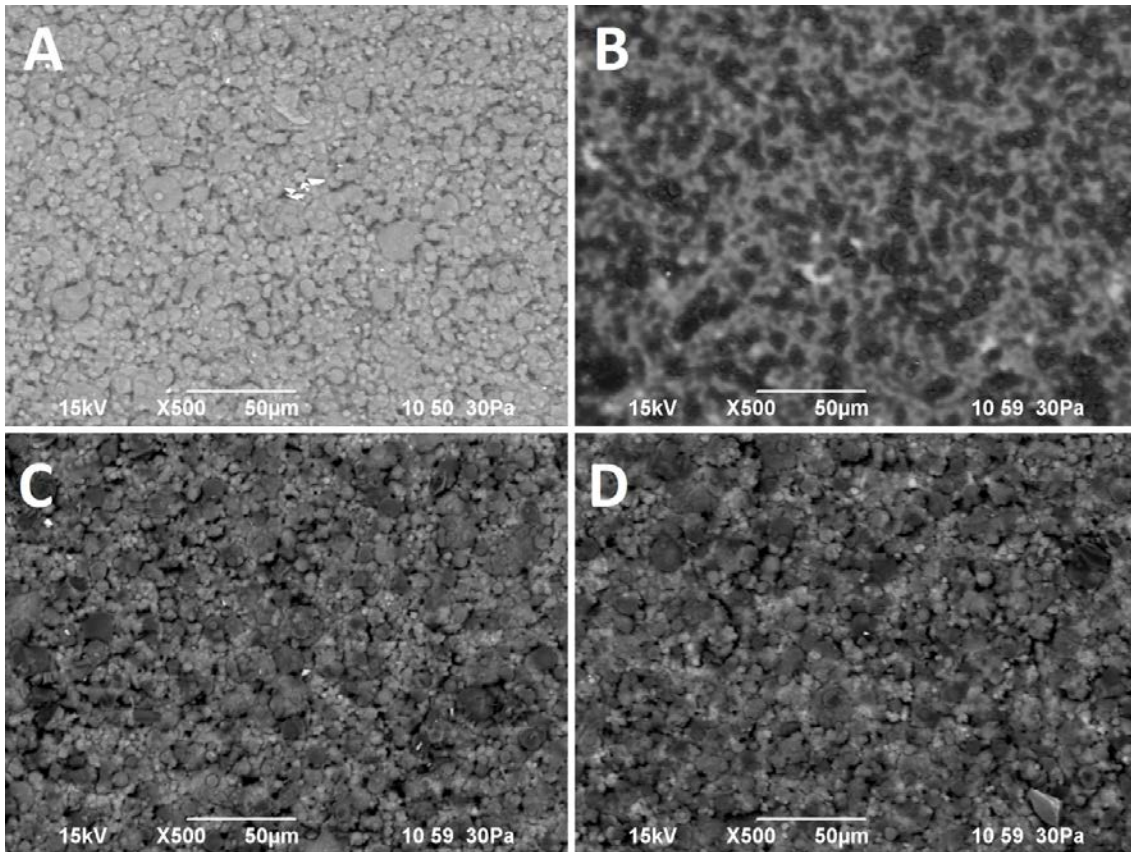


Figure 1. Scanning electron micrograph (SEM) of four thin films deposited with pulsed laser deposition. (A): PMMA only thin film deposited with 10,000 pulses, showing the porous uniform morphology of PMMA, (B): 10,000 pulses of PMMA with silver, showing that more PMMA is deposited per pulse in terms of volume; a darker hue is visible from the silver particulates. (C) Increasing the number of pulses to 14,000 creates a uniform thin film of PMMA and silver, while (D) shows a thicker film made with 20,000 pulses.

The thin films from top-view in Figure 1, the layers looked highly uniform. However, from the side view of the 20,000 pulse PMMA/silver composite film shown in Figure 2, it is possible to see that the thickness varied greatly, ranging from approximately 5.3 to 11.2 μm .

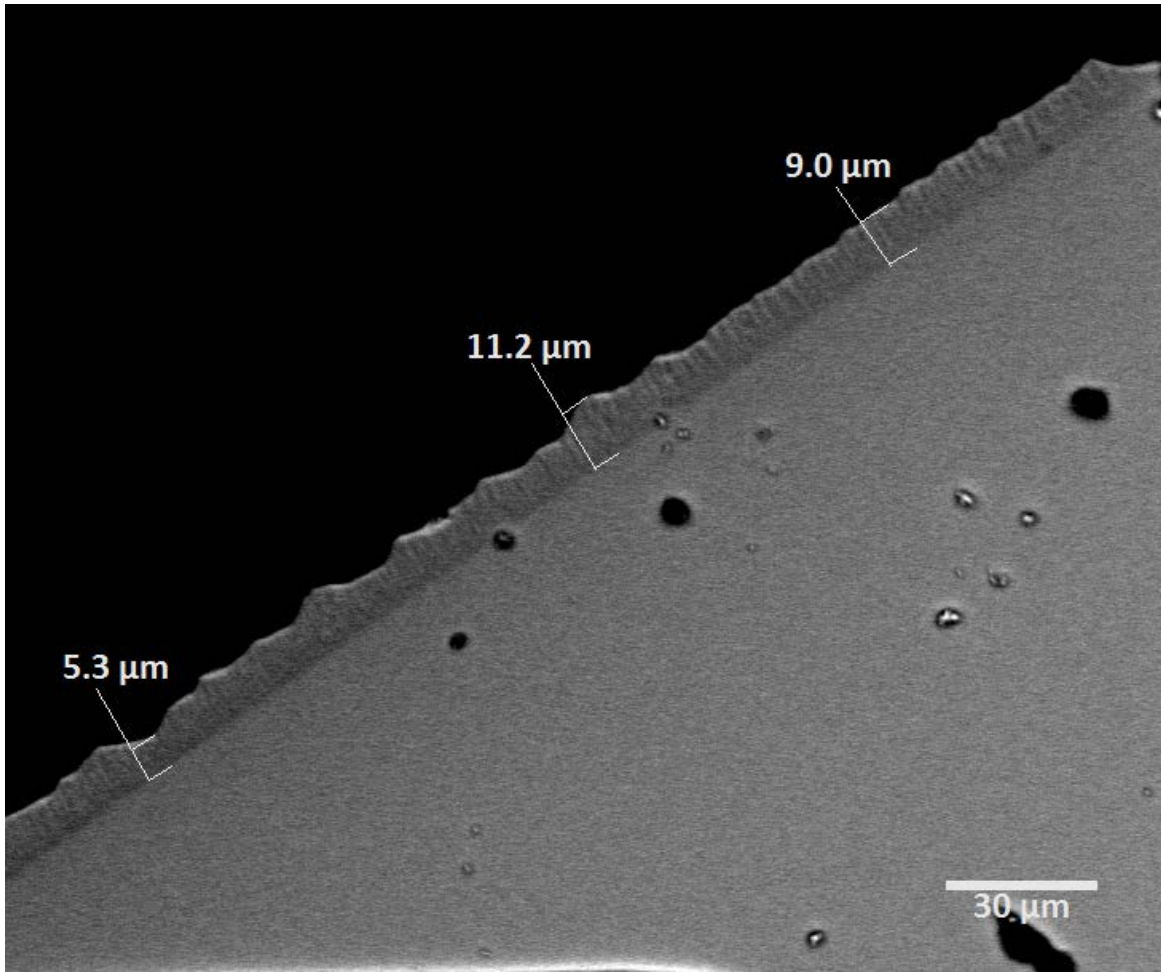


Figure 2. SEM side-view of the 20,000 pulse PMMA/silver composite thin film. Thickness varied between approximately 5-11 μm.

Upon closer investigation with the energy dispersive X-ray spectroscopy (EDX) attachment of the SEM it was possible to see strong carbon and oxygen peaks. The Si peak was visible on the composite films deposited with 10,000 pulses, however, was minimal on the 14,000 pulse composite films' EDX spectrum, shown in Figure 3. The silver peak was clearly distinguishable, although had a much lower count rate than the C and O peaks.

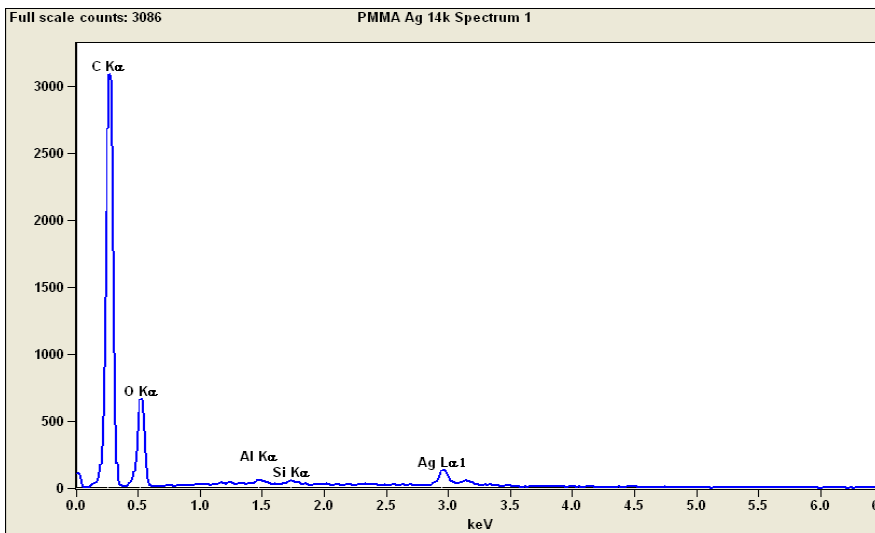


Figure 3. EDX Spectrum of PMMA/silver composite thin film deposited with 14,000 pulses. Highest count rate peaks were C and O, largely present in PMMA, while Ag had a minor, but distinguishable peak.

Using EDX to further determine weight and atom %, the composite films were found to contain approximately 3% silver by weight. The complete weight and atom distribution is shown in Table 1. Trace amounts of aluminum and Si were present in the films due to the aluminum holders used during the deposition and the Si substrates onto which the films were deposited.

Table 1. EDX analysis of weight and atom percentages for the composite PMMA/silver pulsed laser deposited thin films.

Element	Weight %	Atom %
C	75.34 ± 1.64	81.95 ± 1.78
O	21.47 ± 0.53	17.53 ± 0.43
Al	0.19 ± 0.02	0.09 ± 0.01
Si	0.19 ± 0.02	0.09 ± 0.01
Ag	2.82 ± 0.22	0.34 ± 0.03
Total	100.01	100

To determine how a 3% weight content of silver in PMMA translates to dissolution, the coated Si wafers were transferred to cell culture media (Mesenchymal Stem Cell Growth Medium) and incubated for 24 hrs at 37°C and 5% CO₂. Following incubation the extracts were collected and measured with ICP-MS to quantify the amounts of eluted silver shown in Figure 4. The Si wafers and PMMA only thin films had no detectable ionic Ag. Films deposited using 10,000 pulses released 0.76 µg/mL Ag, while films deposited with 14,000 and 20,000 pulses released 1.05 and 1.67 µg/mL Ag, respectively. Assuming the number of pulses directly correlated to the amount of silver deposited the ratio should have been 1 : 1.4 :

2 and instead it was 1 : 1.38 : 2.19, which was relatively close to the theoretical value.

Therefore from the result it is evident that the number of pulses directly corresponds to the total amount of silver that is deposited into the PMMA matrix and to the total amount of silver that can elute in 24 hrs.

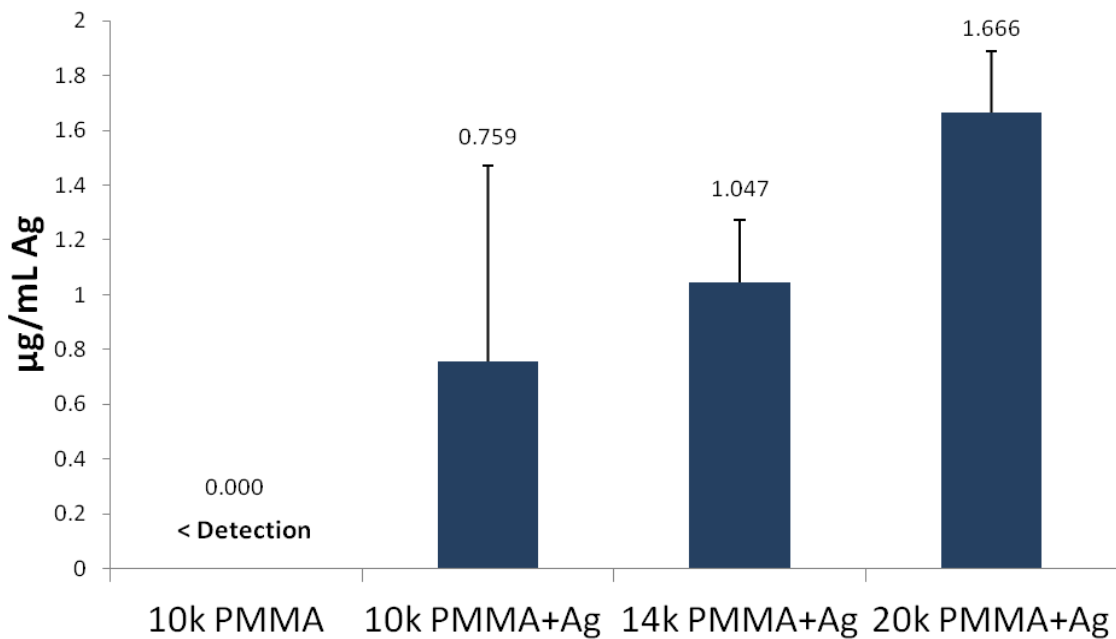


Figure 4. ICP-MS of PMMA/Ag composite thin films showing that 0.76, 1.05, and 1.67 µg/mL Ag was released into cell media after 24 hrs from thin films deposited with 10,000, 14,000 and 20,000 pulses, respectively.

Antibacterial Efficacy of PMMA/Ag composite thin films:

In order to properly simulate the dynamic conditions of medical implants and other devices the antimicrobial efficacy of PMMA/Ag composite thin films was evaluated using the dynamic shake flask test (ASTM E2149) with results shown in Figure 5. The PMMA and Si had nearly identical results to blank controls, meaning these materials had no detectable antimicrobial activity. With the addition of silver into the PMMA film, the number of colonies resulting from the undiluted bacterial solution/extract mixture decreased by 99%, from approximately 2636 colonies for PMMA to 34 colonies for the 10,000 pulse PMMA/Ag composite, the lowest total silver sample out of the tested materials. The remainder of the silver containing samples killed all E. coli in solution preventing any significant colony formation. The silver-only PLD deposited control film also killed all bacteria similar to the PMMA/Ag composite films.

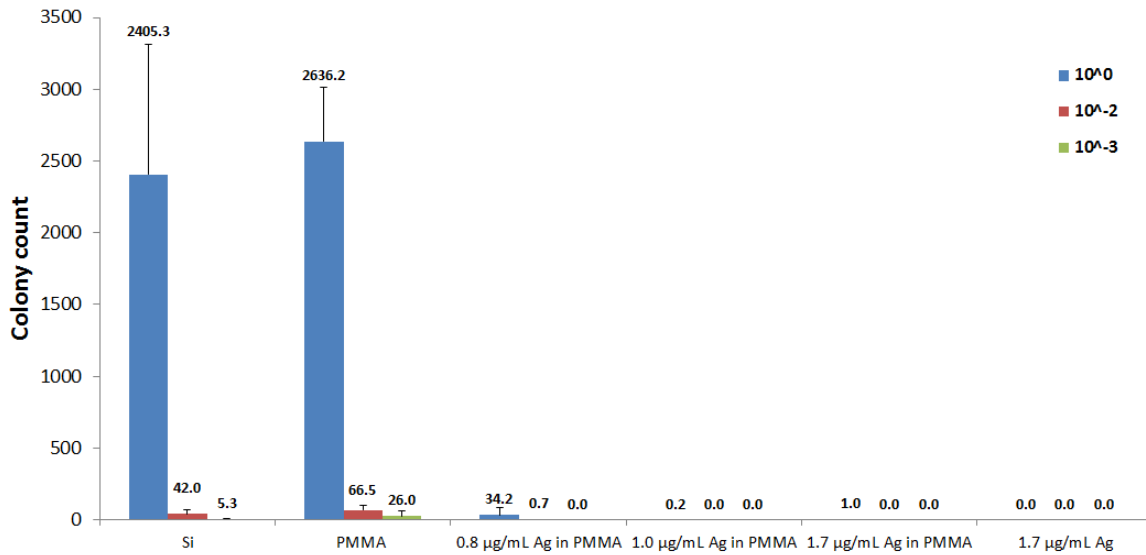


Figure 5. Antimicrobial efficacy of PMMA/Ag composite thin films using dynamic contact conditions. All silver containing samples has significant bacterial activity compared to controls. Uncoated Si wafers and PMMA thin films showed no inherent antimicrobial activity.

Cytocompatibility of PMMA/Ag thin films with human bone marrow stromal cells (hBMSCs):

Silver had a negative effect on bone marrow stromal cell viability as determined with the MTT assay after 24 hrs of incubation, shown in Figure 6. There was a 17% decrease in viability with cells grown on PMMA compared to tissue culture plate controls; however, this decrease was not significant, meaning the PMMA itself did not decrease cell viability. The cell droplet placed onto PMMA was absorbed more than the droplet onto the smooth TCPS

well, which caused faster evaporation and spreading of the cell droplet on the PMMA surface. The 10,000 pulse PMMA/Ag composite (labeled by its release of 0.8 $\mu\text{g/mL}$ Ag in PMMA) showed no significant toxicity as well, with a decrease of roughly 21% from controls. The 14,000 pulse PMMA/Ag composite (labeled 1.0 $\mu\text{g/mL}$ Ag in PMMA) decreased viability by 32% from controls, while the 20,000 pulse PMMA/Ag composite (labeled by its release of 1.7 $\mu\text{g/mL}$ Ag in PMMA) was the most toxic, causing a 72% decrease in hBMSC viability.

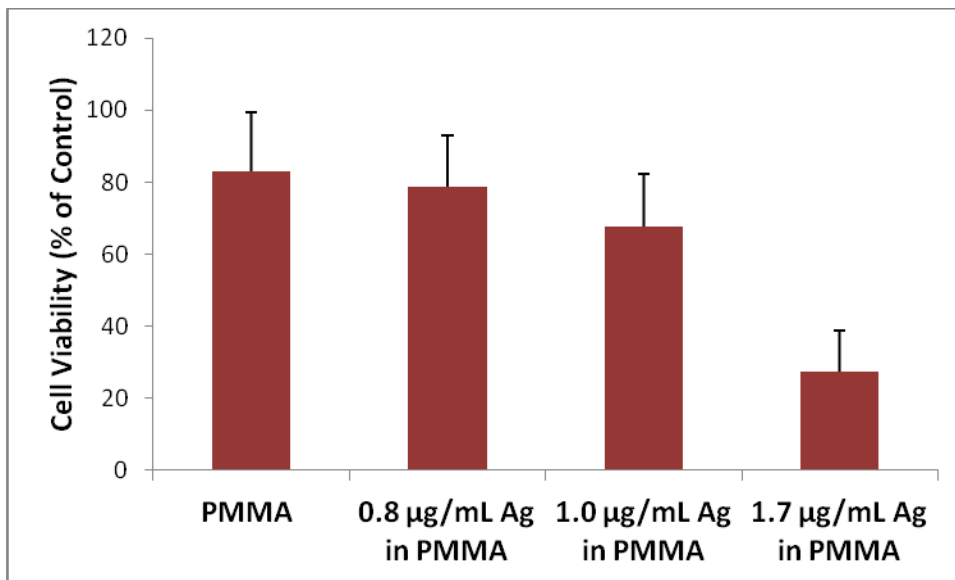


Figure 6. Cell viability of hBMSCs grown on PMMA/Ag composite thin films, measured with the MTT assay after 24 hrs of incubation.

Further investigation with flow cytometry necrosis (7AAD) and apoptosis (Annexin V) dyes showed a dramatic difference in the amount of apoptotic cells from the 10,000 pulse silver containing samples and the 14,000 and 20,000 pulse samples (Figure 7). Some apoptosis and necrosis is expected in all samples due to handling and other experimental conditions. Both PMMA-only and 10,000 pulse PMMA/Ag composite (labeled PMMA + 0.8 $\mu\text{g}/\text{mL}$ Ag) samples showed no significant apoptosis or necrosis although the silver-containing samples had 14% more apoptosis. The remaining 14,000 and 20,000 pulse PMMA/Ag samples showed very high values of apoptosis, 71% and 67% of the total cell population staining positive for apoptosis, respectively. In addition, the 14,000 and 20,000 pulse samples killed 32% and 37% of hBMSCs through necrosis.

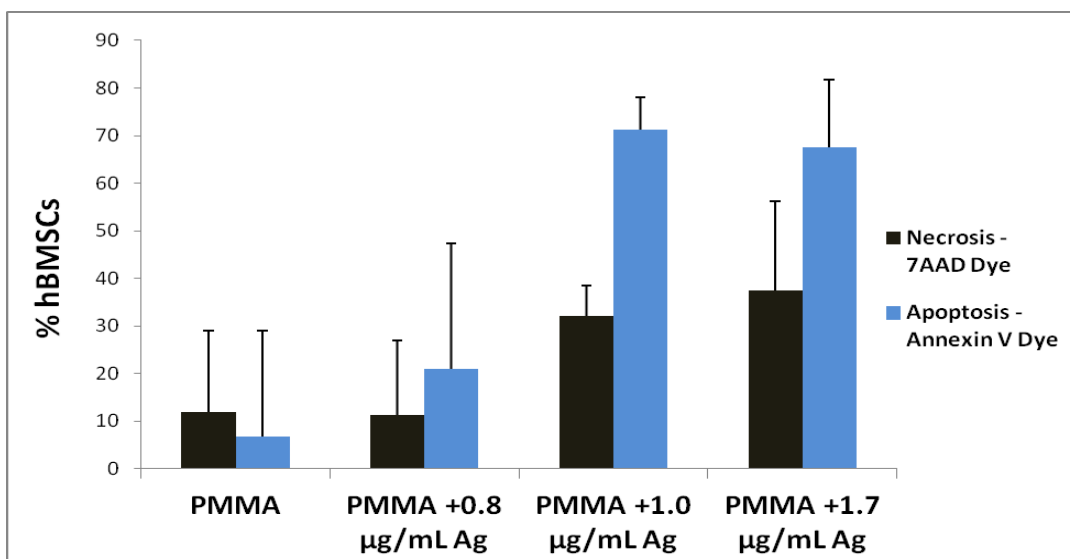


Figure 7. Flow cytometry assay with hBMSCs stained with 7AAD dye for necrosis and Annexin V dye for apoptosis detection. Thin films with PMMA alone or PMMA and 0.8µg/mL eluted silver did not cause significant toxicity, while higher amounts of silver caused considerable apoptosis and necrosis in the cell population.

Discussion:

The loading of silver nanoparticles into PMMA bone cement is not a unique concept. A study by Alt et al, has shown that loading 0.5 – 1% nanosilver by weight into PMMA bone cement had high antibacterial efficacy against *S. epidermidis*, methicillin-resistant *S. epidermidis* (MRSE), and methicillin-resistant *S. aureus* (MRSA), outperforming 2% gentamicin in PMMA while causing no significant toxicity in osteoblast cells.²⁰ The study, however, did not look into what concentration of silver was being released into culture. A more recent *in vitro* study mixed PMMA bone cement with nanosilver particles at a ratio of 4000 µg/g, which roughly translates to 0.4% by weight. The authors also showed very slight decreases in viability due to the presence of silver, no significant inhibition of osteogenic activity and no abnormal changes in morphology of human mesenchymal cells. The authors also, however, did not discuss or show how much silver was exactly eluting from the bone cement in the tested time frame of 24 hrs.²¹ Unlike the two studies described above, the present study did not use 1% silver by weight, instead the amount of silver was increased to 3% by weight (Table 1). In our case the thin films were orders of magnitude thinner than the molded bone cement structures used in the studies described above with thicknesses of several mm. Therefore, it was important for our study to report the amount of silver that leaches out, as opposed to simply stating the weight % of silver placed into a composite material. The combination of nanosilver and PMMA has been used in bone cements, but pulsed laser deposited PMMA/Ag composite thin films are completely novel. Due to the favorable properties of PMMA and the antimicrobial efficacy of silver, these coatings have potential use beyond orthopedics. The process described in this study is highly controlled and

performed at room temperature, which allows it to be used on a large number of different medical materials and devices. The PMMA and silver targets are ablated directly and simultaneously, eliminating any mixing steps that exposes a device surface to potentially harmful MMA monomer, excessive heating and incomplete adhesion. As seen in Figure 1, the deposition character of PLD PMMA is very uniform and although the layer is not completely flat from the cross section view in Figure 2, there are no visible defects under SEM. The nature of pulsed laser deposition creates high energy species in the plume which tend to undergo chemical reactions with the substrate upon deposition, creating a highly adherent coating. This was qualitatively examined in the study, after handling the samples during the experiments, the PMMA coating was observed to be completely intact with no change in texture or color. This observation suggested that only the silver was released and the majority of PMMA was not detaching. The addition of silver coatings with PMMA may not only prevent bacterial growth in a biological environment, but may also likely decrease the chance for contamination during handling and storage of the coated materials.

It is possible to control the morphology of PMMA thin films by altering several deposition parameters during PLD.¹⁷ In the present study silver release into solution was modulated by total silver content (through layer thickness), with the thicker layers deposited with 14,000 and 20,000 pulses eluting more silver into solution than the 10,000 pulse thin films (Figure 4). This result showed that the amount of silver deposited was proportional to the amount of laser pulses applied to the target. In the future it will be possible to examine modifying deposition parameters and the morphology of PMMA to control the rate of release of Ag ions as opposed to modulating the total silver amount alone.

The amount of silver in all thin films had very strong antibacterial activity as evidenced by the results in Figure 5. The 14,000 and 20,000 pulse films released 0.8 and 1.0 $\mu\text{g}/\text{mL}$ silver into solution, respectively, which killed nearly all *E. coli* bacteria under dynamic conditions. The bacterial solution incubated with 10,000 pulse PMMA/Ag films was the only sample that showed noticeable colony formation with 34 colonies, which accounted for about 1% of colonies formed in materials without silver. Only the 10,000 pulse films that released 0.8 $\mu\text{g}/\text{mL}$ silver into solution showed minimal cytotoxicity with bone marrow stromal cells (Figure 6), suggesting that increasing a dose of silver above this threshold can induce toxicity as evidenced by the higher pulse number thin films. Toxicological studies of silver nanoparticles in solution generally find significant cytotoxic response above concentrations of 5 $\mu\text{g}/\text{mL}$ in different cell lines,²²⁻²⁴ which was not tested in this study due to the clear toxicity at a lower threshold. For example, in HT-1080 and A431 cells the IC_{50} (half maximal inhibitory concentration) was determined to be 10.6 and 11.6 $\mu\text{g}/\text{mL}$, respectively. When the cells were challenged with half the IC_{50} , there were signs of acute toxicity, such as oxidative stress, decreased GSH, increased lipid peroxidation and others.²⁵ Our results may suggest that bone marrow stromal cells have more sensitivity towards dissolved silver toxicity.

Conclusions:

Our study showed that with the use of pulsed laser deposition, it is possible to create a durable PMMA/Ag composite thin film with a custom amount of silver. The concentration of silver leaching out of the thin films can be modulated by altering the total pulses and, therefore, the thickness of the film. With this approach it was possible to create a thin film that has minimal cytotoxicity in hBMSCs while having considerable antimicrobial activity against *E. coli*. Future studies will look into the parameters for modifying the PMMA film to further control the release dynamics of silver ions and particulates into solution.

References:

- 1 Schwindling, F. S., Bömicke, W., Hassel, A. J., Rammelsberg, P. & Stober, T. Randomized clinical evaluation of a light-cured base material for complete dentures. *Clin. Oral Investig.* **18**, 1457-1465 (2014).
- 2 Jagger, R. G., al-Athel, M. S., Jagger, D. C. & Vowles, R. W. Some variables influencing the bond strength between PMMA and a silicone denture lining material. *The International journal of prosthodontics* **15**, 55-58 (2001).
- 3 Ram, J., Jain, V. K., Agarwal, A. & Kumar, J. Hydrophobic acrylic versus polymethyl methacrylate intraocular lens implantation following cataract surgery in the first year of life. *Graefes Arch. Clin. Exp. Ophthalmol.* **252**, 1443-1449 (2014).
- 4 Yang, W.-H., Smolen, V. F. & Peppas, N. A. Oxygen permeability coefficients of polymers for hard and soft contact lens applications. *J. Membr. Sci.* **9**, 53-67 (1981).
- 5 Frazer, R. Q., Byron, R. T., Osborne, P. B. & West, K. P. PMMA: an essential material in medicine and dentistry. *J. Long. Term Eff. Med. Implants* **15** (2005).

- 6 Moreira-Gonzalez, A., Jackson, I. T., Miyawaki, T., Barakat, K. & DiNick, V. Clinical outcome in cranioplasty: critical review in long-term follow-up. *J. Craniofac. Surg.* **14**, 144-153 (2003).
- 7 Campoccia, D., Montanaro, L. & Arciola, C. R. The significance of infection related to orthopedic devices and issues of antibiotic resistance. *Biomaterials* **27**, 2331-2339 (2006).
- 8 Jaebon, T. Polymethylmethacrylate: properties and contemporary uses in orthopaedics. *J. Am. Acad. Orthop. Surg.* **18**, 297-305 (2010).
- 9 Tan, H., Lin, W. & Tang, T. The use of antimicrobial-impregnated PMMA to manage periprosthetic infections: controversial issues and the latest developments. *The International journal of artificial organs* **35**, 832-839 (2012).
- 10 Sawant, S. N., Selvaraj, V., Prabhawathi, V. & Doble, M. Antibiofilm properties of silver and gold incorporated PU, PCLm, PC and PMMA nanocomposites under two shear conditions. *PLoS One* **8**, e63311 (2013).
- 11 Darouiche, R. O. Anti-infective efficacy of silver-coated medical prostheses. *Clin. Infect. Dis.* **29**, 1371-1377 (1999).

- 12 Borkow, G. & Gabbay, J. Putting copper into action: copper-impregnated products with potent biocidal activities. *The FASEB journal* **18**, 1728-1730 (2004).
- 13 Sánchez-Valdes, S., Ortega-Ortiz, H., Ramos-de Valle, L., Medellín-Rodríguez, F. & Guedea-Miranda, R. Mechanical and antimicrobial properties of multilayer films with a polyethylene/silver nanocomposite layer. *J. Appl. Polym. Sci.* **111**, 953-962 (2009).
- 14 Damm, C. & Münstedt, H. Kinetic aspects of the silver ion release from antimicrobial polyamide/silver nanocomposites. *Applied Physics A* **91**, 479-486 (2008).
- 15 Liu, J., Sonshine, D. A., Shervani, S. & Hurt, R. H. Controlled release of biologically active silver from nanosilver surfaces. *ACS Nano* **4**, 6903-6913 (2010).
- 16 Kong, H. & Jang, J. Antibacterial properties of novel poly (methyl methacrylate) nanofiber containing silver nanoparticles. *Langmuir* **24**, 2051-2056 (2008).
- 17 Cristescu, R. *et al.* New results in pulsed laser deposition of poly-methyl-methacrylate thin films. *Appl. Surf. Sci.* **208**, 645-650 (2003).
- 18 Dellasega, D. *et al.* Nanostructured high valence silver oxide produced by pulsed laser deposition. *Appl. Surf. Sci.* **255**, 5248-5251 (2009).

- 19 Gittard, S. *et al.* Pulsed laser deposition of antimicrobial silver coating on Ormocer® microneedles. *Biofabrication* **1**, 041001 (2009).
- 20 Alt, V. *et al.* An in vitro assessment of the antibacterial properties and cytotoxicity of nanoparticulate silver bone cement. *Biomaterials* **25**, 4383-4391 (2004).
- 21 Pauksch, L., Hartmann, S., Szalay, G., Alt, V. & Lips, K. S. In Vitro Assessment of Nanosilver-Functionalized PMMA Bone Cement on Primary Human Mesenchymal Stem Cells and Osteoblasts. *PLoS One* **9**, e114740 (2014).
- 22 Samberg, M. E., Oldenburg, S. J. & Monteiro-Riviere, N. A. Evaluation of silver nanoparticle toxicity in skin in vivo and keratinocytes in vitro. *Environmental health perspectives (Online)* **118**, 407 (2010).
- 23 Braydich-Stolle, L., Hussain, S., Schlager, J. J. & Hofmann, M.-C. In vitro cytotoxicity of nanoparticles in mammalian germline stem cells. *Toxicol Sci* **88**, 412-419 (2005).
- 24 Hussain, S., Hess, K., Gearhart, J., Geiss, K. & Schlager, J. In vitro toxicity of nanoparticles in BRL 3A rat liver cells. *Toxicol In Vitro* **19**, 975-983 (2005).

- 25 Arora, S., Jain, J., Rajwade, J. & Paknikar, K. Cellular responses induced by silver nanoparticles: in vitro studies. *Toxicol. Lett.* **179**, 93-100 (2008).

CHAPTER 4: Cytotoxicity of cultured macrophages exposed to antimicrobial zinc oxide (ZnO) coatings on nanoporous aluminum oxide membranes

Authors: Peter E. Petrochenko,^{1,2} Shelby A. Skoog,^{1,2} Qin Zhang,¹ David J. Comstock,³ Jeffrey W. Elam,³ Peter L. Goering,¹ Roger J. Narayan²

¹Division of Biology, Office of Science and Engineering Laboratories, Center for Devices and Radiological Health, U.S. Food and Drug Administration, Silver Spring, MD 20993

²Joint Department of Biomedical Engineering, UNC – Chapel Hill and North Carolina State University, Raleigh, NC 27965

³Energy Systems Division, Argonne National Laboratory, Argonne, IL 60439

Note:

The mention of commercial products, their sources, or their use in connection with material reported herein is not to be construed as either an actual or implied endorsement of such products by the Department of Health and Human Services.

Abstract:

Zinc oxide (ZnO) is a widely used commercial material that is finding use in wound healing applications due to its antimicrobial properties. Our study demonstrates a novel approach for coating ZnO with precise thickness control onto 20 nm and 100 nm pore diameter anodized aluminum oxide using atomic layer deposition (ALD). ZnO was deposited throughout the nanoporous structure of the anodized aluminum oxide membranes. An 8 nm-thick coating of ZnO, previously noted to have antimicrobial properties, was cytotoxic to cultured macrophages. After 48 hours, ZnO-coated 20 nm and 100 nm pore anodized aluminum oxide significantly decreased cell viability by $\approx 65\%$ and 54% , respectively, compared to cells grown on uncoated anodized aluminum oxide membranes and cells grown on tissue culture plates. Pore diameter (20-200 nm) did not influence cell viability.

Keywords: Anodic aluminum oxide, atomic layer deposition, nanoporous materials, zinc oxide, macrophage, cytotoxicity, reactive oxygen species (ROS).

Introduction:

Zinc oxide (ZnO) is a widely utilized commercial material that has recently garnered interest by medical and nanotechnology researchers due to its considerable antimicrobial¹ and UV protection properties.² In a review by Lansdown *et al.*, the authors emphasize the importance of numerous Zn materials that have good clinical evidence showing improved wound healing, anti-infective activity, and higher epithelialization rates.³ A number of commercial materials use ZnO as an active component, such as bandages, stockings, and occlusive adhesive dressings.³ Nanoscale forms of ZnO have been considered for use in nontoxic antimicrobial wound dressings.⁴ In addition, discrete ZnO nanoparticles have been shown to exhibit strong antimicrobial activity against Gram-positive bacteria^{5,6} as well as some preferential toxicity towards cancerous human myeloblastic leukemia cells (HL60) when compared to normal peripheral blood mononuclear cells.⁶ There could be several reasons for preferential cell toxicity; one potential mechanism for this behavior (e.g., for ZnO nanoparticle toxicity) may involve the generation of reactive oxygen species (ROS).⁶ ROS generation, however, is generally assumed to occur after cellular uptake of Zn ions.⁷ ZnO nanoparticles themselves produce little ROS but generate dissolved Zn²⁺ ions, which then enter the cell and cause production of intracellular ROS.⁷

Both ionic Zn and ZnO nanomaterials have been shown to decrease cell viability in various mammalian cell lines. Specific cells of the immune system, for example, respond differently to ZnO nanomaterials. For example, monocyte-derived dendritic cells exhibit a dose-dependent cytotoxic response and increase in the activity of caspases, enzymes which are involved in apoptotic cell death; however, peripheral blood mononuclear cells are not

affected.⁸ At sub-cytotoxic concentrations, ZnO may modulate immune responses in some immune cell types but not others.⁸ In general, the mode of toxicity for ZnO nanomaterials is thought to involve free Zn ions and likely follows a classical dose and time-dependent response for intracellular ROS production and cytotoxicity.⁹

ZnO has been shown to be toxic *in vivo* via certain routes of exposure. For example, ZnO nanoparticles were noted to be more toxic to the lungs than the equivalent dose in ionic (ZnCl₂) form following intratracheal instillation.¹⁰ The particles are thought to be trapped in the lung and continuously release Zn ions that cause toxicity; however, the ionic solution is cleared more easily.¹⁰ When incorporated into hydrogel wound dressing bandages, ZnO nanomaterials impart improved healing and antimicrobial activity.¹¹ Nano-scale ZnO shows good *in vivo* outcomes in skin applications such as sunscreens and cosmetics, where it has limited penetration into skin layers and little or no effect on skin cell morphology, metabolism, or oxidation.¹²

When compared to discrete nanoparticles, very little toxicology literature is available on nanotextured surfaces.¹³ Similar features are present in discrete nanoparticles and on nanotextured surfaces, namely the increased surface area and high radius of curvature inherent to nanoscale features. ZnO can be coated onto nanotextured surfaces without disrupting the underlying surface morphology using a thin film growth process known as atomic layer deposition (ALD). A ZnO-coated nanotextured surface will have a greater surface area for cell interactions than a smooth surface¹⁴; as such, the ZnO-coated nanotextured surface may exhibit a higher rate of Zn ion dissolution. Skoog et al. previously demonstrated that ZnO-coated anodized aluminum oxide membranes exhibit antimicrobial

activity against several bacterial strains associated with skin infection; significant activity against Gram-positive bacteria was noted.¹⁵ They showed that ZnO coatings deposited using ALD leach Zn ions *in vitro*. The extract from the ZnO-coated 20 nm and 100 nm anodized aluminum oxide membranes contained zinc at a concentration of approximately 90 µg/ml.¹⁶ This study raised the question about the cytotoxic potential of the released Zn ions to eukaryotic cells. The objective of the present study was to evaluate macrophage responses (e.g., cytotoxicity and ROS production) of an ALD-grown ZnO coating on a nanoporous anodized aluminum oxide substrate. The underlying inert substrate used in the study was anodized aluminum oxide, which is known to have good cell adhesion and proliferation *in vitro* compared to a standard tissue culture well. Hoess et al. showed that cells interact with 200 nm pores and thus may respond differently to varying pore diameters.¹⁶ Ferraz et al. indicated that differences in nanoporosity elicited different immune responses for 20 and 200 nm diameter nanoporous anodized aluminum oxide *in vivo*.¹⁷ In this study, cellular responses to ZnO-coated and uncoated 20 nm and 100 nm anodized aluminum oxide membranes were evaluated using the MTT cell viability assay and the ROS production assay.

Materials and Methods:

ZnO Deposition:

Anodized aluminum oxide membranes with 20 nm pores and 100 nm pores were acquired from a commercial source (General Electric Healthcare, Maidstone, United Kingdom). These membranes exhibited outside diameters of 13 mm and thicknesses of 60 μm . The 20 nm pore size nanoporous anodized aluminum oxide membranes exhibited pore diameters of 200 nm for $\sim 58 \mu\text{m}$ of the 60 μm thickness and exhibited pore diameters of 20 nm for $\sim 2 \mu\text{m}$ of the 60 μm thickness. The 100 nm pore size nanoporous anodized aluminum oxide membranes exhibited pore diameters of 200 nm for $\sim 58 \mu\text{m}$ of the 60 μm thickness and pore diameters of 100 nm for $\sim 2 \mu\text{m}$ of the 60 μm thickness. The ZnO ALD was conducted at a pressure of ~ 1 Torr using 360 sccm carrier gas flow of ultrahigh purity N_2 in a custom viscous flow reactor. Prior to deposition, the nanoporous anodized aluminum oxide membranes were cleaned *in situ* by flowing ozone, which was generated by flowing 400 sccm ultrahigh purity O_2 through a commercial ozone generator for five minutes at a temperature of 200°C . The ozone concentration generated using this approach was $\sim 10\%$ and the ozone partial pressure was ~ 0.1 Torr. ZnO was deposited on the surfaces of the membranes by iteratively exposing the membranes to diethylzinc (Sigma Aldrich, St. Louis, MO) and water vapors at a deposition temperature of 200°C . For each precursor, a six second exposure at a partial pressure of ~ 0.2 Torr was followed by a five second N_2 purge. The anodized aluminum oxide membranes were coated with 8 nm ZnO as determined by ellipsometry on Si(100) witness samples, which were concurrently coated with the nanoporous anodized aluminum oxide membranes.

Scanning electron microscopy:

Scanning electron microscopy (SEM) was performed using a JEOL 6400 cold field emission scanning electron microscope (JEOL, Tokyo, Japan). Energy dispersive X-ray spectroscopy (EDX) was performed in order to confirm the elemental composition of the surface. The SEM was equipped with an energy dispersive X-ray spectrometer attachment with a Link Pentafet detector (Link Analytical, Redwood City, CA) and a 4Pi Universal Spectral Engine pulse processor (4Pi Analytical, Hillsborough, NC). An accelerated voltage of 20 keV was used in this study.

MTT cell viability assay:

The annealed ZnO-coated nanoporous anodized aluminum oxide membranes and uncoated nanoporous anodized aluminum oxide membranes were assayed for potential cytotoxicity using the MTT (3-[4,5-dimethyl-2-thiazol]-2,5-diphenyl-2H-tetrazolium bromide) assay (CellTiter 96[®] non-radioactive cell proliferation assay) from a commercial source (Promega, Madison, WI). Membranes were sterilized with ultraviolet light (UVP CL-1000, Upland, CA). All membranes were exposed for two hours on each side and rotated 90° every 60 minutes to ensure complete sterilization. Upon completion of ultraviolet sterilization, the membranes were placed in 24-well plates. RAW 264.7 cells (mouse leukemic monocyte macrophage cell line), which were obtained from a commercial source (ATCC, Manassas, VA), were added to the 24-well plates at a cell density of 2×10^5 cells/mL in Dulbecco's Modified Eagle Medium (DMEM). All of the 24-well plates were incubated for either 24 hours or 48 hours. Following incubation, the membranes were moved to a new 24-well plate

so that assays were conducted on cells grown only on the membranes and not in the non-membrane areas of the wells. The new wells contained 0.5 mL MTT-DMEM for macrophages. MTT-DMEM was prepared by adding MTT dye solution:medium at a 15:100 ratio as specified by the kit. A 75 μ l aliquot of MTT dye was added to each well in order to obtain a total volume of 0.5 ml. The plates were then incubated under cell culture conditions for 3 hours. After each incubation period, the solubilization solution/stop mix was added and the plates were incubated again for 1 hour at 37°C and 5% CO₂. The wells were then mixed and the contents transferred to duplicate wells in a 96-well plate for absorbance measurements. Absorbance was measured at $\lambda = 570$ nm (reference wavelength 650 nm) using a 96-well OPTIMax plate reader (Molecular Devices, Sunnyvale, CA). Cells spiked with 5% and 10% dimethyl sulfoxide (DMSO) served as a positive control for the MTT assay. The data were normalized to the uncoated nanoporous anodized aluminum oxide membrane and were expressed as percent viability.

Reactive oxygen species (ROS) production assay:

To investigate oxidative stress, the generation of intracellular ROS was measured by the increasing fluorescence of 2',7'-dichlorofluorescein (DCF). The cell-permeable 2',7'-dichlorodihydrofluorescein (DCF-DA) is oxidized by intracellular reactive oxygen species to the highly fluorescent dichlorofluorescein (DCF). Cells with a density of 2×10^5 cells/mL (2×10^4 cells/well) were cultured in DMEM within a standard transparent 96-well plate overnight. After cells were washed twice with HBSS to remove culture medium, 5 mM DCF-DA in HBSS was added to all of the wells and the plate was incubated at 37° C for 30

minutes. After incubation, the DCF-DA reagent was removed and the cells were washed twice with HBSS. Different concentrations of ZnO extracts in 100 μ l aliquots of culture medium were added to each well. Cells were treated with 200 μ M hydrogen peroxide (H_2O_2) as a positive control. Different concentrations of extracts alone served as controls and were run in parallel to determine if there was any interference with the assay. DCF fluorescence was monitored after various treatments from 30 minutes to 24 hours at excitation of 480 nm and emission of 530 nm using a fluorescence plate reader (Molecular Devices, CA, USA). Extracts were collected by placing sterilized filters into 24-well plates and incubating in 1 ml DMEM media at 37 °C and 5% CO_2 . Wells with media but without membranes served as control extracts. Media was then removed after 24 or 48 hours and was used for further studies. ROS generation was obtained by measuring cells exposed to surface media extracts as opposed to measuring cells directly grown on various surfaces; this approach was utilized in order to see if particulate or ionic leaching was the mode of toxicity as opposed to direct contact between the cells and the surface.

Statistical analysis:

The results from each data set were analyzed with Prism 4 statistical software (GraphPad Inc., La Jolla, CA). The results were expressed as mean \pm standard deviation. Statistical differences between the control and treated group were assessed using a one-way ANOVA with a Bonferroni *post hoc* test. Each experiment was repeated at least three times with each sample assayed in duplicate. A *P* value of less than 0.05 was considered to be statistically significant. For MTT the data were normalized to cells grown in a standard tissue culture

well and the results were expressed as percent viability. Significance level notation was expressed as * for $P < 0.05$, ** for $P < 0.01$, and *** for $P < 0.001$.

Results:

Surface characterization:

Scanning electron microscopy was performed to examine the morphologies of the coated and uncoated nanoporous anodized aluminum oxide membranes. All of the membranes had one side with circular 200 nm diameter pores (designated as Side A (Figures 1A and 1B)), which narrowed to either 20 nm or 100 nm diameter branched pores on the other side (designated as Side B). Side B scanning electron micrographs for the 100 nm uncoated and ZnO-coated nanoporous anodized aluminum oxide membranes are shown in Figures 1C and 1D. Figures 1B and 1D are representative SEM images of the coated membranes; artifacts resulting from the deposition process were noted on the surfaces of the coated membranes.

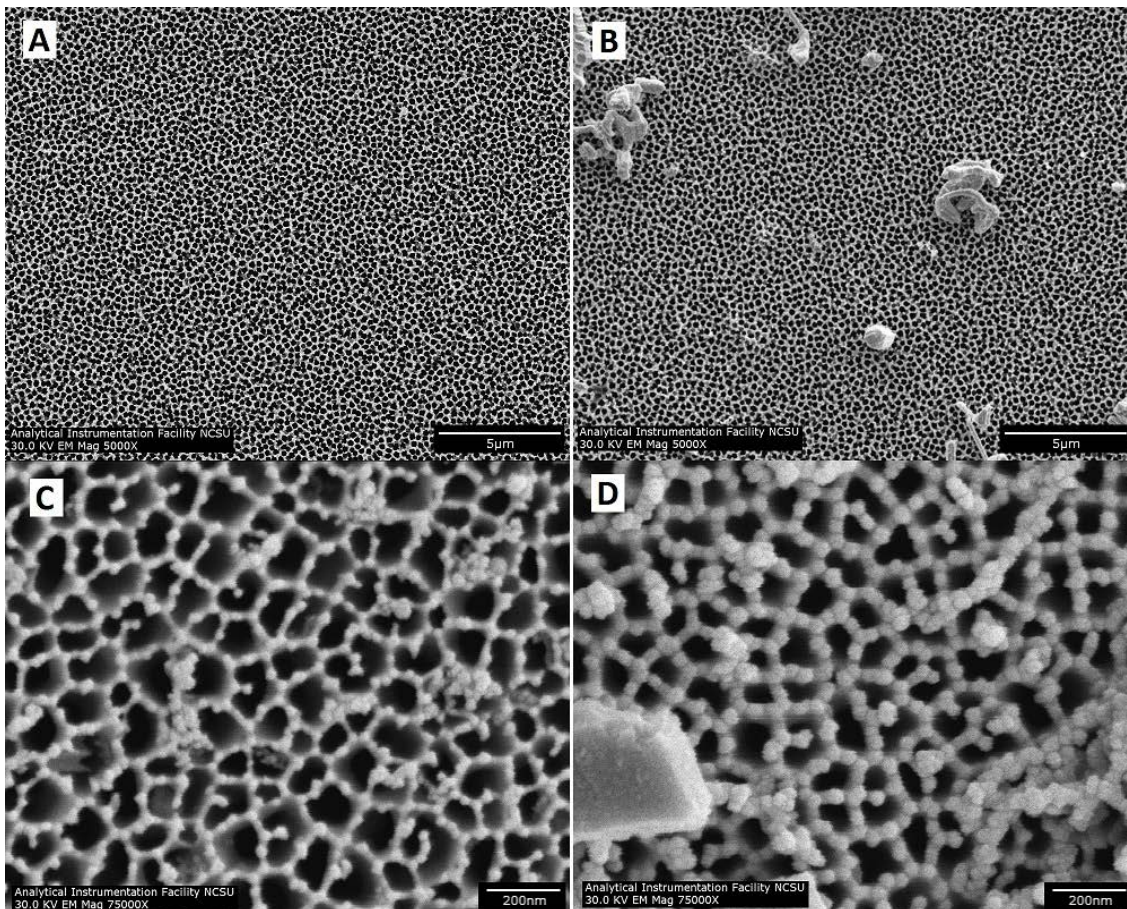


Figure 1. SEM images of both sides of a 100 nm anodized aluminum oxide membrane. **A:** Side A of an uncoated anodized aluminum oxide membrane, showing 200 nm circular pores. **B:** Side A of an 8 nm ZnO-coated anodized aluminum oxide membrane, showing 200 nm circular pores. **C:** Side B of an uncoated anodized aluminum oxide membrane, showing 100 nm branching pores. **D:** Side B of an 8 nm ZnO-coated anodized aluminum oxide membrane, showing 100 nm branching pores.

The deposition artifacts were noticeable in images that were obtained from cleaved cross-sectional specimens (Figure 2A). The majority of the coated membrane surface was free of these artifacts. The pores were noted to continue from one side of the membrane to the other. To determine whether the ALD precursors penetrated through the entire membrane, EDX elemental analysis was used to evaluate Side A, Side B, and the center of the membrane; as noted in the red text of Figure 2A, ZnO was shown to be present in each of these three regions of the nanoporous structure (shown). Figure 2B shows a representative EDX spectrum of the 200 nm pore side (Side A) of a ZnO-coated nanoporous anodized aluminum oxide membrane. Prominent Zn and Al peaks were noted on spectra that were obtained throughout the membrane.

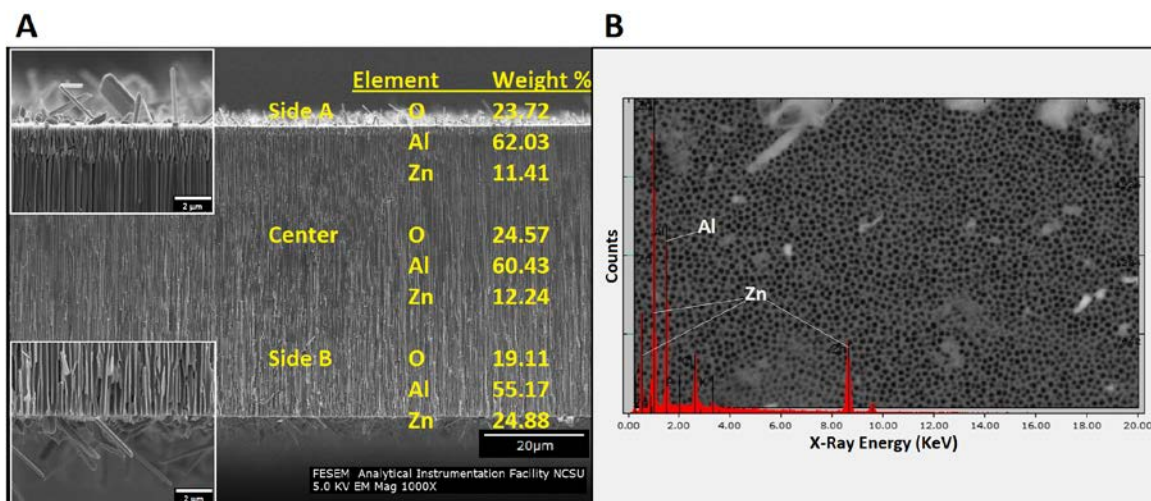


Figure 2. Cross-sectional SEM and elemental analysis of a 20 nm nanoporous anodized aluminum oxide with an 8 nm ZnO coating. **A:** Cross-sectional view of the membrane, showing the crystals present on the surface. **B:** EDX spectrum obtained from the 200 nm circular pore side, showing Al and Zn peaks (Side B).

Cell responses:

No significant differences were noted in cell viability (MTT assay) after 24 hour exposure to any coated or uncoated membrane (Figure 3). The ZnO-coated nanoporous membranes trended towards lower viability values; however, the differences with tissue culture polystyrene plate controls (TCPS) after 24 hours were not statistically significant. Cells exposed to ZnO-coated 20 nm anodized aluminum oxide showed decreased viability; for example, viability of cells exposed to ZnO-coated anodized aluminum oxide was

approximately 32% lower than that of cells grown in culture wells. Viability of cells grown on ZnO-coated 100 nm anodized aluminum oxide was approximately 36% lower than that of cells grown in culture wells. After 48 hours, cell viability for both ZnO-coated 20 nm anodized aluminum oxide and ZnO-coated 100 nm anodized aluminum oxide was significantly lower ($p < 0.01$) than for the corresponding uncoated controls and tissue culture controls. Cell viability for ZnO-coated 20 nm anodized aluminum oxide decreased by approximately 65% and ZnO-coated 100 nm anodized aluminum oxide decreased by approximately 54% from controls. Pore diameter did not appear to influence cell viability for coated or uncoated membranes. There were no differences among cell viability for 10, 100, or 200 nm pore diameter membranes after both 24 and 48 hours (the data for the 200 nm pore surface not included on MTT figure). Moreover, the anodized aluminum oxide substrates themselves did not affect cell viability.

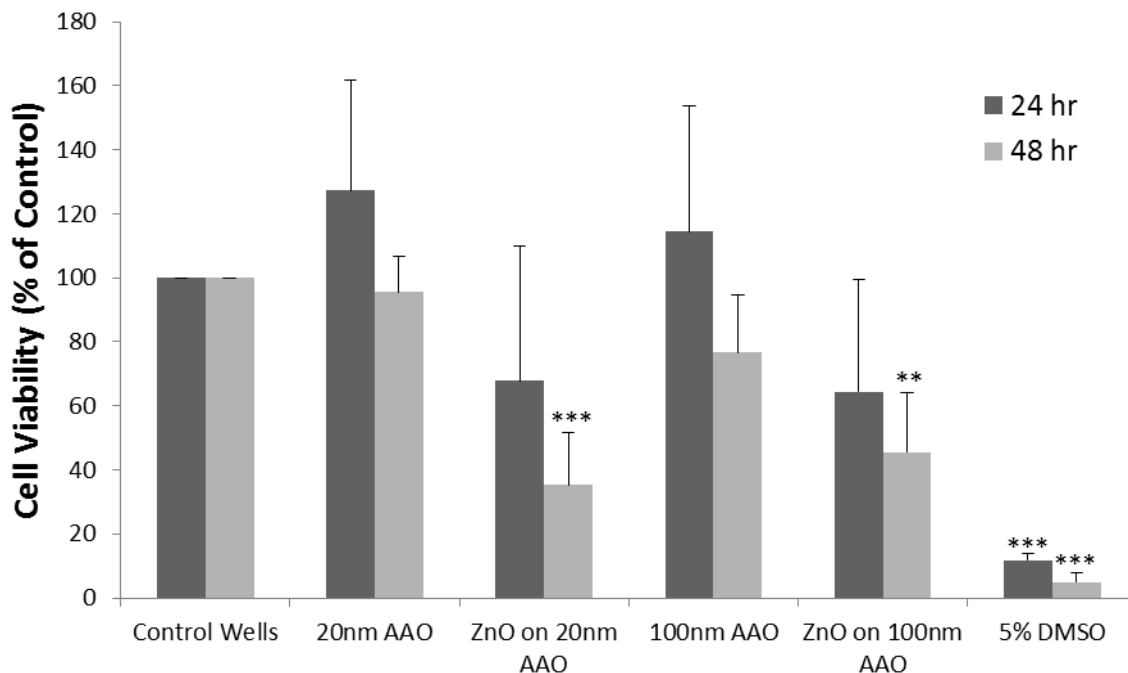


Figure 3. Cell viability (MTT assay) in macrophages cultured on nanoporous uncoated anodized aluminum oxide membranes and nanoporous Zn-coated anodized aluminum oxide membranes. No statistical differences are present at 24 hours. After 48 hours, cells cultured on both 20 and 100 nm ZnO-coated anodized aluminum oxide membranes showed a reduction in cell viability compared with cells cultured on corresponding uncoated anodized aluminum oxide membranes and cells grown on standard tissue culture wells. Statistical significance * $p < 0.001$, ** $p < 0.01$ from cell and media only control.**

Production of intracellular ROS was monitored from 1 to 24 hours after treatment using extracts collected from incubating ZnO-coated membranes for 24 hours (Figure 4). No

significant increases in ROS production were found between any groups at each time point. The H₂O₂ positive control induced a very strong response from the cells; in addition, no interference with the dye was observed.

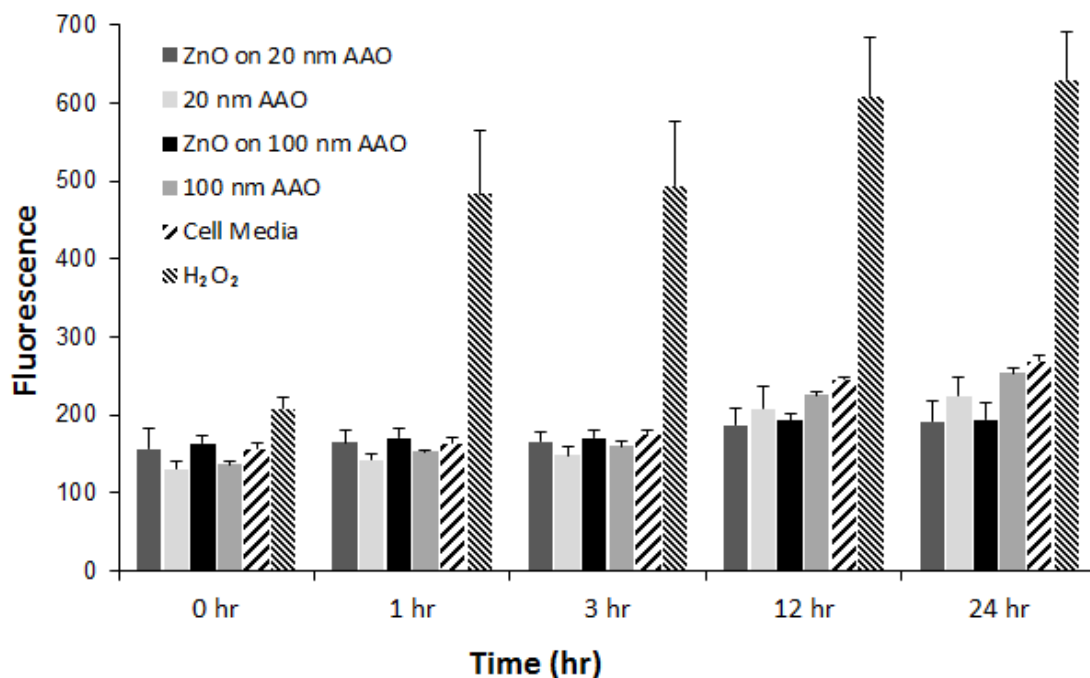


Figure 4. ROS production in macrophages treated with 24-hour extracts from ZnO-coated membranes over 1 hour, 3 hours, 12 hours, and 24 hours. Cells were treated with H₂O₂ as a positive control. All experimental groups, including ZnO-coated and uncoated anodized aluminum oxide, had similar responses to cells grown with fresh media, indicating no significant ROS generation for any surface extract.

Discussion:

Several techniques are available for depositing ZnO coatings onto anodized aluminum oxide membranes, including pulsed laser deposition (PLD),¹⁸ ion beam sputtering,¹⁹ plasma chemical vapor deposition (CVD),²⁰ and spin coating.²¹ ALD has previously been used to deposit nanometer-thick coatings of ZnO on polymer nanofibers with no alteration to the underlying nanofiber structure.²² Cross-sectional SEM/EDX analysis revealed a benefit of using ALD for growth of coatings on nanotextured surfaces, including nanoporous surfaces. The EDX data shown in Figure 2 B indicates that ZnO was deposited throughout the surfaces of the nanoscale pores. The main benefit of ALD is its ability to deposit conformal thin films over complex surface topographies. ALD is also particularly well suited for coating nanoporous anodized aluminum oxide materials and other materials with interconnected pores, which may be difficult to coat by means of other techniques.

In previous work, Palomaki et al. showed that ZnO nanoparticles elicited concentration-dependent cytotoxicity in RAW 264.7 macrophages.²³ The present study was aimed to determine whether cell viability can be affected by atomic layer deposition-grown coatings on nanoporous ZnO surfaces instead of by free ZnO nanoparticles. Previous studies have indicated that the pore size of nanoporous anodized aluminum oxide membranes and coated membranes does not have a significant effect on cell viability.²⁴ As noted in the introduction, our group quantified Zn ion release from 20 nm and 100 nm anodized aluminum oxide membranes with atomic layer-deposition grown 8 nm-thick ZnO coatings into DMEM culture media containing 10% fetal bovine serum by means of inductively coupled plasma mass spectrometry.¹⁶ This study confirms that varying the pore size between

20 nm and 200 nm does not alter cell viability as measured by the MTT assay. Atomic layer deposition enables the amount of coating material that is deposited on the surface and subsequently released during use to be readily controlled. This attribute of atomic layer deposition is beneficial for coating medical devices with materials such as silver or zinc oxide, which are thought to produce antimicrobial activity through ionic interactions.^{25,26}

The commercially-available nanoporous anodized aluminum oxide samples used in this study are anisotropic; one side contains isolated, circular pores with a diameter of ~200 nm (Figure 1 A and B) and the other side contains a “branchlike” structure in which the pore diameter is ~20 or ~100 nm (Figure 1 C and D). Some particles were noted on the surface of the 8 nm thick ZnO coating (Figures 1 and 2). The particles may be attributed to the formation of ZnO crystals due to insufficient precursor purging between exposures or contamination by adventitious dust particles. It should be noted that the majority of the surface area of the coating membrane was free of these particles (Figure 1 B). The EDX elemental analysis showed Zn and Al peaks, which are attributed to the 8 nm thick ZnO coating and the underlying aluminum oxide substrate.

The ZnO-coated membranes examined in this study were previously shown to possess antibacterial activity;¹⁶ however, the cytotoxicity of these materials was not previously examined. It is evident from the MTT cell viability assay results that the ZnO-coated membranes are cytotoxic to macrophages after 48 hours of incubation. No cytotoxicity was evident after 24 hours, which suggests that there is a gradual release of Zn ions into the media over time. In addition, the data suggests that the effect of Zn ions on macrophages may be time-dependent. Zn ions are known to be toxic to a variety of cell

types.²⁷ Many studies measure administration of a single bolus dose; toxicity results may differ if an identical dose is gradually administered over a period of time.

Cell culture methods also apparently have an effect on cell responses to ZnO; for example, keeping cell number and Zn concentration constant, more densely packed monolayers have higher resistance to Zn toxicity than an identical number of cells located further apart from one other.²⁸ The observed relationship between toxicity and seeding density is not fully understood and could occur due to differences in cellular function between isolated cells and cell assemblages. In the present study, cells are dispersed on the surfaces so that they are not directly touching each other, which could potentially make them slightly more susceptible to Zn ion toxicity.

Ionic zinc is known to modulate immune response from monocytes by suppressing TNF-alpha transcription and secretion.²⁹ For example, Grandjean-Laquerriere et al. showed that zinc decreases TNF-alpha production by unstimulated human monocytes.³⁰ Several previous studies have indicated that Zn prevents free radical generation and oxidative stress. In a rat model, Zn has been shown to decrease carbon tetrachloride-induced liver damage³¹ from reactive free radical metabolites and reduce the toxicity of cadmium,³² a known carcinogen. In mice, oral Zn administration decreased alcohol-induced liver damage³³ and toxicity from whole body radiation.³⁴ Rostan *et al.* considered the role of Zn as an antioxidant and discussed mechanisms in which redox stable Zn may replace redox reactive metals such as iron and copper as well as function as a sacrificial site for oxidant attacks.³⁵ It should be noted that the amount of Zn ions in the extract may have not been sufficient to result in measureable production of ROS. Since the ZnO surfaces were toxic only after 48

hours, it is possible that the amount of Zn that had leached out after 24 hours was not sufficient to cause measureable production of ROS.

Conclusion:

In summary, ZnO-coated nanoporous anodized aluminum oxide membranes were shown to produce significant cytotoxicity after 48 hours in macrophages, a common cell type involved in wound repair. It is possible to readily alter the thickness of a ZnO coating that is grown on a surface by means of ALD. Further studies are necessary to determine the optimal thickness of a ZnO coating on nanoporous surfaces that will produce an antimicrobial effect while minimizing cytotoxicity. Although the ZnO-coated membranes were noted to be cytotoxic (MTT assay) after 48 hours, no statistically significant toxicity or ROS production was observed after 24 hours. An exposure time longer than 24 hours appears to be necessary to leach a sufficient amount of Zn ions into media in order to produce an adverse cell response. A threshold Zn ion concentration for ROS generation and reduction in macrophage viability may exist, which was not reached after a 24 hour exposure but was reached after additional exposure.

Acknowledgments and Support:

Peter E. Petrochenko is supported in part by a NSF Award #1041375. Argonne is a U.S. Department of Energy Office of Science laboratory and is operated under Contract No. DE-AC02-06CH11357.

References:

- 1 Leung, Y. H. *et al.* Antibacterial activity of ZnO nanoparticles with a modified surface under ambient illumination. *Nanotechnology* **23**, doi:10.1088/0957-4484/23/47/475703 (2012).
- 2 Abd El-Hady, M. M., Farouk, A. & Sharaf, S. Flame retardancy and UV protection of cotton based fabrics using nano ZnO and polycarboxylic acids. *Carbohydr. Polym.* **92**, 400-406, doi:10.1016/j.carbpol.2012.08.085 (2013).
- 3 Lansdown, A. B. G., Mirastschijski, U., Stubbs, N., Scanlon, E. & Agren, M. S. Zinc in wound healing: Theoretical, experimental, and clinical aspects. *Wound Repair Regen* **15**, 2-16, doi:10.1111/j.1524-475X.2006.00179.x (2007).
- 4 Kumar, P. T. S., Lakshmanan, V. K., Biswas, R., Nair, S. V. & Jayakumar, R. Synthesis and Biological Evaluation of Chitin Hydrogel/Nano ZnO Composite Bandage as Antibacterial Wound Dressing. *J. Biomed. Nanotechnol.* **8**, 891-900, doi:10.1166/jbn.2012.1461 (2012).
- 5 Santimano, M. C. & Kowshik, M. Altered growth and enzyme expression profile of ZnO nanoparticles exposed non-target environmentally beneficial bacteria. *Environ. Monit. Assess.* **185**, 7205-7214 (2013).

- 6 Premanathan, M., Karthikeyan, K., Jeyasubramanian, K. & Manivannan, G. Selective toxicity of ZnO nanoparticles toward Gram-positive bacteria and cancer cells by apoptosis through lipid peroxidation. *Nanomedicine-Nanotechnology Biology and Medicine* **7**, 184-192, doi:10.1016/j.nano.2010.10.001 (2011).
- 7 Song, W. H. *et al.* Role of the dissolved zinc ion and reactive oxygen species in cytotoxicity of ZnO nanoparticles. *Toxicol. Lett.* **199**, 389-397, doi:10.1016/j.toxlet.2010.10.003 (2010).
- 8 Andersson-Willman, B. *et al.* Effects of subtoxic concentrations of TiO₂ and ZnO nanoparticles on human lymphocytes, dendritic cells and exosome production. *Toxicol Appl Pharmacol* **264**, 94-103, doi:10.1016/j.taap.2012.07.021 (2012).
- 9 Kim, Y. H. *et al.* Alveolar Epithelial Cell Injury Due to Zinc Oxide Nanoparticle Exposure. *Am. J. Respir. Crit. Care Med.* **182**, 1398-1409, doi:10.1164/rccm.201002-0185OC (2010).
- 10 Fukui, H. *et al.* Association of zinc ion release and oxidative stress induced by intratracheal instillation of ZnO nanoparticles to rat lung. *Chem. Biol. Interact.* **198**, 29-37, doi:10.1016/j.cbi.2012.04.007 (2012).

- 11 Kumar, P. T. S. *et al.* Flexible and Microporous Chitosan Hydrogel/Nano ZnO Composite Bandages for Wound Dressing: In Vitro and In Vivo Evaluation. *ACS Applied Materials & Interfaces* **4**, 2618-2629, doi:10.1021/am300292v (2012).
- 12 Leite-Silva, V. R. *et al.* The effect of formulation on the penetration of coated and uncoated zinc oxide nanoparticles into the viable epidermis of human skin in vivo. *Eur. J. Pharm. Biopharm.* **84**, 297-308 (2013).
- 13 Ostrowski, A. D., Martin, T., Conti, J., Hurt, I. & Harthorn, B. H. Nanotoxicology: characterizing the scientific literature, 2000-2007. *Journal of Nanoparticle Research* **11**, 251-257, doi:10.1007/s11051-008-9579-5 (2009).
- 14 Li, T., Jia, F., Fan, Y., Ding, Z. & Yang, J. Fabrication of nanoporous thin-film working electrodes and their biosensing applications. *Biosens. Bioelectron.* **42**, 5-11 (2013).
- 15 Skoog, S. A. *et al.* Antibacterial activity of zinc oxide-coated nanoporous alumina. *Materials Science and Engineering B-Advanced Functional Solid-State Materials* **177**, 992-998, doi:10.1016/j.mseb.2012.04.024 (2012).

- 16 Hoess, A., Thormann, A., Friedmann, A. & Heilmann, A. Self-supporting nanoporous alumina membranes as substrates for hepatic cell cultures. *J. Biomed. Mater. Res. Part A* **100A**, 2230-2238, doi:10.1002/jbm.a.34158 (2012).
- 17 Ferraz, N. *et al.* Role of Alumina Nanoporosity in Acute Cell Response. *J. Nanosci. Nanotechnol.* **11**, 6698-6704, doi:10.1166/jnn.2011.4206 (2011).
- 18 Manikandan, E. *et al.* Zinc Oxide Epitaxial Thin Film Deposited Over Carbon on Various Substrate by Pulsed Laser Deposition Technique. *J. Nanosci. Nanotechnol.* **10**, 5602-5611, doi:10.1166/jnn.2010.2478 (2010).
- 19 Hsu, J. C., Lin, Y. H., Wang, P. W. & Chen, Y. Y. Spectroscopic ellipsometry studies on various zinc oxide films deposited by ion beam sputtering at room temperature. *Appl. Opt.* **51**, 1209-1215 (2012).
- 20 Pedersen, J. D., Esposito, H. J. & Teh, K. S. Direct Synthesis and Characterization of Optically Transparent Conformal Zinc Oxide Nanocrystalline Thin Films by Rapid Thermal Plasma CVD. *Nanoscale Res. Lett.* **6**, doi:10.1186/1556-276x-6-568 (2011).
- 21 Zhao, Y. L. *et al.* High-Performance Transistors Based on Zinc Tin Oxides by Single Spin-Coating Process. *Langmuir* **29**, 151-157, doi:10.1021/la304581c (2013).

- 22 Kayaci, F., Ozgit-Akgun, C., Donmez, I., Biyikli, N. & Uyar, T. Polymer-Inorganic Core-Shell Nanofibers by Electrospinning and Atomic Layer Deposition: Flexible Nylon-ZnO Core-Shell Nanofiber Mats and Their Photocatalytic Activity. *Acs Applied Materials & Interfaces* **4**, 6185-6194, doi:10.1021/am3017976 (2012).
- 23 Palomaki, J., Karisola, P., Pylkkanen, L., Savolainen, K. & Alenius, H. Engineered nanomaterials cause cytotoxicity and activation on mouse antigen presenting cells. *Toxicology* **267**, 125-131, doi:10.1016/j.tox.2009.10.034 (2010).
- 24 Walpole, A. R., Xia, Z. D., Wilson, C. W., Triffitt, J. T. & Wilshaw, P. R. A novel nano-porous alumina biomaterial with potential for loading with bioactive materials. *J. Biomed. Mater. Res. Part A* **90A**, 46-54, doi:10.1002/jbm.a.32067 (2009).
- 25 Nagy, A. *et al.* Silver nanoparticles embedded in zeolite membranes: release of silver ions and mechanism of antibacterial action. *Int. J. Nanomedicine* **6**, 1833-1852, doi:10.2147/ijn.s24019 (2011).
- 26 McDevitt, C. A. *et al.* A Molecular Mechanism for Bacterial Susceptibility to Zinc. *PLoS Pathog.* **7**, doi:10.1371/journal.ppat.1002357 (2011).

- 27 Bozym, R. A. *et al.* Free zinc ions outside a narrow concentration range are toxic to a variety of cells in vitro. *Exp. Biol. Med.* **235**, 741-750, doi:10.1258/ebm.2010.009258 (2010).
- 28 Heng, B. C. *et al.* Cytotoxicity of zinc oxide (ZnO) nanoparticles is influenced by cell density and culture format. *Arch. Toxicol.* **85**, 695-704, doi:10.1007/s00204-010-0608-7 (2011).
- 29 von Bülow, V. *et al.* Zinc-dependent suppression of TNF- α production is mediated by protein kinase A-induced inhibition of Raf-1, I κ B Kinase β , and NF- κ B. *The Journal of Immunology* **179**, 4180-4186 (2007).
- 30 Grandjean-Laquerrier, A. *et al.* Influence of the zinc concentration of sol-gel derived zinc substituted hydroxyapatite on cytokine production by human monocytes in vitro. *Biomaterials* **27**, 3195-3200, doi:10.1016/j.biomaterial.2006.01.024 (2006).
- 31 Chvapil, M., Ryan, J. N. & Peng, Y. M. Protective effect of zinc on carbon tetrachloride-induced liver injury in rats. *Exp. Mol. Pathol.* **19**, 186-196 (1973).
- 32 Waalkes, M. P. *et al.* Cadmium carcinogenesis in male Wistar [CrI:(WI) BR] rats: dose-response analysis of tumor induction in the prostate and testes and at the injection site. *Cancer Res.* **48**, 4656-4663 (1988).

- 33 Floersheim, G. L. Protection against acute ethanol toxicity in mice by zinc aspartate, glycols, levulose and pyritinol. *Agents Actions* **16**, 580-584 (1985).
- 34 Floersheim, G. & Floersheim, P. Protection against ionising radiation and synergism with thiols by zinc aspartate. *The British journal of radiology* **59**, 597-602 (1986).
- 35 Rostan, E. F., DeBuys, H. V., Madey, D. L. & Pinnell, S. R. Evidence supporting zinc as an important antioxidant for skin. *Int. J. Dermatol.* **41**, 606-611, doi:10.1046/j.1365-4362.2002.01567.x (2002).

CHAPTER 5: Nanoporous aluminum oxide membranes coated with atomic layer deposition-grown titanium dioxide for biomedical applications: An in vitro evaluation

Peter E. Petrochenko^{1, 2}, Girish Kumar¹, Wujun Fu³, Qin Zhang¹, Jiwen Zheng¹, Chengdu Liang³, Peter L. Goering¹, Roger J. Narayan^{2*}.

¹Division of Biology, Office of Science and Engineering Laboratories, Center for Devices and Radiological Health, U.S. Food and Drug Administration, Silver Spring, MD, USA 20993

² UNC/NCSU Joint Department of Biomedical Engineering, Raleigh, NC 27965-7115

³ Center for Nanophase Materials Sciences, Oak Ridge National Laboratory, Oak Ridge, TN, USA 37831

Note:

The mention of commercial products, their sources, or their use in connection with material reported herein is not to be construed as either an actual or implied endorsement of such products by the Department of Health and Human Services.

Abstract:

The surface topographies of nanoporous anodic aluminum oxide (AAO) and titanium dioxide (TiO₂) membranes have been shown to modulate cell response in orthopedic and skin wound repair applications. In this study, we: 1) demonstrate an improved atomic layer deposition (ALD) method for coating the porous structures of 20, 100, and 200 nm pore diameter AAO with nanometer-thick layers of TiO₂ and 2) evaluate the effects of uncoated AAO and TiO₂-coated AAO on cellular responses. The TiO₂ coatings were deposited on the AAO membranes without compromising the openings of the nanoscale pores. The 20 nm TiO₂-coated membranes showed the highest amount of initial protein adsorption via the micro bicinchoninic acid (micro-BCA) assay; all of the TiO₂-coated membranes showed slightly higher protein adsorption than the uncoated control materials. Cell viability, proliferation, and inflammatory responses on the TiO₂-coated AAO membranes showed no adverse outcomes. For all of the tested surfaces, normal increases in proliferation (DNA content) of L929 fibroblasts were observed from 4-72 hours. No increases in TNF-alpha production were seen in RAW 264.7 macrophages grown on TiO₂-coated AAO membranes compared to uncoated AAO membranes and tissue culture polystyrene (TCPS) surfaces. Both uncoated AAO membranes and TiO₂-coated AAO membranes showed no significant effects on cell growth and inflammatory responses. The results suggest that TiO₂-coated AAO may serve as a reasonable prototype material for the development of nanostructured wound repair devices and orthopedic implants.

Introduction:

Titanium oxide and aluminum oxide materials with nanoporous surfaces have been shown to possess better biological properties than their smooth counterparts. For example, nanoporous titanium dioxide (TiO_2) is a promising orthopedic material, which has previously been shown to enhance osteoblast attachment and proliferation.¹ Anodic aluminum oxide (AAO) membranes have been evaluated for applications in skin wound repair; the nanoporous topography of these materials was shown to modulate keratinocyte phenotype and skin wound healing.² It is possible to obtain nanoporous surfaces that may be suitable for biological applications by anodizing Al to Al_2O_3 via a two-step anodization process. It is possible to coat TiO_2 onto AAO and other nanoporous structures using atomic layer deposition (ALD); this process enables a conformal TiO_2 film of known thickness to be grown on the surface of AAO. Previous work by our group has shown that TiO_2 -coated AAO exhibits similar keratinocyte viability to uncoated AAO.³ Bulk Al_2O_3 is not a novel biomaterial. Many types of Al_2O_3 ceramics have been previously utilized as bearings in total hip replacement implants; these implants have not been associated with adverse events.^{4,5} Al_2O_3 wear particles from orthopedic implants have been shown to possess lower *in vitro* toxicity endpoints than cobalt-chromium alloy (CoCr) wear particles.⁶ Nanoporous Al_2O_3 has gained attention from the biomaterials community due to its tunable pore properties⁷ and good biocompatibility.^{8,9}

Nanoporous AAO is formed through a controllable anodization process that results in a highly dense and repeating porous structure.¹⁰ Structures containing pores with diameters between 20 to 200 nm may be generated using this process. Nanoporous Al_2O_3 has been

proposed as a coating for Ti implants. Cells have been shown to proliferate and attach via focal adhesion points to the pores in the material¹¹; in addition, the immune response has been shown to vary with pore size in *in vivo* studies.¹² ALD is a thin film deposition process that enables complex nanoporous structures such as nanoporous membranes to be conformally coated in a layer-by-layer manner with metallic or ceramic coatings; this self-limited approach provides precise control over film thickness. ALD processes commonly involve binary reactions, in which the two precursors are temporally split from one other by discrete half cycles. Purge steps are typically included after the introduction of each precursor; these steps are used to eliminate excess precursor. As supported by our previous work involving ALD growth of ZnO coatings on AAO membranes, ALD techniques are able to coat all of the exposed inner and outer surfaces of AAO in a uniform manner.⁹

Both of the base materials in this study, TiO₂ and Al₂O₃, have been previously compared in powder form in a L929 murine fibroblast cell model; in this study, TiO₂ showed higher cell proliferation.¹³ Smooth titanium surfaces also showed better results than aluminum surfaces. V79 Chinese hamster cells had increased colony formation on analogous mirror-finished flat surfaces of titanium but not on aluminum surfaces, suggesting a differential response to titanium by fibroblasts. When the same aluminum surface was acid etched to give a higher roughness value and a thicker oxide film, it exhibited good cell colony formation comparable to that of flat titanium.¹³ In another study, electrochemically anodized Ti-Al alloy showed thinner fibrous capsules *in vivo* and showed higher alkaline phosphatase (ALP) activity *in vitro*.¹⁴ Lee et al. showed that alkaline phosphatase activity by MC3T3-E1 cells seeded on oxidized titanium increased as the annealing temperature was

increased from 300 C to 750 C.¹⁵ In addition, nanostructured TiO₂ has been shown to possess antimicrobial efficacy against *Staphylococcus epidermidis*¹⁶ as well as increased osteoblast adhesion.¹⁷ Nanostructured titanium has also been shown to improve cell density over conventional titanium. In a recent study, nanostructured and conventional titanium were functionalized with fibroblast growth factor 2 (FGF-2), increasing cell density on each material. However, the cell density on conventional titanium functionalized with FGF-2 was comparable to that of non-functionalized nanostructured titanium, indicating that nanotopography had a positive effect on cell density comparable to that of FGF-2 functionalization.¹⁸ The goal of the present study was two-fold: 1) to demonstrate a method for coating the porous structure of 20, 100, and 200 nm pore diameter AAO with nanometer-thick layers of TiO₂, and 2) to compare the cellular interactions, including cytotoxicity, proliferation, and morphology, of TiO₂-coated AAO membranes and uncoated AAO membranes.

Methods:**TiO₂ Deposition:**

TiO₂ was coated onto AAO membranes by means of alternative adsorption/hydrolysis of titanium isopropoxide (TIP). The AAO membrane was pre-treated with dilute HNO₃ solution (pH = ~5-6) in order to increase the hydrophilicity. The acid-treated AAO membrane was then rinsed in alcohol and dried under vacuum. Subsequently, the treated AAO membrane was dipped in TIP solution (0.1 M TIP in alcohol) for 30 minutes. TIP molecules were chemisorbed onto the surface of AAO membrane by reacting with surface hydroxyl groups. After rinsing with alcohol and drying, the coated AAO membrane was hydrolyzed in diluted HNO₃ solution (pH~5-6) to recover the hydrophilic surface. On repetition of the above processes, 10 atomic layer coatings were performed. Finally, the coated membrane was sintered at 450 °C for 30 minutes.

Scanning Electron Microscopy/X-ray Spectroscopy:

Scanning electron microscopy (SEM) and energy-dispersive X-ray spectroscopy (EDX) were performed using a Carl Zeiss Merlin field emission scanning electron microscope (Carl Zeiss NTS, Peabody, MA); this instrument was equipped with an energy dispersive X-ray spectrometer attachment. An accelerated voltage of 20 keV was used in this study.

Atomic Force Microscopy:

Atomic force microscopy (AFM) imaging was performed on MFP-3D-Bio AFM instrument from Asylum Research (Santa Barbara, CA). A Model #TAP150A silicon probe (Bruker,

Santa Barbara, CA) with a resonant frequency of 150 kHz was used for tapping mode AFM imaging in air. The TiO₂-coated AAO membranes were sequentially rinsed with acetone, ethanol, and Milli-Q water to remove any organic contamination or particulates; the coated membranes then blow dried with high purity nitrogen gas. The membranes were taped to a glass slide, which was secured on the AFM stage using two magnets. An area of 3 μm × 3 μm was scanned; roughness analysis was obtained by averaging the data from at least three images that were acquired from different areas of the membrane. The 1st order flatten was applied to all AFM images prior to the roughness analysis. The root mean square (RMS), maximum peak, maximum valley, area, and area percent were reported to examine the difference in surface roughness among three different surfaces. It should be noted the “area” results were automatically calculated using the quad triangle method (QTM) in the AFM analysis software. In the QTM method, each group of 4 pixels was drawn as a set of 4 triangles, with the center of the group being shared by all triangles. The surface of each of the 4 triangles was calculated and summed up as total “area.”

Cell Culture:

Annealed TiO₂-coated membranes and uncoated membranes were sterilized with ultraviolet light (UVP CL-1000, Upland, CA). All membranes were exposed for two hours on each side and rotated 90° every 60 minutes to ensure that all of the sides were sterilized. Upon completion of ultraviolet sterilization, the membranes were placed in 24-well plates. RAW 264.7 cells (mouse leukemic monocyte macrophage cell line, ATCC, Manassas, VA) were added to the 24-well plates at a cell density of 2×10^5 cells/ml. L929 cells (mouse fibroblast

cell line, ATCC, Manassas, VA) were added to different 24-well plates at a cell density of 1×10^5 cells/ml. Tissue culture polystyrene (TCPS) controls were obtained by using a hot hole punch to press out tablets with the same diameter as the AAO membranes. All 24-well plates were then incubated for either 24 or 48 hours at 37°C with 5% CO_2 . Some cells may have grown on the surface of the culture well itself but not on the membrane; therefore, only the cells growing on the membranes and the controls were considered. Prior to performing assays, the membranes and controls were moved to a new 24-well plate so that cells growing on well surfaces did not influence measurements by diluting assay outputs. All of the assays were conducted in duplicate; experiments were repeated a minimum of three times.

MTT Assay:

Membranes were assayed for potential toxicity using the MTT assay (CellTiter 96[®] Non-Radioactive Cell Proliferation Assay, Promega, Madison, WI), as previously described.¹⁹ Cells spiked with 5% and 10% dimethyl sulfoxide (DMSO) served as a positive control. The MTT dye was tested for interactions with the AAO membrane and no interference was recorded. The data for the coated membranes were normalized to data for the uncoated membranes and were expressed as percent viability.

Neutral Red Assay:

L929 fibroblasts were grown on the coated membranes, uncoated membranes, and TCPS control materials for 4, 24, or 72 hours. The samples were carefully rinsed with PBS, moved to a new 24-well plate with 1 ml Neutral Red (NR) media (25 µg NR dye/ml RPMI media) in each well, and incubated at 37°C for 3 hours. The NR media was then removed and the samples were rinsed in PBS. 400 µl of desorb (EtOH/acetic acid) solution was added to all of the wells, including the blank wells. Plates were protected from light and shaken for 40 minutes to extract NR dye from the cells. Absorbance was measured at a wavelength of 540 nm using a 96-well OPTIMax plate reader (Molecular Devices, Sunnyvale, CA).

Micro Bicinchoninic Acid Assay:

The total amount of adsorbed proteins on the coated membranes, uncoated membranes, and TCPS control materials was quantified using a micro-BCA Protein Assay Kit (Pierce Biotechnology, Rockford, IL). Samples were incubated with Phenol Red-free cell culture media containing 10% FBS. 30 seconds of exposure to cell culture media was determined to be optimal since the entire surface was found to likely be covered in adsorbed proteins after approximately 2 minutes. TCPS controls were obtained by using a hot hole punch to press out tablets with the same diameter as the AAO membranes. Polydimethylsiloxane (PDMS) gasket molds were used to expose the same area of a single side of each membrane and control tablet. After 30 seconds of exposure to cell media, the membranes and controls were dip washed in PBS 3 times to remove any loosely adsorbed proteins. Samples were then placed into wells within a 24-well plate containing the micro-BCA assay reagents and

incubated for 3 hours at 37°C. The resulting solution was then transferred into triplicate wells of a 96-well plate; absorbance was measured at a wavelength of 562 nm using an OPTIMax plate reader (Molecular Devices, Sunnyvale, CA).

Cell Imaging:

To investigate cell attachment and cell morphology on the test materials, L929 fibroblasts were plated at a density of 1×10^5 cells/ml directly on the coated membranes, uncoated membranes, and TCPS controls; the cells were then incubated for 4, 24, and 72 hours. Media was removed; cells were washed with warm PBS, fixed with 4% paraformaldehyde, and washed with PBS again. 0.2% Triton was used to permeabilize the cell membrane to the dyes. Cells were subsequently washed again and incubated with Molecular Probes® DAPI, Alexa Fluor® 594 phalloidin (Life Technologies, Grand Island, NY), and SYTOX® Green Nucleic Acid Stain (Life Technologies, Grand Island, NY) for 1 hour. The cells were then washed with PBS 3 times and allowed to dry in the dark. Images were acquired using an Axioskop 2 fluorescent microscope (Carl Zeiss, Thornwood, NY) with a 10x objective.

DNA Proliferation Assay:

The Picogreen® DNA assay was used to quantify cell proliferation on the coated membranes, uncoated membranes, and control materials. Samples were washed with PBS and then incubated with lysis buffer (PBS with 0.175 U/ml papain and 14.5 mmol/l L-cysteine) for 18 hours at 60 °C. After incubation, 0.1 ml of lysate was transferred to a clean 96-well plate and diluted with 0.1 ml of Picogreen® reagent (Life Technologies, Carlsbad,

CA), which was diluted as per the manufacturer's protocol. Fluorescence (excitation wavelength=485 nm, emission wavelength=538 nm) was measured using an OPTIMax plate reader (Molecular Devices, Sunnyvale, CA). A DNA standard curve was generated using known DNA concentrations to calibrate readings.

Mouse TNF-alpha Immunoassay:

Mouse tumor necrosis factor alpha (TNF-alpha) is an immunostimulant and a mediator of the inflammatory response. RAW 264.7 macrophages were assayed for potential production of TNF-alpha while exposed to uncoated AAO, TiO₂-coated AAO, and TCPS controls. A sandwich enzyme immunoassay (Quantikine®, R&D Systems Inc, Minneapolis, MN) was used as received following the included instructions as previously described.²⁰ Cells spiked with 10 ng/ml lipopolysaccharide (LPS) served as a positive control. Cells were spiked with 10 pg/ml LPS to activate macrophages.

Statistical analysis:

The results from each data set were analyzed using Prism 4 statistical software (GraphPad Inc., La Jolla, CA). Results were expressed as mean \pm standard deviation. Statistical differences between control and treated groups were assessed using one-way ANOVA, with a Bonferroni *post hoc* test. Each experiment was independently repeated at least 3 times with each assay in duplicate. A *P* value of less than 0.05 was considered to be statistically significant. The data were normalized to the uncoated membranes and were expressed as

percent viability. Significance level notation was expressed as * for $P < 0.05$ and ** for $P < 0.01$.

Results and Discussion:

Atomic Layer Deposition of TiO₂:

The first objective of this study was to demonstrate a suitable process for coating nanoporous AAO with TiO₂. Anodization of Ti is used to obtain the starting porous structure. Recent work by Lavenus et al., showed that nanoporous anodized TiO₂ surfaces with 20, 30, and 50 nm diameter pores had better tissue-material interactions than smooth Ti²¹. Bone-to-implant contact percentages and tensile pull-out forces of nanoporous TiO₂ after implantation in rat tibial tissue were significantly higher than smooth Ti. In addition, human mesenchymal stem cells cultured on nanoporous TiO₂ show osteogenic differentiation without the use of inducing supplements.²¹ The nanoporous AAO samples used in the study are anisotropic; one side of the membrane exhibits large circular pores (Figures 1 A and B), which narrow into smaller “branchlike” pore structures on the opposite side (Figures 1 C and D). Each membrane has a side with circular pores that are approximately 200 nm in diameter. The opposite side, which contains “branchlike” pore structures, is fabricated with a specified pore diameter of either 20 nm or 100 nm.

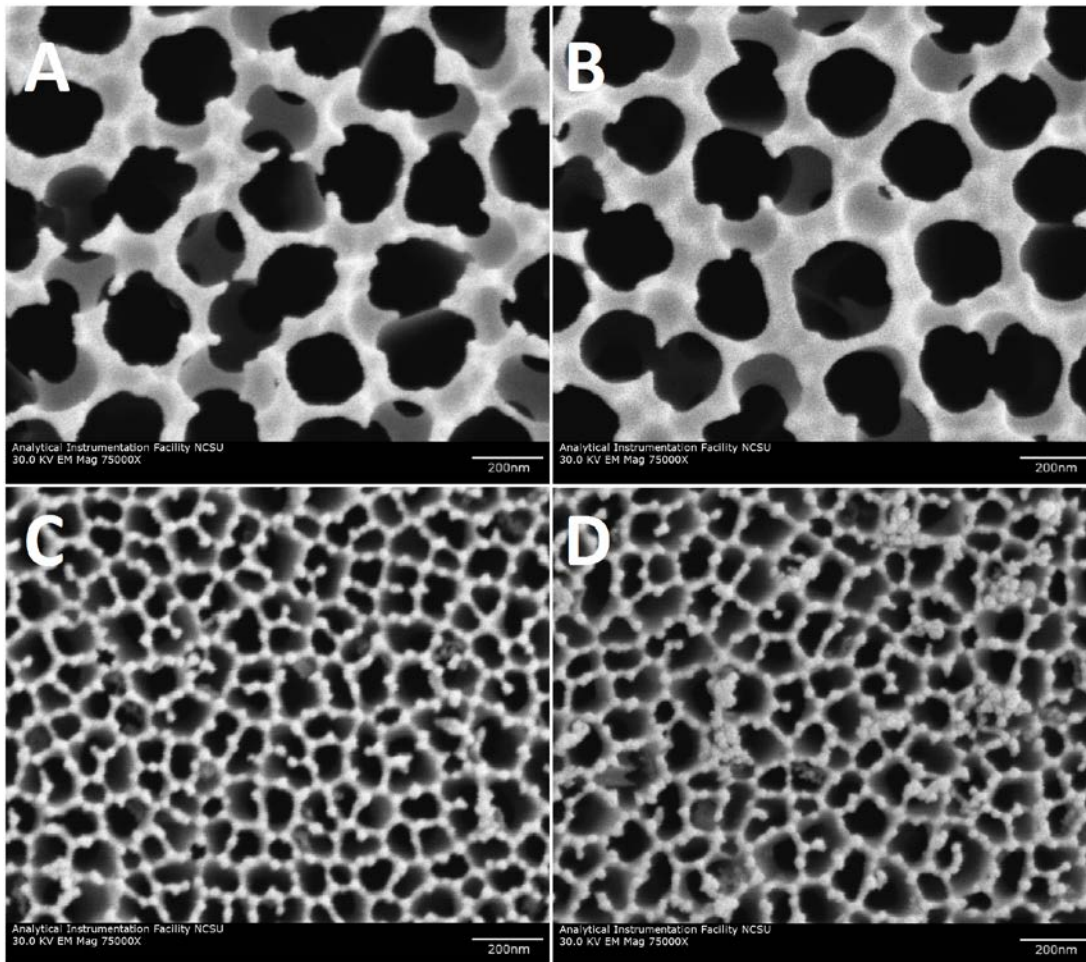


Figure 1. Scanning electron microscope images of a double-sided 200 nm/100 nm AAO membrane before and after atomic layer deposition of TiO_2 . (A): Top side, 200 nm circular pores of uncoated and (B): TiO_2 -coated nanoporous AAO. (C): Uncoated bottom side, showing smaller 100 nm branching pores before and (D): after coating with TiO_2 . All membranes had one side with circular 200 nm pores; in the 20 nm and 100 nm AAO membranes, smaller branched pores appeared on the opposite side. Scale bar is 200 nm.

The nanoporous surfaces used in the study present a difficulty for physical vapor deposition methods and other line-of-sight coating methods. During ALD growth, however, the substrates were completely permeated and heated to facilitate interactions between the chemical solution and all surfaces of the membrane. The TiO₂-coated AAO was further sintered to improve the integrity of the coating. Due to the uniform nature of the coating and the low coating thickness, the surface features of the TiO₂-coated AAO membranes and the uncoated AAO membranes were very similar. EDX results for the TiO₂-coated AAO membranes and the uncoated AAO membranes are shown in Figure 2. The samples can be easily distinguished since the TiO₂-coated AAO membrane shows a prominent Ti signal (shown in red). The versatility of ALD method used lies in its ability to uniformly deposit coatings with controlled thickness onto nanostructured surfaces; this process allows nanoscale surface features of the AAO membranes to be conserved (Figures 1 and 2). It should be noted that ALD may be used to modify the surfaces of polymers and other heat-sensitive materials as well.²⁵ Nanoporous AAO, however, was selected as a substrate for this study due to its wide commercial availability and low cost.

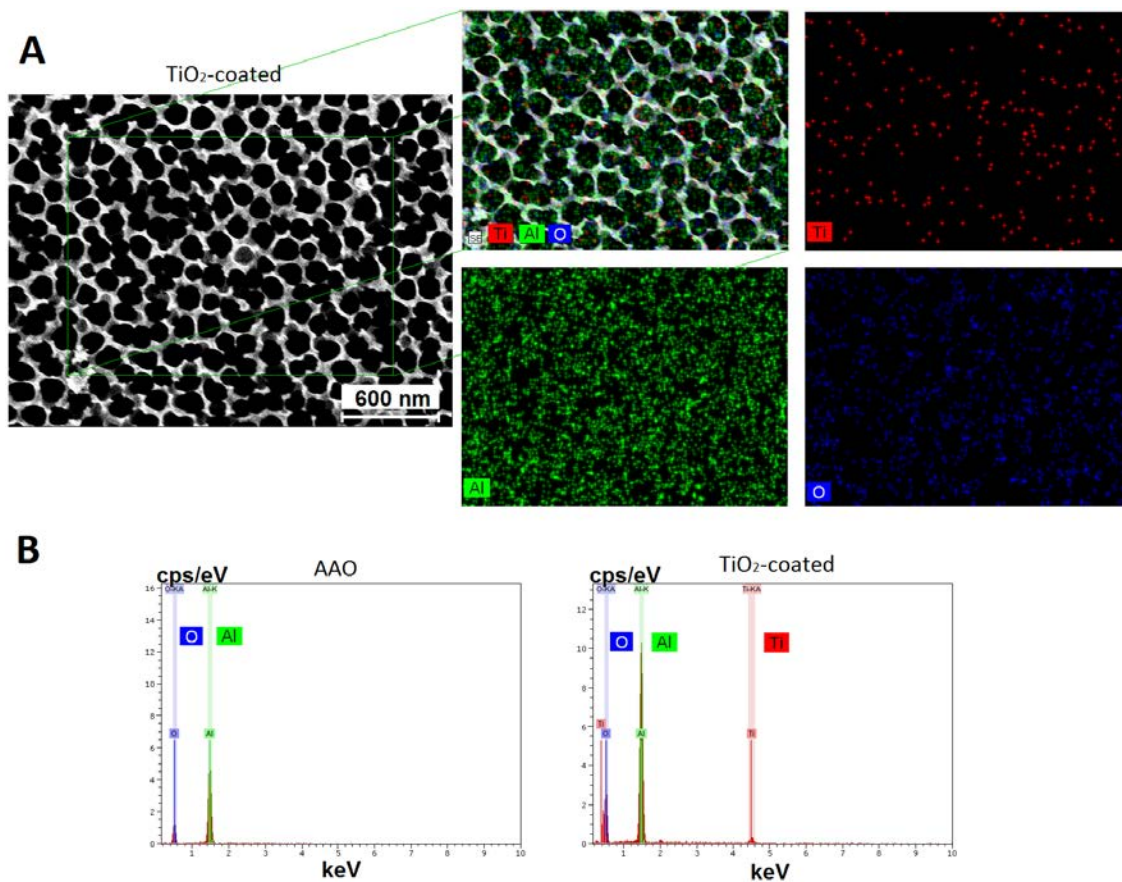


Figure 2. EDX analysis of a TiO₂-coated AAO membrane. A: Split channels show the presence of Al, O, and Ti on the surface. B: Uncoated samples show no Ti signal, confirming that the Ti signal appears only after the coating, annealing, and sterilization process.

Surface Topography and Protein Adsorption:

AFM analysis showed distinct roughness, skew, kurtosis, and exposed surface area properties for the 20, 100, and 200 nm pore surfaces (Figure 3). 200 nm pores had the highest R_{RMS} (root mean square roughness) of 133.5 nm. Root mean square (RMS) roughness gives the overall mean magnitude of surface variations; Max and Min measurements give the highest peak and lowest valley numbers, respectively. The magnitude of variation between the highest peak and lowest valley was over 100 nm for all of the surfaces. Skewness is the lack of symmetry around the data point distribution curve. AFM data from a surface with deep narrow valleys will give a negative skewness; on the other hand, the presence of high narrow peaks coming from the surface will give a positive skewness.²² The 20 nm porous surfaces show a slightly positive skew (0.207), while the 100 and 200 nm porous surfaces have a negative (-0.667 and -0.442, respectively) skewness. Kurtosis is a relative measure of whether the collected force data is more peaked (positive) or flat (negative) compared to a normal curve shape. Low (negative or platykurtic) kurtosis means the data sets have a flat top near the mean and positive (leptokurtic) kurtosis means the data sets have a sharp peaks, rapid declines, and heavy tails. From the AFM data in Figure 3, it can be seen that the branched 20 and 100 nm share similar positive kurtosis values (2.67 and 3.00, respectively); on the other hand, the 200 nm circular pores have a negative (-0.672) kurtosis value.

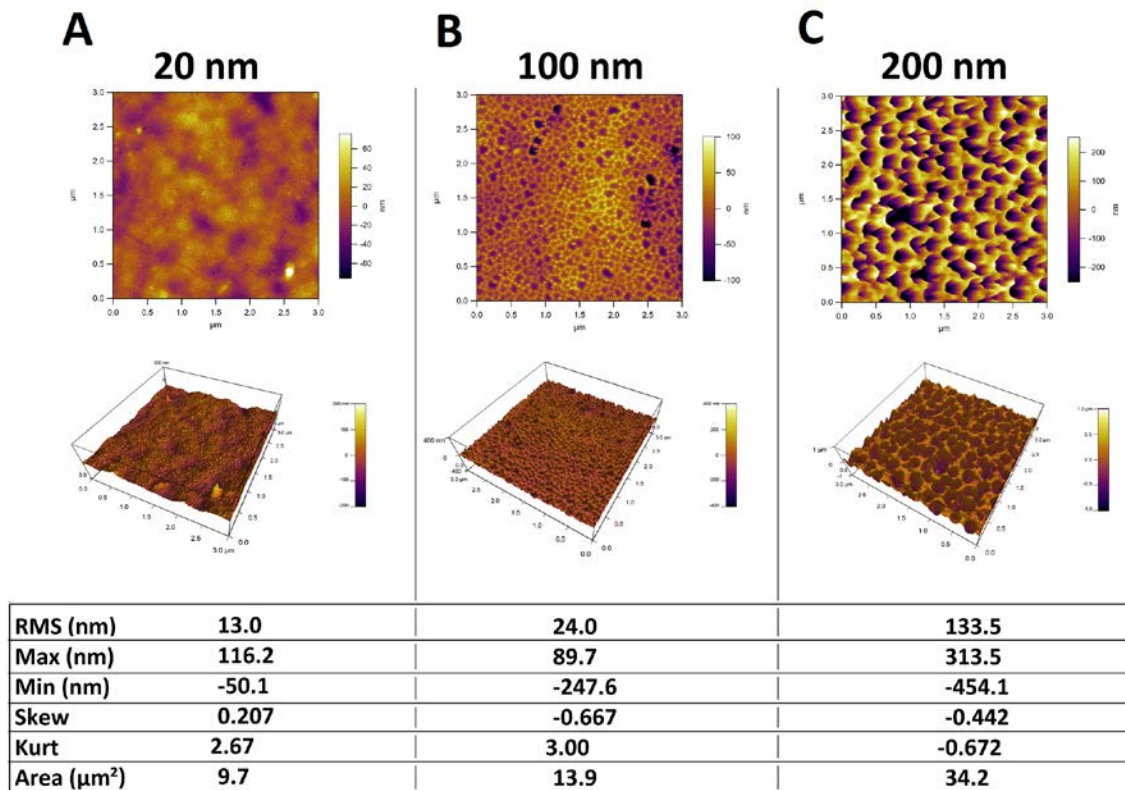


Figure 3. AFM topographical analysis of three porous surfaces: A) 20 nm branchlike pores, B) 100 nm branch-like pores, and C) 200 nm circular pores. Roughness parameters, including skewness, kurtosis and surface area, are reported. Root mean square (RMS) roughness provides the overall mean magnitude of surface variations. Maximum (Max) and minimum (Min) measurements provide the highest peak numbers and lowest valley numbers, respectively. Skewness measures whether the surface has more deep valleys (negative) or protruding narrow peaks (positive). Kurtosis is a relative measure of whether the collected force data is more flat (negative) or peaked (positive) compared with a normal curve shape.

Protein adsorption was measured using the micro-BCA assay to determine if there were any differences in the amount of protein that initially adsorbs to the test materials. The surface area of each type of tested material was different; the total measured protein (μg) was likely affected by the difference in surface area as measured with AFM in Figure 3. The total protein amount, however, could not be normalized to the AFM area since the internal membrane surface was not determined. The TCPS material was estimated as a flat surface, accounting for its lower total protein content. The highest amount of adhered protein was located on the 20 nm TiO_2 -coated AAO membranes. As seen in Figure 4, the 20 nm, 100 nm, and 200 nm TiO_2 -coated AAO membranes and the 200 nm uncoated AAO membrane showed significantly higher amounts of total adsorbed protein than the TCPS controls. The results of the total adherent protein study (Figure 4) may be related to the roughness of the TiO_2 -coated and uncoated AAO membranes (as observed by AFM (Figure 3)). In this study, the 20 nm membranes adsorbed the greatest amount of protein after 30 seconds of incubation with cell media (20% FBS). It is also interesting to note that the 20 nm TiO_2 -coated AAO exhibit higher amounts of protein adsorption than the uncoated AAO; this result suggests that appropriate control over both surface chemistry and roughness may enable optimization of protein adsorption by an implant material.

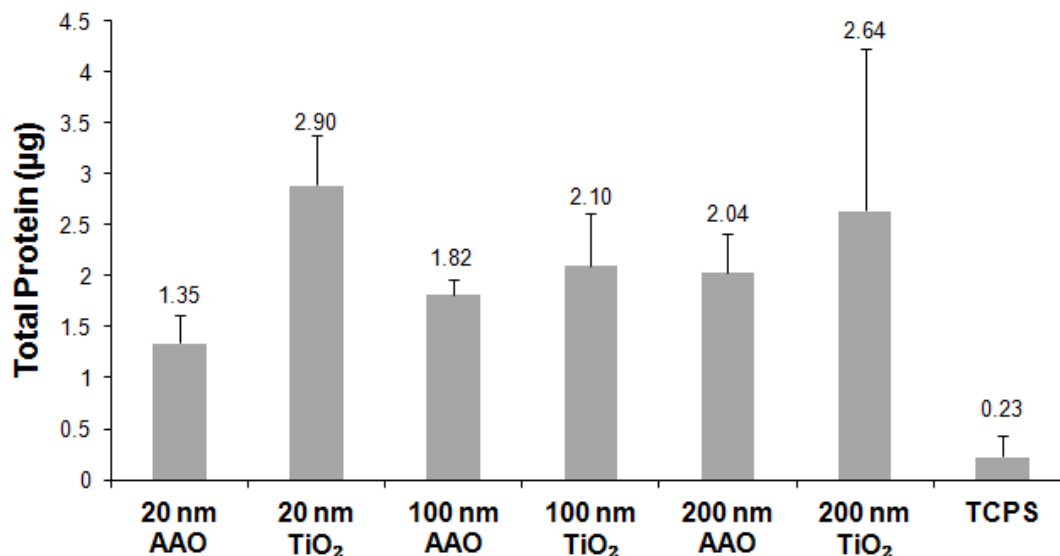


Figure 4. Total protein content measured by the micro-BCA assay after 30 seconds incubation for uncoated AAO membranes and TiO₂-coated AAO membranes with 10% FBS culture medium. 20 nm TiO₂-coated AAO membranes had the highest total amount of adsorbed protein compared to all of the other membranes.

In vitro Cytotoxicity:

The second major objective of the present study was to determine if the TiO₂ coating has an effect on cell viability, growth, and proliferation *in vitro*. Cell-material interactions were evaluated with two cell types: RAW 264.7 murine macrophage cells, which represent a major cell type that is involved in inflammatory responses and L929 fibroblasts, which represent a model cell type involved in wound repair. The MTT cell viability assay served as a preliminary toxicity screen; different pore size surfaces were not AFM sorted prior to testing.

The pore sizes used were randomized from an equivalent set of pore sizes and shapes. No surface-dependent material toxicity was observed since no significant decreases in MTT cell viability were found for either cell type (Figure 5). The MTT results showed that TiO₂-coated AAO membranes exhibit cell viability similar to that of uncoated AAO membranes.

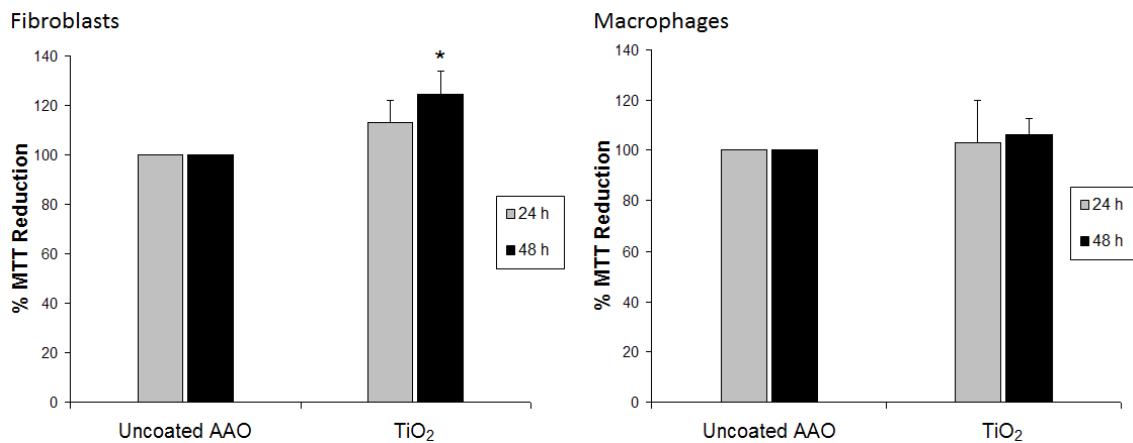


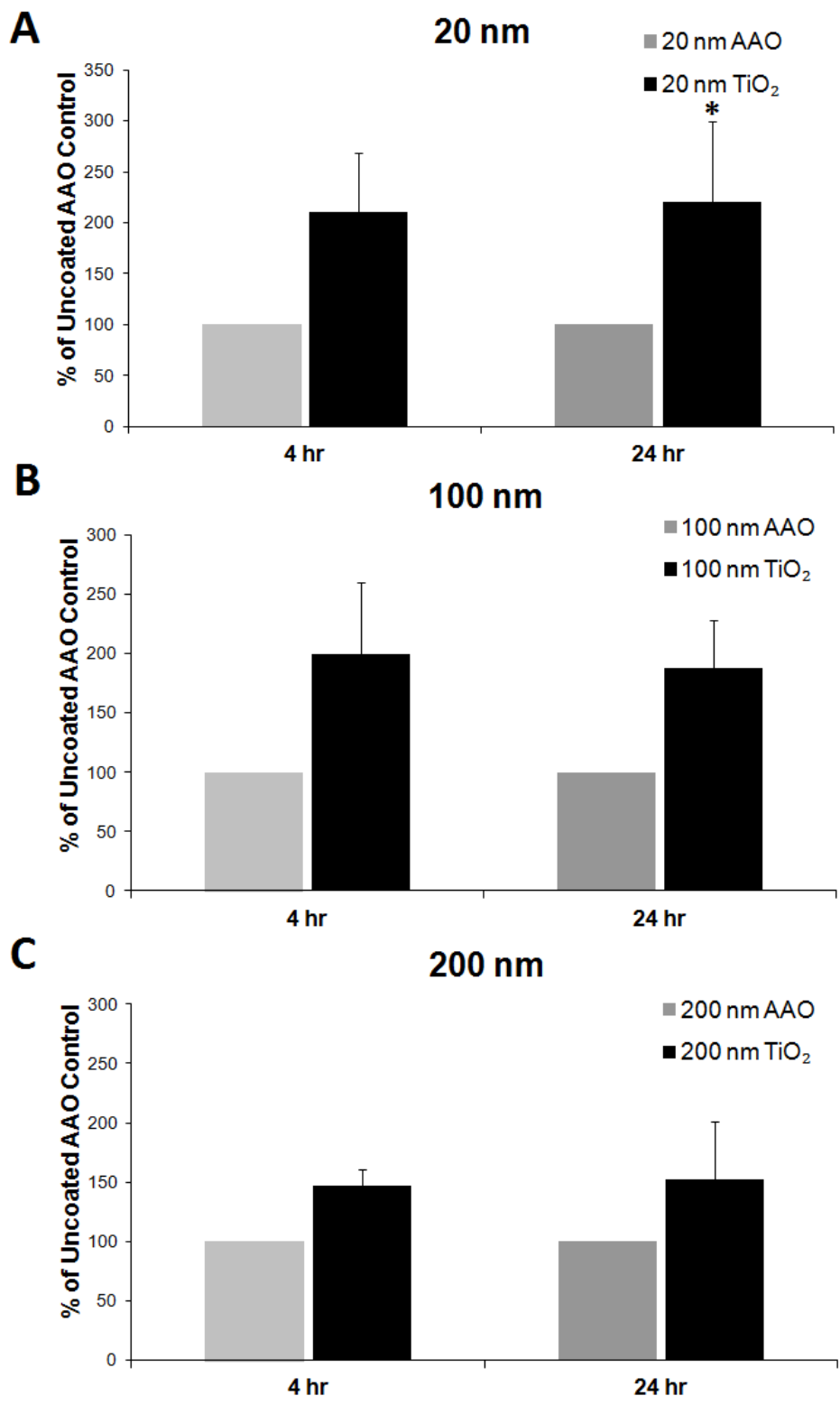
Figure 5. Viability of L929 mouse fibroblast cells and RAW 264.7 mouse macrophage cells grown on uncoated AAO membranes and TiO₂-coated AAO membranes; measurements were obtained using the MTT assay. Results are expressed as percent of uncoated AAO controls for 24 hour and 48 hour exposures. Fibroblasts grown on TiO₂-coated AAO showed higher cell viability after 48 hours, which was statistically significant ($p < 0.05$).

To further confirm the results of the randomized MTT screen, AFM was used to sort the membranes into branchlike 20 nm pores, branchlike 100 nm pores, and 200 nm circular pores; these porous features were not distinguishable from one another with a light microscope. The Neutral Red assay was used to determine whether pore size had an effect on cell viability. Cell viability was measured over 4 hours (initial attachment), 24 hours, and 72 hours (the 72 hour time point was not shown). There was no surface-dependent material toxicity and there were no significant differences in cell viabilities between the TCPS control materials and the AAO membranes with 100 nm or 200 nm pore sizes (Figures 6 B and C, respectively). The assay showed somewhat higher values for TiO₂-coated AAO membranes at all of the time points compared to uncoated AAO membranes and TCPS controls; however, all of the data except for the 24-hour time point for 20 nm TiO₂-coated AAO membranes were not statistically significant. Assay interference with controls was ruled out; in addition, some significant biological variability was observed at the 24-hour time point for the 20 nm TiO₂-coated AAO membranes.

Overall, both the MTT and Neutral Red cytotoxicity assays confirmed that cell viability is not significantly affected by variations in pore size from 20 nm to 200 nm in both uncoated AAO and TiO₂-coated AAO (Figures 5 and 6). An increase in the available surface area theoretically increases the number of attachment points for cell adhesion or cell migration and should not have a negative effect on cell response in and of itself. It is known that the features of the extracellular matrix with which cells interact have components (e.g., fibrils and filaments) that are on the order of several nm to 200 nm^{23,24}; the size of the extracellular matrix component features is similar to the size range of the pores used in this

study. Our results show that relatively small variations in pore shape and diameter within one order of magnitude (20-200 nm) will likely not create a noticeable effect on cell proliferation or elicit a detectable variation in inflammatory response. A previous study has shown that the size of nanoscale pores in Al₂O₃ materials (20 – 200 nm) does not affect the cell viability of MG63 human osteoblast-like cells.²⁵ This is an important finding since minor variations in pore size and shape may not be a significant factor in determining the cellular responses to a scaffold or implant material. Accordingly, the initial MTT viability screen in the present study was performed without selecting for pore diameter (Figure 5). These assays showed no evidence of material- or topography-associated cytotoxicity.

Figure 6. Cell viability measured using the Neutral Red assay for L929 fibroblasts grown on uncoated AAO membranes and TiO₂-coated AAO membranes for 4 and 24 hours. Results were expressed as a percentage of uncoated AAO membrane controls for TiO₂-coated AAO membranes with pore diameters of A) 20 nm, B) 100 nm, and C) 200 nm. Although TiO₂-coated AAO membranes had the highest viabilities at 4 and 24 hours, the differences were only statistically significant ($p < 0.05$) for 20 nm porous membranes after 24 hours.



Cell Proliferation on Nanoporous Membranes:

To examine fibroblast cell proliferation on the membranes, the DNA PicoGreen® Assay was used to quantify the amount of DNA in L929 fibroblasts grown on the uncoated AAO, the TiO₂-coated AAO, and the TCPS controls for 4, 24, and 72 hours (Figure 7). The amount of DNA (ng) increased approximately 2-fold from 4 hours to 72 hours for uncoated AAO membranes and TCPS and 4-fold for TiO₂-coated AAO membranes. However, the amount of DNA at 72 hours was not significantly different between the experimental and control groups. This result may be explained by the fact that cells did not adhere as well to uncoated AAO as to TiO₂-coated AAO and TCPS during initial cell seeding and that proliferation had reached a limiting factor at 72 hours. Cells were seeded and membranes were transferred to new wells at 4 hours. Media was not changed between 4 and 72 hours. The results also showed no significant differences between membranes with 20, 100, and 200 nm pore sizes at all three time points. Neutral Red viability (Figure 6) and DNA PicoGreen® (Figure 7) assays were performed to determine the effect of pore size on cell response for both uncoated AAO and TiO₂-coated AAO. No significant differences were observed for various pore sizes or materials; therefore, the effect of pore size may be too minor to be detected *in vitro* over a short time period.

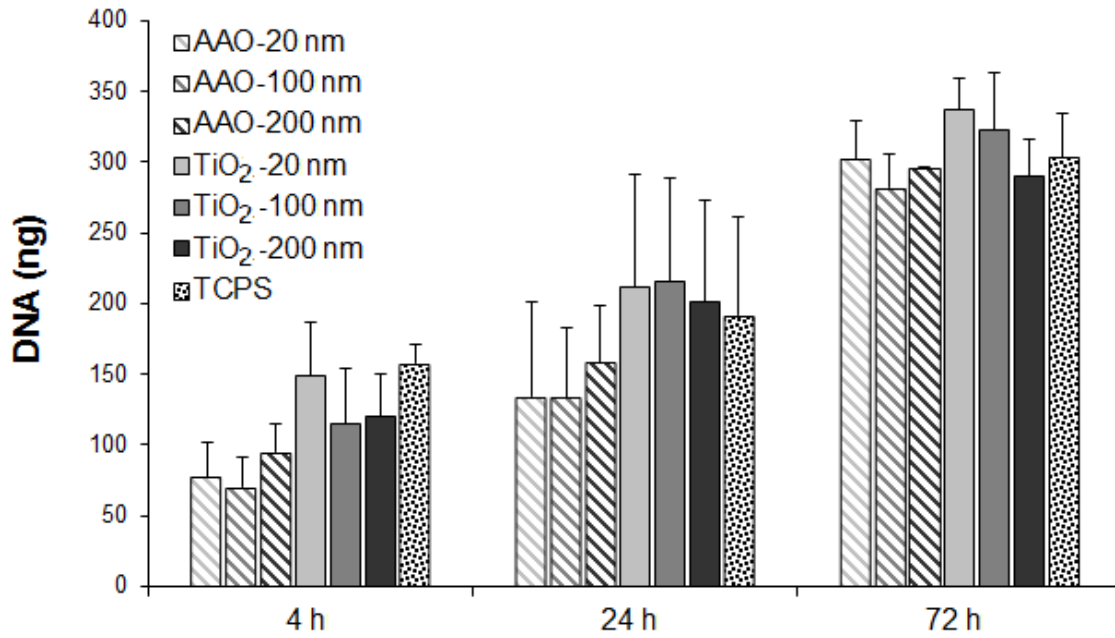


Figure 7. Cell proliferation measured by the DNA PicoGreen® Assay involving L929 fibroblasts grown for 4, 24, and 72 hours on uncoated and TiO₂-coated AAO membranes with pore sizes of 20, 100, and 200 nm. No statistically significant differences between the amounts of DNA were observed at any of the time points.

Inflammatory Response and Cell Imaging:

Neither cell viability nor proliferation of macrophages and fibroblasts was adversely affected by exposure to TiO₂-coated AAO membranes. The possibility of an adverse inflammatory response, however, is not necessarily related to cell viability; further investigation is needed to characterize potential generation of an adverse inflammatory response by the test materials. Macrophages are known to be involved in inflammation and have been shown to be activated by titanium wear particles.²⁶ TNF-alpha is a known cytokine that is produced by macrophages and is involved in systemic inflammation.²⁷ The results of the quantitative sandwich enzyme immunoassay (Figure 8) showed no significant TNF-alpha production in macrophages grown on both uncoated AAO and TiO₂-coated AAO. The possibility existed that macrophages were not activated and did not respond as they would during an inflammatory reaction. Therefore, LPS was used to activate the macrophages prior to seeding cells onto the membranes. The increase in TNF-alpha production was markedly elevated in the presence of LPS as predicted; however, TNF-alpha concentrations were uniform across uncoated AAO membranes and TiO₂-coated AAO membranes, including TCPS controls. The results show that there is no enhanced TNF-alpha production *in vitro* from macrophages grown on uncoated AAO surfaces or TiO₂-coated AAO surfaces.

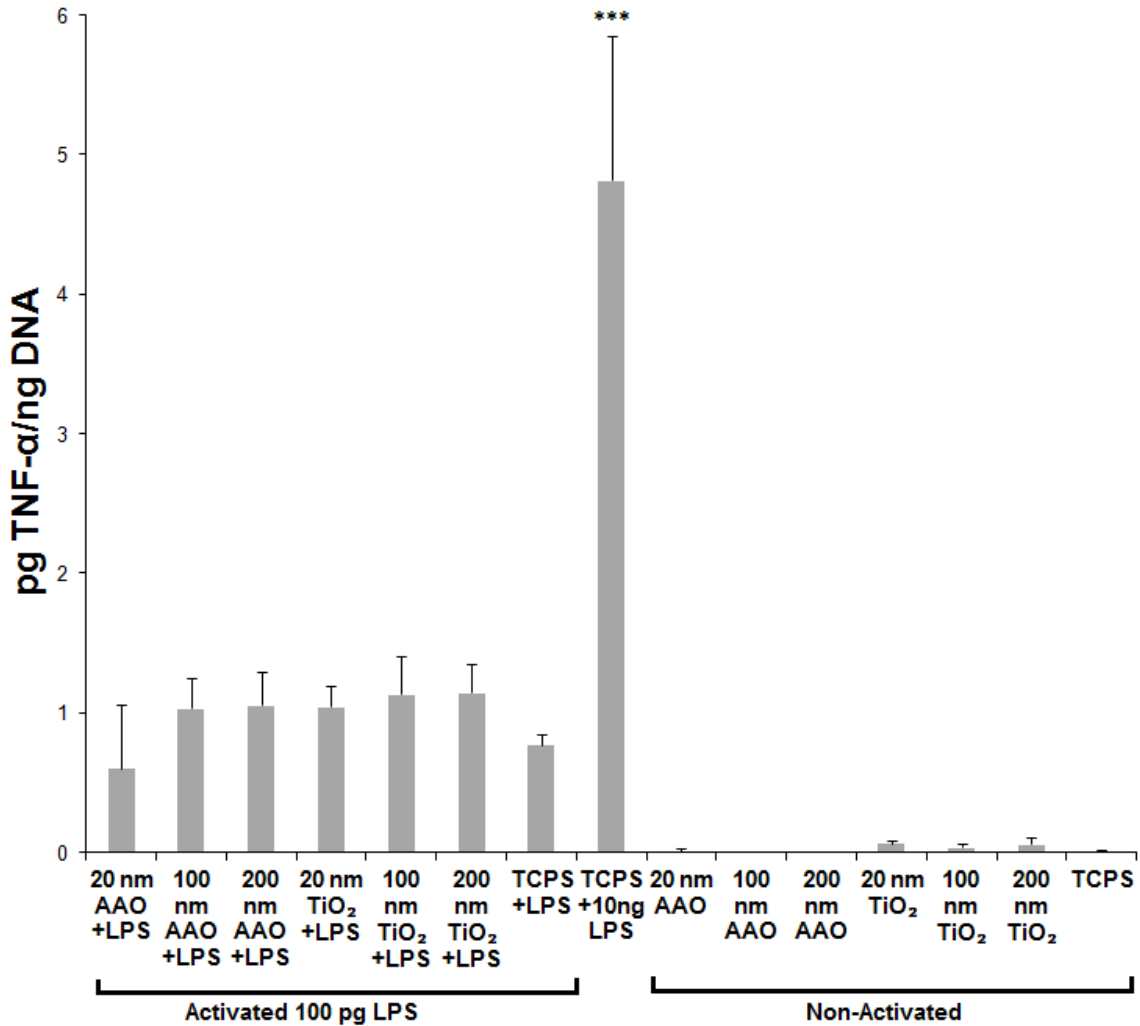


Figure 8. TNF- α production measured after 24 hour exposure for mouse macrophages with or without addition of 10 ng/ml LPS. While macrophages activated by LPS produced higher levels of TNF- α than macrophages not activated by LPS, differences in TNF- α release were observed for macrophages grown on uncoated AAO membranes and TiO₂-coated AAO membranes compared to macrophages grown on TCPS controls.

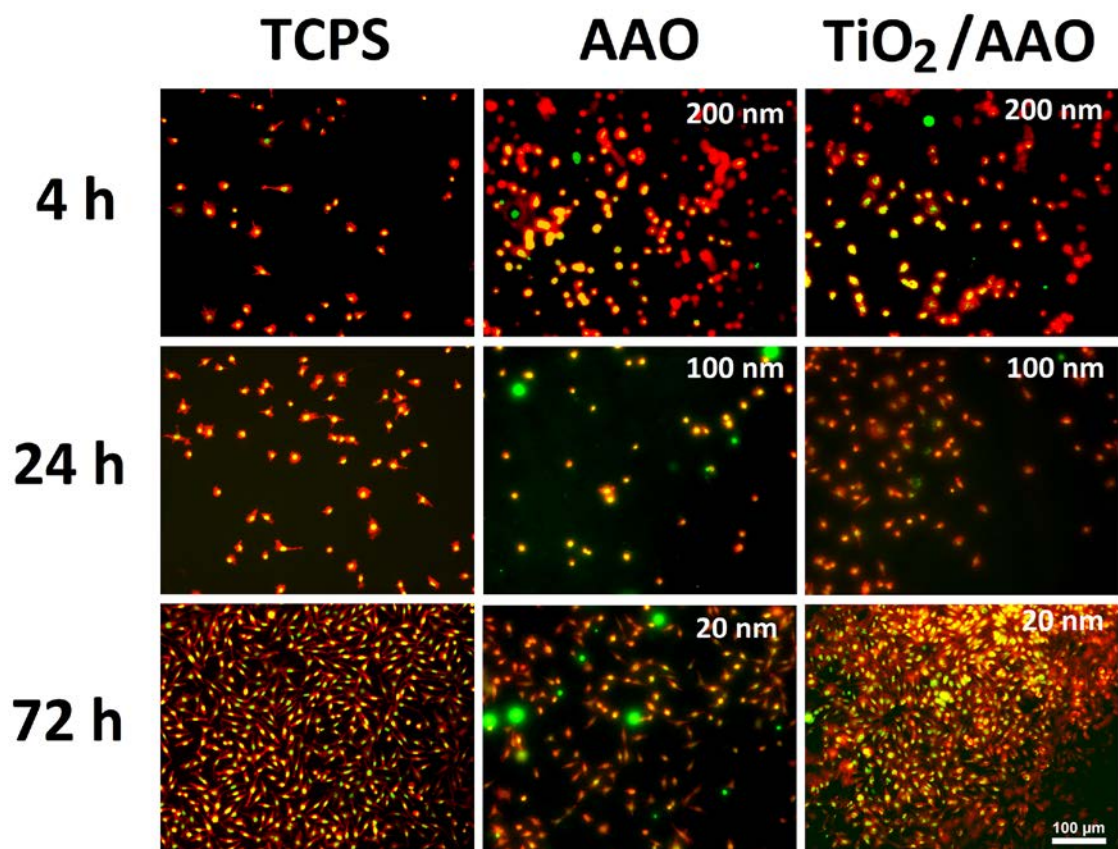
One important feature of nanostructured materials is that they possess a larger exposed surface area than conventional materials; the exposed surface area may participate in cell interactions as well as ion release via particulate release and ionic metal leaching.^{28,29} In the present study, nanoporous uncoated AAO and TiO₂-coated AAO showed no significant adverse effects on cell viability, proliferation, or TNF-alpha production when compared to a standard TCPS tissue culture well surface. These findings correlate with *in vivo* results published in response to the long use of largely particulate forms of TiO₂ in manufacturing, sun screens, and cosmetics. Long-term exposure to TiO₂ through inhalation showed no abnormal clinical effects or excess mortality in rats.³⁰ Relatively large oral doses (5000 mg/kg bodyweight) of TiO₂ in the form of 20 nm and 80 nm discrete nanoparticles did not appear to cause abnormal pathology in mice; however, some signs of acute liver and kidney toxicity were noted.³¹ In addition to testing for cytotoxic responses, implant materials with nanotextured surfaces need to be evaluated for the potential to produce inflammatory responses. In the present study, production of TNF-alpha, a well-known pro-inflammatory cytokine that is involved in stimulation of inflammation and immune cell function, was unaffected by any of the uncoated AAO or TiO₂-coated AAO membranes (Figure 8). Since the *in situ* environment of an implant may exhibit heightened immune and/or inflammatory activity, macrophages were spiked with a calibrated amount of LPS to reflect an activated macrophage response. No differences in TNF-alpha production were observed in this scenario. These results indicated that uncoated AAO and TiO₂-coated AAO were associated with low levels of immune stimulation and may be good candidates for further *in vivo* studies due to the favorable properties of titanium. Nanostructured titanium, specifically, has been

shown to have an effect on osteoblastic differentiation of adherent mesenchymal cells; this attribute may be beneficial for a variety of orthopedic and dental implant applications³²; in addition, nanostructured TiO₂ may possess enhanced antimicrobial activity.³³ Furthermore, TiO₂ exhibits photocatalytic activity on exposure to UV light.³⁴ ALD may be used to deposit the same surface chemistry of TiO₂ as uniform coatings on surfaces with complex nanoscale features¹⁹; this approach preserves the nanoscale structure (e.g., the nanoscale pores) of the substrate material, potentially making the substrate more favorable for biomedical use.

Qualitative cell images shown in Figure 9 revealed no difference in cell morphology or density. Cells were more uniformly spread in a monolayer on the TCPS surfaces, whereas the cell layer was more varied on the nanoporous surfaces. As seen in the images, L929 fibroblasts attached with fairly similar individual morphologies across the nanostructured surfaces. Cells were spread very evenly on TCPS well plates; on the other hand, cells were more clumped and sometimes formed multilayers on uncoated AAO and TiO₂-coated AAO after 72 hours, particularly on TiO₂-coated AAO. The results of the imaging study further confirmed the results of the cell viability and proliferation experiments. Although a small trend was present, with 20 nm surfaces potentially showing a different response than 100 nm and 200 nm surfaces, our findings confirm that the variation in pore size is not associated with a significant change in either cell viability, proliferation, or morphology that is detectable by the *in vitro* assays used in this study. It should be noted, however, that the 20 nm TiO₂-coated AAO membranes are the best candidates for further consideration as implant materials since they have the greatest amount of protein adhesion, which may facilitate cell attachment. Perhaps either examining membranes with smaller pore sizes or comparing

membranes with pore sizes over several orders of magnitude may reveal a greater variation in cell response.

Figure 9. Fluorescent images of L929 fibroblasts grown on nanoporous membranes and smooth controls after 4, 24, and 72 hour exposure. Nuclei stained green (SYTOX® Green) and actin stained red (Alexa Fluor® 594 phalloidin). Similar cell morphologies were visible among all uncoated and coated nanoporous membranes. The nanoporous membranes showed more disordered and multilayered cell structures compared to smooth TCPS. Scale bar=100 μm .



Conclusions:

Both uncoated AAO membranes and TiO₂-coated AAO membranes exhibited no cytotoxicity. ALD proved to be an effective method for coating structures with small-scale features without altering the nanoscale surface features of the structures. In addition, TiO₂-coated AAO membranes demonstrated no *in vitro* cytotoxicity and therefore might represent a class of materials with excellent biocompatible properties. The present study also provided a better understanding of the factors that affect medical devices with nanoscale surface modifications. The question of whether varying surface porosity and/or surface roughness affects cell viability and the question of whether another physical and/or chemical parameter induces an adverse cellular response are important concerns when assessing the safety of a medical device. Devices with an identical surface chemistry (e.g., Al₂O₃ or TiO₂) but with minor variations in surface nanoporosity and/or nanotexture within the same order of magnitude may not alter cell viability or proliferation; however, variations in nanoscale structure may alter the dynamics of protein adsorption on the medical device surface.

List of Abbreviations:

Anodic aluminum oxide (AAO)

Titanium dioxide (TiO₂)

Atomic layer deposition (ALD)

X-ray spectroscopy (EDX)

Atomic force microscopy (AFM)

Scanning electron microscopy (SEM)

Titanium isopropoxide (TIP)

3-(4,5-dimethylthiazol-2-yl)-2,5-diphenyltetrazolium bromide (MTT)

Tissue culture polystyrene (TCPS)

Micro Bicinchoninic Acid (micro-BCA)

Polydimethylsiloxane (PDMS)

Tumor necrosis factor alpha (TNF-alpha)

Acknowledgments and Support:

Peter E. Petrochenko is supported in part by NSF Award #1041375. ALD coating of TiO₂ on AAO was conducted at the Center for Nanophase Materials Sciences, which is sponsored at Oak Ridge National Laboratory by the United States Department of Energy's Division of Scientific User Facilities.

References:

- 1 Rivera-Chacon, D. *et al.* Fibronectin and vitronectin promote human fetal osteoblast cell attachment and proliferation on nanoporous titanium surfaces. *J. Biomed. Nanotechnol.* **9**, 1092 (2013).
- 2 Parkinson, L. G., Rea, S. M., Stevenson, A. W., Wood, F. M. & Fear, M. W. The Effect of Nano-Scale Topography on Keratinocyte Phenotype and Wound Healing Following Burn Injury. *Tissue Eng. Part A* **18**, 703-714, doi:10.1089/ten.tea.2011.0307 (2012).
- 3 Narayan, R. J., Monteiro-Riviere, N. A., Brigmon, R. L., Pellin, M. J. & Elam, J. W. Atomic layer deposition of TiO₂ thin films on nanoporous alumina templates: Medical applications. *Jom* **61**, 12-16, doi:10.1007/s11837-009-0081-z (2009).
- 4 Affatato, S., Traina, F., De Fine, M., Carmignato, S. & Toni, A. Alumina-on-alumina hip implants a wear study of retrieved components. *J. Bone Joint Surg.-Br. Vol.* **94B**, 37-42, doi:10.1302/0301-620x.94b1.26956 (2012).
- 5 Yeung, E. *et al.* Mid-Term Results of Third-Generation Alumina-on-Alumina Ceramic Bearings in Cement less Total Hip Arthroplasty A Ten-Year Minimum

- Follow-up. *J. Bone Joint Surg.-Am. Vol.* **94A**, 138-144, doi:10.2106/jbjsj.00331 (2012).
- 6 Tsaousi, A., Jones, E. & Case, C. P. The in vitro genotoxicity of orthopaedic ceramic (Al₂O₃) and metal (CoCr alloy) particles. *Mutat. Res., Genet. Toxicol. Environ. Mutagen.* **697**, 1-9, doi:10.1016/j.mrgentox.2010.01.012 (2010).
- 7 Kumeria, T. & Losic, D. Controlling interferometric properties of nanoporous anodic aluminium oxide. *Nanoscale Res. Lett.* **7**, doi:10.1186/1556-276x-7-88 (2012).
- 8 La Flamme, K. E. *et al.* Biocompatibility of nanoporous alumina membranes for immunoisolation. *Biomaterials* **28**, 2638-2645, doi:10.1016/j.biomaterials.2007.02.010 (2007).
- 9 Petrochenko, P. E. *et al.* Cytotoxicity of cultured macrophages exposed to antimicrobial zinc oxide (ZnO) coatings on nanoporous aluminum oxide membranes. *Biomatter* **3** (2013).
- 10 Vida-Simiti, I., Nemes, D., Jumate, N., Thalmaier, G. & Sechel, N. Self-Ordered Nanoporous Alumina Templates Formed by Anodization of Aluminum in Oxalic Acid. *Jom* **64**, 1143-1147, doi:10.1007/s11837-012-0406-1 (2012).

- 11 Karlsson, M., Palsgard, E., Wilshaw, P. R. & Di Silvio, L. Initial in vitro interaction of osteoblasts with nano-porous alumina. *Biomaterials* **24**, 3039-3046, doi:10.1016/s0142-9612(03)00146-7 (2003).
- 12 Ferraz, N. *et al.* Role of Alumina Nanoporosity in Acute Cell Response. *J. Nanosci. Nanotechnol.* **11**, 6698-6704, doi:10.1166/jnn.2011.4206 (2011).
- 13 Okazaki, Y., Katsuda, S., Furuki, Y. & Tateishi, T. Effects of aluminum oxide film on fibroblast L929 and V79 cell viabilities. *Mater. Trans. JIM* **39**, 1063-1069 (1998).
- 14 Lee, Y. M. *et al.* In vivo and in vitro response to electrochemically anodized Ti-6Al-4V alloy. *J. Mater. Sci.-Mater. Med.* **19**, 1851-1859, doi:10.1007/s10856-007-3265-5 (2008).
- 15 Lee, Y.-J. *et al.* Surface characteristics of thermally treated titanium surfaces. *J Periodontal Implant Sci.* **42**, 81-87 (2012).
- 16 Puckett, S. D., Taylor, E., Raimondo, T. & Webster, T. J. The relationship between the nanostructure of titanium surfaces and bacterial attachment. *Biomaterials* **31**, 706-713, doi:10.1016/j.biomaterials.2009.09.081 (2010).

- 17 Colon, G., Ward, B. C. & Webster, T. J. Increased osteoblast and decreased Staphylococcus epidermidis functions on nanophase ZnO and TiO₂. *J. Biomed. Mater. Res. Part A* **78A**, 595-604, doi:10.1002/jbm.a.30789 (2006).
- 18 Zile, M. A., Puckett, S. & Webster, T. J. Nanostructured titanium promotes keratinocyte density. *J. Biomed. Mater. Res. Part A* **97A**, 59-65, doi:10.1002/jbm.a.33028 (2011).
- 19 Petrochenko, P. E. *et al.* Prevention of Ultraviolet (UV)-Induced Surface Damage and Cytotoxicity of Polyethersulfone Using Atomic Layer Deposition (ALD) Titanium Dioxide. *Jom* **65**, 550-556, doi:10.1007/s11837-013-0565-8 (2013).
- 20 Choi, J. *et al.* Comparison of cytotoxic and inflammatory responses of photoluminescent silicon nanoparticles with silicon micron-sized particles in RAW 264.7 macrophages. *J. Appl. Toxicol.* **29**, 52-60, doi:10.1002/jat.1382 (2009).
- 21 Lavenus, S. *et al.* Cell differentiation and osseointegration influenced by nanoscale anodized titanium surfaces. *Nanomedicine* **7**, 1045-1066 (2012).
- 22 Gadelmawla, E., Koura, M., Maksoud, T., Elewa, I. & Soliman, H. Roughness parameters. *J. Mater. Process. Technol.* **123**, 133-145 (2002).

- 23 Hirsch, A. *et al.* Imposed layer-by-layer growth of ZnO on GaN/sapphire substrates using pulsed laser interval deposition. *Thin Solid Films* **519**, 7683-7685, doi:10.1016/j.tsf.2011.05.057 (2011).
- 24 Timpl, R., Sasaki, T., Kostka, G. & Chu, M.-L. Fibulins: a versatile family of extracellular matrix proteins. *Nat. Rev. Mol. Cell Biol.* **4**, 479-489 (2003).
- 25 Walpole, A. R., Xia, Z. D., Wilson, C. W., Triffitt, J. T. & Wilshaw, P. R. A novel nano-porous alumina biomaterial with potential for loading with bioactive materials. *J. Biomed. Mater. Res. Part A* **90A**, 46-54, doi:10.1002/jbm.a.32067 (2009).
- 26 Mishra, P. K. *et al.* Micrometer-Sized Titanium Particles Can Induce Potent Th2-Type Responses through TLR4-Independent Pathways. *J. Immunol.* **187**, 6491-6498, doi:10.4049/jimmunol.1101392 (2011).
- 27 Beutler, B. *et al.* Identity of tumour necrosis factor and the macrophage-secreted factor cachectin. *Nature* (1985).
- 28 Chakraborty, A., Kundu, B., Basu, D., Pal, T. K. & Nandi, S. K. In vivo bone response and interfacial properties of titanium-alloy implant with different designs in rabbit model with time. *Indian J. Dent. Res.* **22**, 277 (2011).

- 29 Lee, S. *et al.* Peri-implant and systemic release of metallic elements following insertion of a mandibular modular endoprosthesis in *Macaca fascicularis*. *Acta Biomater.* **5**, 3640-3646, doi:10.1016/j.actbio.2009.05.028 (2009).
- 30 Lee, K., Trochimowicz, H. & Reinhardt, C. Pulmonary response of rats exposed to titanium dioxide (TiO₂) by inhalation for two years. *Toxicol Appl Pharmacol* **79**, 179-192 (1985).
- 31 Wang, J. *et al.* Acute toxicity and biodistribution of different sized titanium dioxide particles in mice after oral administration. *Toxicol. Lett.* **168**, 176-185 (2007).
- 32 Valencia, S., Gretzer, C. & Cooper, L. F. Surface Nanofeature Effects on Titanium-Adherent Human Mesenchymal Stem Cells. *Int. J. Oral Maxillofac. Implants* **24**, 38-46 (2009).
- 33 Cui, C. X., Gao, X., Qi, Y. M., Liu, S. J. & Sun, J. B. Microstructure and antibacterial property of in situ TiO₂ nanotube layers/titanium biocomposites. *J. Mech. Behav. Biomed. Mater.* **8**, 178-183, doi:10.1016/j.jmbbm.2012.01.004 (2012).
- 34 Lilja, M. *et al.* Photocatalytic and antimicrobial properties of surgical implant coatings of titanium dioxide deposited through cathodic arc evaporation. *Biotechnol. Lett.* **34**, 2299-2305, doi:10.1007/s10529-012-1040-2 (2012).

CHAPTER 6: Surface damage and cytotoxicity induced by ultraviolet irradiation of nanoporous polysulfone is prevented by atomic layer deposition of titanium dioxide

Authors: Peter E Petrochenko^{1,2}, Giovanna Scarel³, G Kevin Hyde³, Gregory N Parsons³, Shelby Skoog^{1,2}, Qin Zhang¹, Peter L Goering¹, Roger J Narayan²

¹Division of Biology, Office of Science and Engineering Laboratories, Center for Devices and Radiological Health, U.S. Food and Drug Administration, Silver Spring, MD

²Joint Department of Biomedical Engineering, UNC – Chapel Hill and North Carolina State University, Raleigh, NC

³ Department of Chemical and Biomolecular Engineering, North Carolina State University, Raleigh, NC

Keywords: biomaterials, polymers, nanomaterials, membranes

Abstract:

Polysulfone (PES) is a high performance biocompatible polymer that exhibits degradation when exposed to ultraviolet (UV) light. PES can be fabricated with controlled nanoporosity for potential dermal and other biological applications. Titanium dioxide (TiO_2) is commonly used in sunscreens and may be atomic layer deposited (ALD) to protect PES from UV damage. The goal of the present study was to determine whether the self-limiting ALD coating method successfully deposited TiO_2 onto PES, protected it from UV irradiation, and reduced macrophage cytotoxicity. Energy-dispersive X-ray spectroscopy (EDX) showed a Ti peak on the spectra of coated samples. Uncoated PES exposed to UV for 30 min visibly changed color, while TiO_2 -coated PES showed no color change, indicating limited degradation. Macrophages exposed to UV-treated PES for 48 hrs reduced cell viability (via MTT assay) to 18% of control. In contrast, cell viability for UV-treated TiO_2 -coated PES was 90% of control. Non-UV treated PES showed no decrease in cell viability. Therefore, ALD of TiO_2 thin films is a useful technique to protect PES and other sensitive polymers from UV damage, while retaining low cytotoxicity to macrophages, an important cell type involved in wound healing.

Practical Application:

Nanostructured surfaces are becoming increasingly useful for tissue scaffold and wound dressing applications. These surfaces are frequently manufactured from biocompatible polymers that may be susceptible to ultraviolet (UV) damage. One such polymer is nanoporous polysulfone (PES), which undergoes rapid degradation upon UV exposure.

Titanium dioxide (TiO_2) is a known UV absorber used in sunscreens and cosmetics. This metal oxide can be coated onto nanostructured polymers using a self-limiting atomic layer deposition (ALD) approach at relatively low temperatures. A uniform TiO_2 coating can protect sensitive polymer surfaces from UV sources such as germicidal lamps and sunlight exposure. This is beneficial for wound dressings and other medical devices that are exposed to UV light during sterilization or throughout their lifetime. TiO_2 thin film coatings have low toxicity and may be useful as UV protectants on biocompatible polymer surfaces.

Note:

The mention of commercial products, their sources, or their use in connection with material reported herein is not to be construed as either an actual or implied endorsement of such products by the Department of Health and Human Services.

Introduction:

Poly(aryl-ether sulfones), also called poly(ether sulfones), polysulfones (PES) are heat-resistant, high-performance biocompatible polymers. Their rigid sulfone groups give them a relatively high glass transition temperature, T_g , while the ether linkages allow for some flexibility. Traditional use of PES involves flame retardant and medical materials that require autoclave sterilization. PES is non-degradable and can be fabricated with controlled nanoporosity or electrospun into nanofibrous membranes,¹ which make it useful in specialized filtration media² and dialyzers³. Aside from filtration and dialysis applications, PES is a relatively novel biomaterial in the medical field and is mainly used as a more costly polycarbonate replacement when high temperature or hydrolysis resistance is necessary. Over the past decade, however, it has gained attention as a suitable tissue engineering scaffold material and as a material that can be fabricated with nanometer-scale topographical features. Earlier studies of PES point to some potential biocompatibility issues with membranes used in hemodialysis and immune cell activation⁴ as well as the possibility of bisphenol-A release from bulk polysulfone material.⁵ Recent studies, however, show surface-modified PES hollow fiber membranes to have a favorable tissue responses and good biocompatibility *in vivo*.⁶ *In vitro*, PES with pore sizes below 100 μm was associated with extensive long-term cell growth and integration across a variety of cell lines.⁷ PES has been used as a drug delivery wound dressing⁸ and the future for PES is still promising with potential use in enhanced surfaces for drug delivery,⁹ cell differentiation,^{10,11} and wound therapy.¹¹ For dermal applications, for example, PES can be coupled with chitosan and chondroitin sulfate for improved healing.¹¹

Nanoporous PES may be beneficial for cell growth due the increased surface area available for tissue integration and cell attachment. A recent study compared electrospun PES nanofibrous scaffolds to conventional gauze and bandage for wound dressing applications. The nanofibrous PES scaffolds formed a porous structure that resulted in higher epithelial regeneration and greater fibroblast maturation. It also showed improved collagen deposition and faster edema resolution in a mouse model, when compared to that of a conventional gauze material.¹²

One property of PES that must be noted for external applications is its sensitivity to ultraviolet (UV) light. PES is known to degrade upon exposure to UV irradiation.¹³ If the polymer is used in a device that has the potential to be exposed to UV light, such as a wound dressing, it is imperative that it be protected to prevent degradation. PES may become exposed to UV from other sources. Since many PES polymerization¹⁴ and surface grafting procedures¹⁵ use UV sources, it is important to address and limit the amount of exposure during fabrication. Germicidal UV lamps, UV-sterilization procedures and exposure to sunlight also have the potential to damage exposed PES surfaces.

For the present study, TiO₂ was chosen over other metal oxides to assess its properties as a UV blocker and maintain the biocompatibility of PES. As opposed to using a metal oxide for UV protection in polymers, UV stabilizing organic compounds can also be added to polymers to absorb some of the harmful radiation.¹⁶ Their absorption spectrum, however, will vary between different types of chemicals. For medical applications, absorption of shortwave UV spectra used in most germicidal lamps¹⁷ or sunlight UV spectra may be of high importance. TiO₂ can be tuned with dopants to have photocatalytic activity

and absorbance at both UV and visible wavelengths.¹⁸⁻²⁰ The goal of this study was to determine 1) if TiO₂ can be coated onto PES at relatively low temperatures using Tetrakis (dimethylamino) titanium (TDMAT) and water as precursors, 2) whether the resulting TiO₂ thin film protects nanoporous PES from UV damage, and 3) the effects of UV-irradiated TiO₂-coated PES on macrophage cell viability.

Materials and Methods:

Sample Fabrication:

TiO₂ deposition was carried out in a custom-built, hotwall viscous flow tube reactor. The reactor, film stoichiometry and characterization have been described previously.²¹ TDMAT and water were used as the precursor and the reactant, respectively. TDMAT was purchased from a commercial source (Strem Chemicals, Newburyport, MA, USA). The precursor cell was maintained at 27°C and the precursor was dosed into the reactor using an argon carrier gas. Argon was obtained from a commercial source (National Welders, Charlotte, NC, USA) and was passed through a Drierite® Air Purifier (W.A. Hammond Drierite Co. Ltd., Xenia, OH, USA) to remove water. Deionized water (DI), obtained from a DI water system (Millipore, Billerica, MA) was used as the reactant and was kept at 27°C during the runs in a stainless steel bubbler. Water was introduced into the reactor without an argon carrier gas.

Polysulfone membranes for coating and controls were obtained from a commercial source (Whatman). These 0.8- μ m pore diameter membranes exhibited good sample-to-sample uniformity and had visible circular pores. A custom-made, quartz sample holder was used to hold the samples during ALD experiments. Five 3 cm \times 3 cm area spots were available for loading of samples on the quartz sample holder, whose positions were numbered one, pointing towards the flow, to five, pointing towards the pump; position one was the first to receive doses from the source lines. During ALD processing, pressure was maintained at 2 Torr. Cycles consisted of a 10-s argon purge, 5-s TDMAT dose, 10-s argon purge, and 5-s water dose. Prior to ALD processing, the substrates were introduced into the reactor, heated in vacuum ($5 \times 3 \times 10^{-6}$ Torr) to 100°C, and dried for 3 min. Optimal

processing times for purging and dosing were determined using quadrupole mass spectrometry (QMS) with a TC100 quadrupole mass spectrometer (Leybold-Inficon, East Syracuse, NY, USA). Scans were conducted over a range of 50 Da. Every point was measured with a dwell time of 16 ms. Because of the range and the capability of the QMS, data points could only be obtained every 2 s.

Thickness measurements of the TiO₂ films on silicon substrates were measured by ellipsometry, using an Auto EL ellipsometer (Rudolph Technologies Inc., Flanders, NJ, USA) and an incidence angle of 75°. Three measurements were made at random spots on each sample to analyze the uniformity of the TiO₂ films. Film thickness was obtained by applying 100 ALD cycles and approximated at 21 nm.

EDX/SEM:

Scanning electron microscopy (SEM) was performed using a JEOL 6400 Cold Field Emission Scanning Electron microscope (JEOL, Tokyo, Japan); this instrument was equipped with an energy dispersive X-ray (EDX) spectrometer attachment with a Link Pentafet detector (Link Analytical, Redwood City, CA) and a 4Pi Universal Spectral Engine pulse processor (4Pi Analytical, Hillsborough, NC). An accelerated voltage of 20 keV and 5 keV was used.

Cell Exposure:

TiO₂-coated nanoporous polyethersulfone (PES) membranes and uncoated 0.8- μ m diameter nanoporous PES membranes (47 mm PES, Whatman, Kent, UK) membranes were sterilized with a 254-nm UV source (UVP CL-1000, Upland, CA). All membranes were exposed for 30 minutes on each side to ensure that both sides were sterilized. Upon completion of ultraviolet sterilization, the membranes were cut to fit the bottom of the wells using a hole punch and placed into 96-well plates. Non-UV sterilized PES samples were cut and handled in a sterile environment, but did not undergo UV sterilization. RAW 264.7 cells (mouse leukemic monocyte macrophage cell line, ATCC, Manassas, VA) were added to the 96-well plates at a cell density of 2×10^5 cells/mL. Cells were then incubated for either 24 h or 48 h.

MTT Assay:

TiO₂-coated and uncoated PES membranes were assayed for potential toxicity using the MTT assay (CellTiter 96[®] Non-Radioactive Cell Proliferation Assay, Promega, Madison, WI). MTT medium was prepared by adding dye solution at a 15:100 ratio to media as specified by the kit. 15 μ L of MTT dye was added to each well to a total volume of 115 μ L. The plates were then incubated under cell culture conditions for 3 h. After each incubation period the Solubilization Solution/Stop Mix was added and the plates were incubated again for 1 h at 37°C. The wells were then mixed and the contents transferred to duplicate wells in a 96-well plate for absorbance measurements. Absorbance was measured at $\lambda = 570$ nm (reference wavelength 650 nm) using a 96-well OPTIMax plate reader (Molecular Devices, Sunnyvale, CA). Cells spiked with 5% dimethyl sulfoxide (DMSO) served as a positive

control. Cells grown on the bottom of standard tissue culture polystyrene (TCPS) wells were used as negative controls. The data were normalized to the TCPS controls and were expressed as percent viability. All experimental and control materials were tested for interference with MTT dye against TCPS and did not cause detectable interference with the assay.

Statistical Analysis:

The results from each data set were analyzed using Prism 4 statistical software (GraphPad Inc., La Jolla, CA). Results were expressed as mean \pm standard deviation. Statistical differences between control and treated group were assessed using one-way ANOVA, with a Bonferroni *post hoc* test. Each experiment was repeated at least 3 times with each assay in duplicate. A *P* value of less than 0.05 was considered statistically significant.

Results:

SEM images of the PES membranes revealed small crack formations throughout the porous structure of UV-treated PES (Figure 1D). The pore size on the TiO₂-coated PES was smaller than the Whatman 0.8 μm controls, which was evident from the SEM images (Figure 1A). The pore size was estimated to be approximately 350 nm for the coated sample. The uncoated samples had a nanoporous structure ranging from approximately 400 – 900 nm embedded within a larger microporous structure partially visible on the SEM. By calibrating the instrument and decreasing the SEM voltage, better resolution could be achieved so that the underlying pore structure of the controls could be observed/analyzed, while higher voltages showed the larger surface pore structure.

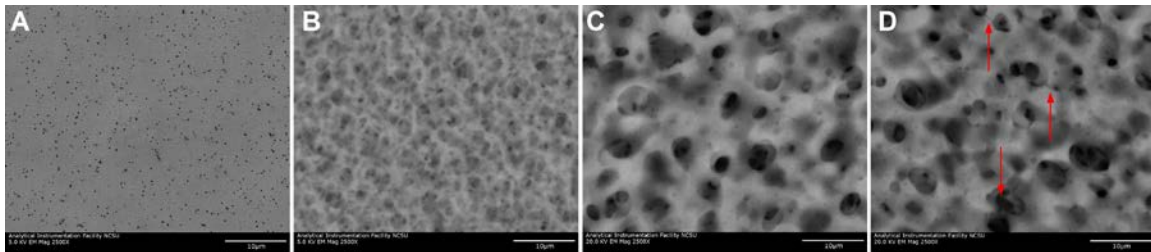


Figure 1. SEM images of PES: (A) 21 nm layer of TiO₂ on PES with smaller pores at 5 kV; (B) Uncoated, non-UV treated PES at 5 kV with visible fine pore structure; (C) Uncoated non-UV treated PES at 20 kV to emphasize large pores; (D) Uncoated UV-treated PES with visible crack formations (red arrows).

EDX analysis showed that Ti was present on the PES surface of the coated samples (Figure 2A). No elemental chemical differences were seen between UV-treated and non-treated PES surfaces (Figure 2B and 2C). UV sterilized samples visibly changed color from a plain white to a yellow hue after an exposure of 30 min on each side (Figure 3). The TiO₂-coated PES did not show any visible change in color after UV exposure.

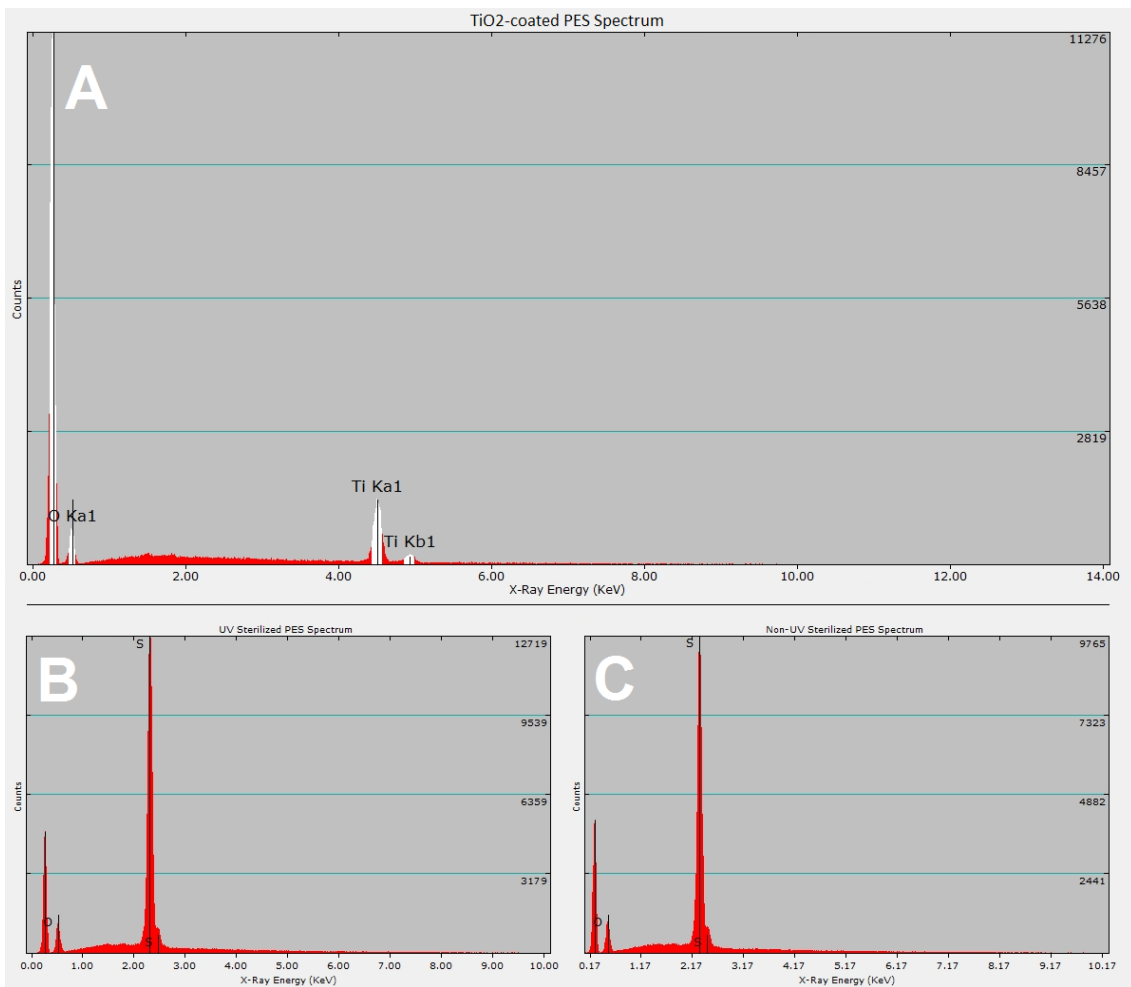


Figure 2. EDX Spectra confirming presence of (A) TiO₂ layer on PES, and nearly identical spectra of (B) UV-treated PES and (C) untreated PES.

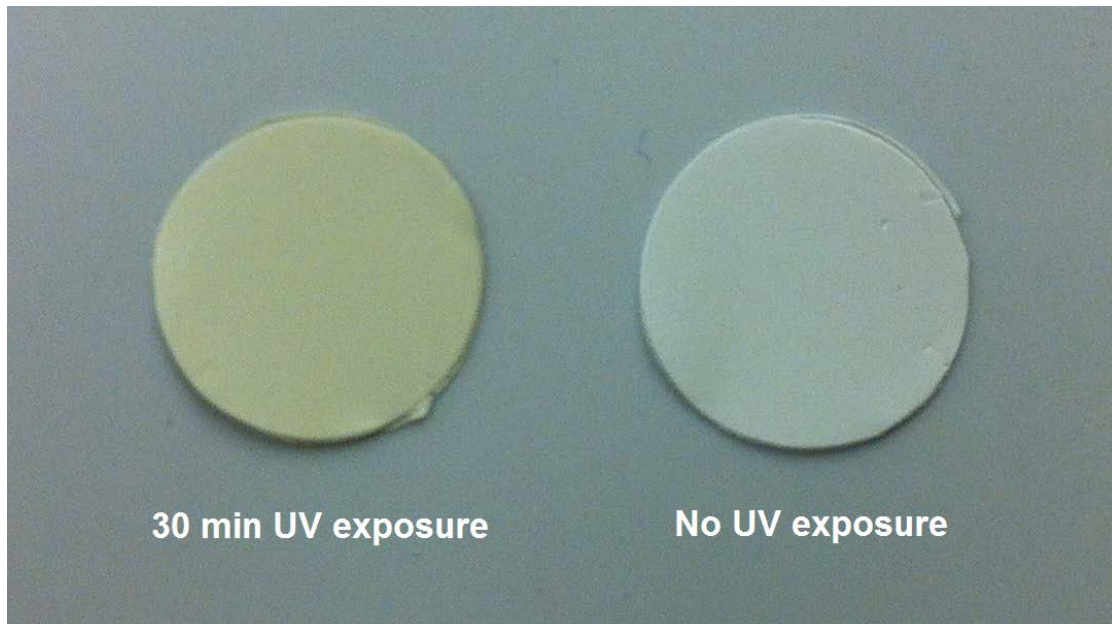


Figure 3. Color difference in uncoated PES cutouts before and after 30 min UV exposure on each side.

UV-treated PES without TiO_2 coatings showed the lowest cell viability using the MTT assay (Fig. 4). After 24 h or 48 h incubation of macrophages with UV-sterilized PES, cell viability was 51% and 18%, respectively, of control cells. In contrast, TiO_2 -coated PES exposed for 30 min to UV treatment did not affect cell viability, which was not significantly different from controls. After 24 h or 48 h incubation of macrophages with TiO_2 -coated PES, cell viability was 107% and 89%, respectively, of control cells. Non-sterilized (no UV exposure) PES exhibited no significant differences in cell viability compared to control cells; viability was 89% after 24 h exposure and 74% after 48 h exposure.

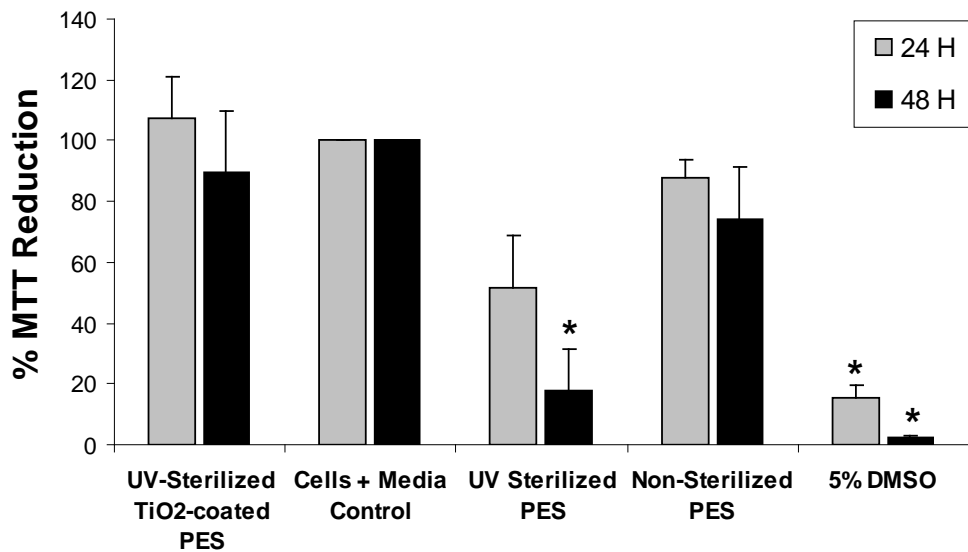


Figure 4. Macrophage cell viability of different PES surfaces and controls expressed as a percentage of the cell and media control. Percentages were calculated by comparing raw absorbance values from reduced MTT dye. Results are expressed as mean \pm SD from independent experiments. Significance is shown as the difference between a given group and control cells for raw data values * $p < 0.05$.

Discussion:

Surface properties of various polymers including PES are an important consideration for a wide range of applications, namely those in medicine. For any implanted device, exposed surfaces are the first points of contact with the biological environment. It is necessary to ensure that the surface of an implant is non-toxic before and after sterilization as well as throughout its lifetime. Devices are commonly sterilized using ethylene oxide (EO), gas plasma, gamma irradiation, and electron beam irradiation. UV-sterilization is generally not used for polymers due to the possibility of damage through chain degradation. Discoloration and cracking occurs in many polymers after short UV exposures, and longer exposures lead to further damage. UV irradiation is thought to create chain bond scission and produce free radicals on secondary or tertiary carbons,²² which then react with available oxygen and produce a color change. For PES, the C-S and C-O bonds are cleaved due to photon action and the color change from UV-induced polymer degradation is well characterized due to its use in UV exposure dosimeters.²³

PES has been shown to change both its surface and chemical properties due to photooxidative degradation during UV irradiation,²⁴ which was visible in the tested samples. TiO₂ thin film surfaces have relatively low cytotoxicity²⁵ and the material has applications for its UV-absorption properties in sun screens²⁶ as well as medical device coatings.²⁷ In the present study, atomic layer deposited (ALD) TiO₂ coatings were fabricated on nanoporous PES surfaces to assess its biocompatibility for potential biological and medical applications. Our results were consistent with the general low cytotoxicity of TiO₂ surfaces. UV-Irradiation of PES resulted in the polymer becoming highly cytotoxic to macrophages, which

was likely related to induction of changes in surface physical and/or chemical properties. In contrast, TiO₂-coated PES surfaces were well-tolerated by macrophages.

In the present study we demonstrate a novel approach to limiting UV damage to PES using an atomic layer deposited thin film coating of titanium dioxide (TiO₂). TiO₂ thin films can be coated onto both nanoparticles²⁸ and nanoscale surfaces²⁹ using atomic layer deposition (ALD) techniques. ALD was selected in order to preserve the nanoporous structure of PES substrates and provide a uniform self-limited coating. Low temperature ALD has been demonstrated with Tetrakis (dimethylamino) titanium (IV), or TDMAT on several substrates,^{30,31} but most processes involve plasma-assisted deposition on polymers.³² Additionally, low temperature ALD produces film coatings across a variety of polymers; however, the structural properties of the films depend strongly on the starting polymer composition.³³

TDMAT was chosen as the chemical precursor, since it is a known reagent that is easily available, readily undergoes hydrolysis with water to form TiO₂, and has a high growth rate per cycle (GPC) at relatively low temperatures.³⁴ In a review by Parsons *et al.*,³⁵ the authors underline the significance of reaction temperature and its influence on ALD layer saturation and uniformity for porous or other non-planar surfaces. The selected temperature has to be within a range where it thermally activates the deposition reaction, produces a self limiting half-reaction, and does not decompose the precursors. Relatively low ALD reaction temperatures also allow for wider ranging applications with other synthetic and biological polymer materials. Metal oxides, such as ZnO, for example, have been deposited using ALD to provide UV protection properties and prevent discoloration and embrittlement of paper.³⁶

The presence of cracking throughout the PES sample seen in Figure 1D may suggest polymer degradation and chain scission at the polymer surface. Since the cytotoxic response observed in macrophages was increased significantly after UV-irradiation of un-coated PES, there is the possibility of chemical leaching during degradation. The lack of evidence of degradation in the UV-treated TiO₂-coated polymer samples, however, correlated well with the lack of cytotoxicity. A possible solution to preventing UV damage could be to coat UV-sensitive polymers with nm-thick layers of TiO₂. A thin coating on the nanoscale is necessary for nanoporous or other materials with various nanotopographies in order to maintain the nanostructure of the original substrate. PES has good mechanical and thermal properties, which make it a suitable material for medical applications. If a PES device or material comes in contact with a UV source at any point during its storage or use, it may become damaged resulting in adverse health responses in patients. Although in our case the material had a noticeable change in color, our results do not distinguish whether the toxicity coincides accordingly with the amount of color change. The lack of noticeable color change on TiO₂-coated PES suggested that the vast majority of the PES surface was coated. The cytotoxicity and EDX results further support the idea that the TiO₂-layer is coated with few defects, which is an important consideration, since an uneven layer may allow partial areas to become damaged, discolored, and/or cytotoxic.

An additional benefit is that such photocatalytic activity from UV exposure magnifies the inherent antimicrobial action of TiO₂. The germicidal effect from UV exposure has been shown to significantly increase on surfaces coated with TiO₂³⁷ through photo-induced activation of TiO₂.^{38,39} This may have applications for sterilization of surfaces, reduction of

infections on wound dressings and other external applications from natural sunlight exposure. Although bacterial interactions are not addressed in the present study, it is a potential benefit of the proposed surface and may be addressed in the future.

Conclusions:

In summary, deposition of a TiO₂ ALD thin film was shown to be an effective non-cytotoxic UV-blocker for PES. The coated polymer did not change in color or show any physical damage or cracking. A uniform TiO₂ coating can protect sensitive polymer surfaces from UV sources such as germicidal lamps and sunlight exposure. External applications of PES such as wound dressings may also benefit from UV protection. Future studies will be needed in order to determine which physico-chemical changes, e.g., chemical leachates, are responsible for the cytotoxic response in macrophages and if this response is observed across other cell types. The optimal level of TiO₂ thickness could be additionally determined to match a given level of exposure.

Acknowledgements:

Peter E. Petrochenko is supported in part by a NSF/FDA Scholar-in-Residence Award #1041375.

Conflict-of-interest statement:

The authors declare no commercial or financial conflict of interest.

References:

- 1 Min, M. H. *et al.* Fabrication of Micro-Nano Structure Nanofibers by Solvent Etching. *J. Nanosci. Nanotechnol.* **11**, 6919-6925, doi:10.1166/jnn.2011.4224 (2011).
- 2 Lufrano, F. *et al.* Design of efficient methanol impermeable membranes for fuel cell applications. *Phys. Chem. Chem. Phys.* **14**, 2718-2726, doi:10.1039/c2cp23477g (2012).
- 3 Wang, M. *et al.* Phosphate removal model: An observational study of low-flux dialyzers in conventional hemodialysis therapy. *Hemodial. Int.* **16**, 363-376 (2012).
- 4 Sirolli, V., Ballone, E., Di Stante, S., Amoroso, L. & Bonomini, M. Cell activation and cellular-cellular interactions during hemodialysis: Effect of dialyzer membrane. *Int. J. Artif. Organs* **25**, 529-537 (2002).
- 5 Howdeshell, K. L. *et al.* Bisphenol A is released from used polycarbonate animal cages into water at room temperature. *Environ. Health Perspect.* **111**, 1180-1187, doi:10.1289/ehp.5993 (2003).
- 6 Dahe, G. J. *et al.* In Vivo Evaluation of the Biocompatibility of Surface Modified Hemodialysis Polysulfone Hollow Fibers in Rat. *PLoS One* **6**, doi:e25236

- 10.1371/journal.pone.0025236 (2011).
- 7 Unger, R. E. *et al.* Growth of human cells on polyethersulfone (PES) hollow fiber membranes. *Biomaterials* **26**, 1877-1884, doi:10.1016/j.biomaterials.2004.05.032 (2005).
 - 8 Andreattavanleyen, S., Smith, D. J., Bulgrin, J. P., Schafer, I. A. & Eckert, R. L. DELIVERY OF GROWTH-FACTOR TO WOUNDS USING A GENETICALLY-ENGINEERED BIOLOGICAL BANDAGE. *J. Biomed. Mater. Res.* **27**, 1201-1208 (1993).
 - 9 Sivaraman, K. M. *et al.* Porous polysulfone coatings for enhanced drug delivery. *Biomedical Microdevices* **14**, 603-612, doi:10.1007/s10544-012-9639-6 (2012).
 - 10 Christopherson, G. T., Song, H. & Mao, H. Q. The influence of fiber diameter of electrospun substrates on neural stem cell differentiation and proliferation. *Biomaterials* **30**, 556-564, doi:10.1016/j.biomaterials.2008.10.004 (2009).
 - 11 Attia, J. *et al.* Evaluation of Adhesion, Proliferation, and Functional Differentiation of Dermal Fibroblasts on Glycosaminoglycan-Coated Polysulfone Membranes. *Tissue Eng. Part A* **14**, 1687-1697, doi:10.1089/ten.tea.2007.0057 (2008).

- 12 Babaeijandaghi, F. *et al.* Accelerated Epidermal Regeneration and Improved Dermal Reconstruction Achieved by Polyethersulfone Nanofibers. *Tissue Eng. Part A* **16**, 3527-3536, doi:10.1089/ten.tea.2009.0829 (2010).
- 13 Colucci, M. Suggested interpretation of polysulfone dosimeter mathematical response. *Photochem Photobiol* **83**, 1428-1435, doi:10.1111/j.1751-1097.2007.00182.x (2007).
- 14 Deng, H. Y., Xu, Y. Y., Chen, Q. C., Wei, X. Z. & Zhu, B. K. High flux positively charged nanofiltration membranes prepared by UV-initiated graft polymerization of methacryloethyl trimethyl ammonium chloride (DMC) onto polysulfone membranes. *J. Membr. Sci.* **366**, 363-372, doi:10.1016/j.memsci.2010.10.029 (2011).
- 15 Rahimpour, A. UV photo-grafting of hydrophilic monomers onto the surface of nanoporous PES membranes for improving surface properties. *Desalination* **265**, 93-101, doi:10.1016/j.desal.2010.07.037 (2011).
- 16 Chai, R. D., Chen, S. J. & Zhang, J. Combined effect of hindered amine light stabilizer and ultraviolet absorbers on photodegradation of poly(vinyl chloride). *J. Vinyl Addit. Technol.* **18**, 17-25, doi:10.1002/vnl.20285 (2012).

- 17 Tasaki, T. *et al.* Degradation of methyl orange using short-wavelength UV irradiation with oxygen microbubbles. *J. Hazard. Mater.* **162**, 1103-1110, doi:10.1016/j.jhazmat.2008.05.162 (2009).
- 18 Xiang, X., Chang, D., Jiang, Y., Liu, C. M. & Zu, X. T. Optical properties of anatase TiO₂ films modified by N ion implantation. *Can. J. Phys.* **90**, 39-43, doi:10.1139/p11-136 (2012).
- 19 Liu, S., Guo, E. Y. & Yin, L. W. Tailored visible-light driven anatase TiO₂ photocatalysts based on controllable metal ion doping and ordered mesoporous structure. *J. Mater. Chem.* **22**, 5031-5041, doi:10.1039/c2jm15965a (2012).
- 20 Liu, L. F., Dong, X. Y., Yang, F. L. & Yu, J. C. Photocatalytic reduction of nitrate by Ag/TiO₂ catalyst. *Chin. J. Inorg. Chem.* **24**, 211-217 (2008).
- 21 Hyde, G. K. *et al.* Atomic layer deposition of titanium dioxide on cellulose acetate for enhanced hemostasis. *Biotechnol. J.* **6**, 213-223, doi:10.1002/biot.201000342 (2011).
- 22 Ayoub, A. & Massardier-Nageotte, V. The effect of UV-irradiation and molten medium on the mechanical and thermal properties of polystyrene-polycarbonate blends. *J. Appl. Polym. Sci.* **124**, 1096-1105, doi:10.1002/app.35094 (2012).

- 23 Parisi, A. V. & Kimlin, M. G. Personal solar UV exposure measurements employing modified polysulphone with an extended dynamic range. *Photochem Photobiol* **79**, 411-415, doi:10.1562/0031-8655(2004)79<411:spsuem>2.0.co;2 (2004).
- 24 Pei, X. Q. & Wang, Q. H. Ultraviolet irradiation induced changes in the surface of phenolphthalein poly(ether sulfone) film. *Appl. Surf. Sci.* **253**, 4550-4553, doi:10.1016/j.apsusc.2006.10.011 (2007).
- 25 Kommireddy, D. S., Sriram, S. M., Lvov, Y. M. & Mills, D. K. Stem cell attachment to layer-by-layer assembled TiO₂ nanoparticle thin films. *Biomaterials* **27**, 4296-4303, doi:10.1016/j.biomaterials.2006.03.042 (2006).
- 26 Krasnikov, I., Popov, A., Seteikin, A. & Myllyla, R. Influence of titanium dioxide nanoparticles on skin surface temperature at sunlight irradiation. *Biomedical Optics Express* **2**, 3278-3283 (2011).
- 27 Hu, H. *et al.* Antibacterial activity and increased bone marrow stem cell functions of Zn-incorporated TiO₂ coatings on titanium. *Acta Biomater.* **8**, 904-915, doi:10.1016/j.actbio.2011.09.031 (2012).

- 28 King, D. M. *et al.* Atomic layer deposition of TiO₂ films on particles in a fluidized bed reactor. *Powder Technol.* **183**, 356-363, doi:10.1016/j.powtec.2008.01.025 (2008).
- 29 Tupala, J., Kemell, M., Harkonen, E., Ritala, M. & Leskela, M. Preparation of regularly structured nanotubular TiO₂ thin films on ITO and their modification with thin ALD-grown layers. *Nanotechnology* **23**, doi:125707 10.1088/0957-4484/23/12/125707 (2012).
- 30 Park, J., Han, J. & Song, O. Crystallized Nano-thick TiO₂ Films with Low Temperature ALD Process. *Korean J. Met. Mater.* **48**, 449-455, doi:10.3365/kjmm.2010.48.05.449 (2010).
- 31 Kaariainen, T. O., Cameron, D. C. & Tanttari, M. Adhesion of Ti and TiC Coatings on PMMA Subject to Plasma Treatment: Effect of Intermediate Layers of Al₂O₃ and TiO₂ Deposited by Atomic Layer Deposition. *Plasma Processes Polym.* **6**, 631-641, doi:10.1002/ppap.200900038 (2009).
- 32 Kaariainen, T. O., Lehti, S., Kaariainen, M. L. & Cameron, D. C. Surface modification of polymers by plasma-assisted atomic layer deposition. *Surf. Coat. Technol.* **205**, S475-S479, doi:10.1016/j.surfcoat.2011.03.094 (2011).

- 33 Spagnola, J. C. *et al.* Surface and sub-surface reactions during low temperature aluminium oxide atomic layer deposition on fiber-forming polymers. *J. Mater. Chem.* **20**, 4213-4222, doi:10.1039/c0jm00355g (2010).
- 34 Xie, Q. *et al.* Atomic layer deposition of TiO₂ from tetrakis-dimethyl-amido titanium or Ti isopropoxide precursors and H₂O. *J. Appl. Phys.* **102**, doi:083521 10.1063/1.2798384 (2007).
- 35 Parsons, G. N., George, S. M. & Knez, M. Progress and future directions for atomic layer deposition and ALD-based chemistry. *Mrs Bulletin* **36**, 865-871, doi:10.1557/mrs.2011.238 (2011).
- 36 Hanson, C. A., Oldham, C. J. & Parsons, G. N. Paper deacidification and UV protection using ZnO atomic layer deposition. *Journal of Vacuum Science & Technology A* **30**, doi:10.1116/1.3656251 (2012).
- 37 Szczawinski, J., Tomaszewski, H., Jackowska-Tracz, A. & Szczawinska, M. E. Survival of *Staphylococcus aureus* exposed to UV radiation on the surface of ceramic tiles coated with TiO₂. *Pol J Vet Sci* **14**, 41-46, doi:10.2478/v10181-011-0006-y (2011).

- 38 Pleskova, S. N. *et al.* Photoinduced Bactericidal Activity of TiO₂ Films. *Applied Biochemistry and Microbiology* **47**, 23-26, doi:10.1134/s0003683811010091 (2011).
- 39 Ahn, S.-J., Han, J.-S., Lim, B.-S. & Lim, Y.-J. Comparison of Ultraviolet Light-Induced Photocatalytic Bactericidal Effect on Modified Titanium Implant Surfaces. *Int. J. Oral Maxillofac. Implants* **26**, 39-44 (2011).

CHAPTER 7: Laser 3D printing with sub-microscale resolution of porous elastomeric scaffolds for supporting human bone stem cells

Peter E. Petrochenko^{1, 2}, Jan Torgersen³, Peter Gruber³, Lucas A. Hicks², Jiwen Zheng¹, Girish Kumar¹, Roger J. Narayan², Peter L. Goering¹, Robert Liska⁴, Jürgen Stampfl³, Aleksandr Ovsianikov³

¹ Office of Science and Engineering Laboratories, U.S. Food and Drug Administration (FDA), Silver Spring, Maryland, USA.

² Joint Dept of Biomedical Engineering, University of North Carolina at Chapel Hill, NC, USA.

³ Institute of Materials Science and Technology, Vienna University of Technology, Favoritenstrasse 9-11, Vienna, Austria

⁴ Institute of Applied Synthetic Chemistry, Vienna University of Technology, Getreidemarkt 9, Vienna, Austria

Note:

The mention of commercial products, their sources, or their use in connection with material reported herein is not to be construed as either an actual or implied endorsement of such products by the Department of Health and Human Services.

Abstract:

A reproducible method is needed to fabricate 3D scaffold constructs that results in periodic and uniform structures with precise control at sub-micrometer and micrometer length scales. In this study, fabrication of scaffolds by two-photon polymerization (2PP) of a biodegradable urethane and acrylate-based photoelastomer is demonstrated. This material supports 2PP processing with sub-micrometer spatial resolution. The high photoreactivity of the biophotoelastomer permits 2PP processing at a scanning speed of 1000 mm/second, facilitating rapid fabrication of relatively large structures ($>5 \text{ mm}^3$). These structures are custom printed for *in vitro* assay screening in 96-well plates and are sufficiently flexible to enable facile handling and transplantation. Our results indicate that stable scaffolds with porosities of greater than 60% can be produced using 2PP. Human bone marrow stromal cells grown on 3D scaffolds exhibited increased growth and proliferation compared to smooth 2D scaffold controls. 3D scaffolds adsorbed larger amounts of protein than smooth 2D scaffolds due to their larger surface area; the scaffolds also allowed cells to attach in multiple planes and to completely infiltrate the porous scaffolds. The flexible photoelastomer material is biocompatible *in vitro* and is associated with facile handling, making it a viable candidate for further study of complex 3D-printed scaffolds.

Keywords:

3D printing, two photon polymerization (2PP), scaffold, biodegradable, elastomer

Introduction:

The success of any medical device or scaffold is influenced by the initial physical interaction between cells and the implant surface^{1,2}. Millions of patients are using cardiovascular, dental, orthopedic and other types of implanted devices (e.g., resorbable sutures, pacemakers, and hip joints) as well as external skin- and/or blood-contacting devices (e.g., wound dressings and catheters). The use of scaffolding materials is limited mostly to acellular scaffolds such as bone fillers or resorbable stents. There is growing interest, however, to use both cellular and acellular scaffolds for creating artificial tissues. In tissue engineering, cells are placed within a scaffold that guides cell development. The biocompatibility profile of these biomaterials is evaluated according to established consensus protocols (e.g., ISO 10993 – *Biological Evaluation of Medical Devices*)³. As per ISO 10993 standards, the biocompatibility of a medical device should be evaluated for both chemically- and physically-induced responses. Responses to chemical leachates from a biomaterial can be easily evaluated by using standard extraction protocols; however, there is no established test protocol available to evaluate cellular responses to structural/physical cues associated with the surface of biomaterial. In order to both understand the biocompatibility of biomaterials with surface cues, it is important to develop a robust and physiologically relevant *in vitro* cell culture model. Three-dimensional (3D) cell culture has advantages for studying cell responses to the surface texture and topography of medical devices and tissue engineering scaffolds since it provides a more physiologically-relevant platform for examining cell functions such as attachment and spreading [4]. As such, 3D cell culture may contribute to improving the overall biocompatibility evaluation of a biomedical device

material or a scaffold material⁴. When implanted, a biomedical device surface or scaffold surface is immediately coated with proteins as it comes in contact with blood, mesenchymal cells, and other non-hematopoietic cells. Therefore, multiple factors are considered when optimizing a biomedical device material or scaffold for such interactions. Surface chemistry, charge^{5,6}, the possibility of chemical leaching^{7,8}, protein adsorption⁹, and other factors¹⁰ are considered when selecting a biomaterial. Aside from chemical considerations, physical properties achieved during fabrication, such as geometry¹¹, stiffness¹², and roughness¹³ of the surface, can affect the manner in which cells adhere, proliferate, and differentiate. Several investigators have hypothesized that cell shape, elongation, and orientation play significant roles in guiding cell division^{14,15}, ultimately affecting the success of a biomedical device or scaffold. Stiffness, in particular, has a broad effect on cell signaling, motility, and proliferation¹⁶, with different optimal stiffness values corresponding to specific tissue types outlined in the discussion section.

Textured implant materials elicit different cell responses than smooth ones. Early studies of dental implants provide an example of the basic differences between smooth and textured surfaces; for example, smooth titanium shows poorer performance (lower osseointegration) than a textured version^{17,18}. This response has been clearly demonstrated in animal studies¹⁹, including the involvement of the Wnt (wingless integration) signal transduction pathway activation due to textured topography²⁰; however, the specific topographical features that elicit such changes in cell behavior and tissue response are not fully understood. Before addressing specific cellular processes and signaling pathways, it is necessary to establish a highly reproducible model for producing the 3D scaffold

environment that is responsible for modification of cell behavior and response. Various methods, such as fiber bonding, freeze drying, particulate leaching, spin casting, and solvent casting, exist for creating useful microscale and nanoscale texture and porosity in polymeric scaffold materials; however, these approaches have limited capabilities for directly creating custom 3D features from an exact replica of a 3D computer model. For example, freeze drying of collagen can be used to create a variety of structures with microscale porosities²¹; however, this technique does not enable creation of a wide variety of geometries achievable with 3D printing²².

Recent advances in microelectronics fabrication have allowed for surface geometry manipulation on the micrometer and sub-micrometer scales. Although some techniques such as photolithography, nanoimprinting, dip-pen lithography, and others have been available for a decade or longer²³, they have only recently begun to gain the attention of the medical device industry as a platform for understanding fundamental cell responses. In the present study, a novel technique emerging from the photolithography-based microfabrication field called two-photon polymerization (2PP) was employed²⁴. This 3D printing approach is achieved by two-photon absorption-based selective polymerization of a photosensitive monomer solution. The material is polymerized locally in the vicinity of the focal point of the beam of the femtosecond laser; no polymerization occurs outside the targeted area. By adjusting the number of laser pulses and the laser energy, the volume of the polymerized material can be controlled; selective polymerization of material below the diffraction limit of the wavelength of light can be obtained. 2PP can be used to produce custom scaffolds with resolution on the sub-micrometer scale²⁴. In addition to medical applications, use of 2PP for

nanophotonics²⁵ and telecommunications²⁶ applications has been considered. 2PP has been previously used to create tissue and cell scaffolds²⁷⁻³⁰, grids to examine cell behavior [30], ossicular replacement prostheses [31], and microneedle arrays with customized geometries [32, 33]. The synthesis of photosensitive materials can be adjusted to achieve desirable chemical and physical properties (e.g., swelling, stiffness, and degradation rate), allowing for custom manufacturing of tissue-specific biomaterials. It was recently demonstrated that 3D structures can be prepared from gelatin-based photopolymer formulations with high water content; live cells can be trapped within the gelatin-based photopolymer structures during 2PP processing²².

2PP laser printing has been used successfully with a variety of polymeric materials^{22,31}. The present study expands the use of 2PP to an elastomer material which allows the creation of durable large scale scaffolds which retain their shape, resist tearing, and have favorable stiffness for a variety of cell and tissue types. The resulting scaffolds are fabricated relatively rapidly and allow for facile handling with standardized biological assays. Fabricating scaffolds that are large enough to be fitted in a 96-well plate from a durable, non-brittle, and customizable material is a milestone for 2PP processing. We have previously shown the polymerizable photoelastomer used in the study to be suitable for 3D printing applications and to exhibit low chemical cytotoxicity³². In the present study, 3D-printed scaffold samples from this material were produced in sufficient numbers for evaluation of cell responses using: (1) a comparatively fast 2PP linear structuring speed of 1000 mm/second and (2) a customized scaffold geometry for use in standard 96 well plates. The porosity was modified to allow for long-term culture of bone marrow stromal cells and allow

them to easily explore the scaffold in all directions. The offset stacked honeycomb structure allowed for improved cell seeding by making it less likely for cells to fall through the pores during the seeding process. We concluded that the 3D scaffolds fabricated from the photoelastomer by 2PP exhibited no cytotoxicity; on the other hand, they induced cell growth and proliferation to a higher degree than smooth 2D structures and traditional smooth tissue culture well polystyrene (TCPS).

Methods:

Scaffold Design and Fabrication:

The scaffold material was based on a commercially available urethane diacrylate (UDA) resin known as Genomer 4215 (Rahn AG, Zurich, Switzerland). This aliphatic polyester urethane resin was chosen as base monomer since urethane groups have good cell adhesion behavior and polyUDAs have good structural rigidity. A combination of two reactive diluents, 2-hydroxyethyl acrylate and ethylene glycol bistioglycolate, was used to tailor the physical properties of the photoactive polymer^{33,34}. Cleavable bonds in the backbone of the resulting polymer from the addition of cleavable chain transfer agents made the polymer theoretically biodegradable to long term enzyme exposure. The M2CHK photoinitiator, specially designed to have a large two-photon absorption cross-section, was used at a concentration of 0.1 wt%³⁵. Irgacure 819 (Ciba, Basel, Switzerland) at a concentration of 0.2 wt% was used for UV-cured samples.

A Ti:sapphire femtosecond laser (High Q, Femtotrain) was used to illuminate samples with pulses at approximately 80 fs, with a 75 MHz repetition rate, and an 800 nm wavelength. An acousto-optical modulator was used to adjust beam intensity. The liquid monomer solution was suspended between two glass cover slips in a 1mm thick silicon well. Three linear translations allowed for complete 3D movement. The femtosecond laser beam was focused with a microscope objective into the sample. Patterns were obtained by scanning the beam within the sample by a galvo scanner (HurryScan, ScanLab) according to the input CAD model. A CCD camera was used for monitoring the process and taking live images as seen in Figure 1(c). A detailed description of the laser system setup has been previously

reported by our group ³⁶. A stacked cylindrical honeycomb structure design was used in order to provide cells with scaffold matrix contacts in multiple planes. The cylinder layers were printed on top of each other with an offset. When viewed from top, the center of a circle on the top layer was directly over the point joining three circles below (Figure 1(a)). Cylinders overlapped laterally and vertically to join the structure; the structure exhibited sufficient mechanical robustness for handling during characterization studies. Custom software was used to print the honeycomb structures. Arrays such as the one shown in Figure 2 were used to select the optimal writing speed, laser power, number of layers, and other parameters. After printing, structures were developed in a solution of 70% ethyl alcohol and 30% acetone. The acetone/alcohol solution is critical for removing any unpolymerized material (without swelling of the structured polymer) from the volume of the solution that was not illuminated with the laser beam.

Atomic Force Microscopy:

Atomic force microscopy (AFM) imaging was performed using a MFP-3D-Bio atomic force microscope (Asylum Research, Santa Barbara, CA). A Model #TAP150A silicon probe with resonant frequency of 150 kHz (Bruker, Santa Barbara, CA) was used for tapping mode AFM imaging in air. The samples were sequentially rinsed with acetone, ethanol, and Milli-Q water to remove any organic contaminations or particulates. The samples were subsequently blow dried with high purity nitrogen gas. To obtain Young's modulus data, flat elastomer samples were immersed in phosphate buffered saline (PBS), which served as a simulacrum of physiological fluid. The Hertz model of an AFM tip was used to estimate the Young's modulus by measuring the indentation; the force and spring

constant of the tip were known parameters and an approximation was used for the Poisson's ratio.

Cell Culture:

Following development, the printed scaffolds were transferred into 100% ethyl alcohol for 24 hours to remove any residual photoinitiator and unpolymerized monomer. Scaffolds were then washed in PBS for 1 hour and dried thoroughly under vacuum in order to facilitate movement of cells onto the scaffold. A single 10 μ L droplet of concentrated suspension containing approximately 8,000 human bone marrow stromal cells (hBMSCs) (Lonza, Walkersville, MD) was dropped onto the scaffold and allowed to adhere for two hours at 37 °C. A 0.2 mL aliquot of Mesenchymal Stem Cell Growth Medium (MSCGM) (Lonza, Walkersville, MD) was added to the 96-well and incubated for the appropriate time for biological assays in a humidified atmosphere containing 5% CO₂. Following incubation, the scaffolds were moved to a new well plate so cells grown on the polystyrene surfaces of the wells did not influence assay measurements. The process is summarized in a schematic shown in Figure 3.

Scanning Electron Microscopy (SEM):

Scanning electron microscopy (SEM) performed using a JSM 6390LV scanning electron microscope (JEOL, Tokyo, Japan). Low vacuum mode and minimal Ag sputtering were used for imaging of the cell samples. An accelerated voltage of 20 keV was used for imaging.

Preparation of Biological Specimens for SEM:

Cells were seeded at a density of 8000 cells/scaffold and cultured for 14 days. Specimens were rinsed with calcium-free PBS, fixed with 1% volume fraction of glutaraldehyde, subjected to graded alcohol dehydrations, rinsed with hexamethyldisilazane

(HMDS), and then sputter coated with silver as follows: 1) rinse cells 2X with PBS to remove media and debris; 2) then 1% glutaraldehyde in PBS for 1 hour; 3) then PBS for 10 minutes, twice; 4) - 9) then 10%, 25%, 50%, 70%, 95%, 100% ethanol, respectively (10 minutes each step); 10) then HMDS for 10 minutes (replaces critical point dryer). The specimens were subsequently placed on a piece of filter paper in a partially covered glass Petri and left to dry overnight. The samples were mounted, sputter coated with 20 nm of silver, and imaged using scanning electron microscopy. This procedure was performed in 96-well plates with 200 μ L of liquid per st

critical point dryer (CPD) with similar results.

MTT Assay:

Scaffolds were assayed for potential cytotoxicity using the MTT (3-[4,5-dimethyl-2-thiazol]-2,5-diphenyl-2H-tetrazolium bromide) assay (CellTiter 96[®] Non-Radioactive Cell Proliferation Assay) (Promega, Madison, WI). The MTT assay is based on an assessment of mitochondrial metabolic activity. MTT medium was prepared by adding dye solution at a 15:100 ratio to media as specified by the kit. A 15 μ L aliquot of MTT dye was added to each well in order to obtain a total volume of 100 μ L. The plates were then incubated under 37^o C, 5% CO₂, 95 % humidity cell culture conditions for three hours. After each incubation period, the Solubilization Solution/Stop Mix was added and the plates were incubated again for one hour at 37^oC. The wells were then mixed and the contents were transferred to duplicate wells in a 96-well plate for absorbance measurements. Absorbance was measured at a wavelength of 570 nm (reference wavelength=650 nm) using a 96-well OPTIMax plate reader (Molecular Devices, Sunnyvale, CA). Cells spiked with 5% and 10% dimethyl sulfoxide

(DMSO) served as a positive cytotoxicity control. The MTT dye was tested for interactions with the scaffold material; no interference was recorded from scaffolds that were incubated in 100% ethanol for 24 hours. The data were normalized to TCPS 96-well plate cut outs and expressed as percent viability. TCPS controls were obtained by using a hot hole punch, which was used to press out tablets with the same diameter as the photoelastomer 3D scaffolds.

Micro Bicinchoninic Acid (BCA) Assay:

Total amount of adsorbed proteins onto the porous 3D scaffolds, smooth elastomer material, and TCPS controls was quantified using a Micro Bicinchoninic Acid (BCA) Protein Assay Kit (Pierce Biotechnology, Rockford, IL). Samples were incubated with Phenol Red-free cell culture media containing 10% FBS. A preliminary study was conducted to optimize the time of exposure to cell culture medium, with exposures ranging from several seconds to hours. The optimal exposure time was determined to be 30 seconds, since the maximum amount of protein adhered to the surface after about 2 minutes. After 30 seconds of exposure to cell media, the membranes and controls were dip-washed in PBS three times to remove any loosely adsorbed proteins. Samples were placed into an appropriately labeled test tube containing 1 mL of working reagent provided by the test kit, mixed well, and incubated in a water bath at 60 °C for 1 hour. The test tubes were cooled to room temperature and absorbance was measured at a wavelength of 562 nm using an OPTIMax plate reader (Molecular Devices, Sunnyvale, CA). Absorbance was subtracted from blanks. Protein concentration was calculated by preparing a standard curve of the average corrected 562 nm reading for each BCA standard versus its concentration in $\mu\text{g/mL}$. Results for TCPS and

smooth elastomer were normalized to a projected area of a circle with a 3 mm radius and results for the 3D scaffold were normalized to a regular hexagon with a circumcircle radius of 3.075 mm; the circle and circumcircle had areas of 28.3 mm² and 24.6 mm², respectively.

DNA Proliferation Assay:

The Picogreen DNA assay was used to quantify cell numbers after 72 hours in culture on the scaffolds and the controls. Samples were washed with PBS and then incubated with lysis buffer (PBS with 0.175 U/mL Papain and 14.5 mmol/L L-cysteine) for 18 hours at 60 °C. After incubation, 0.1 mL of lysate was transferred to a clean 96-well plate and diluted with 0.1 mL of Picogreen reagent (Invitrogen, Carlsbad, CA), which was diluted per manufacturer's protocol. Fluorescence (excitation wavelength=485 nm, emission wavelength=538 nm) was measured using an OPTIMax plate reader (Molecular Devices, Sunnyvale, CA). A standard curve of known DNA concentration was used to estimate the total DNA content in each sample.

Statistical analysis:

The results from each data set were analyzed using Prism 4 statistical software (GraphPad Inc., La Jolla, CA). Results were expressed as mean \pm standard deviation. Statistical differences between the control and the treated group were assessed using a Student's T-test for comparing two means and one-way ANOVA, with a Bonferroni *post hoc* test if more than 2 means were compared. Samples were assayed in duplicate for each assay and each experiment was repeated at least 3 times. A *P* value of less than 0.05 was considered statistically significant. For some assays, data were normalized to cells growing in

standard tissue culture wells and expressed as percent viability. Significance level notation was expressed as * for $P < 0.05$, ** for $P < 0.01$, and *** for $P < 0.001$.

Results:

Design:

A photoelastomer material with good suitability for 3D printing was selected for this study. The formulation includes a highly viscous urethane based-acrylate, Genomer 4215, which was responsible for the elastomer-like behavior due to the presence of urethane groups. To adjust the viscosity, a reactive diluent, 2-hydroxyethyl acrylate, was used. To adjust the network density and therefore the final mechanical properties, a difunctional thiol was selected as chain transfer agent. Two different photoinitiators were used in the formulation. Irgacure 819 was used for simple flood curing of test specimens. M2CHK is a suitable two-photon initiator that is accessible by a straightforward one-step synthetic route. Final structures were printed at a speed of 1000 mm/second, laser power of 300 mW, and contained cylinders with outer and inner diameters of 260 μm and 200 μm , respectively (wall thickness= 60 μm). A voxel (volume pixel) refers to the volume of material that is polymerized from being illuminated with a focused laser beam. If there is no overlap between the voxels then the unpolymerized regions will separate. A distance of 500 nm between the voxels resulted in the nanotexture seen in Figure 1(a, c). The scaffold held together between the layers, since the voxels overlapped sufficiently along the vertical direction, essentially eliminating a gap between the layers. It could be easily manipulated, as seen in Figure 1(d), and placed into a 96-well plate. A hexagonal structure seen in Figure 1(b) was used to allow for easy handling and optimal coverage of the wells.

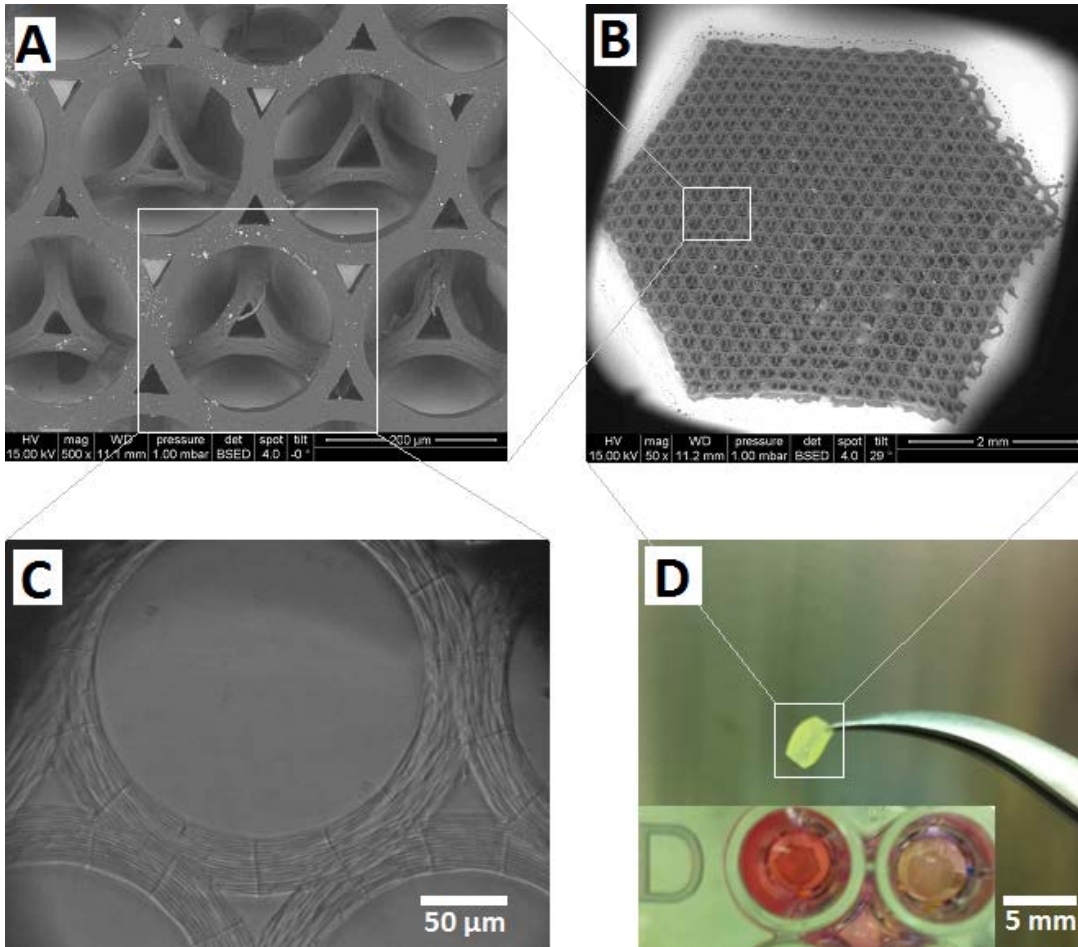


Figure 1. Scanning electron micrographs (A, B), optical micrograph (C), and color photograph (D) of scaffold structure. Enlarged views of 2PP scaffolds with overlapping offset cylinder layers (A), which are composed of a hexagonal porous features (B), a visible nanoscale texture, and structural reinforcements; visual monitoring of scaffold fabrication was performed using optical microscopy (C). Fabricated scaffolds were easily handled without damage and placed into 96-well plates (shown in (D)) for biological evaluation.

The scaffold remained flat on the bottom of the well. Optimal processing parameters were selected by varying two parameters at a time as shown in an array (Figure 2) with writing speed and laser power as variables. The final processing parameters were optimized; they included a 1 m/s scanning speed, 300 mW power, 500 nm hatch (width between illuminated voxels), 4 μm height between voxels (exposed layers), 22 layers per cylinder stack, and 10% overlap of cylinder structures (for joining individual cylinders into a honeycomb structure).

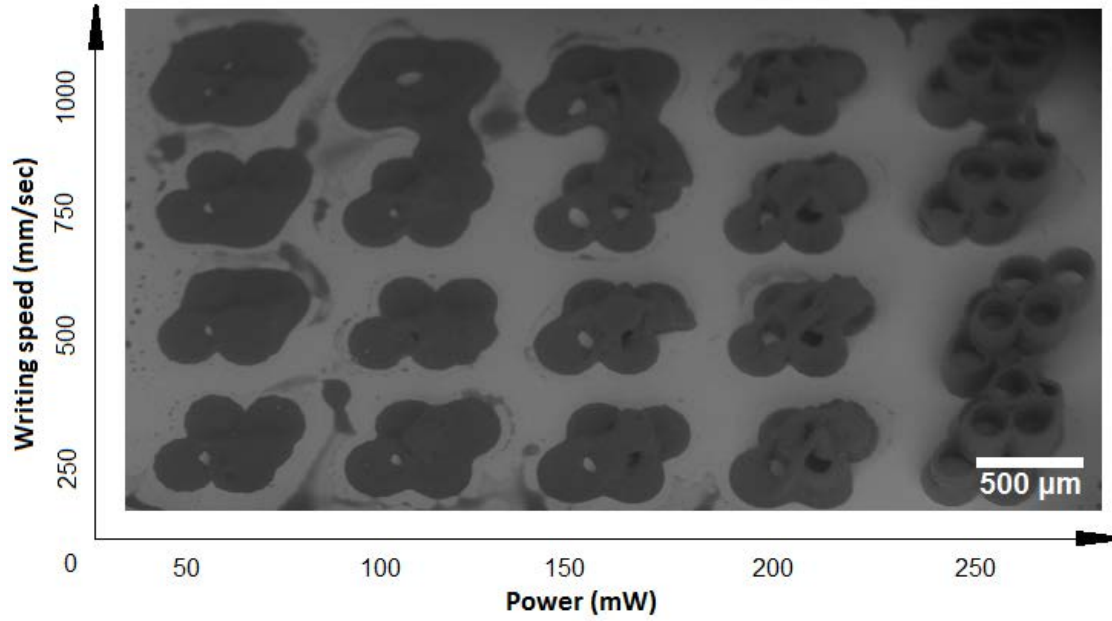


Figure 2. Sample 5 x 4 array of double layer cylinder test structures after developing in ethyl alcohol/acetone. Insufficient laser power causes structures to collapse during development. Similar arrays were used to determine multiple processing parameters.

Mechanical Characterization:

Preliminary tests were made using a relatively flat material that was polymerized by a CL-1000 UV lamp (UVP LLC, Upland, CA). After extracting the materials according to the procedure in Figure 3, the biological evaluation revealed that cells exhibited healthy morphology and provided comparable MTT results to cells grown in TCPS wells. Processing of material into 3D structures was subsequently undertaken. The offset cylindrical structure was made to be resilient and could be stretched and bent without any visible damage or cracking that could be observed using SEM. After being exposed to cell culture conditions for up to 30 days, the scaffolds retained their shape and porosity without showing significant structural damage. Amide crosslinks in the material are less subject to hydrolysis than other linkages such as ethers, for example. Amides are cleavable by enzymes *in vivo* and tend to degrade relatively slowly, thus providing the necessary durability for long term applications such as suturing or bone replacement. Physical and chemical properties of the material are discussed in detail by Baudis *et al*³². Although slight variation in Young's modulus was present on the surface, Young's modulus remained at 96 ± 2 kPa after incubation in PBS for both the flat material and the 3D scaffolds shown in Figure 1. The photoelastomer formulation described above with a value of 96 kPa was selected for further study due to the biomedical applicability of this material to skeletal muscle, arteries, and other tissues³⁷⁻³⁹.

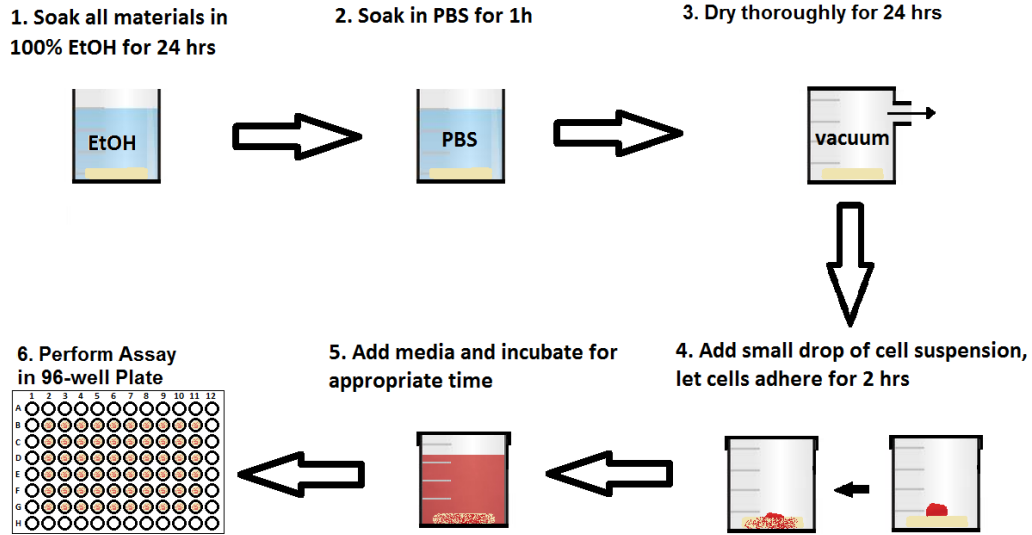


Figure 3. Scaffold cell culture method schematic, which describes cleaning of scaffolds in ethanol and PBS followed by vacuum drying. Cells were aliquoted in a small drop to the 3D scaffold, allowed to attach for 2 hours, covered in media, and examined with the appropriate assays.

Cell Viability:

The MTT assay was used to assess the cytotoxicity of the scaffolds. The assay measures the cell mitochondrial activity of oxidoreductive enzymes that reduce the tetrazolium (MTT) dye to an insoluble form, giving a purple color that is measured with a visible spectrophotometric plate reader. The measured reaction is representative of the overall cellular metabolic activity in the hBMSCs and corresponds to their viability. It should be noted that all of the disks and scaffolds were transferred into a new well after a minimum of 2 hours and that the 3D scaffolds appeared to retain cells extremely well following the initial seeding. The measurements were performed with assay supernatant only transferred from treatment wells. Cells on 3D scaffolds showed higher absorbance values than either smooth TCPS or smooth photoelastomer material disks of the same diameter after 48 hours (Figure 4).

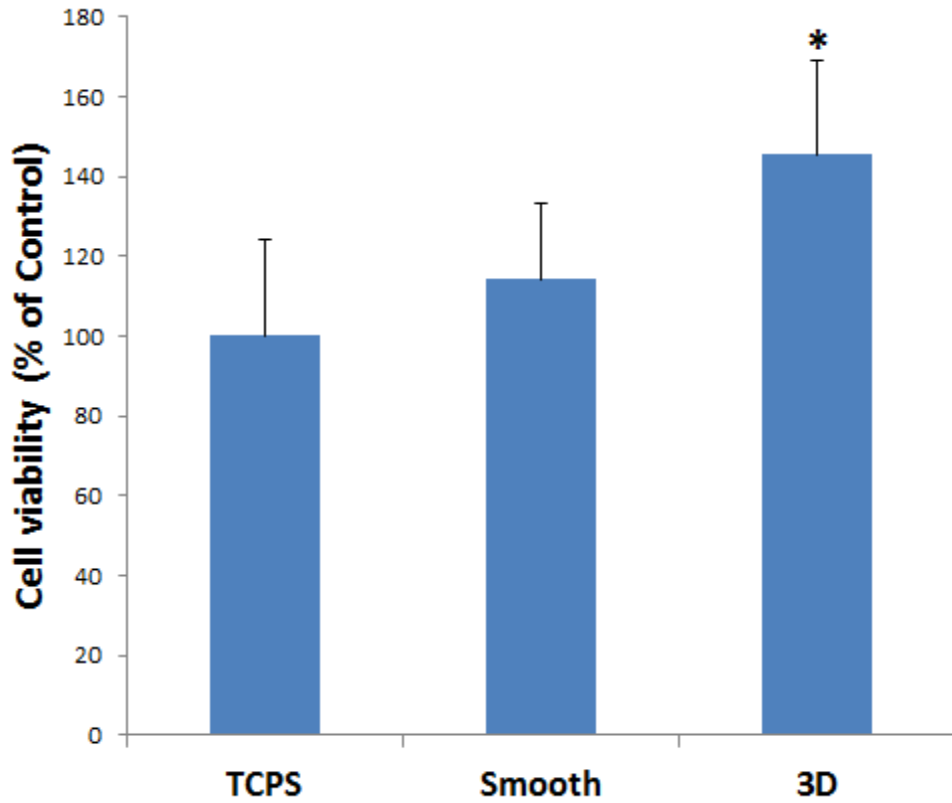


Figure 4. Human bone marrow stromal cell viability measured by the MTT assay after 48 hours of incubation. Cells growing on the 3D structure had higher viability, reflecting a higher number of adherent and metabolically active cells (asterisk indicates statistical significance, $p < 0.05$). Values shown are expressed as percent of tissue culture polystyrene controls.

Cell Proliferation:

Total DNA was calculated by lysing cells on the scaffolds and control materials and then measuring the amount of PicoGreen fluorescence relative to a standard curve (Figure 5). The 3D stacked cylinder scaffolds showed the highest fluorescence and the highest amounts of DNA present after 72 hours. This is a result of increased cell proliferation, better cell attachment than the smooth samples, and/or improved cell retention from seeding as well as during media changes and transfers. Control well plate cut-out disks, labeled “TCPS” in Figure 5, had the lowest total DNA value; however, the value was not significantly different from that of smooth elastomer disks. The amount of DNA present on the 3D scaffold was significantly greater than that on the TCPS.

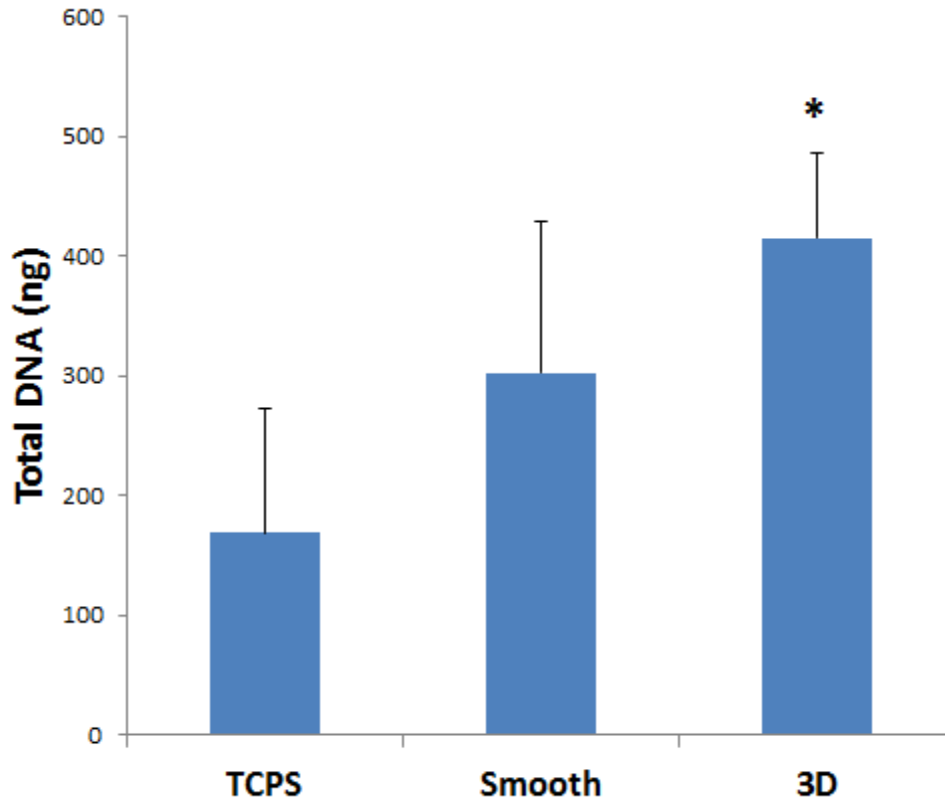


Figure 5. Total DNA content measured by the PicoGreen dsDNA fluorescent nucleic acid stain after 72 hours. 3D scaffolds show the largest amount of DNA present, possibly due to a greater surface area available for cell spreading and proliferation. The asterisk indicates that the 3D mean was statistically significant ($p < 0.05$) from tissue culture polystyrene.

Protein Adsorption:

Initial protein interaction plays an important role in cell adhesion, spreading, and proliferation^{40,41}. Protein adsorption after a 30 second incubation period was measured using the Micro BCA assay. This assay was used to determine if there were any differences in the amount of protein (concentration) that adhered to smooth and porous surfaces. The results in Figure 6 showed that the 3D scaffolds had twice as much adsorbed protein as the smooth samples. It should be noted that the 3D scaffolds had a higher surface area and a porous design. The smooth elastomer samples and TCPS controls did not show significantly different protein adsorption rates. The results suggest that the elastomer material behaves similarly to a standard tissue culture well under the simulated physiological conditions and that 3D scaffolds allow for greater protein adsorption due to differences in surface area and design.

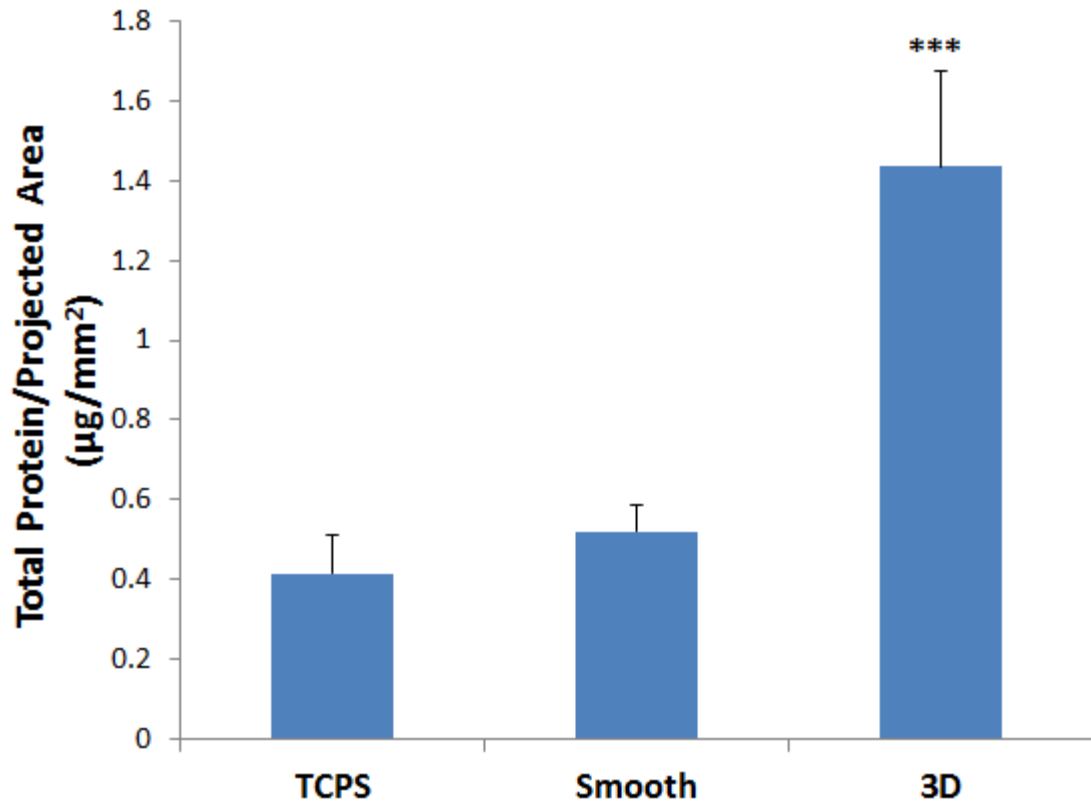


Figure 6. Total adsorbed protein content per unit projected area of a tissue culture polystyrene well plate, smooth elastomer material, and 3D scaffold elastomer material. 3D scaffold elastomer materials were shown to adsorb twice as much protein after 30 seconds as smooth elastomer materials or tissue culture polystyrene materials. Projected area was estimated as a circle for tissue culture polystyrene, as a circle for smooth elastomer, and as a hexagon for the 3D elastomer. The asterisk indicates that the 3D mean value was statistically significant ($p < 0.001$) for tissue culture polystyrene.

Cell Imaging:

The smooth elastomer samples showed normal cell morphology nearly indistinguishable from that of TCPS controls, as imaged by SEM (Figure 7(a)). Cells showed considerable spreading and minor overlap but maintained a single confluent layer. Smooth samples did not show fine cellular projections as seen in Figure 7(b, c). Cells seeded onto 3D scaffolds exhibited greater spreading and stretching; these cells exhibited much more elongated shapes and very thin cytoplasm projections. After the first week, cells invaded the cylindrical layers; however, the pores remained partially open (similar to the pore shown in Figure 7(b)). With additional time in culture, the pores became covered and the cells combined together to form a sheet over the pores (Figure 7(d)).

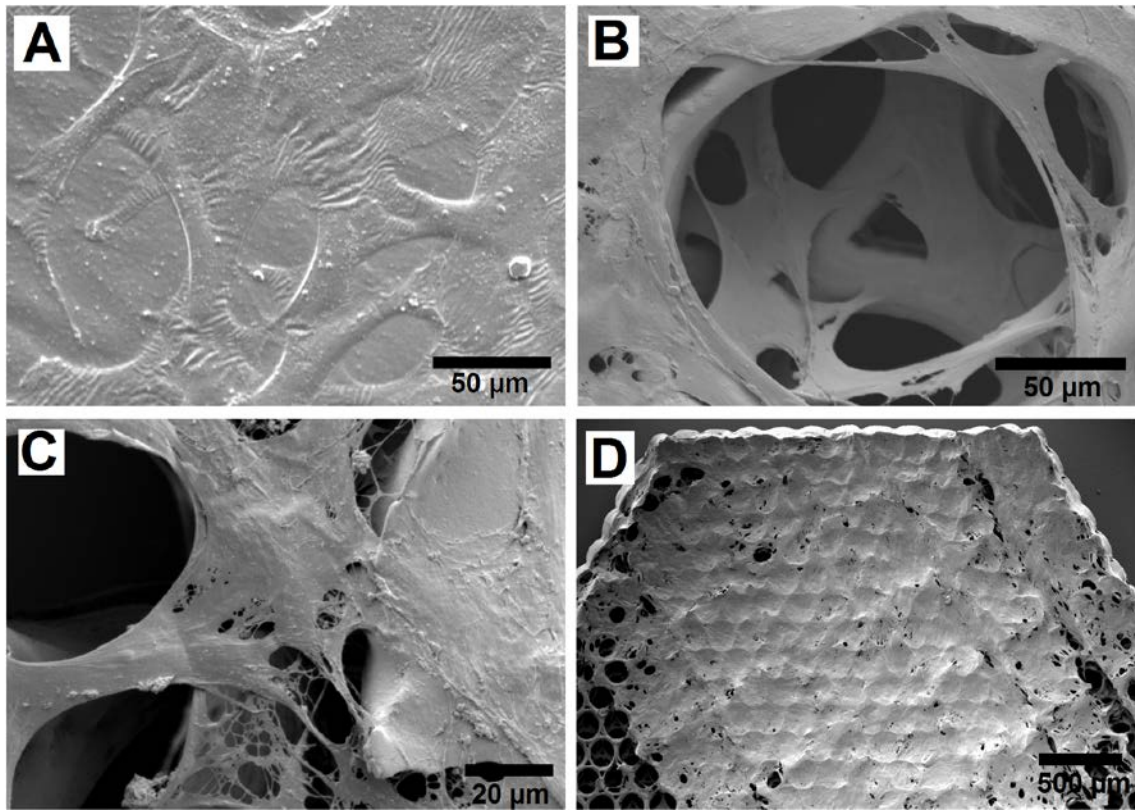


Figure 7. Representative SEM images of human bone marrow stem cell morphology on smooth and 3D samples. (A) The smooth elastomer shows normal cell spreading in two dimensions. The cylindrical structure allows for 3D cellular spreading (B-D) and formation of intricate filament networks as seen in (C). After approximately 14 days, the scaffolds are covered with a thick “tissue-like” cover as seen in (D). This cover penetrates into the pores and completely covers them when viewed from above.

Discussion:

The design of the 3D scaffold was an attempt to enable cell movement in all of the planes; in addition, it provided an intentional void for cells interaction with relatively large pores. If cells were not growing and actively exploring the scaffold in all of the directions, they would not be able to stretch across the distance of a pore. The cylinder inner diameter of 200 μm presented a sufficiently large distance that a single bone marrow stromal cell could not stretch across shortly after seeding. Rather than being a morphological parameter it was a geometric constraint. The results showed that cells were able to gradually create connections, slowly growing out and eventually closing the cylinder; a sheet of cells stretched across the opening (as seen in Figure 7(b-d)). Prior to this event, the cells invaded the inner surfaces of the scaffold as well. Therefore, the selected pore diameter (200 μm) indeed facilitated cell seeding and migration and at the same time supported tissue formation within the pores after initial cell proliferation. The “hatch” or distance between illuminated regions of the material was adjusted to give the structure nanoscale roughness as seen in Figure 1(a) and Figure 1(c). Previous work by Mozumder et al. indicates that introduction of surface roughness on the sub-micrometer scale may have a positive effect on cell adhesion and spreading⁴². Repetitive sub-micrometer surface nanotopography with a periodicity of 200 – 430 nm has been shown to increase human embryonic kidney cell proliferation⁴³. 3D cell culture gels induce higher cell proliferation than their 2-D culture counterparts for several types of cells, including smooth muscle, endothelial, and fibroblast cells⁴⁴. This study, however, does not address sub-micrometer topography, but rather develops a model for 3D cell culture with a flexible scaffold that has potential to protect the culture during transplantation and during other

mechanical stress exposures that require significant material elasticity. An inherent limitation of submicron laser 3D printing is that as resolution increases into the submicron range, the printing time also increases. Fine features require a more tightly focused beam that creates a smaller voxel. Therefore, less volume is polymerized at one time and requires the focal point to be moved along a greater distance, similar to how it is faster to paint a wall with a large paintbrush as opposed to a smaller one. One way to decrease printing time, however, is to increase the scanning speed, which in our study is relatively fast at 1000 mm/s.

Although cell response is dependent on a combination of factors (e.g., surface polarity and functional groups), scaffold stiffness also plays a major role in determining cell fate. For example, epithelial cells prefer softer polyacrylamide gels (150 Pa); increasing stiffness (up to 5 kPa) may promote malignant behavior⁴⁵. Muscle cells, however, show little cell response on soft polyacrylamide gels (1 kPa) and develop striations on gels with stiffness similar to muscle (up to 12 kPa)⁴⁶. Chondrocytes have been successfully cultured on alginate gels that are mechanically similar to cartilage with a Young's modulus at or greater than 75 kPa⁴⁷. The Young's modulus of the photoelastomer evaluated in the present study could be modified by altering the chemical composition; using the present formulation, the Young's modulus of 96 kPa was similar to that of skeletal muscle³⁷, the spinal cord³⁸, arteries³⁹, and other tissues⁴⁸. While the effects of stiffness are not necessarily required in static monolayer cell culture, a customized stiffness value is suitable for other biological applications such as use in mechanically dynamic culture or in implants; materials in these applications are subjected to repeated or cyclical mechanical stress. In the case of implantation, the possibility of failure is decreased by use of a flexible material that can withstand some wear and be

easily handled. The physical properties of a material may be further optimized for improved fixation with screws or sutures. The chemical biodegradation and swelling properties of a material can be adjusted depending on the intended use. Originally, this material was designed to have unusually high tear resistance for use in vascular grafts that are subject to sewing.

For *in vitro* cell culture assays, the custom printed 3D constructs were used in a standardized 96-well plate format; assays involving the 96-well plate format are traditionally performed on cell monolayers or more rarely on 3D culture inserts. The results showed that a 3D structure allows for cells to grow, spread, and proliferate more vigorously in the 96-well structure on a short time scale, potentially simulating cell behavior that is more closely related to the 3D cell environment *in vivo*. The case for 3D cell culture has been gaining strength as it is more closely related to the physiological and morphological environment experienced by cells within tissues. The apparently increased cell proliferation shown by MTT and DNA assays (Figures 4 and 5) on the 3D scaffolds compared to the smooth surfaces revealed that the 3D structure may influence cell response on a relatively short time scale of 3 days or less. The hBMSCs interacted with a much larger scaffold surface area with both the sub-micrometer (texture) and micrometer (geometry) scales; it may be possible that the higher cell proliferation rates resulted from increases in cell adhesion and retention on the 3D scaffolds. For the biological assays, all of the controls and scaffolds were transferred to new wells; some cells may have been lost in the control samples due to poor adhesion. The results suggest that 3D scaffold surface allowed for higher cell mobility and adhesion than the smooth surfaces; as such, the 3D scaffold surface provided better results than the smooth

surfaces in the acute toxicity assays described in the present study. The results of these short term *in vitro* tests provide a strong rationale for translation to *in vivo* and clinical studies. The elastomer performed as well as TCPS; in addition, the smooth elastomer demonstrated similar protein adsorption characteristics to TCPS. Although the 3D scaffold adsorbed a higher amount of protein than the smooth elastomer, this result can be attributed to the fact that the 3D scaffold has a higher available surface area for protein interaction. The highly porous 3D scaffold also may have trapped a small amount of residual proteins that were not washed off completely prior to the assay measurements. Since the Micro BCA assay offers a linear working range of 2 - 40 $\mu\text{g/mL}$, even a minor change in adsorbed protein may be detected. The greater amount of initially adhered protein on the 3D scaffold than on the smooth elastomer may explain the greater amount of cell adhesion on the 3D scaffold than on the smooth elastomer. In addition, the cells may become trapped within the 3D scaffold and may be able to create focal adhesions in multiple planes within the porous structure (see Figure 7(b)).

Conclusions:

The present study described use of 2PP structuring to create durable and large-scale photoactive polymer scaffolds. To our knowledge, this is the first paper to date showing the use of 2PP direct laser writing with an elastomer material. The advantages of 3D-printed stable scaffolds with sub-micrometer resolution pave the way for more complex small-scale medical devices, tissue engineering scaffolds, and implants. The resulting custom 3D-printed scaffolds are conducive to cell growth and may be tailored for use with other cell types by controlling (a) the nanoscale surface topography and (b) the overall geometric macroscale structure. The scaffolds in our study were designed for standardized 96-well plate assays in order to facilitate medium-throughput testing of various 3D constructs with tunable parameters. Using a similar approach, functional tissue-specific implants may be fabricated in the future in which the scaffold material requires high structural and textural complexity. The high reproducibility of 2PP makes it a useful approach to create standardized 3D *in vitro* cell testing platforms for future studies.

Acknowledgments:

Peter E. Petrochenko and Lucas Hicks were supported in part by NSF Award #936110. We thank Carl Simon for valuable scientific discussions. SEM imaging of the scaffolds was carried out using facilities at the University Service Centre for Transmission Electron Microscopy at the Vienna University of Technology.

References:

- 1 Le Guehennec, L., Soueidan, A., Layrolle, P. & Amouriq, Y. Surface treatments of titanium dental implants for rapid osseointegration. *Dent. Mater.* **23**, 844-854, doi:10.1016/j.dental.2006.06.025 (2007).
- 2 Harvey, A. G., Hill, E. W. & Bayat, A. Designing implant surface topography for improved biocompatibility. *Expert Rev. Med. Devices* **10**, 257-267 (2013).
- 3 in *Part 5: Tests for in vitro cytotoxicity* 1-34 (International Organization for Standardization, 2009).
- 4 Rampichova, M. *et al.* Elastic three-dimensional poly (epsilon-caprolactone) nanofibre scaffold enhances migration, proliferation and osteogenic differentiation of mesenchymal stem cells. *Cell Prolif.* **46**, 23-37, doi:10.1111/cpr.12001 (2013).
- 5 Llopis-Hernandez, V., Rico, P., Ballester-Beltran, J., Moratal, D. & Salmeron-Sanchez, M. Role of Surface Chemistry in Protein Remodeling at the Cell-Material Interface. *PLoS One* **6**, doi:10.1371/journal.pone.0019610 (2011).
- 6 Mrksich, M. A surface chemistry approach to studying cell adhesion. *Chem. Soc. Rev.* **29**, 267-273, doi:10.1039/a705397e (2000).

- 7 Verné, E. *et al.* Surface silver-doping of biocompatible glass to induce antibacterial properties. Part I: massive glass. *J. Mater. Sci.: Mater. Med.* **20**, 733-740 (2009).
- 8 Chakraborty, A., Kundu, B., Basu, D., Pal, T. K. & Nandi, S. K. In vivo bone response and interfacial properties of titanium-alloy implant with different designs in rabbit model with time. *Indian J. Dent. Res.* **22**, 277 (2011).
- 9 Aliuos, P. *et al.* Inhibition of fibroblast adhesion by covalently immobilized protein repellent polymer coatings studied by single cell force spectroscopy. *J. Biomed. Mater. Res. Part A* (2013).
- 10 Monchaux, E. & Vermette, P. Effects of surface properties and bioactivation of biomaterials on endothelial cells. *Frontiers in bioscience (Scholar edition)* **2**, 239 (2010).
- 11 Almeida, L. R. *et al.* New biotextiles for tissue engineering: development, characterization and in vitro cellular viability. *Acta Biomater.* **9**, 8167-8181, doi:10.1016/j.actbio.2013.05.019 (2013).
- 12 Winer, J. P., Janmey, P. A., McCormick, M. E. & Funaki, M. Bone marrow-derived human mesenchymal stem cells become quiescent on soft substrates but remain responsive to chemical or mechanical stimuli. *Tissue Eng. Part A* **15**, 147-154 (2008).

- 13 Qu, C. *et al.* Osteoblast behavior on various ultra short pulsed laser deposited surface coatings. *Materials Science and Engineering: C* (2012).
- 14 Théry, M. & Bornens, M. Cell shape and cell division. *Curr. Opin. Cell Biol.* **18**, 648-657, doi:10.1016/j.ceb.2006.10.001 (2006).
- 15 Théry, M. *et al.* The extracellular matrix guides the orientation of the cell division axis. *Nat. Cell Biol.* **7**, 947-953 (2005).
- 16 Wells, R. G. The role of matrix stiffness in regulating cell behavior. *Hepatology* **47**, 1394-1400 (2008).
- 17 Wiskott, H. & Belser, U. C. Lack of integration of smooth titanium surfaces: a working hypothesis based on strains generated in the surrounding bone. *Clin. Oral Implants Res.* **10**, 429-444 (1999).
- 18 Pilliar, R. M. Overview of surface variability of metallic endosseous dental implants: textured and porous surface-structured designs. *Implant Dent.* **7**, 305-314 (1998).
- 19 Hacking, S. *et al.* Surface roughness enhances the osseointegration of titanium headposts in non-human primates. *J. Neurosci. Methods* (2012).

- 20 Wang, W. *et al.* The role of the Wnt/ β -catenin pathway in the effect of implant topography on MG63 differentiation. *Biomaterials* (2012).
- 21 Murphy, C. M., Haugh, M. G. & O'Brien, F. J. The effect of mean pore size on cell attachment, proliferation and migration in collagen-glycosaminoglycan scaffolds for bone tissue engineering. *Biomaterials* **31**, 461-466, doi:10.1016/j.biomaterials.2009.09.063 (2010).
- 22 Ovsianikov, A. *et al.* Laser photofabrication of cell-containing hydrogel constructs. *Langmuir* (2013).
- 23 Liu, X., Chu, P. K. & Ding, C. Surface nano-functionalization of biomaterials. *Materials Science and Engineering: R: Reports* **70**, 275-302 (2010).
- 24 Ovsianikov, A., Mironov, V., Stampfl, J. & Liska, R. Engineering 3D cell-culture matrices: multiphoton processing technologies for biological and tissue engineering applications. *Expert Rev. Med. Devices* **9**, 613-633, doi:10.1586/erd.12.48 (2012).
- 25 Li, L. *et al.* High-Performance Microring Resonators Fabricated with Multiphoton Absorption Polymerization. *Advanced Materials* **20**, 3668-3671 (2008).

- 26 Deubel, M. *et al.* Direct laser writing of three-dimensional photonic-crystal templates for telecommunications. *Nat. Mater.* **3**, 444-447 (2004).
- 27 Tayalia, P., Mendonca, C. R., Baldacchini, T., Mooney, D. J. & Mazur, E. 3D Cell-Migration Studies using Two-Photon Engineered Polymer Scaffolds. *Advanced materials* **20**, 4494-4498 (2008).
- 28 Ovsianikov, A., Schlie, S., Ngezahayo, A., Haverich, A. & Chichkov, B. N. Two-photon polymerization technique for microfabrication of CAD-designed 3D scaffolds from commercially available photosensitive materials. *J. Tissue Eng. Regen. Med.* **1**, 443-449 (2007).
- 29 Raimondi, M. T. *et al.* 3D structural niches engineered via two-photon laser polymerization promote stem cell homing. *Acta Biomater.* (2012).
- 30 Ovsianikov, A. *et al.* Laser fabrication of 3D gelatin scaffolds for the generation of bioartificial tissues. *Materials* **4**, 288-299 (2011).
- 31 Claeysens, F. *et al.* Three-dimensional biodegradable structures fabricated by two-photon polymerization. *Langmuir* **25**, 3219-3223 (2009).

- 32 Baudis, S. *et al.* Elastomeric degradable biomaterials by photopolymerization-based CAD-CAM for vascular tissue engineering. *Biomed. Mater.* **6**, 055003 (2011).
- 33 Schuster, M. *et al.* Evaluation of biocompatible photopolymers I: Photoreactivity and mechanical properties of reactive diluents. *Journal of Macromolecular Science, Part A* **44**, 547-557 (2007).
- 34 Schuster, M. *et al.* Evaluation of biocompatible photopolymers II: further reactive diluents. *Monatshefte für Chemie-Chemical Monthly* **138**, 261-268 (2007).
- 35 Li, Z. *et al.* A Straightforward Synthesis and Structure–Activity Relationship of Highly Efficient Initiators for Two-Photon Polymerization. *Macromolecules* **46**, 352-361 (2013).
- 36 Torgersen, J. *et al.* Photo-sensitive hydrogels for three-dimensional laser microfabrication in the presence of whole organisms. *J. Biomed. Opt.* **17**, 105008-105008 (2012).
- 37 Linder-Ganz, E. & Gefen, A. Mechanical compression-induced pressure sores in rat hindlimb: muscle stiffness, histology, and computational models. *J. Appl. Physiol.* **96**, 2034-2049 (2004).

- 38 Chang, G.-L., Hung, T.-K. & Feng, W. W. An in-vivo measurement and analysis of viscoelastic properties of the spinal cord of cats. *J. Biomech. Eng.* **110**, 115 (1988).
- 39 Guo, X., Lu, X., Ren, H., Levin, E. R. & Kassab, G. S. Estrogen modulates the mechanical homeostasis of mouse arterial vessels through nitric oxide. *American Journal of Physiology-Heart and Circulatory Physiology* **290**, H1788-H1797 (2006).
- 40 Gang, W., Jiahui, W., Xiaofeng, C. & Yingjun, W. Impact of self-assembled monolayer films with specific chemical group on bFGF adsorption and endothelial cell growth on gold surface. *J. Biomed. Mater. Res. Part A* (2013).
- 41 Wang, J. *et al.* The effects of pulsed electromagnetic field on the functions of osteoblasts on implant surfaces with different topographies. *Acta Biomater.* (2013).
- 42 Mozumder, M. S., Zhu, J. & Perinpanayagam, H. Titania-polymeric powder coatings with nano-topography support enhanced human mesenchymal cell responses. *J. Biomed. Mater. Res. Part A* **100**, 2695-2709 (2012).
- 43 Rebollar, E. *et al.* Proliferation of aligned mammalian cells on laser-nanostructured polystyrene. *Biomaterials* **29**, 1796-1806 (2008).

- 44 Kishimoto, S. *et al.* Three-dimensional culture using human plasma-medium gel with fragmin/protamine microparticles for proliferation of various human cells. *Cytotechnology*, 1-12 (2013).
- 45 PaszeK, M. J. *et al.* Tensional homeostasis and the malignant phenotype. *Cancer Cell* **8**, 241-254 (2005).
- 46 Engler, A. J. *et al.* Myotubes differentiate optimally on substrates with tissue-like stiffness pathological implications for soft or stiff microenvironments. *The Journal of cell biology* **166**, 877-887 (2004).
- 47 Genes, N. G., Rowley, J. A., Mooney, D. J. & Bonassar, L. J. Effect of substrate mechanics on chondrocyte adhesion to modified alginate surfaces. *Arch. Biochem. Biophys.* **422**, 161-167 (2004).
- 48 Levental, I., Georges, P. C. & Janmey, P. A. Soft biological materials and their impact on cell function. *Soft Matter* **3**, 299-306 (2007).

CONCLUSIONS

The work described here signifies the importance of thoroughly characterizing nanomaterials prior to evaluating their biological responses. Each engineered nanomaterials model requires a unique set of applicable characterization techniques. For example, metallic coatings that cause toxicity through leaching require the amount and rate of the leachate to be quantified and optimized for best performance; for coatings or nanosurfaces that mediate cell response through nanotexture, a roughness value should be reported using atomic force microscopy to successfully determine the optimal parameter from biological studies. Direct control of the geometrical, physical, and chemical properties on a material surface opens the ability of preventing adverse responses and magnifying the desirable responses. Nanoscale surface morphology should be a consideration for any medical device material that comes in contact with the bodily environment. With the ability of 3D printing on the nanoscale described in this thesis it is possible to directly study the effect of nanoscale surface morphology and its effects on a variety of biological conditions and *in vivo* and *in vitro* models. Overall, the unique properties of nanomaterials reported in these studies have the potential to drastically improve the antimicrobial efficacy, biocompatibility and tissue regeneration capabilities of future and existing medical devices.